Thermally reduced graphene oxide using atmospheric pressure tube furnace for microsupercapacitor applications

By

Vusani Muswa Maphiri

A thesis submitted in partial fulfilment of the requirements for the degree of

DOCTOR OF PHILOSOPY (PH.D.)

in the Department of Physics

in the Faculty of Natural and Agricultural Science

University of Pretoria

Hatfield, Pretoria

Supervisor: Prof. N.I. Manyala

April 2022

Declaration

I, **Vusani Muswa Maphiri** declare that the thesis, which I hereby submit for the degree **Doctor of Philosophy (Ph.D)** at the University of Pretoria, is my own work and has not previously been submitted by me for a degree at this or any other tertiary institution.

SIGNATURE : _____ DATE: _____

Dedication

This thesis is dedicated to anyone who played any significant role in my life i.e. school teachers, university lectures, transport facilitator, friend and families.

I would also like to dedicate to certain individuals; my parents: My late father Mr Muhangwi Simon Mutswana and my mother Mrs Ntsundeni Merylin Maphiri. The mother of my baby Ms Adivhaho Netshianane; My first born babe Tshifaro Merylin Maphiri ;and the main members of families I stayed with: My aunty Mrs Tshilidzi Yvonne Maphiri – Ramukhithi, My brother Mr Azwianewi Patrick Mutswana (vho-pat) and his wife Mrs Collen Takalani Tshivhenga Mathala – Mutswana.

Acknowledgements

Most importantly and firstly I would like to thank "**NWALI**" for my good health and ability to complete this programme. Secondly, Prof Ncholu Manyala (my supervisor) for his endless support and effort to ensure the quality of this work. Many thanks to the administrative staff: Mrs S. Seymore and Mrs E. Meyburgh for their assistance.

I would also like to thank my sponsors for the financial support. This study was sponsored by the South African Research Chairs Initiative of the Department of Science and Technology, National Research Foundation (NRF) of South Africa (Grant No.61056) together with the financial support from the University of Pretoria.

My sincere thanks to the members (Mrs Erna Van Wilpe, Ms Charity Maepa and Mr Coenraad Snyman) of Microscopy and Microanalysis at the University of Pretoria, especially Ms Charity Maepa for her late hours assistance. I would like to express my appreciation to the many members (Dr Ndeye Fatou Sylla, Dr Ndeye Maty Ndiaye-Fall, Dr Kabir Oyedotun, Dr Delvina Japhet Tarimo, Dr Abdulmajid Mirghni, Dr Badr Mohammed, Dr Nkiyase Rantho, Dr Khavharendwe Rambau, Dr Bridget Mutuma, Dr. Jack Madito, Dr. Okikiola Olaniyan, Dr. Oladepo Fasakin, Mr Samba Sarr, Mrs Daba Bakhoum, Mr Tjatji Tjebane, Mrs Amanda Bubu, Ms Abigail Phori, Mrs Phathutshedzo Murovhi, Mr Gift Rutavi, Mr Itumeleng Ramatlhape, Mr Vianney Kitenge) of the carbon group (Prof. N. Manyala's group) from the University of Pretoria for their assistance, support and useful discussions. I would also like to thank Dr Ndeye Fatou Sylla, Dr. Oladepo Fasakin, Mr Samba Sarr, and Mrs Daba

Bakhoum for proofreading my manuscripts, while Mr Gift Rutavi proofread my manuscript and also thesis.

Lastly, I would like to thank my many brothers and sisters and mother for their encouragement, moral support, love and prayers. I am greatly indebted to my family i.e. my daughter Tshifaro Merylin Maphiri, and her Mother Adivhaho Netshianane for their moral support, love, prayers and feeding me. Thanks to my brothers: Mr Lovemore Mutswana, Dr Godfrey (Rumi) Mutswana, Mr Muneiwa Ramukhithi, and Mr Lufuno Maphiri; and my sisters: Ms Thuso Mashudu Ramukhithi and Ms Livhuwani Dakalo Knittor Ramakhithi; and my uncle Mr Douglas Ntshavheni Maphiri and My mother Ntsundeni Merylin Maphiri for everything.

Abstract

This work is divided into two parts, namely supercapacitor (SC) and microsupercapacitor (µ-SC). In general, the electrochemical properties of thermally reduced graphene oxide (TRGO) were investigated for both SC and µ-SC energy storage applications. The TRGO materials was successfully prepared via a series of techniques which mainly involved oxidation of graphite using Hummer's method and the reduction of the oxygen functional groups (OFGs) on graphene oxide (GO) using atmosphere pressure chemical vapour deposition (AP-CVD) in argon atmosphere. The structural, morphological and electrical characterization of substrate (Nickel foam (NF) and microscopic glass (MSG)), prepared GO and TRGO were done using X-ray diffraction (XRD), Raman spectrometer, Fourier transform infrared (FT-IR) spectrometer, ultraviolet–visible spectroscopy (UV-Vis), atomic force microscopy (AFM), scanning electron microscopy (SEM), energy-dispersive X-ray spectrometer (EDS) and four point probe (4PP).

In the SC part, TRGO-200 (numeric at the end of TRGO is the reducing temperature (RT)) was directly reduced on NF (current collector) using AP – CVD. This novel method avoided the use of binders such as polyvinylidene difluoride (PVDF) and conductive additives such as carbon nanotube and carbon acetylene black (CAB). This method is also simpler, quicker, cheaper and more effective compared to the conventional electrode preparation route where GO can be thermally reduced separately then prepared into a slurry paste with the aid of PVDF, CAB and drops of N-methyl-2-pyrolidone (NMP). The three electrode electrochemical measurements in 6 M KOH showed a maximum specific capacity of 52.64 mA h g^{-1} at 0.5 A g^{-1}, while the asymmetric device consisting of TRGO on NF and peanut shell activated carbon (PAC) i.e., TRGO/NF//PAC showed a specific energy and power of

18.72 W h kg^{-1} and 547.52 W kg^{-1} respectively at 1 A g^{-1}; and 14.10 W h kg^{-1} and 2.5 kW kg^{-1} at 5 Ag^{-1}. The high coulombic efficiency of 99% and capacitance retention of 80% was achieved indicating an outstanding stability, suggesting a significant progress in the fabrication of binder- less and conductive enhancement free electrodes for SC energy storage devices.

On the µ-SC part, a novel all – solid – state TRGO µ-SCs fabrication method was demonstrated which was simply prepared by an airbrush spray coater, AP – CVD and a mask – free AxiDraw sketching apparatus. Similar to the SC electrode preparation, this method was also quick, safe, easily scalable and cost effective as compared to the traditional µ-SC preparation method such as screen printing, inkjet printing, laser scribing and photolithography. The structure of TRGO on MSG was analysed using various techniques which indicated a decrease in oxygen functional groups (OFGs), leading to the restacking, and change of colour and transparency of the graphene sheets. The electrochemical performance showed a rectangular shape cyclic voltammetry (CV) depicting outstanding characteristics of electric double layer capacitor (EDLC) behaviour. The µ-SC with 14 digits per unit area (cm^{-2}) showed the highest capacitance over other µ-SCs with various numbers of digits per unit area i.e. 6, 22 and 26 cm^{-2}. This behaviour is mainly attributed to increased electric field strength as compared to the µ-SC with 6 cm^{-2}. When the number of digits per unit area exceeds 14 cm^{-2} the electric field increase leading to the charge flow leakage within the electrolyte and electrode (short circuit) decreasing the capacitance. In addition, this work clearly shows the importance of OFGs on the electrochemical performance of the SCs and µ-SCs, also narrating that binder-less and conductive additive-free devices can also deliver energy and power comparable to those with binder and conductive enhancement.

Table of Contents

Abbreviation and Symbol

Activated Carbons	ACs	Millilitre	ml
Ampere	A	Molar	M
Angular frequency	ω	Negative charge	Q_-
Area	A	Nickel foam	NF
Areal capacitor	C_{areal}	N-Methyl-2-pyrrolidone	NMP
Argon	Ar	Number of digits per unit area	n
Atmosphere pressure chemical vapour deposition	AP-CVD	One dimension	1D
Atomic force microscopy	AFM	Oxygen functional group	OFG
Breadth	B	Permeability	ε_r,
Capacitance	C	Phosphoric acid	H_3PO_4
Carbon acetylene black	(CAB)	Pi	π
Carbon nanotubes	CNTs	Poly(methyl methacrylate)	PMMA
Charge transfer resistance	R_{CT}	Polyaniline	PANI
Chemical vapour deposition	CVD	Polytetrafluoroethylene	PTFE
Copper	Cu	Polyvinylidene fluoride	PVDF
Counter electrode	CE	Polyvinylidene fluoride	PVDF
Current	i	Positive charge	Q_+
Cyclic voltammetry	CV	Potassium chloride	KCL
Degree Celsius	℃	Potassium hydroxide	KOH
Deionised water	DW	Potassium permanganate	$KMnO_4$
Dielectric constant	ε_0	Potential (voltage)	ΔV
Diffuse layer	C_D	Pseudocapacitor	PC
Direct current	I	Real capacitance	C'
Distance	d	real impedance	Z'
Edge	E	Redox electrochemical capacitor	REC

Electrical double-layer capacitor	EDLC	Reduced graphene oxide	rGO
Electrochemical impedance spectroscopy	EIS	Reducing temperature	RT
Electrolyte resistance	R_e	Reference electrode	RE
Energy-dispersive X-ray spectroscopy	EDS	Relaxation time	τ
Equivalent series resistance	ESR	Revolution pre minute	rpm
Faraday's constant	F	Scanning electron microscopy	SEM
Fifth generation	5G	Scanning rate	v
Four point probe	4PP	Second	s
Fourier transform infrared spectrometer	FTIR	Silver/silver chloride	Ag/AgCl
Frequency	f	Solution resistance	R_s
Full width half maximum	FWHM	Specific capacitance	C_s
Galvanostatic charge-discharge	GCD	Specific current	I_s
Gas constant	R	Specific energy	E_s
Gram	g	Specific power	P_s
Graphene oxide	GO	Square metre	m^2
Hour	h	Stern layer	C_H
Hybrid capacitors	HCs	Successive ionic layer adsorption and reaction	SILAR
Hydrogen peroxide	H_2O_2	Sulphuric acid	H_2SO_4
Imaginary capacitance	C''	Supercapacitor	SC
Imaginary impedance	Z"	Temperature	T
Impedance	$\boldsymbol{Z}$	Thermal reduced graphene oxide	TRGO
Integral	$\int$	Three dimension	3D
Interspace distance	i	Time	t
Ion diffusion coefficient	D	Total capacitance	C_T
Kilogram	kg	Two dimension	2D
Length	L	Ultraviolet–visible spectroscopy	UV-Vis

Litre	L	Underpotential deposition	UPD
Manganese sulphate	$MnSO_4$	Warburg coefficient	σ_w
Maximum power	P_{max}	Water	H_2O
Metre	m	Width	W
Microscopic glass	MSG	Working electrode	WE
Microsupercapacitor	µ-SC	X-ray diffraction	XRD
Milligram	mg		

List of Figures

List of Equations

Chapter 1 Introduction

1.1. Problem statement

According to the Worldometer [1], the world population is currently at approximately 8 billion people with a growth rate of about 1.09% per year which amounts to 83 million new people per year. South Africa is ranked number 25 on the list of population per country with a population of roughly 58 million and a population growth rate of 1.20% per year [2]. This rapid increase of people leads to an increase in demand of consumables. The increase of consumables is also propelled by the development of new technology. Energy in the form of electricity is one of the most important consumable in this era. Researchers, scientists and engineers in the fields of energy development, production and storage are constantly facing challenges to meet the ever growing energy demand.

Most of the utilized energy today is attained from non-renewable resources and the minority is derived from renewable sources as illustrated in Figure 1.1. Non-renewable energy sources have a negative impact on our environment, the burning of fossil fuel leaves huge amounts of carbon-based by-product materials in our environment which causes global warming leading to climate change and its related problems such as the rising of sea level and melting of polar ice [3–5]. The nuclear fission of uranium ($^{238}_{92}U$) also imposes a challenge of disposing the nuclear waste materials which are very dangerous to all living organisms. The nuclear wastes are very radioactive and have very long decay times (half-lives), thus the waste stay radioactive for a long time [6,7] These non-renewable energy sources are sooner or later doomed to run out, hence we cannot heavily rely on them. Thus, due to the high energy

consumption and depletion of natural resources the world is engaged in a transition to alternative energy to meet this ever increasing energy demand.

On the other hand, renewable energy sources seem to be the sustainable alternative energy that is ecologically healthy and beneficial to our present and future generations i.e. renewable energy sources have significantly less side effects as compared to the non-renewable energy sources. Renewable energy has attracted outstanding attention within the past few years. Only a fraction of energy used today is generated from renewable sources such as solar, wind, tidal and many more (Figure 1.1). Most of these renewable energy sources are highly intermittent in nature and have to be supplemented by energy storage device such as a supercapacitor (SC) [8–10], batteries [11,12] and flywheels [13].

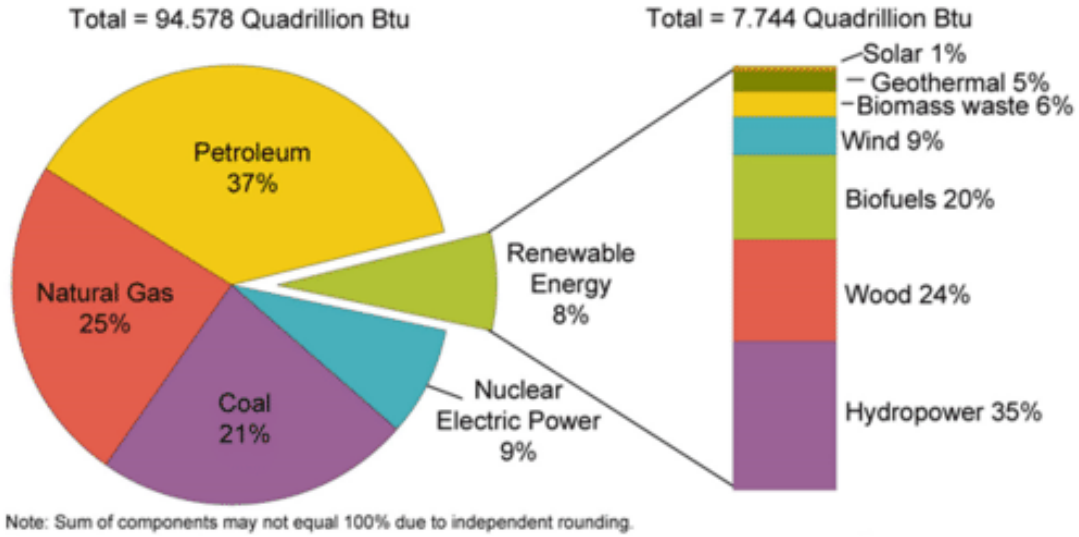

Figure 1.1. United States energy consumption by Energy Source, Renewable energy sources contributed 8% of the energy consumption (2009). Source: U.S. Energy Information Administration [14]

Currently, batteries such as lithium – ion have high specific energy, while supercapacitors (SC) have the highest specific power. In addition to that, SCs are cost effective, have a long life span, are efficient and environmentally safe. SCs are promising energy storage devices of the future, which have been developed and advanced for the past few decades. The significance of SCs in comparison to other energy storage and conversion devices is displayed within the Ragone plot in Figure 1.2. It can be seen that SC spans the gap between batteries and conventional capacitors. The specific energy of SC is smaller in comparison to that of battery or fuel cells. Hence, researchers focus on the fabrication of SC devices that can compete with other energy storage and conversion devices while preserving the traditional capacitor properties such as long life span and high specific power.

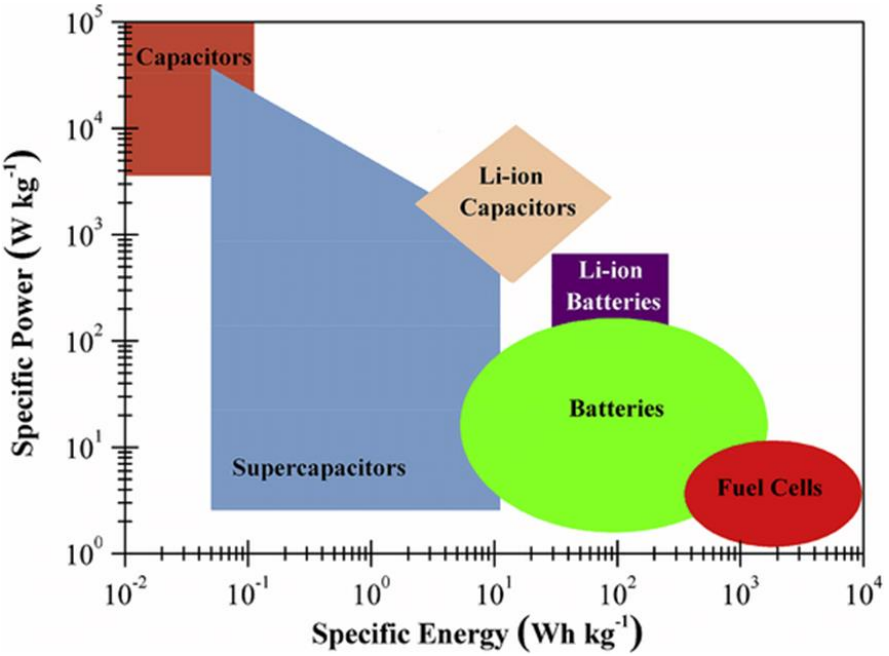

Figure 1.2. Ragone plot for different kinds of electrochemical energy storage devices. Adapted from Ref.[15,16]

Due to the properties of conventional SC and advancement of technology within fields such as medical, textile, mobile and nano-energy generation requires revamped, redesigned and miniaturised SC energy storage with different architecture labelled as microsupercapacitors (μ-SC) [17–19]. In addition, the advent of the fifth-generation (5G) communication within the fourth industrial revolution has further encouraged the development and spread of research interest in fields of the Internet of Things (IoTs) and microdevices [20,21]. In these applications, a huge and diverse network of interconnected microdevices communicate with each other without any sort of delay and disruption. This will ultimately benefit various fields such as wearable electronics and personal health care. Given this ubiquity of self-operating microdevices that can be embedded in the human body, it is of great importance to develop and advance maintenance-free micropower devices that will be compatible with the microdevices. These maintenance free micro-energy storages (μ-SCs) can be fabricated differently for various purposes and applications such as in textile for wearable technology using Polyethylene terephthalate (PET) and two dimensional materials (i.e. graphene/graphene oxide) as illustrated in Figure 1.3. In medical applications μ-SC is applicable in heart-beat monitoring device (pacemaker) and electronic stethoscope among others.

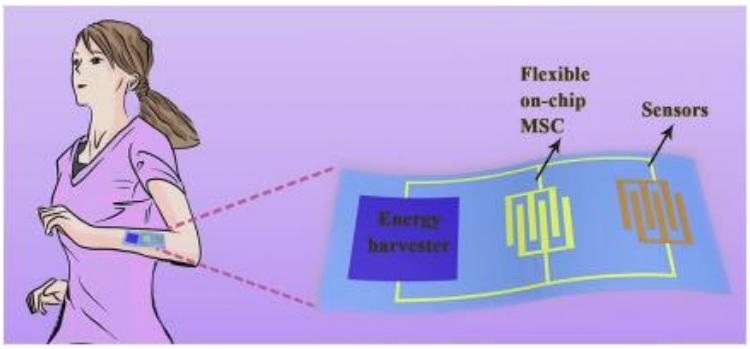

Figure 1.3. Flexible on chip μ-SC integrated on a circuit for wearable technology [22]

These µ-SC devices give us the ability to develop and construct distributed energy sources that harvest energy from renewable source such as mechanical triggering and vibration i.e. triboelectric nanogenerator [23] and piezoelectric [24]. Most of the energy harvest modules for µ-SCs are not so conventional like solar and wind energy sources. To fabricate such self-powered devices, an energy storage module is of very importance since it captures charges from the energy harvesting module onto the sensors (for obtaining data) and transponder (for transmitting the captured data). Micro-batteries or thin film batteries store more energy than µ-SCs, which would make them candidates for micro-power source, however, due to the limited lifespan and lower specific power, the microdevices will require periodic maintenance and replacement of the micro-batteries. In addition, the low specific power will also limit the functions of the high power requiring microdevices. Thus, µ-SCs are the best choice for IoTs devices and other microdevices since they have a long lifespan i.e., less maintenance and have high specific power.

This work demonstrates a simple, novel method of fabricating µ-SC energy storage devices, which is composed of a spray coater, AP-CVD and an AxiDraw sketching apparatus. Unlike other methods which required extremely expensive equipment, are time demanding and are health threatening such as laser techniques [25], and photolithography [26,27]. Thus, this method yielded results comparable to those from other techniques.

1.2. Aim and objectives

The aims and objectives of this research are divided into two parts as follows:

1. Synthesis and characterization of TRGO electrodes for high-performance binder-less and conductive agent free SC applications
    - Oxidation of graphite using Hummers' method into GO, then reducing the GO directly on nickel foam current collector
    - Evaluation of the effects of reducing temperature of the SC performances
    - Effects of different aqueous electrolytes on the SC performance

2. Synthesis and characterization of TRGO μ-SCs for micro-energy storage
    - Preparation and characterisation of TRGO thin films
    - Fabrication of μ-SCs from the TRGO thin films and evaluation of the effects of reducing temperature on the electrochemical performance
    - Evaluation of the effect of the interdigitated electrodes on the supercapacitor performance

1.3. Thesis layout

This thesis is divided into five chapters: *Chapter 1* gives an insight to the study problem together with aims and objectives of this study. *Chapter 2* provides the fundamental information on SCs and μ-SCs. *Chapter 3* gives a brief description of the experimental techniques used to prepare the active materials, fabricate the electrochemical devices and the techniques used to analyse the active material. The detailed discussions of the obtained results are discussed in subchapters of *Chapter 4*, while *Chapter 5* contains the general conclusion and future work.

Reference

[1] http://www.worldometers.info/world-population/ (obtained on the 9/04/2022)

[2] https://www.worldometers.info/world-population/south-africa-population/ (obtained on the 9/04/2022)

[3] R. Yasmeen, R. Tao, W. Jie, I.U.H. Padda, W.U.H. Shah, The repercussions of business cycles on renewable & non-renewable energy consumption structure: Evidence from OECD countries, Renew. Energy. 190 (2022) 572–583. https://doi.org/10.1016/J.RENENE.2022.03.138.

[4] Y. Kuo, A. Maneengam, C. Phan The, N. Binh An, A.A. Nassani, M. Haffar, A. Qadus, Fresh evidence on environmental quality measures using natural resources, renewable energy, non-renewable energy and economic growth for 10 Asian nations from CS-ARDL technique, Fuel. 320 (2022) 123914. https://doi.org/10.1016/J.FUEL.2022.123914.

[5] M.M. Islam, M. Irfan, M. Shahbaz, X.V. Vo, Renewable and non-renewable energy consumption in Bangladesh: The relative influencing profiles of economic factors, urbanization, physical infrastructure and institutional quality, Renew. Energy. 184 (2022) 1130–1149. https://doi.org/10.1016/J.RENENE.2021.12.020.

[6] Z. Xixi, Q. Tongkun, W. Yecheng, Optimal strategies for stakeholders of Fukushima

nuclear waste water discharge in Japan, Mar. Policy. 135 (2022) 104881. https://doi.org/10.1016/J.MARPOL.2021.104881.

[7] J. Richter, M.J. Bernstein, M. Farooque, The process to find a process for governance: Nuclear waste management and consent-based siting in the United States, Energy Res. Soc. Sci. 87 (2022) 102473. https://doi.org/10.1016/J.ERSS.2021.102473.

[8] D.J. Tarimo, K.O. Oyedotun, A.A. Mirghni, N.F. Sylla, N. Manyala, High energy and excellent stability asymmetric supercapacitor derived from sulphur-reduced graphene oxide/manganese dioxide composite and activated carbon from peanut shell, Electrochim. Acta. 353 (2020) 136498. https://doi.org/10.1016/j.electacta.2020.136498.

[9] G. Rutavi, D.J. Tarimo, V.M. Maphiri, M. Ncholu, Two-step electrodeposition of Hausmannite sulphur reduced graphene oxide and cobalt-nickel layered double hydroxide heterostructure for high-performance supercapacitor, (2022) 1–14. https://doi.org/10.1002/er.7922.

[10] D.T. Bakhoum, K.O. Oyedotun, S. Sarr, N.F. Sylla, V.M. Maphiri, N.M. Ndiaye, B.D. Ngom, N. Manyala, A study of porous carbon structures derived from composite of cross-linked polymers and reduced graphene oxide for supercapacitor applications, J. Energy Storage. 51 (2022) 104476. https://doi.org/10.1016/J.EST.2022.104476.

[11] A. Rafie, J.W. Kim, K.K. Sarode, V. Kalra, A review on the use of carbonate-based electrolytes in Li-S batteries: A comprehensive approach enabling solid-solid direct

conversion reaction, Energy Storage Mater. (2022). https://doi.org/10.1016/J.ENSM.2022.03.015.

[12] J. Wang, Y. Zhang, L. Yu, K. Cui, T. Fu, H. Mao, Effective separation and recovery of valuable metals from waste Ni-based batteries: A comprehensive review, Chem. Eng. J. 439 (2022) 135767. https://doi.org/10.1016/J.CEJ.2022.135767.

[13] B. Wang, F. Gao, R. Stanislawski, G. Królczyk, P. Gardoni, Z. Li, Fusion Deconvolution for Reliability Analysis of A Flywheel-Battery Hybrid Energy Storage System, J. Energy Storage. 49 (2022) 104095. https://doi.org/10.1016/J.EST.2022.104095.

[14] Https://Openoregon.Pressbooks.Pub/Envirobiology/Chapter/11-2-Non-Renewable-Energy-Sources/ (obtained on the 9/04/2022)

[15] L.M. Da Silva, R. Cesar, C.M.R. Moreira, J.H.M. Santos, L.G. De Souza, B.M. Pires, R. Vicentini, W. Nunes, H. Zanin, Reviewing the fundamentals of supercapacitors and the difficulties involving the analysis of the electrochemical findings obtained for porous electrode materials, Energy Storage Mater. 27 (2020) 555–590. https://doi.org/10.1016/J.ENSM.2019.12.015.

[16] R. Kötz, M. Carlen, Principles and applications of electrochemical capacitors, Electrochim. Acta. 45 (2000) 2483–2498. https://doi.org/10.1016/S0013-4686(00)00354-6.

[17] Y.M. Yue, N.Liu, Y. Ma, Y.Gao, Microsupercapacitor, M. Composite, Si. Highly Self-Healable 3D MXene-Graphene Composite Aerogel, Acs Nano. (2018)

[18] G. Xiong, C. Meng, R.G. Reifenberger, P.P. Irazoqui, T.S. Fisher, A review of graphene-based electrochemical microsupercapacitors, Electroanalysis. 26 (2014) 30–51. https://doi.org/10.1002/elan.201300238.

[19] V.M. Maphiri, G. Rutavi, N.F. Sylla, S.A. Adewinbi, O. Fasakin, N. Man-, Novel Thermally Reduced Graphene Oxide Microsupercapacitor Fabricated via Mask - Free AxiDraw Direct Writing, (2021) 1–15.

[20] K. Zhan, Sports and health big data system based on 5G network and Internet of Things system, Microprocess. Microsyst. 80 (2021) 103363. https://doi.org/10.1016/J.MICPRO.2020.103363.

[21] L. Long, Research on status information monitoring of power equipment based on Internet of Things, Energy Reports. 8 (2022) 281–286. https://doi.org/10.1016/J.EGYR.2022.01.018.

[22] R. Jia, G. Shen, F. Qu, D. Chen, Flexible on-chip micro-supercapacitors: Efficient power units for wearable electronics, Energy Storage Mater. 27 (2020) 169–186. https://doi.org/10.1016/J.ENSM.2020.01.030.

[23] C. Lin, J. Yu, Z. Hua, J. Lan, H. Huang, D. Lu, S. Cao, X. Ma, Development progress, performance enhancement routes, and applications of paper-based triboelectric

nanogenerators, Chem. Eng. J. 430 (2022) 132559. https://doi.org/10.1016/J.CEJ.2021.132559.

[24] S. Yu, Y. Tai, J. Milam-Guerrero, J. Nam, N. V. Myung, Electrospun organic piezoelectric nanofibers and their energy and bio applications, Nano Energy. (2022) 107174. https://doi.org/10.1016/J.NANOEN.2022.107174.

[25] L. Liu, D. Ye, Y. Yu, L. Liu, Y. Wu, Carbon-based flexible micro-supercapacitor fabrication via mask-free ambient micro-plasma-jet etching, Carbon N. Y. 111 (2017) 121–127. https://doi.org/10.1016/j.carbon.2016.09.037.

[26] Z. Niu, L. Zhang, L. Liu, B. Zhu, H. Dong, X. Chen, All-solid-state flexible ultrathin micro-supercapacitors based on graphene, Adv. Mater. 25 (2013) 4035–4042. https://doi.org/10.1002/adma.201301332.

[27] E. Kim, B.J. Lee, K. Maleski, Y. Chae, Y. Lee, Y. Gogotsi, C.W. Ahn, Microsupercapacitor with a 500 nm gap between MXene/CNT electrodes, Nano Energy. 81 (2021) 105616. https://doi.org/10.1016/J.NANOEN.2020.105616.

Chapter 2 Literature review

2.1. Introduction

This work focuses on the application of supercapacitors (SCs) and microsupercapacitors (μ-SCs) for electrochemical energy storage. This chapter briefly presents a summary of the different energy storage mechanisms of SCs, μ-SCs architecture, different interdigitated μ-SCs fabrication techniques, and other parameters involved in the performance evaluation such as electrolytes and electrode materials. Fabrication and testing of an electrochemical cell as well as evaluation of the electrode materials and microsupercapacitors are also discussed.

2.2. Microsupercapacitors

Supercapacitors (SCs) also known as electrochemical capacitors (ECs) or ultracapacitors have attracted overwhelming attention in areas of applications such as electric vehicles, cameras, and cell phones [1,2]. These devices are an alternative to batteries even though they have low specific energy. However, they counteract batteries by possessing better electrochemical properties such as unlimited lifespan (theoretically calculated to > 10^5 cycles) and higher specific power. Moreover, these SCs devices span the gap between batteries and conventional capacitors by having higher specific energy than the latter and

having higher specific power than the former [3]. The Ragone plot of SCs and other electrochemical energy storage and energy conversion devices is displayed in Figure 1.2, while the Ragone plot of microsupercapacitors (μ-SCs), other micro-energy storage devices and micro-power consuming devices such as sensors and short-range communications modules like Bluetooth is displayed in Figure 2.1. It can be seen that even if the energy stored in μ-SC is very small, it is enough to power short-range communication and sensors for several minutes at a charge [4].

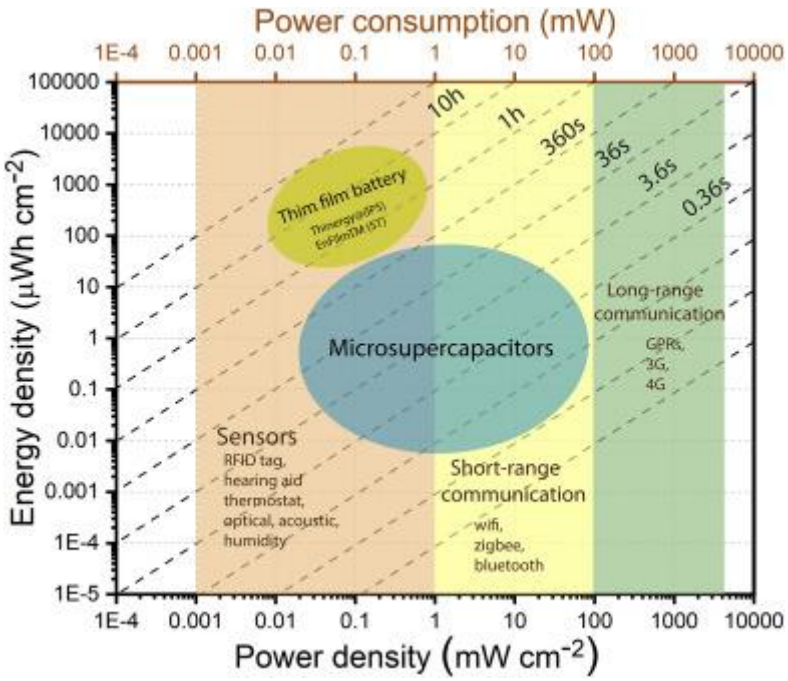

Figure 2.1. Ragone plot illustrating power and energy density (also referred to as specific energy and power) of microsupercapacitors, while the shaded vertical areas illustrate power consumption of various microelectronics (top axis). Adopted from Ref [4]

Conventional SCs are too bulky and rigid for microdevices. In addition, the assembly methods of conventional SCs is not compatible with the fabrication and preparation techniques of the microelectronic industries. Note that, the term “microsupercapacitor (μ-SC)” describe SC devices which are small enough to be integrated into a microelectronic device and these μ-SCs come in many flavours (architecture design) as displayed in Figure 2.2. These devices can be classified into one, two and three dimension configurations. Among these different architectures the in-plane interdigital design also referred to as interdigitated or comb-style design offers more advantage than other μ-SCs design in that they have a shorter ion diffusion distance, easy integration with other microelectronics, substantial exposure of the electrode material to the electrolyte and they allow fabrication of electrodes from various materials [4–8]. This work is focused on the interdigitated design mainly due to the above mentioned properties. Within this work the term “μ-SC” also refers to the interdigitated design unless specified.

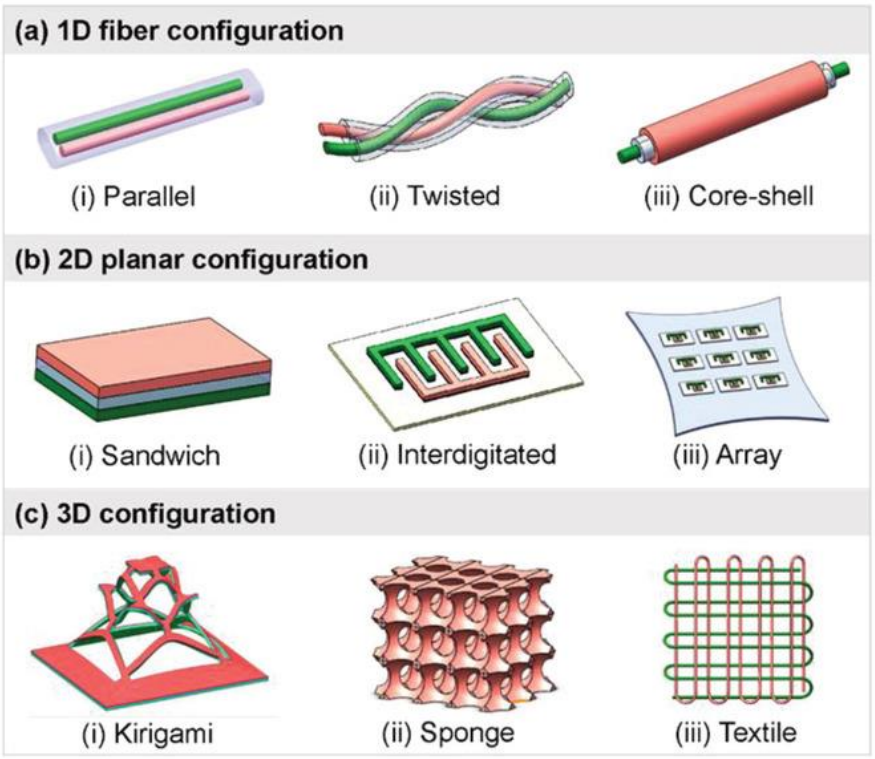

Figure 2.2. Various architectures of μ-SC. (a) one dimensional (linear, fibre) configuration composed of parallel, twisted and core-shell; (b) two dimensional (planar) configurations composed of sandwich, interdigitated and array; and (c) three-dimensional configuration composed of kirigami, sponge and textile. Adopted from Ref [5]

2.3. Energy storage mechanisms

In general, SCs and μ-SCs can be classified based on their electrochemical charge storage mechanisms, which are electric double layer capacitor (EDLC), pseudocapacitors also referred to as redox electrochemical capacitors (RECs) and hybrid capacitors which is the

union of the EDLC and RECs. The flow chart in Figure 2.3 displays an overview of each class of SC energy storage mechanism and indicates an example of the active materials within those classes.

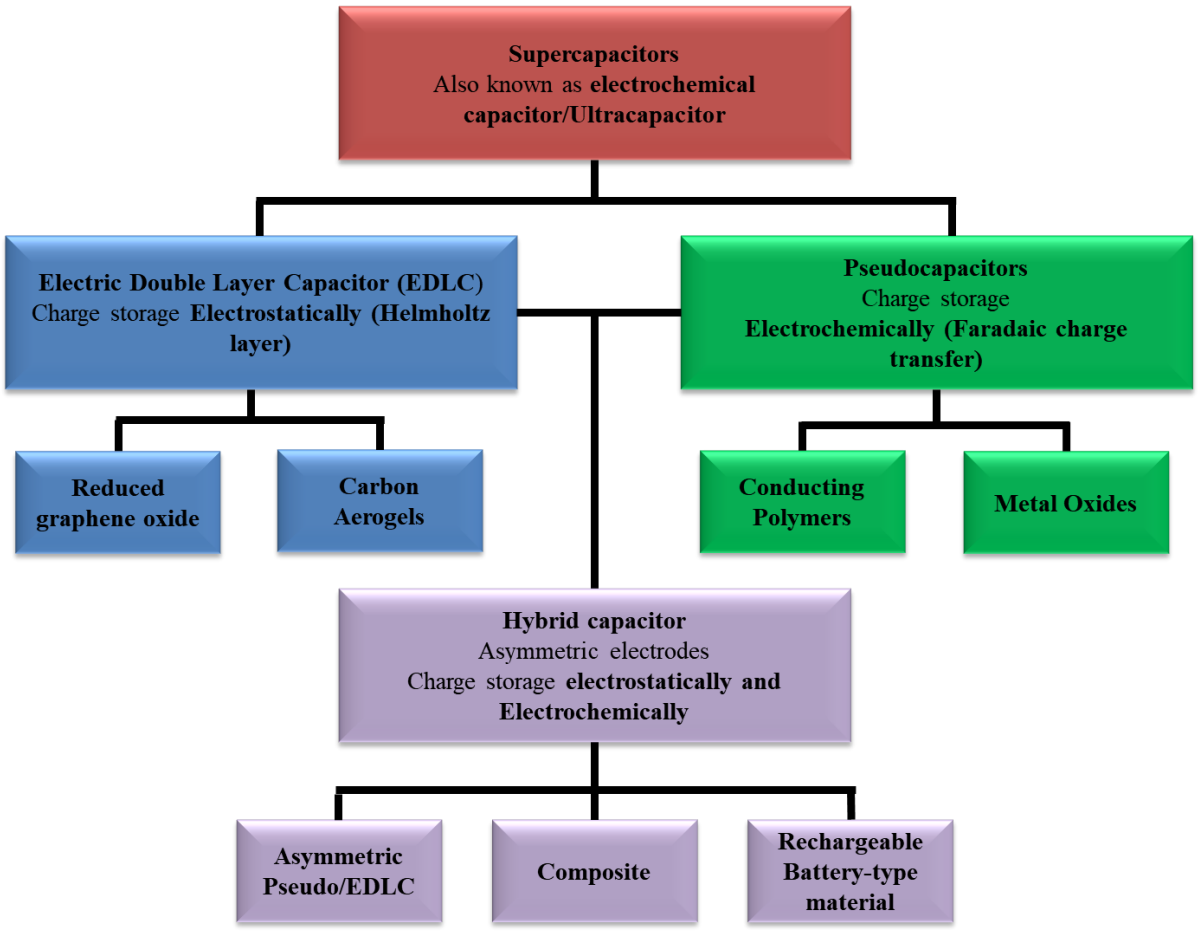

Figure 2.3. The classification of electrochemical capacitors based on charge storage mechanism. Adapted from Ref [9].

Figure 2.4 (a) and (b) shows the schematic of a typical SC and μ-SC devices, respectively, which consists of two working electrodes i.e. positive (cathode) and negative (anode) composed of active material deposited on current collector, an electrolyte which can be either aqueous [10,11], gel [12,13] or solid state [14], and a separator that separates the two electrodes. In the SC a membrane like filter paper is often used [15,16] while in interdigitated μ-SC a space similar to conversional capacitor is used [7,17]. Note that in μ-SC some active material such as laser reduced graphene oxide and thermally reduced graphene oxide does not require a current collector since the active material is extremely conductive. This was illustrated by Gao *et al*. [7] when fabricating laser reduced graphene/MnO nanocomposite electrodes for microsupercapacitors.

In accordance, with the charge storage mechanism of the electroactive material and device architecture of both SC and μ-SC discussed above and also displayed in Figure 2.3, the electroactive material charge storage mechanism can be classified into the three categories: EDLC, pseudocapacitance and battery type. These charge storage mechanisms which occur on both or either of the electrodes are illustrated schematically in Figure 2.4 (c) – (g).

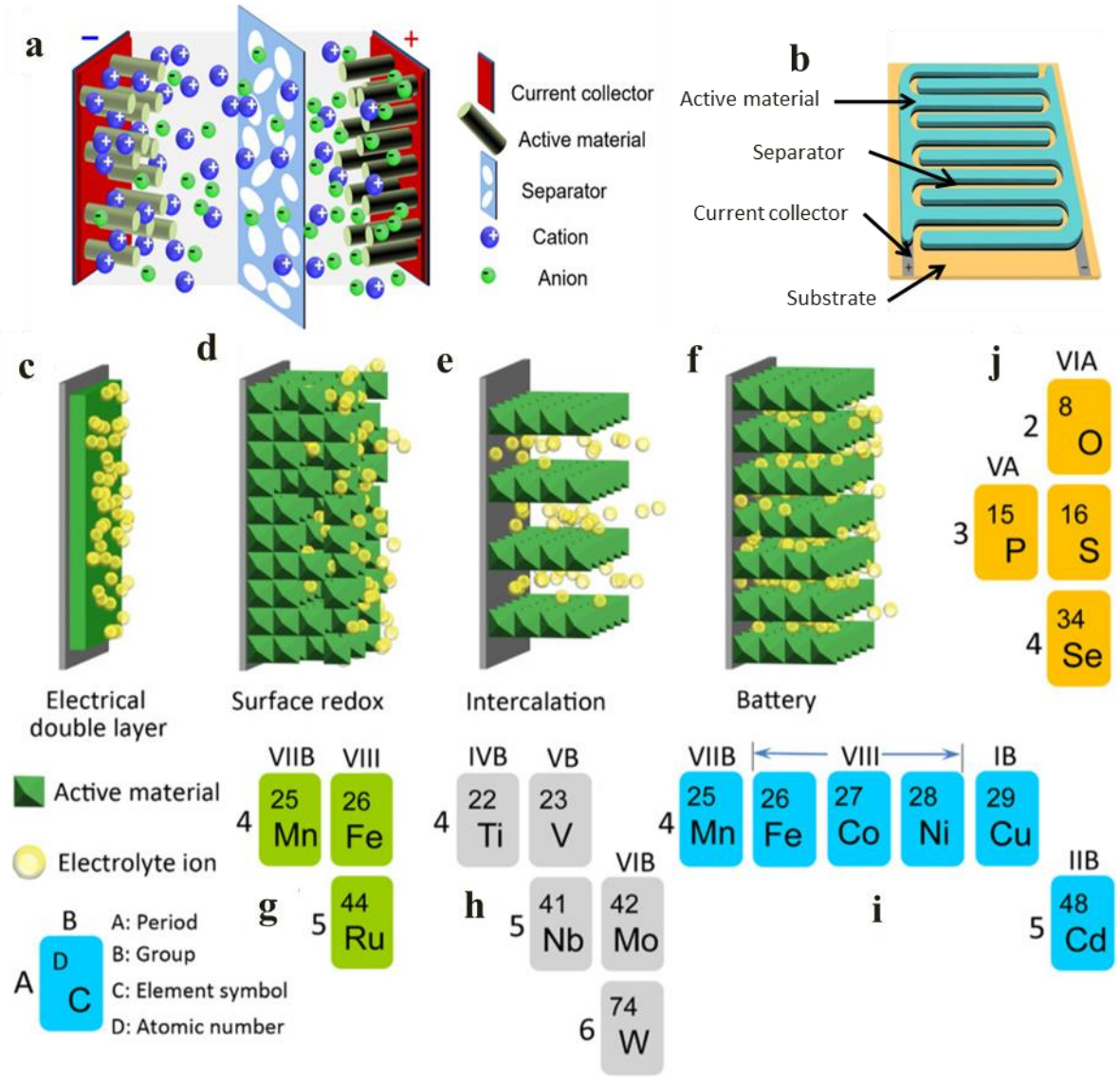

Figure 2.4. The schematic illustrating a typical structure of a (a) SC and (b) μ-SCs device. Illustration of SCs electrode energy storage mechanism: (c) electrical double layer capacitor (EDLC), (d) surface redox capacitance, (e) intercalation capacitance and (f) battery behaviour. Classification of elements based on the different charge storage mechanisms: (g) surface redox capacitance, (h) intercalation capacitance, (i) battery behaviour and (j) anions used to co-ordinate with these transition metal elements. Adapted from Ref [18,19]

2.3.1. Electric double layer capacitor

The EDLC schematic is illustrated in Figure 2.4 (c). This process is controlled by a reversible adsorption/desorption of electrolyte ions at the electrode/electrolyte interface which forms an electrical double layered region. Briefly, atoms, ions or molecules within the electrolyte adheres on to the conductive surface of the electroactive material (which is mostly carbon based) within the electrode due to the charges difference of the conductive surface and the electrolyte ions. Furthermore, in the anode the applied potential will negatively polarise the electrode material where the cations will electrostatically adhere onto that surface, while on the cathode the opposite occurs with the electrode material being positive and the electrostatically adhered ions being negative (anions). The process occurs on the cathode and anode simultaneous, resulting in an electric double layer where charge transfer takes place at electrode/electrolyte interface.

The EDL was first modelled and introduced by Hermann von Helmholtz in the mid-19th century. This proposed model is referred to as the “Helmholtz double layer” displayed in Figure 2.5 (a), which consists of the formation of two layers: Positive (electrode material) and negative (electrolyte) charges at the electrode/electrolyte interface. This also happens on the other electrode where the material will be negatively charged while the cations adhere to it. The distance between the two layers on either side of the EDL is in the nanometre regime which is significantly smaller than separation distance between the conventional capacitor plates. The capacitance (C) in farads (F) of the charge stored via the EDLC mechanism is presented as follows:

$$C = \frac{\varepsilon_r \varepsilon_0 A}{d} \qquad \text{…. 2.1}$$

where ε_r, ε_0, A, and d are the relative permeability (Fcm^{-1}) of the electrolyte, dielectric constant of the electrolyte, total surface area in square metre (m^2) of the electroactive material, and charge separation distance in metre (m), respectively.

From equation 2.1, it can be seen that the EDLC capacitance is directly proportional to the surface area of the active material and indirectly proportional to the charge separation i.e. the distance between the positively and negatively charge layers. EDLC capacitors have a very high surface area (from carbon based materials) and a very small charge separation distance [20,21] , which gives them the ability to carry a lot of charge, compared to conversional parallel plate capacitors, hence "SUPERCAPACITORS".

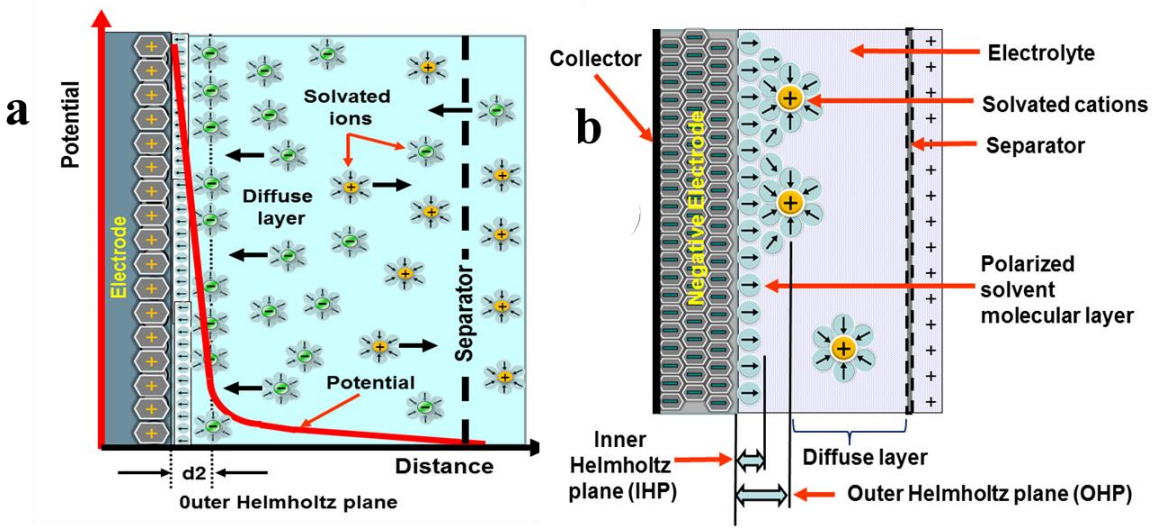

Figure 2.5. Different EDLC charge storage mechanism models (a) Helmholtz and (b) Stern model. Adopted from Ref [22]

The Helmholtz model omitted some important phenomena occurring within the surface (electroactive material) of electrode such as surface ionic interaction [23]. This model was modified into the Gouy and Chapman model, where omitted concepts within the Helmholtz model were included, such as the presence of the diffusion layer, and ion interaction within the EDL interface [24]. This model was finally modified into the Stern model displayed in Figure 2.5 (b), this is an amalgamation of the concepts and theories from both Helmholtz; and Gouy and Chapman models. These new model shows the presence of several ionic distributed regions which are the Stern layer (also known as compact layer) containing the inner and outer Helmholtz plane and the diffuse layer. Thus, the total EDLC capacitance (C_T) corresponds to the capacitance obtained from Stern layer (C_H) and diffuse layer (C_D).

$$\frac{\mathbf{1}}{\boldsymbol{C_T}} = \frac{\mathbf{1}}{\boldsymbol{C_H}} + \frac{\mathbf{1}}{\boldsymbol{C_D}} \qquad \ldots 2.2$$

In conclusion, the EDLC processes heavily dependent on the accessible surface area of the electroactive material and electrolyte ions charge separation. In general, carbon based materials exhibit the EDLC behaviour, during the charging process the electrons travels from the negative electrode to the positive electrode through an external circuit and during the discharge the reverse processes occurs. Thus, there is no charge transfer across the electrode/electrolyte interface. Note that the EDLCs have no chemical reaction involved during the energy storage mechanism and are electrochemically stable due to the energy storage processes which are physical and highly reversible; hence EDLCs have a very long life-span. In addition the amount of charge stored and discharge in the EDLCs also relies on

the movement and amount of adsorbed ions rather than batteries that relies on slower chemical reactions [21,23–25].

2.3.2. Pseudocapacitor

Pseudocapacitance (PC) is mainly divided into two categories: surface redox reactions displayed in Figure 2.4 (d) and intercalation displayed in Figure 2.4 (e). These PCs are based on fast and highly reversible Faradaic redox reactions (oxidation-reduction) or processes within the electroactive material or at the surface of the electroactive material which endows PCs devices with much higher charge storage capacity. On the contrary, EDLCs store charge on the electrolyte/electrode interface purely by electrostatic process, while PCs uses Faradaic redox processes implying a charge transfer between electrolyte and electrode through the double layer at an applied potential. The surface redox reactions of PC process stores charges through adsorption/desorption of electrolyte ions (i.e. on the cations and anions) onto the surface of the electroactive material then followed by faradaic redox reactions. The surface redox reactions can be further be divided into underpotential deposition (UPD) and redox PC as displayed in Figure 2.6. Note that some of the materials that exhibit surface redox reaction are displayed in Figure 2.4 (g).

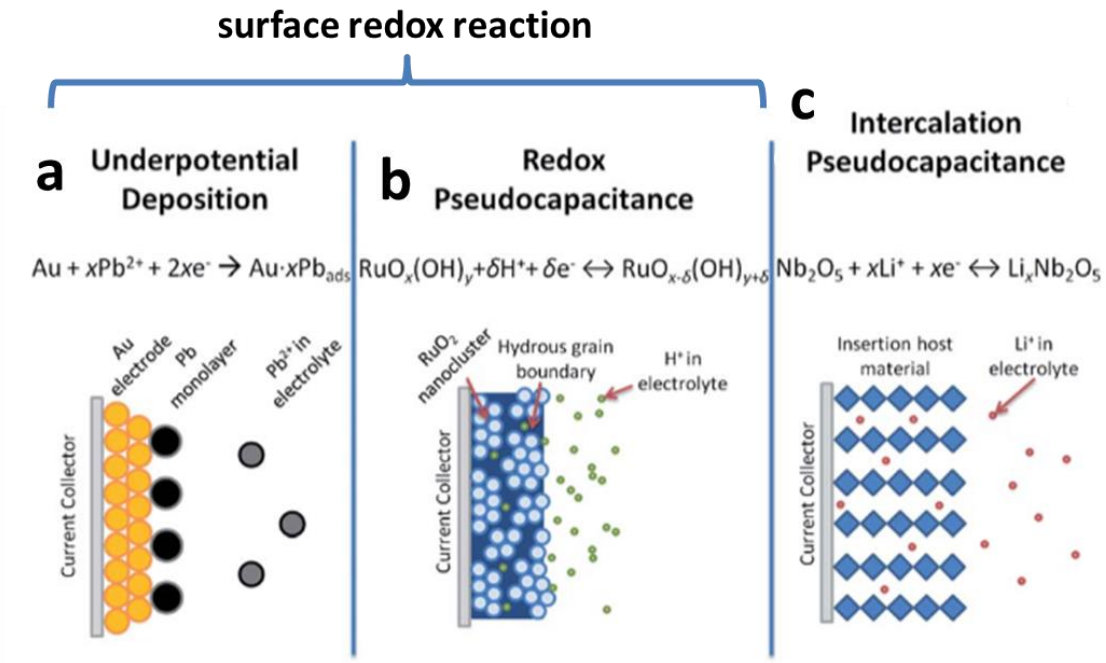

Figure 2.6. Schematics of different PCs charge storage mechanism; (a) underpotential deposition, (b) redox PC, and (c) intercalation PC. Adopted from Ref [26]

The UPD occurs when the absorbed ions monolayer on the surface of a dissimilar metal substrate is deposited at lower potential than the redox potential. The potential difference between the low applied potential and redox potential leads to charge transfer between the metal substrate and deposited metal monolayer [27–29]. A typical example of a UPD is the deposition of lead (Pb) on a gold (Au) substrate surface as displayed in Figure 2.6 (a) [26]. The Redox PCs charge storage mechanism happens when the ions adsorbed onto the surface or near the surface of electrochemically active material such as RuO_2 and MnO_2 result in a charge transfer, this is also illustrated schematically in Figure 2.6 (b) [26,30].

Lastly, the intercalation PC charge storage mechanism occurs when electrolyte ions tunnels into the Faradaic electrode material followed by redox charge transfer without changing the crystal structure/phase of the electroactive material. An example of the intercalation PC would be insertion Li^+ ions into Nb_2O_5, also displayed in Figure 2.6 (c). Some of the materials which belong to the class of intercalation PC are displayed in Figure 2.4 (h). [26,30–33]

In general, PC can store as much charge as some batteries, but they suffer from low specific capacitance, short life span, and poor electrical conductivity. Note that the battery-type processes together with the material involved are displayed in Figure 2.4 (f) and (i), respectively. Anions used to co-ordinate transition metal elements used in both SC and batteries are displayed in Figure 2.4 (j).

2.3.3. Hybrid capacitors

Hybrid capacitors (HCs) utilise both storage mechanisms i.e. EDLCs and Faradaic, hence HCs combine high specific power and long life span for EDLC together high specific capacitance from the Faradaic material due to rich redox reactions and great electrochemical activities. Thus, HCs can archive a higher electrochemical performance. Moreover, these two processes occur simultaneously, but one of them dominates, leading to higher capacitance and/or higher operating potential window. In addition, the most common HCs architecture consists of a battery type i.e. Faradaic or intercalation storage mechanism as a cathode

electrode and EDLC storage mechanism material as an anode electrode (this architecture is also known as asymmetric capacitor). These can also be achieved by preparing a pair of different electrode materials using with dissimilar charge storage mechanism: Different metal oxides, doping conducting polymer materials, composite materials prepared from a carbon material incorporated into a conducting polymer or metal oxide. Hybrid capacitor can be classified into battery-type, composite and asymmetric [16,34–36]. These SC devices are considered to be the future of electrochemical energy storage since they combine the best properties of both EDLC and Faradaic storage mechanisms as shown in Figure 2.3 and Figure 2.4.

Briefly, this class of SCs also offer the following advantages: Hierarchical porous structure, large surface area, reduced charge transfer resistance, good cyclic stability, increased life span, good material conductivity, swift ion transport and increased electrochemical active site. Hence, HCs are considered to be the future energy storage devices [37–39].

2.4. Materials and fabrication

It has been shown in Figure 2.4 (a) and (b) that SCs and μ-SCs, mainly consists of the electrode, electrolyte and a separator. The electroactive material within the electrode is one of the most important components of these electrochemical energy storage devices. The electroactive material plays an important role of carrying the charges which leads to the determination of specific energy and power. The electrode materials can be classified into

three types: Carbon based materials (activated carbon, carbon nanotube, and graphene) [36,40–42]; conducting polymers (polythiophene, polyaniline, polyphenylene and sulphide) [43–45] and metal oxide/hydroxides (MnO_2, NiO and VO_2; and two-dimensional layered transition-metal dichalcogenides (MoS_2, NiS_2 and VS_2) [16,32,46]. Figure 2.4 (g) – (j) also indicates the most commonly used electrochemical materials (elements) and also corresponds them to the underlying charge storage mechanisms [18,19,26,47].

The SC and μ-SC electrodes can be prepared using various techniques. These techniques heavily depend on the chemical and physical properties of the substrate and electroactive material. In the fabrication of SC electrodes on nickel foam (NF) only few techniques such as slurry paste [15,35], electrodeposition [16,48], chemical vapour deposition [49,50], hydrothermal [51,52], dip -coating [53,54] and successive ionic layer adsorption and reaction (SILAR) [55,56] are applicable due to architecture of NF. These techniques are able to deposit material into the inner NF surface unlike a technique such a spin coating [57]. Slurry paste is the most used method in SC NF-electrode where the electroactive material either carbon based, polymers, metal oxide/hydroxide and/or composite are mixed together with binder such as Polyvinylidene fluoride (PVDF) and Polytetrafluoroethylene (PTFE) and conductive enhanceing agent such as carbon acetylene black (CAB) and carbon nanotubes (CNTs) are mixed in N-Methyl-2-pyrrolidone (NMP) solvent until a homogenous paste is formed. The slurry paste is then applied to the NF via a paint brush [15,35,40,58]. In addition, slurry paste gives the ability of controlling the mass of the electroactive material onto NF. Moreover, oxygen functional groups on the surface of GO makes it highly soluble in solvents such as water and ethanol i.e. GO can be pasted then dried on NF or sprayed on a flat substrate such as microscopic glass.

Several authors have shown that reduced graphene oxide (rGO) has the tendency of restacking into a bulk material due to the presence of van der Waals forces, this has been used to fabricate free standing graphene oxide film [13,61]. This work took advantage of the above-mentioned GO and rGO in the fabrication of thermal reduced graphene oxide (TRGO) directly on NF i.e. TRGO/NF in the absence of binders and conductive enhancement. This allows for the electrochemical evaluation of the electroactive material without influences from binders and conductive enhancement. Moreover, chemical reduction using reducing agents such as hydrazine and ascorbic acid (vitamin C) often introduces functional groups such as amino nitrogen atoms and some O-group [62], respectively.

On the other hand, conversional µ-SC fabrication methods are displayed in Figure 2.7 and have been utilised in the fabrication of the next-generation electrochemical energy storage devices. In general, the preparation methods in Figure 2.7 have the following challenges: Sufficient resolution of the electrode patterns is defined by the patterning methods, compatibility with the conditions employed in the semiconductor industry to enable integration with other electronic components and depositing electroactive material effectively onto micro sized current collector patterns without short circuiting the positive and negative electrodes [4]. Note that this work is dedicated to interdigitated µ-SC only.

As stated above, the fabrication method relies on the chemical and physical properties of both the substrate and electroactive material. In the µ-SC device fabrication, the desired output also plays an important role in the choice substrate and electrode material. The fabrication methods displayed in Figure 2.7 have attracted overwhelming attention for the µ-SC manufacturing due to their simplicity, low cost, scalability and more interestingly, their

ability to prepare electrodes with unique form such as stretchability, wearability and flexibility [4,5,43,63].

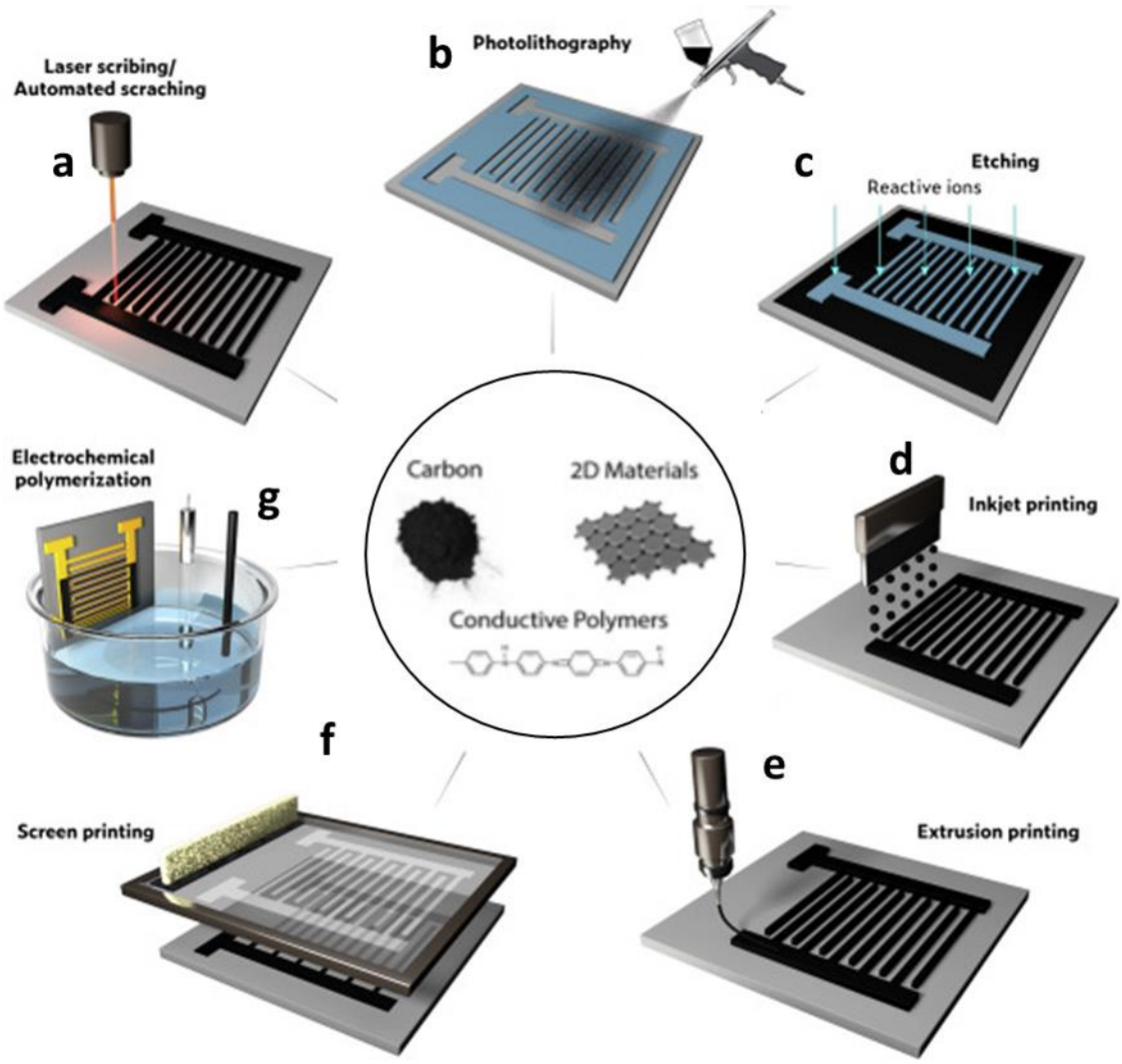

Figure 2.7. Different fabrication methods for interdigital microsupercapacitors. (a) Laser scribing/automated scratching (e.g. AxiDraw), (b) photolithography and spray coating, (c) etching, (d) inkjet printing, (e) extrusion printing and 3D printing, (f) screen printing and (g) electrochemical polymerization. Adopted from Ref [4,47]

In general, these fabrication techniques have been categorized into: Direct patterning of solid material on the desired substrate (e.g. Laser scribing and automated scratching displayed in Figure 2.7 (a)) and transferring material ink into different µ-SC patterns (photolithography, etching, inkjet printing, extrusion printing, screen printing and electrochemical polymerization in Figure 2.7 (b) – (g)). However, these techniques can be better classified as masked and mask-free techniques, mask-free techniques do require some form of scaffold or stencil for electrode fabrication, and thus they are controlled by a driven stage connected to a computer. There are laser scribing and automated scratching in Figure 2.7 (a) together with Inkjet in Figure 2.7 (d) and extrusion in Figure 2.7 (e) printing. These mask-free techniques are straightforward microfabrication method, and only used the required electroactive material i.e. there are very little or no wasted material as compared to other masked technique.

These techniques have been used in the preparations of different MXene, graphene and other two-dimensional materials based µ-SC. The µ-SC schematic is designed with software such as Inkscape and AutoCAD then transposed onto fabrication device like a 3D printer for extrusion printing [47,64], AxiDraw for automated scratching [65,66] and paper printer for inkjet printing [4,47,67] which will print out the actual µ-SC. This process allows easy scalability, and optimization since fabricating µ-SC is very quick and highly reproducible.

The masked techniques such as photolithography in Figure 2.7 (b), etching in Figure 2.7 (c), screen printing in Figure 2.7 (f); and electrochemical polymerization and deposition in Figure 2.7 (g) have also been used for the fabrication of µ-SC. All these fabrications techniques

require some form of a scaffold or stencil (mask). In photolithography, the light is exposed through a very expensive photomask, the photosensitive photoresist can be patterned to any shape as designed [67,68]; while etching selectively removes the unwanted material via a chemical mask such a Poly(methyl methacrylate) (PMMA) and upon removal it leaves residues [69,70]. Screen printing uses a chemical permeable fabric scaffold with the desired pattern. The electroactive material is printed through the fabric scaffold leaving out the desired pattern [4,8,47,67]. Lastly, electrochemical polymerization and deposition can be done on a pre-patterned current collector. Thus, during the process, charged particles in the suspension move towards the electrode with opposite polarity and coagulate on it. These processes have been used in metal oxide/hydroxide and Polyaniline (PANI) [71,72]. Generally, these fabrications have a very high waste ratio e.g. electrodeposition/ electrochemical polymerization and screen printing requires high amounts of precursor material to fabricate few µ-SC device, some material are trapped within the screen printing equipment

In this study, the µ-SCs were prepared as follows: GO was sprayed onto the MSG, then thermally reduced using CVD, followed by µ-SC electrode patterning using automated scratching (AxiDraw) fabrication technique. Similar to the SC electrode fabrication, this method also allows the electrochemical performance evaluation of the TRGO µ-SCs without external influences from additives such as binder, conductive agent and by-product from chemicals reduction agents.

Several graphene reducing techniques have been developed and reported, such as thermal reduction, chemical reduction, electrochemical, ball milling and many more [62,73,74] In our work, thermal reduction was deemed more suitable mainly due to the following reasons:

Safe, quick, effective, does not leave by-products within rGO matrix, offers the ability to study the effects of oxygen functional groups (OFGs) during the reduction process. Thus, TRGO SCs and μ-SCs were fabricated and evaluated for electrochemical energy storage application.

2.5. Electrolytes

As important as electroactive materials are, electrolytes are also very important and constitute as SCs or μ-SCs basic components which significantly influence the electrochemical performance. The electrolyte supplies ionic conduction essential for charge storage and ion transport. The significance of the electrolyte heavily depends on the ionic concentration, size, type and its electrode material interaction. For the electrolytes to be suitable in electrochemical energy storage application, they have to meet the following requirements: High electrochemical stability, high ionic conductivity, wide voltage window, low resistivity, low volatility, low toxicity and low cost. These electrolytes are located within anode and cathode of the SC and μ-SC devices (Figure 2.4 (a) and (b), respectively), while the ions in electrolytes are transported through the separator. It is worth mentioning that in the three-electrode configuration, the electrodes i.e. working, counter, and reference electrodes are immersed in the aqueous electrolyte. The electrolytes can be classified as liquid, solid state and redox active electrolyte. Furthermore, liquids can be divided into aqueous, organic, and ionic liquids electrolytes, while the solid state can be classified into dry state polymer, gel

polymer and inorganic electrolytes. Lastly redox active electrolytes can be also classified into Aqueous, organic, ionic liquid and gel polymer electrolytes [20,75,76].

In the SC study, aqueous electrolytes such as KOH, NaOH and Na_2SO_4 were used in SC rather than other liquid electrolytes, since they provide higher ionic conductivity. These electrolytes are quick and simple to prepare (in comparison to organic electrolytes which need strict processes and conditions to prepare) and can be used in atmospheric environment. Moreover, aqueous electrolytes based SCs display a higher capacitance and higher power than organic electrolytes, probably due to the small ionic radius and higher ionic conductivity. The aqueous electrolytes based SCs have exceeded the limited theoretical operating voltage of 1.23 V attributed to the decomposition of water at high applied potential windows. Aqueous electrolytes based SCs have shown the ability to reach higher operating potential windows of ~ 2 V due to the synergy between the electrodes and the electrolytes. [20,21]

In the µ-SCs study, gel electrolytes were used. Generally, these electrolytes are prepared via the gelation of polymer matrix such as Polyvinyl alcohol (PVA) and PMMA; and electrically conductive compounds such as acidic, basic and salts that contains conductive ions. Phosphoric (H_3PO_4) acid, sulphuric (H_2SO_4) acid and potassium hydroxide (KOH) are the most frequently used conductive compound used with PVA matrix. Several studies have shown PVA-H_3PO_4 is the most suitable electrolyte for graphene – based µ-SCs mainly due to the smaller ionic radius of H^+ that can quickly and easily diffuse within the graphene layers as compared to large K^+ and Na^+ ions. In addition H_3PO_4 can produce more free ions than H_2SO_4 and KOH at the same molarity [71,77,78]. Thus, PVA-H_3PO_4 gives higher

capacitance and it was used as gel electrolyte in the fabrication of TRGO μ-SC within this work.

2.6. Electrochemical testing and evaluation

The electrochemical performance of the electrode is investigated using the three-electrode configuration displayed in Figure 2.8. Note that the three-electrode configuration is also referred to as half-cell, while the two-electrode configuration is referred to as full-cell or device. The three-electrode setup consists of a working electrode (WE), counter electrode (CE) and reference electrode (RE). The WE is usually made of electroactive material pasted on current collector which serves as a platform where electrochemical reaction occurs. In this work, nickel foil was used as current collector for the WE. The type of the CE and RE depends on the electrolyte used, in this work aqueous electrolytes were utilized and the corresponding CE and RE were glassy carbon and silver/silver chloride (Ag/AgCl) filled with three molar potassium chloride (3 M KCl), respectively. The RE electrode which has a stable and known electrode potential is usually used as a benchmark in the determination of the potential of a WE without allowing current thought it, whereas the CE completes the circuit and allows the required current through the circuit to balance the current generated at WE [20,21,79]

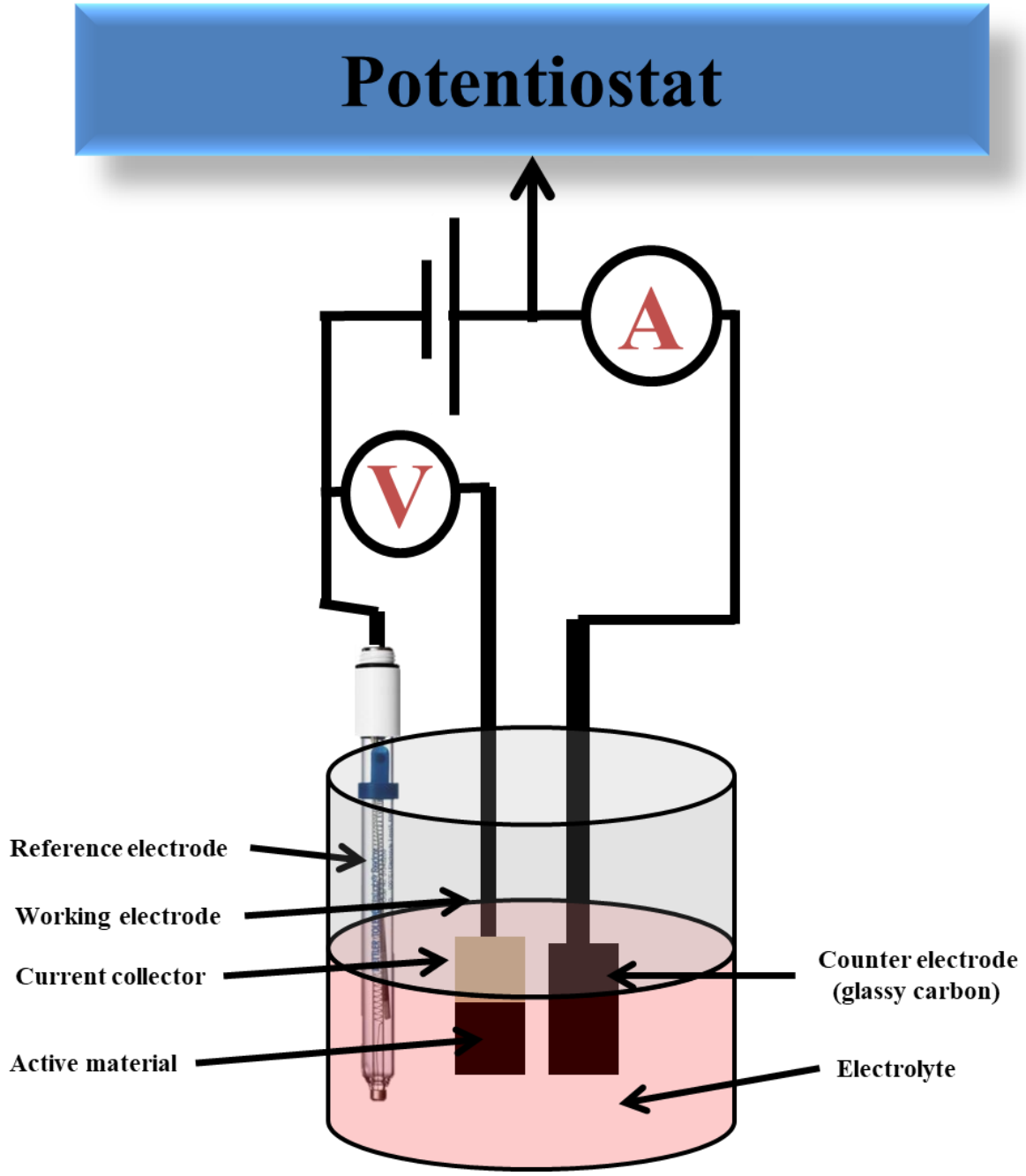

Figure 2.8. Schematic diagram of three electrode configuration.

For the two-electrode cell setups for SC and µ-SC are illustrated in Figure 2.9 (a) and (b), respectively. It can be seen that the CE and RE are joined together and connected to the negative, while the WE and sense (S) are also joined and connected to the positive side. The connections of the SC and µ-SC are displayed in red and in blue, respectively. In this setup, the potential of the device is being measured which also includes the contributions from electrolyte and the interactions of the electrolyte and CE. The S measure voltage drop cross WE, electrolyte and CE [21].

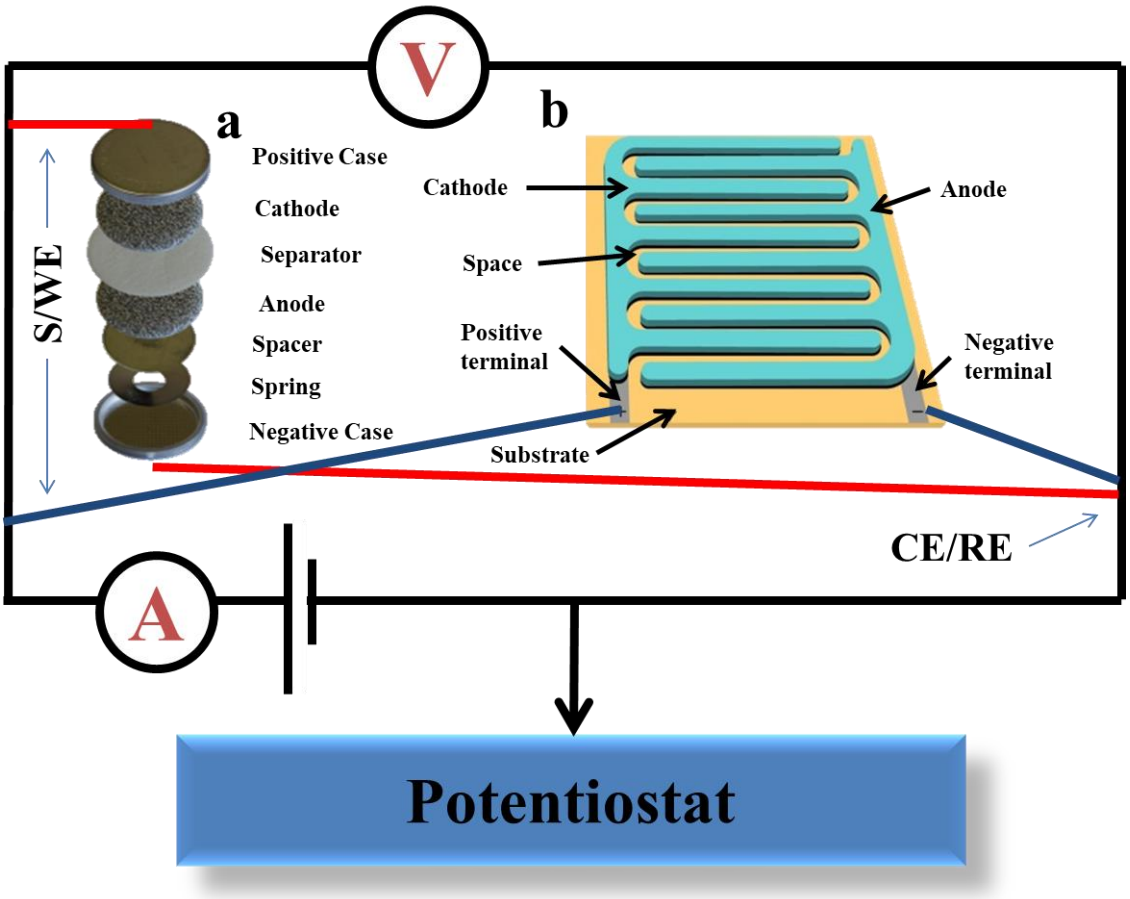

Figure 2.9. The schematic view of two electrode cell (a) SC (connected in red) and (b) µ-SC (connected in blue), including the coin cell architecture

In this work the two-electrodes was used to measure symmetric μ-SCs and asymmetric SC devices. The asymmetric device is referred to as any device with a combination of positive and negative electrodes with dissimilar properties such as different mass, thickness and type of material. On the contrary symmetric device has the same parameters. Note that the asymmetric devices are the best SC architecture due to the fact that different materials can be used in order to expand the operating potential window, and also use different energy storage mechanisms to boost the specific power and energy [16,35,38].

As previously mentioned, the electrochemical performance of the device is determined mainly by the electrodes and electrolytes, which are the most important components. For instance the following parameters are affected by the choice of the electrode and electrolyte: Life span, capacitance/capacity, resistance and stability. The electrode preparation and fabrication including electroactive material coating process is very important. As a result, a strict preparation process and fabrication is required to achieve high performance. In recent studies, NF has been used as a current collector to study electrochemical performance of electrode materials for supercapacitor applications due to higher electrical conductivity, low cost, availability, chemical stability in aqueous electrolyte, and mechanical strength to also act as a scaffold for the electroactive material [21,40,80].

The electrochemical performance of the prepared electrodes is evaluated using cyclic voltammetry (CV), galvanostatic charge discharge (GCD) and electrochemical impendence spectroscopy (EIS).

2.6.1. Cyclic voltammetry

The cyclic voltammetry (CV) was utilized to determine the effects of thermodynamics and electron transport dynamics on the boundaries in-between the electroactive materials and electrolyte ions of the electrochemical device, by interpreting the reactions happening on or in the surface of the electroactive material. The CV is applicable in two or three electrodes configuration and the measurement is carried out at a certain potential, in which the applied potential can be measured at various scan rate (e.g. 5, 10, 20, 50, 100 mVs^{-1} and so on). The CV measurements are performed by cycling the potential of WE and monitoring the resulting current. Thus, the CV curve is a plot of current response as a function of applied potential as illustrate in Figure 2.10 (a) – (c), which also describes the nature of the occurring storage mechanism on the electrode/electrolyte interphase. For instance, the CV displayed in Figure 2.10 (a), reveals the electrochemical double layer i.e. rectangular CV curve behaviour, while Figure 2.10 (b) displays the CV plot of PC and lastly the CV curve displayed in Figure 2.10 (c) corresponds to that of battery-type i.e. it exhibit redox peaks due to Faradaic reactions. The anodic and cathodic scan of the EDLCs curve is similar, suggesting that the measured current is independent of the applied potential, while in PCs and battery-type the charge accumulation (observed current) on the electrode is dependent on the applied potential [45,79–81].

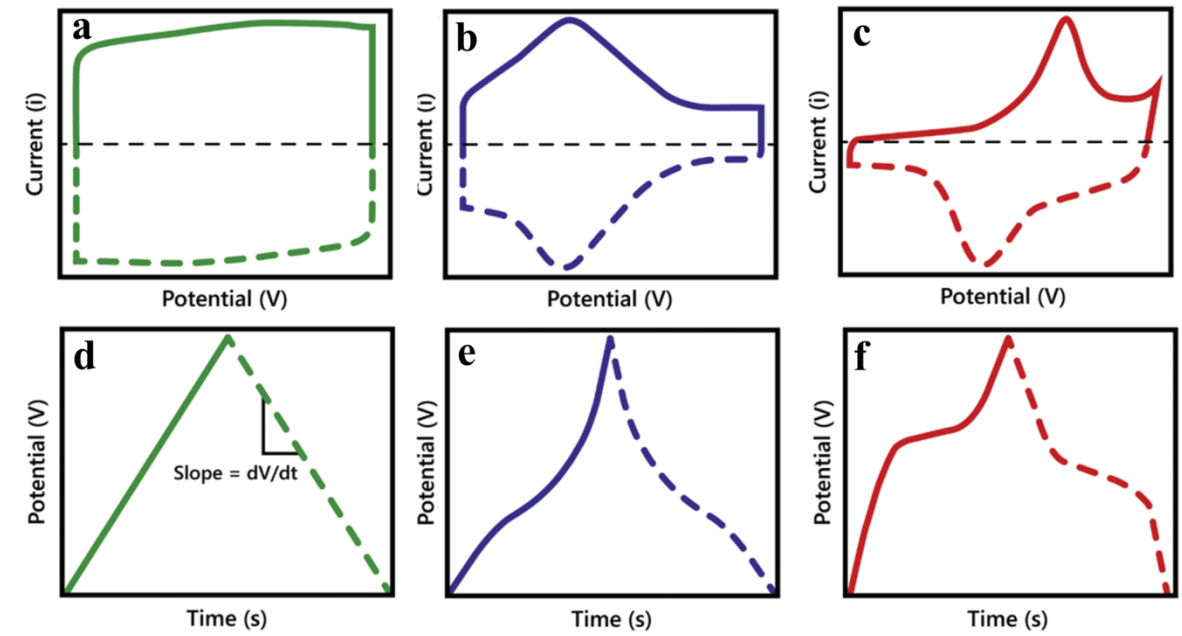

Figure 2.10. Supercapacitor output behaviour of three main types of electrodes; (a) and (d) electrochemical double layer capacitor, (b) and (e) pseudocapacitive, and (c) and (f) battery type. (a) – (c) schematic of cyclic voltammetry and (d) – (f) corresponding galvanostatic charge-discharge. Adopted form Ref [81].

The CV curve can be used to determine various electrochemical properties of the electrode materials such as the specific capacitance (C_s) in farads per gram (Fg^{-1}) which can be done using the following equation (2.3):

$$C_s = \frac{\int I_s dV}{v \Delta V} \quad \ldots 2.3$$

Where I_s, ΔV and v is the specific current, potential window and scanning rate, respectively. In two electrodes asymmetric device there is differences in the specific capacitance and/or

capacity, a charge balance, for the two-electrode evaluation where the masses of the electrodes were determined based on the charge balancing equation below (2.4) – (2.6):

$$\boldsymbol{Q_+ = Q_-} \quad \ldots 2.4$$

$$\boldsymbol{3.6 m_+ \times Q_{s+} = m_- \times \Delta V_- \times C_{s-}} \quad \ldots 2.5$$

$$\boldsymbol{\frac{m_+}{m_-} = \frac{C_{s-} \times \Delta V_-}{3.6 \times Q_{s+}}} \quad \ldots 2.6$$

where Q_+, Q_-, Q_{s+}, C_{s-}, m_+, m_- and ΔV are the charge for positive, charge for negative, specific capacity for the positive electrode (mAh g^{-1}), specific capacitance (F g^{-1}) for the negative electrode, masses (mg) of the positive and negative electrodes and ΔV is the potential window (V), respectively [15,16,20,21,30].

Other properties such as the EDLC and Faradaic contribution can be determined from the CV using the Power law and Trasatti's method. Under the power law (2.7):

$$\boldsymbol{i = a\upsilon^b} \quad \ldots 2.7$$

the current (i) corresponding to the scan rate (υ) are plotted in log-log scale of current versus scan rate, and a and b are adjustable parameters. The b value of 0.5 indicates that the current is controlled by diffusion behaviour and the b value of 1 indicates that the current is controlled by surface controlled behaviour (EDLC) [61,82]. In addition, the Transatti's method calculates the quantity of the contribution from the EDLC and Faradaic controlled behaviour. First, the total capacitance is calculated from the reciprocal of the extrapolated

intercept of the $1/C_T$ versus $\upsilon^{0.5}$ and the EDL capacitance (C_{EDL}) was estimated from the extrapolated intercept of C_{EDL} versus $\upsilon^{-0.5}$ while the pseudocapacitance (C_p) was obtained from the difference between C_T and C_{EDL} (2.8) [61,83]

$$\boldsymbol{C_T = C_{EDL} + C_{pseudo}} \quad \ldots 2.8$$

2.6.2. Galvanostatic charge-discharge

The Galvanostatic charge-discharge (GCD) is one of the most important electrochemical characterization tool used for determining the electrochemical performance i.e. specific power and energy, voltage holding, stability and self-discharge. The GCD is carried out by applying a current between the WE and CE and the generated voltage is measured with respect to RE as a function of time, as illustrated in Figure 2.10 (d) – (f). During the GCD measurements, the lower and upper potential limits are pre-set for the WEs, while the current push the voltage to the upper limit. After the upper limit is reached, the current reverses dragging the voltage to the initial lower limits and the next cycle begins again and again. Similarly to the CV curves, the GCD curve also reveals the electrochemical charge storage behaviour of the electrode as EDLCs (Figure 2.10 (d)), pseudocapacitors (Figure 2.10 (e)) and battery-type (Figure 2.10 (f)) [20,81]

Specific capacitance can also be determined from the GCD depending on the nature of the storage mechanism; In EDLC behaviour the following equation (2.9) is applicable

$$\boldsymbol{C_s = \frac{I_s \Delta t}{\Delta V}} \quad \ldots 2.9$$

where $\boldsymbol{I_s}$, $\boldsymbol{\Delta t}$ and $\boldsymbol{\Delta V}$ are the specific current (A g^{-1}), discharge time (s) and cell potential (V), respectively [16]. If the GCD curve shows Faradaic behaviour the specific capacity can be calculated by integrating the area under the GCD curve using the following equation:

$$\boldsymbol{C_s = \frac{2 I_D \int V dt}{\Delta V^2}} \quad \ldots 2.10$$

In the case of Faradaic behaviour, the working potential or voltage in case of full cell is non-linear with time; hence specific capacity is reported. The specific capacity of the electrode can be calculated using the following equation:

$$\boldsymbol{Q = \frac{I_s \Delta t}{3.6}} \quad \ldots 2.11$$

Specific energy (E_s) in W h Kg^{-1} and specific power (P_s) in W kg^{-1} can be calculated from the GCD curve using equation (2.12 and 2.13) and (2.14) [45,84], respectively.

$$\boldsymbol{E_s = \frac{I_s}{3.6} \int_{V_i}^{V_f} V \, dt} \quad \ldots 2.12$$

Equation 2.12 reduces to equation 2.13 in the case of EDLC behaviour

$$\boldsymbol{E_s = \frac{1}{2} C V^2} \quad \ldots 2.13$$

$$\boldsymbol{P_s = \frac{E_s}{\Delta t} \times 3600} \quad \ldots 2.14$$

where I_s, $\int_{V_i}^{V_f} V\,dt$ and Δt are the specific current (A g^{-1}), integral under the area of the discharge time (V s) and discharge time (s), respectively. The maximum power (P_{max}) in W kg^{-1} of the device is obtained using the following equation [45,85]:

$$\boldsymbol{P_{max} = \frac{\Delta V^2}{4m(ESR)}} \quad \ldots 2.15$$

where ΔV, m and ESR are the cell potential (V), mass in kg and equivalent series resistance.

2.6.3. Electrochemical impedance spectroscopy

The electrochemical impedance spectroscopy (EIS) is used to further evaluate the electrochemical behaviour of the prepared electrode materials i.e. parameter such as resistance, ion diffusion and charge storage mechanism. It is operated at different potential windows, the obtained EIS response of the material can also be used to identify the energy storage mechanism .i.e EDLC, PC and battery type similarly to CV and GCD. The EIS is often represented in Nyquist plot (imaginary component (Z'') as a function of real components (Z') of the impedance) as displayed in Figure 2.11 (a). The EIS can also be illustrated in terms of the Bode plot showing impedance phase angle as a function of

frequency, with an ideal impedance phase angel of 90° illustrating ideal SC behaviour [85,86].

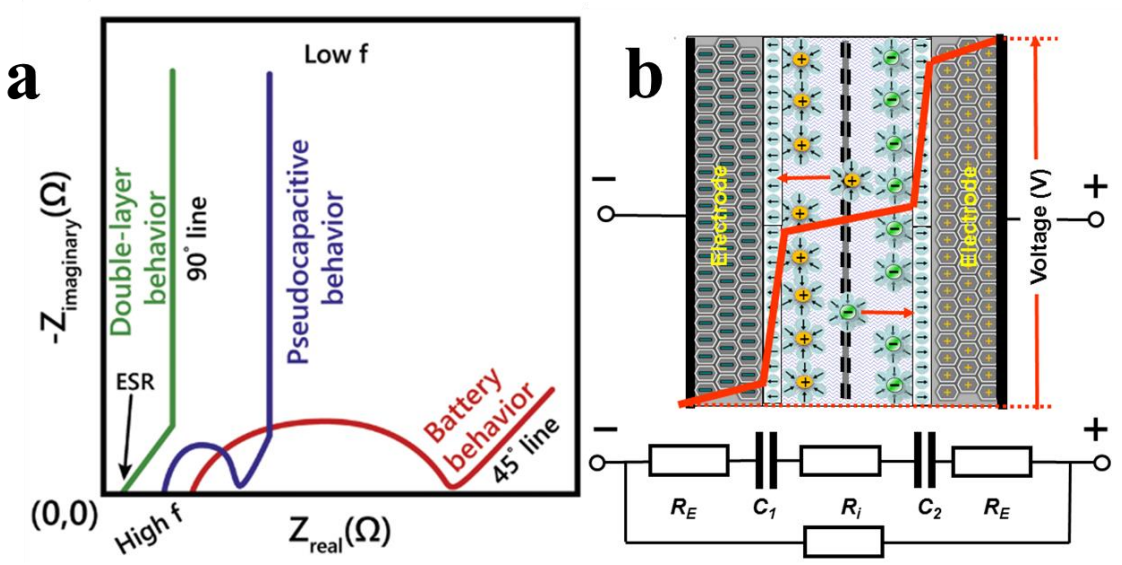

Figure 2.11. (a) A typical Nyquist plot for an EDLC (green), pseudocapacitive materials (blue) and battery type (red). (b) Schematic of SC device with a voltage distribution and the corresponding simulated circuit diagram. Adopted form Ref [81,87].

It can be seen from Figure 2.11 (a) that the Nyquist plot consists of a lower and a higher-frequency region. In the high frequency region, the semi-circle is assigned to charge transfer resistance (RCT) which is relative to the electronic conductivity, and equivalent series resistance (ESR) which is the *x* value of the starting point of the EIS plot, representing the sum of resistance within the electrolyte, interfacial resistance electrolyte/electrode and resistance between electrode and current collector. In the lower frequency region, imaginary

and real capacitance, ion diffusion coefficient and ion length can be determined. An ideal supercapacitor exhibits a vertical line parallel to the imaginary impedance axis, while the fabricated SC shows a deviating vertical line at an angle of 45º in mid-frequency region represents the ionic diffusion mechanism (Warburg resistance) [81,87].

The real and imaginary components of the capacitance ($C'(\omega)$) and ($C''(\omega)$), respectively, can be determined by the evaluation of complex capacitance model presented by the following equations (2.15) – (2.18):

The impedance $Z(\omega)$ with $\omega = 2\pi f$ is expressed as

$$\boldsymbol{Z(\omega)} = \frac{\mathbf{1}}{\boldsymbol{j\omega \times C(\omega)}} \quad \ldots 2.16$$

$$\boldsymbol{C'(\omega)} = \frac{\boldsymbol{Z''(\omega)}}{\boldsymbol{\omega|Z(\omega)|^2}} \quad \ldots 2.17$$

$$\boldsymbol{C''(\omega)} = \frac{\boldsymbol{Z'(\omega)}}{\boldsymbol{\omega|Z(\omega)|^2}} \quad \ldots 2.18$$

$$\boldsymbol{|Z(\omega)|^2 = Z'(\omega)^2 + Z''(\omega)^2} \quad \ldots 2.19$$

where ω, $C(\omega)$, $Z'(\omega)$ and $Z''(\omega)$ are the angular frequency, real impedance and imaginary impedance, respectively. The ($C'(\omega)$) shows accessible capacitance while $C''(\omega)$ gives a relaxation time ($\tau = 1/2\pi f$, where f is the peak of the frequency).

The ion diffusion coefficient (D) of the electrolyte ions into the active electrode material can be determined using equation 2.20, but first the Warburg coefficient σ_w can be estimated using the equation (2.19) [88,89]:.

$$\boldsymbol{Z'(\omega) = R_e + R_{ct} + \sigma_w \omega^{-0.5}} \quad \ldots 2.20$$

where R_e, R_{ct}, and $\omega^{-0.5}$ are the electrolyte resistance, charge transfer resistance, real impendence corresponding to the angular frequency in the low frequency region. Note that R_e, R_{ct} parameters are independent of the frequency. Thus, the slope obtained from $Z'(\omega)$ dependence on the reciprocal square root of the lower angular frequencies ($\omega^{-0.5}$) and the D is obtained from the following equation (2.20) [88]:

$$\boldsymbol{D = 0.5\left(\frac{RT}{AF^2\sigma_w C}\right)^2} \quad \ldots 2.21$$

where R is the gas constant (8.314 J mol^{-1} K^{-1}), T is the temperature (298.5 K), A is the total area (cm^2) of the µ-SC fingers, F is the Faraday's constant (96,500 C mol^{-1}) and C is the molar concentration of H^+ ions

Reference

[1] I.D. Yildirim, E. Erdem, E. Göğüş, Applications of Supercapacitors in Space Vehicles and Interplanetary Devices, Encycl. Energy Storage. (2022) 677–681. https://doi.org/10.1016/B978-0-12-819723-3.00019-6.

[2] A.G. Olabi, Q. Abbas, A. Al Makky, M.A. Abdelkareem, Supercapacitors as next generation energy storage devices: Properties and applications, Energy. 248 (2022) 123617. https://doi.org/10.1016/J.ENERGY.2022.123617.

[3] N.N. Loganathan, V. Perumal, B.R. Pandian, R. Atchudan, T.N.J.I. Edison, M. Ovinis, Recent studies on polymeric materials for supercapacitor development, J. Energy Storage. 49 (2022) 104149. https://doi.org/10.1016/J.EST.2022.104149.

[4] Q. Jiang, Y. Lei, H. Liang, K. Xi, C. Xia, H.N. Alshareef, Review of MXene electrochemical microsupercapacitors, Energy Storage Mater. 27 (2020) 78–95. https://doi.org/10.1016/J.ENSM.2020.01.018.

[5] X. Chen, N.S. Villa, Y. Zhuang, L. Chen, T. Wang, Z. Li, T. Kong, Stretchable Supercapacitors as Emergent Energy Storage Units for Health Monitoring Bioelectronics, Adv. Energy Mater. 10 (2020) 1902769. https://doi.org/10.1002/AENM.201902769.

[6] M. Pathak, C.S. Rout, Miniaturized energy storage: microsupercapacitor based on two-

dimensional materials, Fundam. Supercapacitor Appl. 2D Mater. (2021) 311–358. https://doi.org/10.1016/B978-0-12-821993-5.00005-4.

[7] M. Gao, X. Dong, K. Wang, W. Duan, X. Sun, C. Zhu, W. Wang, Laser direct preparation and processing of graphene/MnO nanocomposite electrodes for microsupercapacitors, J. Energy Storage. 33 (2021) 102162. https://doi.org/10.1016/j.est.2020.102162.

[8] X. Zhang, W. Zhao, L. Wei, Y. Jin, J. Hou, X. Wang, X. Guo, In-plane flexible solid-state microsupercapacitors for on-chip electronics, Energy. 170 (2019) 338–348. https://doi.org/10.1016/J.ENERGY.2018.12.184.

[9] P. Simon, Y. Gogotsi, Materials for electrochemical capacitors, Nat. Mater. 7 (2008) 845–854. https://doi.org/10.1038/nmat2297.

[10] Q. Du, M. Zheng, L. Zhang, Y. Wang, J. Chen, L. Xue, W. Dai, G. Ji, J. Cao, Preparation of functionalized graphene sheets by a low-temperature thermal exfoliation approach and their electrochemical supercapacitive behaviors, Electrochim. Acta. 55 (2010) 3897–3903. https://doi.org/10.1016/j.electacta.2010.01.089.

[11] D. Dong, Y. Zhang, T. Wang, J. Wang, C.E. Romero, W. ping Pan, Enhancing the pore wettability of coal-based porous carbon as electrode materials for high performance supercapacitors, Mater. Chem. Phys. 252 (2020) 123381. https://doi.org/10.1016/J.MATCHEMPHYS.2020.123381.

[12] X. Mao, J. Xu, X. He, W. Yang, Y. Yang, L. Xu, Y. Zhao, Y. Zhou, All-solid-state flexible microsupercapacitors based on reduced graphene oxide/multi-walled carbon nanotube composite electrodes, Appl. Surf. Sci. 435 (2018) 1228–1236. https://doi.org/10.1016/j.apsusc.2017.11.248.

[13] B. Xu, H. Wang, Q. Zhu, N. Sun, B. Anasori, L. Hu, F. Wang, Y. Guan, Y. Gogotsi, Reduced graphene oxide as a multi-functional conductive binder for supercapacitor electrodes, Energy Storage Mater. 12 (2018) 128–136. https://doi.org/10.1016/j.ensm.2017.12.006.

[14] L. Liu, D. Ye, Y. Yu, L. Liu, Y. Wu, Carbon-based flexible micro-supercapacitor fabrication via mask-free ambient micro-plasma-jet etching, Carbon N. Y. 111 (2017) 121–127. https://doi.org/10.1016/j.carbon.2016.09.037.

[15] D.T. Bakhoum, K.O. Oyedotun, S. Sarr, N.F. Sylla, V.M. Maphiri, N.M. Ndiaye, B.D. Ngom, N. Manyala, A study of porous carbon structures derived from composite of cross-linked polymers and reduced graphene oxide for supercapacitor applications, J. Energy Storage. 51 (2022) 104476. https://doi.org/10.1016/J.EST.2022.104476.

[16] G. Rutavi, D.J. Tarimo, V.M. Maphiri, M. Ncholu, Two-step electrodeposition of Hausmannite sulphur reduced graphene oxide and cobalt-nickel layered double hydroxide heterostructure for high-performance supercapacitor, (2022) 1–14. https://doi.org/10.1002/er.7922.

[17] G. Xiong, C. Meng, R.G. Reifenberger, P.P. Irazoqui, T.S. Fisher, A review of

graphene-based electrochemical microsupercapacitors, Electroanalysis. 26 (2014) 30–51. https://doi.org/10.1002/elan.201300238.

[18] T. Wang, H.C. Chen, F. Yu, X.S. Zhao, H. Wang, Boosting the cycling stability of transition metal compounds-based supercapacitors, Energy Storage Mater. 16 (2019) 545–573. https://doi.org/10.1016/J.ENSM.2018.09.007.

[19] N.A. Kyerematen, T. Brousse, D. Pech, Microsupercapacitors as miniaturized energy-storage components for on-chip electronics, Nat. Nanotechnol. 12 (2017) 7–15. https://doi.org/10.1038/nnano.2016.196.

[20] N.F. Sylla, Activated carbon from peanut shell and its molybdenum based nanocomposites for supercapacitor applications, (2020).

[21] M.N. Rantho, Synthesis and characterization of vanadium disulfide nanosheets and carbonized iron cations adsorbed onto polyaniline for high-perfomance supercapacitor applications, Univ. Pretoria. (n.d.).

[22] https://commons.wikimedia.org/wiki/Main_Page (obtained on 12/03/2022)

[23] M. Endo, T. Takeda, Y.J. Kim, K. Koshiba, K. Ishii, High Power Electric Double Layer Capacitor (EDLC ' s); from Operating Principle to Pore Size Control in Advanced Activated Carbons, Carbon Sci. 1 (2001) 117–128.

[24] M. Khademi, D.P.J. Barz, Structure of the Electrical Double Layer Revisited: Electrode Capacitance in Aqueous Solutions, Langmuir. 36 (2020) 4250–4260.

https://doi.org/10.1021/acs.langmuir.0c00024.

[25] A. Dixit, S. Middya, S. Mitra, S. Maity, M. Bhattacharjee, D. Bandyopadhyay, Unexplored Pathways to Charge Storage in Supercapacitors, J. Phys. Chem. C. 123 (2019) 195–204. https://doi.org/10.1021/acs.jpcc.8b10326.

[26] V. Augustyn, P. Simon, B. Dunn, Pseudocapacitive oxide materials for high-rate electrochemical energy storage, Energy Environ. Sci. 7 (2014) 1597–1614. https://doi.org/10.1039/c3ee44164d.

[27] R. Li, Q. Li, L. Xiao, X. Bai, S. Ji, J. Zhang, M. An, P. Yang, Se-induced underpotential deposition of amorphous CoSe2 ultrathin nanosheet arrays as high-efficiency oxygen evolution electrocatalysts for zinc–air batteries, Mater. Today Energy. 22 (2021) 100882. https://doi.org/10.1016/J.MTENER.2021.100882.

[28] J. Xu, R. Li, C.Q. Xu, R. Zeng, Z. Jiang, B. Mei, J. Li, D. Meng, J. Chen, Underpotential-deposition synthesis and in-line electrochemical analysis of single-atom copper electrocatalysts, Appl. Catal. B Environ. 289 (2021) 120028. https://doi.org/10.1016/J.APCATB.2021.120028.

[29] Y. Zhang, D. Li, R.G. Compton, Arsenic (III) detection with underpotential deposition on gold, J. Electroanal. Chem. 909 (2022) 116154. https://doi.org/10.1016/J.JELECHEM.2022.116154.

[30] P. Murovhi, D.J. Tarimo, K.O. Oyedotun, N. Manyala, High specific energy

asymmetric supercapacitor based on alpha-manganese dioxide/activated expanded graphite composite and activated carbon-polyvinyl alcohol, J. Energy Storage. 32 (2020) 101797. https://doi.org/10.1016/j.est.2020.101797.

[31] C. Dai, C. Gu, B. Liu, Y. Lyu, X. Yao, H. He, J. Fang, G. Zhao, Preparation of low-temperature expandable graphite as a novel steam plugging agent in heavy oil reservoirs, J. Mol. Liq. 293 (2019) 111535. https://doi.org/10.1016/j.molliq.2019.111535.

[32] L. Yang, S. Cheng, X. Ji, Y. Jiang, J. Zhou, M. Liu, Investigations into the origin of pseudocapacitive behavior of Mn3O4 electrodes using in operando Raman spectroscopy, J. Mater. Chem. A. 3 (2015) 7338–7344. https://doi.org/10.1039/c5ta00223k.

[33] A. V. Dolbin, M. V. Khlistyuck, V.B. Esel'Son, V.G. Gavrilko, N.A. Vinnikov, R.M. Basnukaeva, I. Maluenda, W.K. Maser, A.M. Benito, The effect of the thermal reduction temperature on the structure and sorption capacity of reduced graphene oxide materials, Appl. Surf. Sci. 361 (2016) 213–220. https://doi.org/10.1016/j.apsusc.2015.11.167.

[34] X. Jiang, Z. Li, J. Yao, Z. Shao, X. Chen, One-step synthesis of soy protein/graphene nanocomposites and their application in photothermal therapy, Mater. Sci. Eng. C. 68 (2016) 798–804. https://doi.org/10.1016/j.msec.2016.07.034.

[35] D.J. Tarimo, K.O. Oyedotun, A.A. Mirghni, N.F. Sylla, N. Manyala, High energy and

excellent stability asymmetric supercapacitor derived from sulphur-reduced graphene oxide/manganese dioxide composite and activated carbon from peanut shell, Electrochim. Acta. 353 (2020) 136498. https://doi.org/10.1016/j.electacta.2020.136498.

[36] A.A. Mirghni, K.O. Oyedotun, O. Fasakin, B.A. Mahmoud, D.J. Tarimo, N. Manyala, High-performance bimetallic Ni-Mn phosphate hybridized with 3-D graphene foam for novel hybrid supercapacitors, J. Energy Storage. 31 (2020) 101584. https://doi.org/10.1016/j.est.2020.101584.

[37] A. Gopalakrishnan, S. Badhulika, Flexible supercapacitors based on 2D materials, Fundam. Supercapacitor Appl. 2D Mater. (2021) 253–310. https://doi.org/10.1016/B978-0-12-821993-5.00013-3.

[38] B. Mordina, R. Kumar, N.S. Neeraj, A.K. Srivastava, D.K. Setua, A. Sharma, Binder free high performance hybrid supercapacitor device based on nickel ferrite nanoparticles, J. Energy Storage. 31 (2020) 101677. https://doi.org/10.1016/J.EST.2020.101677.

[39] M. Wieczorek, M. Lewandowski, A mathematical representation of an energy management strategy for hybrid energy storage system in electric vehicle and real time optimization using a genetic algorithm, Appl. Energy. 192 (2017) 222–233. https://doi.org/10.1016/J.APENERGY.2017.02.022.

[40] F. Barzegar, L. Zhang, A. Bello, N. Manyala, X. Xia, Three dimensional modelling of

the components in supercapacitors for proper understanding of the contribution of each parameter to the final electrochemical performance, J. Mater. Chem. A. 6 (2018) 17481–17487. https://doi.org/10.1039/c8ta04736g.

[41] D.J. Tarimo, K.O. Oyedotun, A.A. Mirghni, N. Manyala, Sulphur-reduced graphene oxide composite with improved electrochemical performance for supercapacitor applications, Int. J. Hydrogen Energy. 45 (2020) 13189–13201. https://doi.org/10.1016/j.ijhydene.2020.03.059.

[42] A. Kumar, N. Kumar, Y. Sharma, J. Leu, T.Y. Tseng, Synthesis of Free-Standing Flexible rGO/MWCNT Films for Symmetric Supercapacitor Application, Nanoscale Res. Lett. 14 (2019) 1–17. https://doi.org/10.1186/s11671-019-3100-1.

[43] X. Mao, X. He, J. Xu, W. Yang, H. Liu, Y. Yang, Y. Zhou, Three-Dimensional Reduced Graphene Oxide/Poly(3,4-Ethylenedioxythiophene) Composite Open Network Architectures for Microsupercapacitors, Nanoscale Res. Lett. 14 (2019). https://doi.org/10.1186/s11671-019-3098-4.

[44] F. Santos, J.P. Tafur, J. Abad, A.J. Fernández Romero, Structural modifications and ionic transport of PVA-KOH hydrogels applied in Zn/Air batteries, J. Electroanal. Chem. 850 (2019) 113380. https://doi.org/10.1016/J.JELECHEM.2019.113380.

[45] M.N. Rantho, M.J. Madito, N. Manyala, High-performance symmetric supercapacitor device based on carbonized iron-polyaniline/nickel graphene foam, J. Alloys Compd. 819 (2020) 152993. https://doi.org/10.1016/j.jallcom.2019.152993.

[46] V. Raman, D. Rhee, A.R. Selvaraj, J. Kim, K. Prabakar, J. Kang, H.K. Kim, High-performance flexible transparent micro-supercapacitors from nanocomposite electrodes encapsulated with solution processed MoS2 nanosheets, Sci. Technol. Adv. Mater. 22 (2021) 875–884. https://doi.org/10.1080/14686996.2021.1978274.

[47] J. Coelho, M.P. Kremer, S. Pinilla, V. Nicolosi, An outlook on printed microsupercapacitors: Technology status, remaining challenges, and opportunities, Curr. Opin. Electrochem. 21 (2020) 69–75. https://doi.org/10.1016/j.coelec.2019.12.004.

[48] U. Evariste, G. Jiang, B. Yu, Y. Liu, P. Ma, One-step electrodeposition of molybdenum nickel cobalt sulfides on ni foam for high-performance asymmetric supercapacitors, J. Energy Storage. 29 (2020) 101419. https://doi.org/10.1016/J.EST.2020.101419.

[49] M.J. Madito, K.S. Matshoba, F.U. Ochai-Ejeh, N. Mongwaketsi, C.B. Mtshali, M. Fabiane, N. Manyala, Nickel-copper graphene foam prepared by atmospheric pressure chemical vapour deposition for supercapacitor applications, Surf. Coatings Technol. 383 (2020) 125230. https://doi.org/10.1016/j.surfcoat.2019.125230.

[50] S. Liu, Y. Yin, K. San Hui, K.N. Hui, S.C. Lee, S. Chan Jun, Nickel hydroxide/chemical vapor deposition-grown graphene/nickel hydroxide/nickel foam hybrid electrode for high performance supercapacitors, Electrochim. Acta. 297 (2019) 479–487. https://doi.org/10.1016/J.ELECTACTA.2018.11.070.

[51] X. Li, Q. Zha, Y. Ni, Ni-Fe Phosphate/Ni Foam Electrode: Facile Hydrothermal Synthesis and Ultralong Oxygen Evolution Reaction Durability, ACS Sustain. Chem. Eng. 7 (2019) 18332–18340. https://doi.org/10.1021/ACSSUSCHEMENG.9B03711/SUPPL_FILE/SC9B03711_SI_001.PDF.

[52] P. Miao, J. He, Z. Sang, F. Zhang, J. Guo, D. Su, X. Yan, X. Li, H. Ji, Hydrothermal growth of 3D graphene on nickel foam as a substrate of nickel-cobalt-sulfur for high-performance supercapacitors, J. Alloys Compd. 732 (2018) 613–623. https://doi.org/10.1016/J.JALLCOM.2017.10.243.

[53] X. Sun, G. Pan, H. Qi, Z. Sun, Dip-coating prepared nickel-foam composite cathodes with hydrophobic layer for atenolol elimination in electro-Fenton system, J. Electroanal. Chem. 856 (2020) 113725. https://doi.org/10.1016/J.JELECHEM.2019.113725.

[54] L. Lai, M. Clark, S. Su, R. Li, D.G. Ivey, X. Zhu, Dip-coating synthesis of rGO/α-Ni(OH)2@nickel foam with layer-by-layer structure for high performance binder-free supercapacitors, Electrochim. Acta. 368 (2021) 137589. https://doi.org/10.1016/J.ELECTACTA.2020.137589.

[55] J. Saddique, X. Cheng, H. Shi, R. Wu, Y. Zhang, High-performance Ni-Co sulfide nanosheet-nanotubes grown on Ni foam as a binder free electrode for supercapacitors, Appl. Sci. 9 (2019). https://doi.org/10.3390/app9153082.

[56] A. Lakshmi-Narayana, M. Dhananjaya, N. Guru-Prakash, A. Mauger, C.M. Julien, O.M. Hussain, Li2TiO3/Ni foam composite as high-performance electrode for energy storage and conversion, Heliyon. 5 (2019) e02060. https://doi.org/10.1016/J.HELIYON.2019.E02060.

[57] B. Yilbas, A. Al-Sharafi, H. Ali, Coating. Electrospun organic piezoelectric nanofibers and their energy and bio applications, Nano Energy 2019.

[58] N.F. Sylla, N.M. Ndiaye, B.D. Ngom, D. Momodu, M.J. Madito, B.K. Mutuma, N. Manyala, Effect of porosity enhancing agents on the electrochemical performance of high-energy ultracapacitor electrodes derived from peanut shell waste, Sci. Rep. 9 (2019) 1–15. https://doi.org/10.1038/s41598-019-50189-x.

[59] H. Cheng, J. Lin, Y. Su, D. Chen, X. Zheng, H. Zhu, Green synthesis of soluble graphene in organic solvent via simultaneous functionalization and reduction of graphene oxide with urushiol, Mater. Today Commun. 23 (2020) 100938. https://doi.org/10.1016/J.MTCOMM.2020.100938.

[60] Y. Zhao, Z. Wu, S. Guo, Z. Zhou, Z. Miao, S. Xie, R. Huang, L. Li, Hyperbranched graphene oxide structure-based epoxy nanocomposite with simultaneous enhanced mechanical properties, thermal conductivity, and superior electrical insulation, Compos. Sci. Technol. 217 (2022) 109082. https://doi.org/10.1016/J.COMPSCITECH.2021.109082.

[61] Y. Xu, C. Huang, A. Hu, Z. Fan, C. Chen, Y. Yang, Q. Tang, C. Jiang, X. Chen, N-

rich reduced graphene oxide film with cross-coupled porous networks as free-standing electrode for high performance supercapacitors, Appl. Surf. Sci. 563 (2021) 150303. https://doi.org/10.1016/J.APSUSC.2021.150303.

[62] S. Claramunt, A. Varea, D. Lópezlópez-Díaz, M. Mercedes Velázquezvelázquez, A. Cornet, A. Cirera, The Importance of Interbands on the Interpretation of the Raman Spectrum of Graphene Oxide, J. Phys. Chem. C. 119 (2015) 10123–10129. https://doi.org/10.1021/acs.jpcc.5b01590.

[63] J. Wang, F. Li, F. Zhu, O.G. Schmidt, Recent Progress in Micro-Supercapacitor Design, Integration, and Functionalization, Small Methods. 3 (2019). https://doi.org/10.1002/smtd.201800367.

[64] C. Chae, Y. Bin Kim, S.S. Lee, T.H. Kim, Y. Jo, H.S. Kim, S.K. Kim, Y. Choi, S. Jeong, All-3D-printed solid-state microsupercapacitors, Energy Storage Mater. 40 (2021) 1–9. https://doi.org/10.1016/J.ENSM.2021.04.038.

[65] E. Quain, T.S. Mathis, N. Kurra, K. Maleski, K.L. Van Aken, M. Alhabeb, H.N. Alshareef, Y. Gogotsi, Direct Writing of Additive-Free MXene-in-Water Ink for Electronics and Energy Storage, Adv. Mater. Technol. 4 (2019) 1800256. https://doi.org/10.1002/admt.201800256.

[66] V.M. Maphiri, G. Rutavi, N.F. Sylla, S.A. Adewinbi, O. Fasakin, N. Man-, Novel Thermally Reduced Graphene Oxide Microsupercapacitor Fabricated via Mask — Free AxiDraw Direct Writing, (2021) 1–15.

[67] K.U. Laszczyk, Design and technology processes used for microsupercapacitors, Microsupercapacitors. (2022) 215–255. https://doi.org/10.1016/B978-0-08-102888-9.00004-5.

[68] E. Kim, B.J. Lee, K. Maleski, Y. Chae, Y. Lee, Y. Gogotsi, C.W. Ahn, Microsupercapacitor with a 500 nm gap between MXene/CNT electrodes, Nano Energy. 81 (2021) 105616. https://doi.org/10.1016/J.NANOEN.2020.105616.

[69] B. Dousti, S. Babu, N. Geramifard, M.Y. Choi, J.B. Lee, S.F. Cogan, G.S. Lee, Highly flexible all-solid-state microsupercapacitors for on chip applications using a transfer-free fabrication process, J. Power Sources. 520 (2022) 230779. https://doi.org/10.1016/J.JPOWSOUR.2021.230779.

[70] N. Gupta, U. Mogera, G.U. Kulkarni, Ultrafast planar microsupercapacitor based on defect-free twisted multilayer graphene, Mater. Res. Bull. (2022) 111841. https://doi.org/10.1016/J.MATERRESBULL.2022.111841.

[71] V. Vijayakumar, M. Ghosh, R. Soni, B. Anothumakkool, S. Kurungot, M. Winter, J.R. Nair, The role and the necessary features of electrolytes for microsupercapacitors, Microsupercapacitors. (2022) 47–116. https://doi.org/10.1016/B978-0-08-102888-9.00003-3.

[72] A.S. Sarac, H.D. Gilsing, A. Gencturk, B. Schulz, Electrochemically polymerized 2,2-dimethyl-3,4-propylenedioxythiophene on carbon fiber for microsupercapacitor, Prog. Org. Coatings. 60 (2007) 281–286.

https://doi.org/10.1016/J.PORGCOAT.2007.07.025.

[73] J. Yang, S. Deng, J. Lei, H. Ju, S. Gunasekaran, Electrochemical synthesis of reduced graphene sheet-AuPd alloy nanoparticle composites for enzymatic biosensing, Biosens. Bioelectron. 29 (2011) 159–166. https://doi.org/10.1016/j.bios.2011.08.011.

[74] O. Mondal, S. Mitra, M. Pal, A. Datta, S. Dhara, D. Chakravorty, Reduced graphene oxide synthesis by high energy ball milling, Mater. Chem. Phys. 161 (2015) 123–129. https://doi.org/10.1016/j.matchemphys.2015.05.023.

[75] M.Z. Iqbal, S. Zakar, S.S. Haider, Role of aqueous electrolytes on the performance of electrochemical energy storage device, J. Electroanal. Chem. 858 (2020) 113793. https://doi.org/10.1016/J.JELECHEM.2019.113793.

[76] Q. Gou, S. Zhao, J. Wang, M. Li, J. Xue, Recent Advances on Boosting the Cell Voltage of Aqueous Supercapacitors, Nano-Micro Lett. 2020 121. 12 (2020) 1–22. https://doi.org/10.1007/S40820-020-00430-4.

[77] M. Le Thai, S. Qiao, R.K. Dutta, G. Jha, A.F. Ogata, G.T. Chandran, R.M. Penner, Collateral Advantages of a Gel Electrolyte for MnO2 Nanowire Capacitors: Higher Voltage and Reduced Volume, ACS Energy Lett. 2 (2017) 1162–1169. https://doi.org/10.1021/acsenergylett.7b00172.

[78] Q. Chen, X. Li, X. Zang, Y. Cao, Y. He, P. Li, K. Wang, J. Wei, D. Wu, H. Zhu, Effect of different gel electrolytes on graphene-based solid-state supercapacitors, RSC

Adv. 4 (2014) 36253–36256. https://doi.org/10.1039/C4RA05553E.

[79] B. Abdulhakeem, Three dimensional graphene composites for energy storage applications by Bello Abdulhakeem A thesis submitted in partial fulfilment of the requirements for the degree of DOCTOR OF PHILOSOPHY (PHD) IN PHYSICS Faculty of Natural and Agricultural Sciences, Univ. Pretoria. (2014).

[80] F. Barzegar, Synthesis and characterization of activated carbon materials for supercapacitor applications, Univeristy of Pretoria (2018).

[81] T.S. Mathis, N. Kurra, X. Wang, D. Pinto, P. Simon, Y. Gogotsi, Energy Storage Data Reporting in Perspective—Guidelines for Interpreting the Performance of Electrochemical Energy Storage Systems, Adv. Energy Mater. 9 (2019) 1–13. https://doi.org/10.1002/aenm.201902007.

[82] R. Cheruku, D.S. Bhaskaram, G. Govindaraj, Variable range hopping and relaxation mechanism in graphene oxide sheets containing sp3 hybridization induced localization, J. Mater. Sci. Mater. Electron. 29 (2018) 9663–9672. https://doi.org/10.1007/s10854-018-9003-6.

[83] C. Huang, J. Zhang, N.P. Young, H.J. Snaith, P.S. Grant, Solid-state supercapacitors with rationally designed heterogeneous electrodes fabricated by large area spray processing for wearable energy storage applications, Sci. Rep. 6 (2016) 1–15. https://doi.org/10.1038/srep25684.

[84] C. Karaman, E. Bayram, O. Karaman, Z. Aktaş, Preparation of high surface area nitrogen doped graphene for the assessment of morphologic properties and nitrogen content impacts on supercapacitors, J. Electroanal. Chem. 868 (2020) 114197. https://doi.org/10.1016/j.jelechem.2020.114197.

[85] M.N. Rantho, M.J. Madito, N. Manyala, Symmetric supercapacitor with supercapattery behavior based on carbonized iron cations adsorbed onto polyaniline, Electrochim. Acta. 262 (2018) 82–96. https://doi.org/10.1016/j.electacta.2018.01.001.

[86] P.L. Taberna, P. Simon, J.F. Fauvarque, Electrochemical Characteristics and Impedance Spectroscopy Studies of Carbon-Carbon Supercapacitors, J. Electrochem. Soc. 150 (2003) A292. https://doi.org/10.1149/1.1543948.

[87] https://commons.wikimedia.org/wiki/File:EDLC-Voltage_distributionDutchtxt (obtained on 15/03/2022)

[88] Y. Cui, X. Zhao, R. Guo, Improved electrochemical performance of La0.7Sr0.3MnO3 and carbon co-coated LiFePO4 synthesized by freeze-drying process, Electrochim. Acta. 55 (2010) 922–926. https://doi.org/10.1016/J.ELECTACTA.2009.08.020.

[89] D. Qu, The study of the proton diffusion process in the porous MnO2 electrode, Electrochim. Acta. 49 (2004) 657–665. https://doi.org/10.1016/j.electacta.2003.08.030.

Chapter 3 Preparation and analytical techniques

3.1. Introduction

This chapter covers the methods and techniques that were used in the making and analysis of the conventional SC and µ-SC electrodes; and devices. The first part of this chapter focuses on the preparation and fabrication methods, the last part focuses on the analysis techniques used within this study.

The TRGO electroactive material used in both SC and µ-SC was prepared by Hummers' method, sprayed or pasted on the MSG or NF substrate, then subsequently thermally reduced using AP-CVD in argon environment at various temperatures to form TRGO-X where X represent the reducing temperature which are 200, 300, 400 and 500℃. The electrolyte (aqueous electrolyte) for SC was prepared by dissolving pallets such as KOH in deionised water (DW), as for the µ-SC, the gel electrolyte was prepared by hydrolysing PVA followed by the addition H_3PO_4 acid. The TRGO/NF electrode and its related device was analysed in aqueous electrolyte in both two and three electrode configurations. Moreover, the TRGO-X on MSG was patterned using the AxiDraw and used together with the gel electrolyte in fabricating two electrode devices.

The synthesized materials, fabricated electrodes and/or devices that were investigated in this study were characterized using the following techniques: The X-ray diffraction (XRD) was

used to investigate the crystal structure. The scanning electron microscopy (SEM) and energy dispersive X-ray spectroscopy (EDS) was used to obtain the surface morphology and elemental information. Raman microscopy was used to obtain the structural properties, while the atomic force microscope (AFM) was used to measure the surface roughness and topology of the thin films. Fourier transformation infrared (FT-IR) spectroscopy was used to measure surface functional groups. Ultraviolet–visible spectroscopy (UV-Vis) was used to measure light transparency and absorption of the prepared samples. Four point probe (4PP) was used to determine the sheet resistance of the TRGO films. The electrochemical energy storage performance of the SC and µ-SC were carried out using potentiostat while monitoring the cyclic voltammetry (CV), galvanostatic charge-discharge (GCD) and Electrochemical impedance spectroscopy (EIS).

3.2. Preparation techniques

3.2.1. Hummers method

Hummers' method was developed in the 50s by Hummers and Offeman as a safer, quicker and effective way to prepare graphene oxide. This method is an advancement of the Staudenmaier's method which has drawbacks such as fuming nitric acid, possibility of explosion, time consuming, and low yield. Thus, Hummers' method is a better alternative to the Staudenmaier's method; it mainly uses cooled sulphuric acid, potassium permanganate

and the precursors like graphite. The process occurs at a low temperature of approximately 50 ℃ for a short time of less than 3 hours [5,6]

In this work, 1 g of graphite powder was slowly added into an agitated 120 ml cooled sulphuric acid (H_2SO_4) until a black homogeneous solution was obtained. Potassium permanganate ($KMnO_4$) was then added into the black homogeneous solution. The solution was continuously stirred at 250 rpm for 180 min at 50 ℃ and then left to cool to room temperature. Deionised water (100 mL) was added together with 20 ml of hydrogen peroxide (H_2O_2) to stop the reaction by reducing the remaining $KMnO_4$ into a water soluble manganese sulphate ($MnSO_4$) as described by the equation below (3.1):

$$\mathbf{2KMnO_4 + 3H_2SO_4 + 5H_2O_2 = 2MnSO_4 + K_2SO_4 + 8H_2O + 5O_2} \quad \ldots 3.1$$

The GO was cleaned via the decantation method which involves adding DW into the GO solution and let it settles, decanting, adding DW, letting the GO settle, decant, repeating until the pH was neutral ensuring that GO becomes impurity free. The GO solute was then centrifuged at 5000 rpm for 5 min The obtained GO was then dried in an oven at 60 ℃ and stored for SC electrode and μ-SC fabrication and characterisation [4–6]

3.2.2. Preparation of electrode

The electrode preparation methods utilised in the work, in both SC and µ-SC are binder-less and also do not require any sort of conductive enhancers. This is primarily due to the high conductivity of rGO. This also simplified the µ-SC fabrication by removing the current collector, which led to the simplicity of the fabrication method. This developed method present a significant progress in the fabrication of binder and conductive enhancement for electrochemical energy storage devices.

3.2.2.1. Supercapacitor

The electrode for the SC was prepared via Slurry paste. In brief, the dried GO was mixed with ethanol via string and sonication until a slurry paste (solution) is achieved. The slurry was then pasted onto nickel foam (NF) current collector, which was then dried in an oven over night.

3.2.2.2. Microsupercapacitors

3.2.2.2.1. Spray coating

The thin film used in the fabrication of the interdigitated μ-SC was prepared via spray coating method illustrated in Figure 3.1. The GO solution was also prepared by mixing dried GO and ethanol, but a less viscous solution was archived as compared to the GO solution for slurry pasting for SC electrode. The GO solution was poured into the airbrush which was connected to a pressurised argon (Ar) or nitrogen (N_2) glass cylinder, then GO was sprayed onto the microscopic glass (MSG) [4].

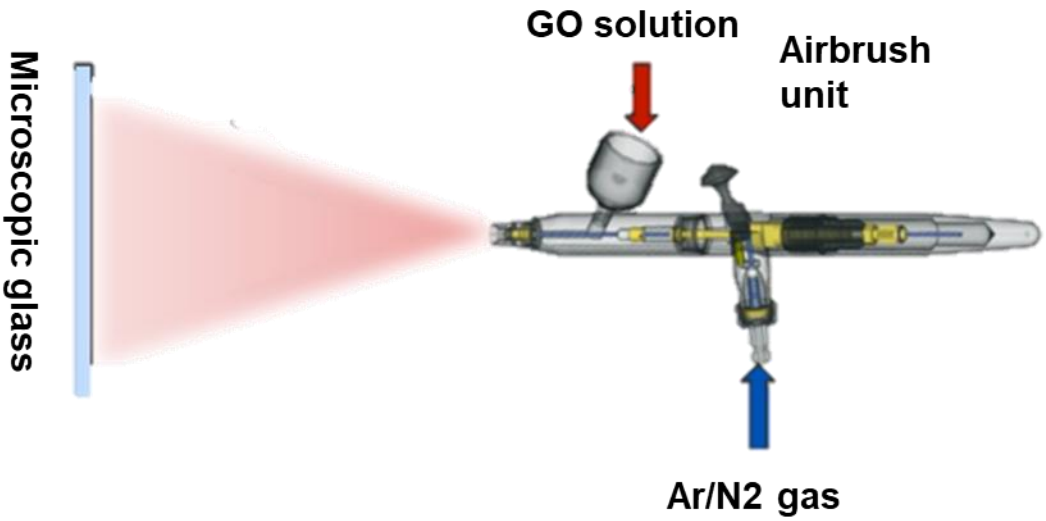

Figure 3.1. Schematic setup of a spray coater

3.2.2.2.2. AxiDraw

An AxiDraw sketching instrument (Figure 3.2 (a)) is coupled with a sharp blade pen (Figure 3.2 (b)), rather than a pen marker as illustrated in Figure 3.2 (a). The AxiDraw equipment was controlled by AxiDraw extension add-on on the Inkscape software. The sharp blade pen is used to remove the active material to create the positive and negative electrodes [7]. This mask-free electrode fabrication technique has got the following advantages: Simple, cheap and quick as compared to other electrode fabrication techniques.

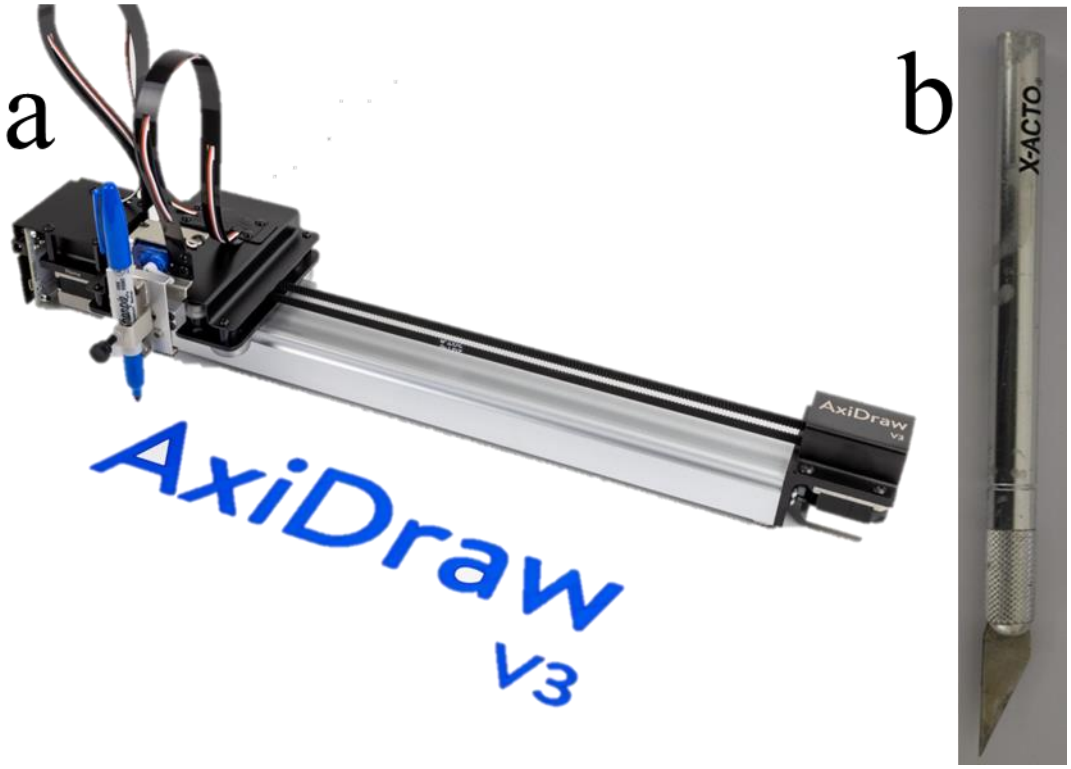

Figure 3.2. (a) An AxiDraw sketching instrument and (b) sharp blade pen.

The Inkscape project schematic of the µ-SC with 6 digits per unit area is displayed in Figure 3.3 (a), while the corresponding TRGO patterned interdigitated electrodes are displayed in Figure 3.3 (b). It can be seen that the Inkscape drawn schematic is identical to the Axidraw pattern. The inkscape defined parameter which are number of digits per unit area (n), width (W) Length (L) and Breadth (B), and Edge (E) were obtained on the patterned TRGO µ-SC as defined on the Inkscape project. Interspace (i) is determined by the thickness of the tip of the sharp blade pen. The interspace distance was determined by SEM as displayed in Figure 3.3 (c).

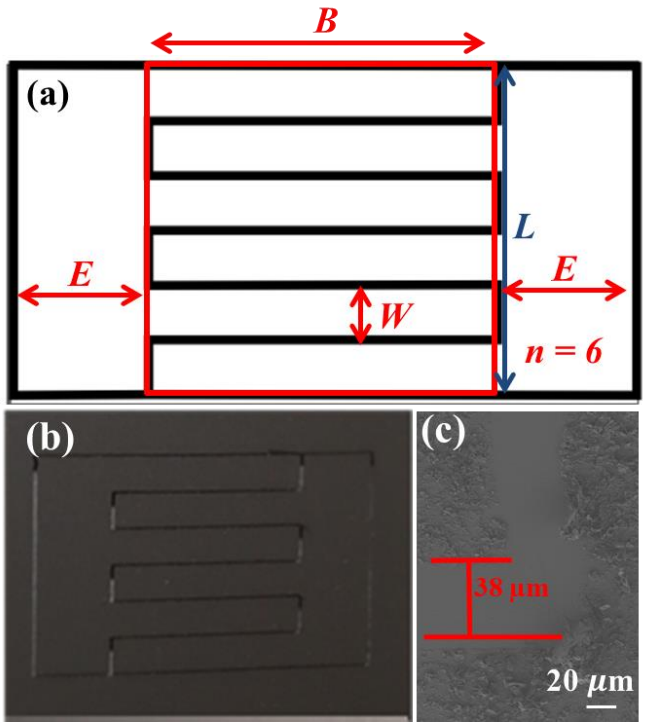

Figure 3.3 (a) Inkscape project schematic (with labelled parameter) and (b) digital image of TRGO patterned of µ-SC with 6 digits per unit area and (c) SEM image of the interspacing distance.

3.2.3. Atmospheric pressure chemical vapour deposition/tube furnace

The chemical vapour deposition (CVD) consists of a reaction chamber, pressure sensor, and heating element. The chamber was connected to an inlet gas monitored by a flow meters and an outlet gas as shown in Figure 3.4. This technique is mostly used for production of high-purity material in bulk either in thin-film or in powder form, where the CVD process utilizes dynamic system of flowing gaseous precursors reacting chemically within the reaction chamber under various heating condition. In this work, CVD was operated in atmospheric pressure, hence atmospheric pressure chemical vapour deposition (AP-CVD). It was used to remove the oxygen functional groups (OFGs) within the surface of GO in an argon gas environment which mainly prevent the reactions between carbon the GO and oxygen from the environment into carbon mono/dioxide.

In brief, GO on NF/MSG was placed within the reaction chamber; Ar gas was introduced into the system to purge the atmospheric environment and also to create its own inert environment. In simple terms, during the reduction the heat is generated from the heaters within the CVD, which led to the removal of the OFGs on the surface the GO sheets. This is a very effective, simple, and safe method of reducing GO [8–10].

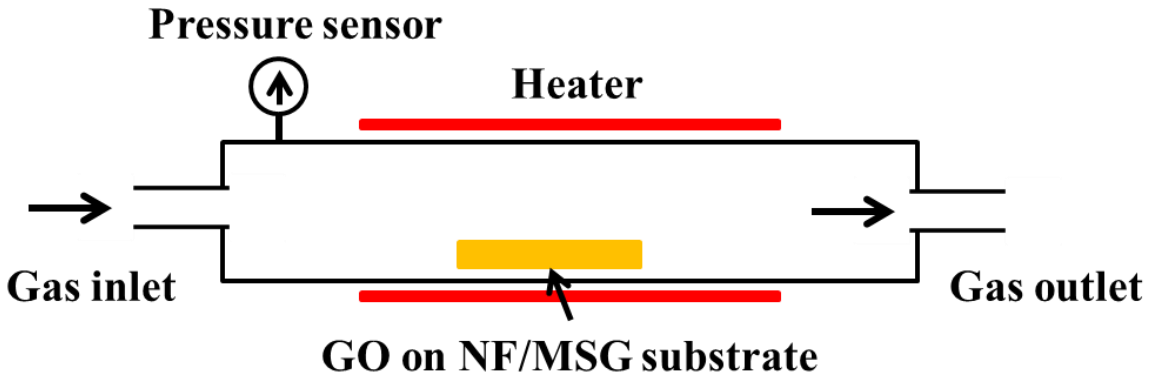

Figure 3.4. The schematic diagram of a horizontal CVD

3.2.4. Electrolyte preparation

The electrolyte is the substance located between the two-working electrode in device configuration. This substance supplies the electrochemical device with ions essential for charge storage. Moreover, the significance of the electrolyte heavily depends on the ionic concentration, size, type and its electrode material interaction. The electrolytes utilised in this work were aqueous electrolyte in conventional SC and a gel electrolyte in μ-SC devices.

3.2.5.1. Aqueous electrolyte

The electrolyte was prepared by dissolving pellets of potassium hydroxide (KOH) in deionised water. The molarity (C) of the electrolyte is calculated using the following equation:

$$\boldsymbol{M = C \times V \times Mr} \quad \ldots 3.2$$

where M is the mass of the pellets in gram is, V is the volume of the deionised water in dm^3, and Mr is the relative molar mass in g/dm^{-3}.

3.2.5.2. Gel electrolyte

The PVA gel electrolyte was prepared by hydrating PVA under a constant stirring and heating at 90 ℃ until the solution turns clear or transparent as illustrated in Figure 3.5. The volume ratio (in %) of H_3PO_4 and PVA were thoroughly mixed to fabricate PVA-H_3PO_4.

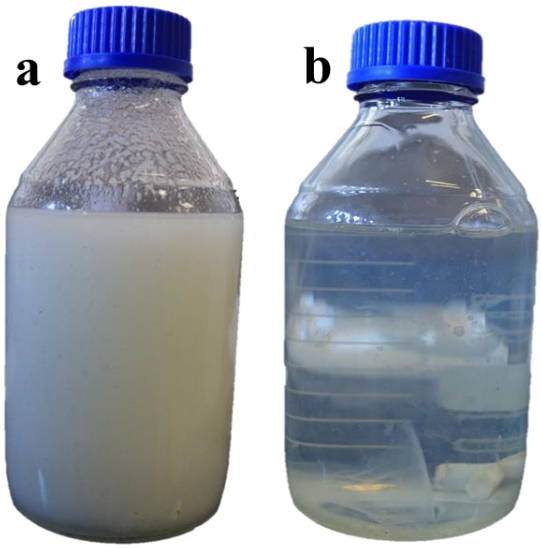

Figure 3.5. Solution of PVA and deionised water (a) before gelation and (b) after gelation.

3.3. Analysing techniques

3.3.1. X-ray diffraction

The X-ray diffraction (XRD) is a non-destructive analytical technique used for bulk phase structural identification of crystalline materials which includes organic and inorganic samples like metals, minerals and ceramics. The XRD can be used to study various crystal unit cell structure parameters such as atomic spacing (interplanar spacing), crystallite size, and phase quantification [11,12].

With reference to the powder XRD (PXRD); during the PXRD operation (a schematic is displayed in Figure 3.6 (a)), the X-rays are generated at the cathode ray tube (source, X-ray tube), then pass through the slit to produces monochromatic radiation and directed towards the sample. Interaction between incident X-rays and the sample material produces different rays via constructive interference when a condition satisfies the Bragg's Law shown in Figure 3.6 (b) and mathematically displayed using equation (3.3) [2,3]:

$$\boldsymbol{n\lambda = 2d \sin \theta} \qquad \ldots 3.3$$

where n, λ, d, and θ are a positive integer, wavelength of the incident X-rays, interplanar spacing and scattering angle, respectively.

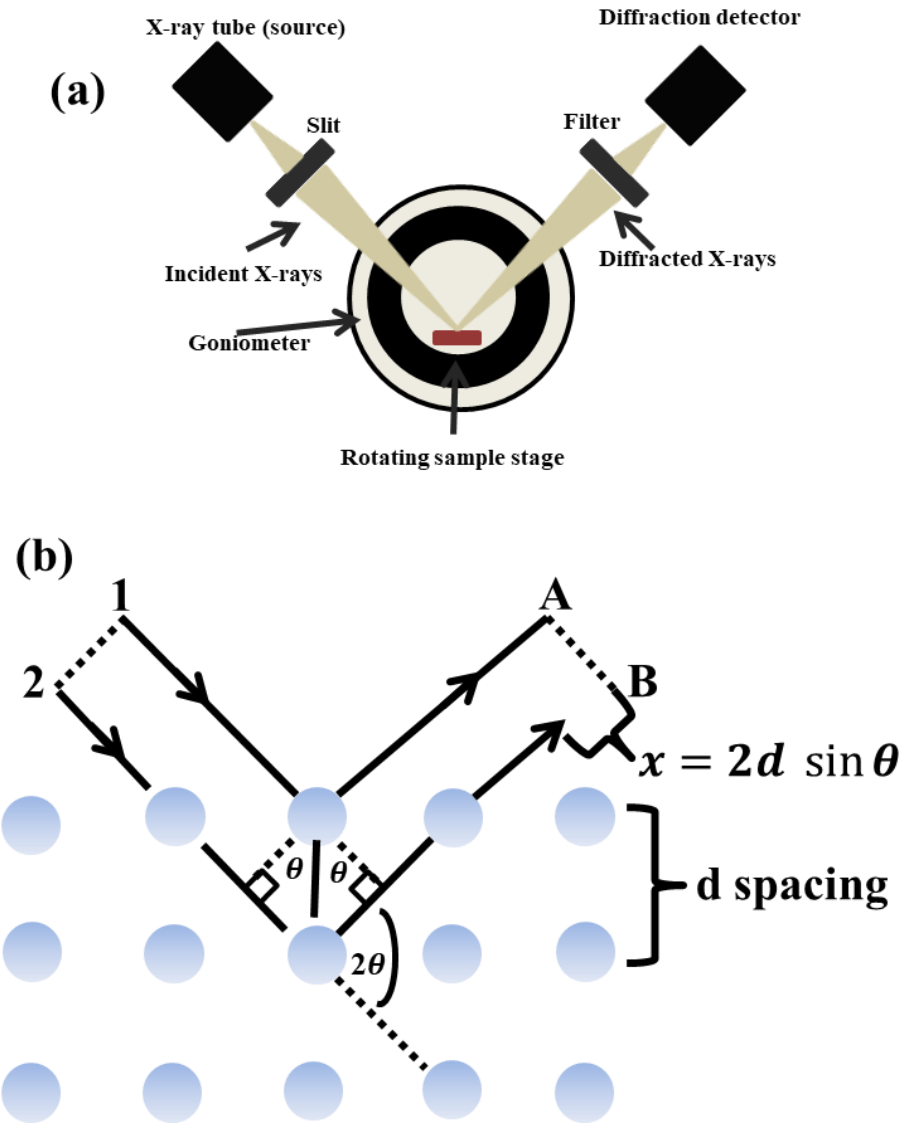

Figure 3.6. Schematic (a) detailing the basic components of X-ray diffractometers, and (b) illustration of the diffraction by crystallised atoms.

The X-ray analysis was done under Copper (Cu) X-ray source with a known wavelength λ = 0.15406 nm. The goniometer displayed in Figure 3.6 (a) is used to measure the angle at which constructive interference occurs. Bragg's equation 3.3 was used to determine the d

spacing in Figure 3.6 (b) of the analysed material, and the XRD plot of the scattered X-ray intensity as a function of the diffraction scattering angle 2θ which is unique for each and every material is displayed in Figure 3.7 (graphite [2,3])

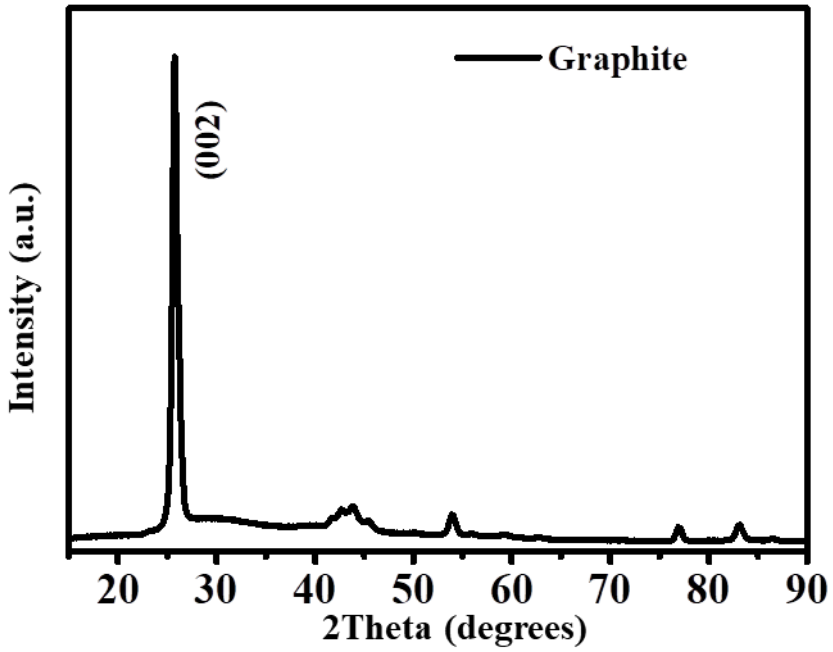

Figure 3.7. The XRD pattern of graphite. (Adopted from this study)

3.3.2. Fourier transform infrared spectroscopy

Fourier Transform Infrared (FTIR) Spectroscopy is a non-destructive analytical technique that uses detection of molecular vibration based on the processes of infrared absorption (transmittance) and Raman scattering to identify inorganic and organic compounds. The schematic of the FTIR is shown in Figure 3.8 (a), which elucidate the following basic components: Radiation (infrared) source, interferometer (interferogram), mirrors and detector. The incident photon from the infrared source is scattered upon interaction of the photons and the chemical bonds within the examined material. The signal from the material moves through a fixed mirror and a beam splitter onto a rapidly moving mirror to reduce the noise then into an interferometer to a computer. The generated FTIR plot shows the intensity of the chemical vibration notch in transmittance percentage as a function of wavenumber as displayed in Figure 3.8 (b).

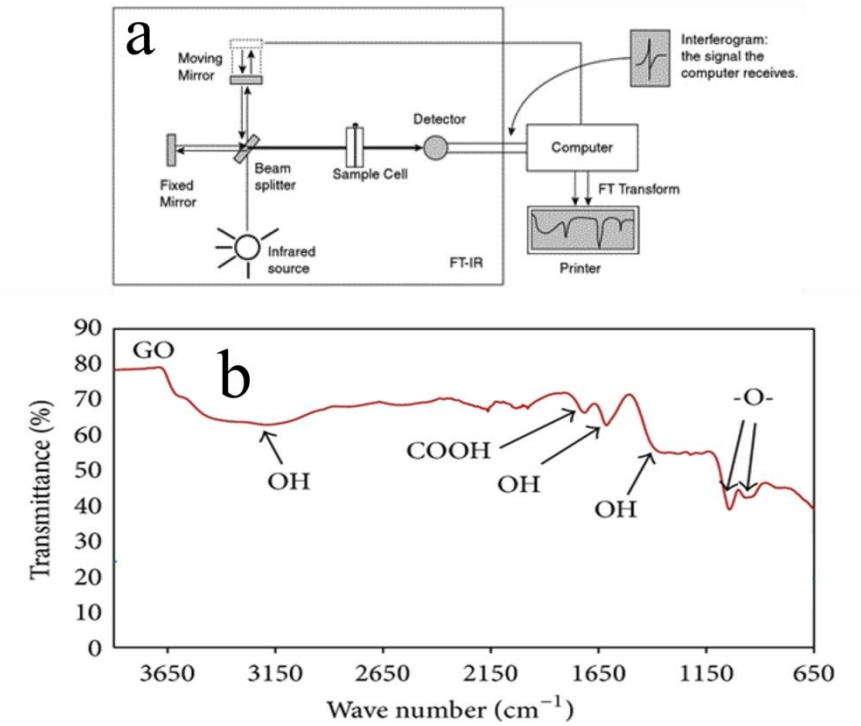

Figure 3.8. (a) Schematic diagram of an FTIR instrument and (b) FTIR spectrum of GO. (Adopted from [13] and [14], respectively)

3.3.3. Raman spectroscopy

Raman spectroscopy is a non-destructive vibrational technique, just like the FTIR, it has a high molecular specificity making it an excellent technique for material analysis especially carbon based materials such as graphene, carbon nanotube and fullerene. It can provide structural information such as crystallinity; chemical phase and structure; and molecular interactions [15–17].

In summary, Raman spectroscopy analyses the scattered incident photons from the laser source after the interaction of the laser with the examined material's chemical bond. The interaction of the chemical bonds within the material and the incident photons with an energy of $\hbar\omega_L$ (where $\hbar$ is the planks constant and $\omega_L$is the laser angular frequency) creates a time-dependent perturbation which increases the ground states energy (E_{gs}) to $E_{gs} + \hbar\omega_L$ making the material's molecule unstable. Since the molecule is unstable i.e. the molecule has no stationary state, the photons are emitted back and forth from the ground state to the virtual state. If the energy/frequency of the emitted photon is the same as the incident one (elastic scattering), this is referred to as Rayleigh scattering. On the contrary, if the molecule returns to a ground state and photons lose and gain some energy (inelastic scattering), this process is referred to as Stokes and Anti-Stokes process respectively. These processes i.e. Rayleigh scattering, Stokes and Anti-Stokes process are displayed schematically in Figure 3.9 (a), and the plot in Figure 3.9 (b) shows a typical Raman spectrum of the processes.

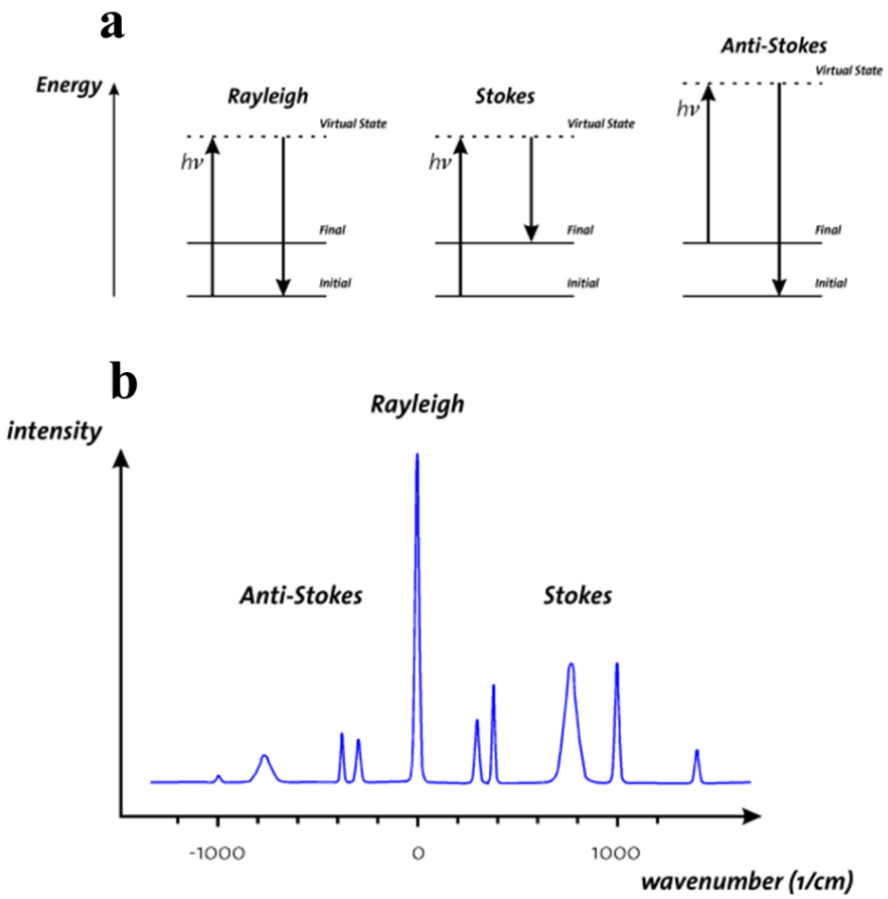

Figure 3.9. (a) Energy level diagram for Raman scattering, and (b) a typical Raman spectrum. Adopted from confocal Raman microscopy manual from WITec.

Components of a typical Raman spectrometer system are illustrated in Figure 3.10. In general, the detection of the Raman spectrum occurs after the elimination of the Rayleigh scattering mainly by the optical filter together with the diffraction grating used to disperse the Raman scattered light. The weak Raman scattered intensity is analysed by an extremely sensitive detector, the charge-couple devices (CCDs) which are commonly used in Raman

detectors due to their low signal-to noise ratios and high quantum efficiencies. Within the CCDs, the charge collection from the scattered photons are directly proportional to the Raman scattering intensity. These Raman systems or other Raman systems have several laser source options which are often chosen based on the desired wavelength and spot [3,18,19].

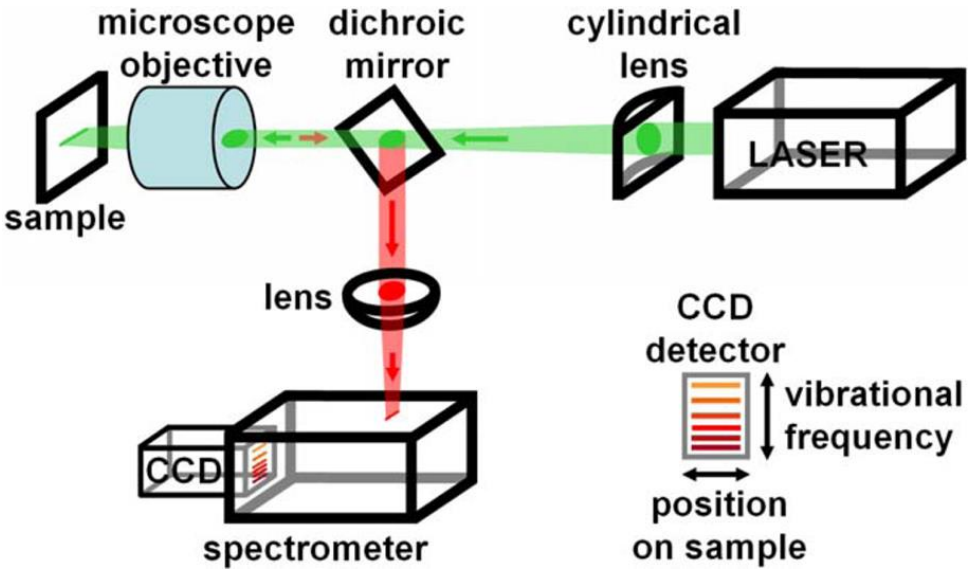

Figure 3.10. Schematic illustration of the beam path for confocal Raman microscopy. Adopted from Ref [18]

3.3.4. Atomic force microscopy

The Atomic force microscopy (AFM) is a form of scanning probe microscope developed in the 80s. The AFM has become a powerful tool in fields of science and engineering, which explores the surface properties and structures. The basic components of a typical AFM instrument are illustrated in Figure 3.11. The AFM has a probe with a very sharp tip attached to a microfabricated silicon cantilever. The scanning of the sample surface by the probe is carried with the piezoelectric scanner, which moves sideways, and expanding or shrink within response to the applied voltages. A laser beam is reflected from the cantilever onto the segmented (into 4 parts) photodiode detector, that detects vertical and lateral distortion and deflections of the cantilever. The AFM can be measured in different modes such as contact, tapping and non-contact. In general, the probe or the sample moved vertically altering the distance between the surface and probe [19–22].

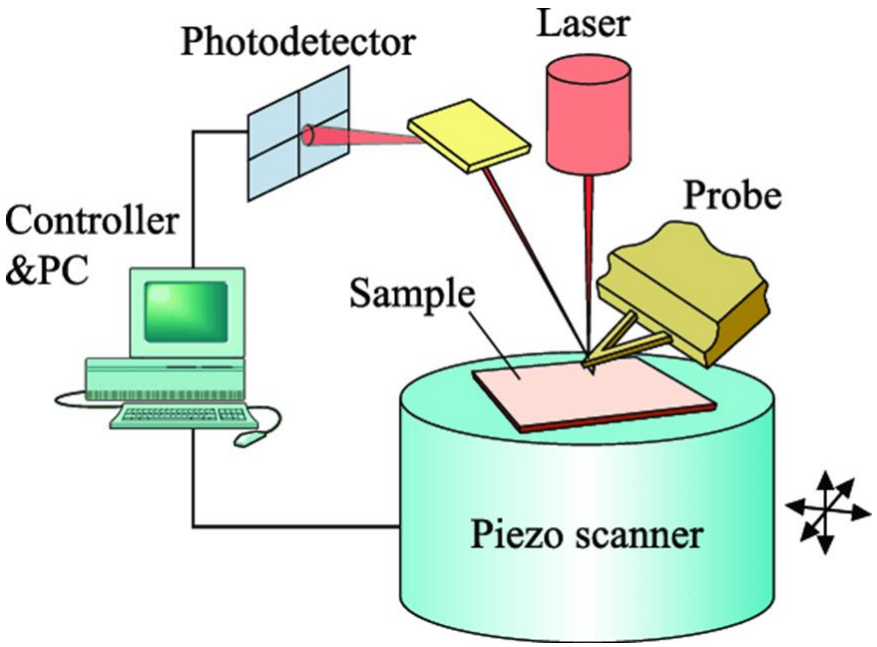

Figure 3.11. Schematic drawing of the atomic force microscopy. Adopted from Ref [22].

3.3.5. Scanning electron microscopy and energy-dispersive x-ray spectroscopy

Scanning electron microscopy (SEM) is a technique mainly used for surface images of any material within the micro to nanometer range. Typical SEM images or analysis yields information about composition, topography, morphology and crystallography of materials. The SEM utilised as focused beam of electrons under extreme vacuum condition to capture high resolution and obtain high levels of magnification. When a focused electron interacts

with the sample's surface, it generates low energy (~ 50 eV) secondary electrons which are used for image construction by measuring the intensity of the secondary with respect to the position of the primary scanning electrons. The low magnification SEM images of GO is displayed in Figure 3.12 (a) which shows GO has a rough sheet-like morphology.

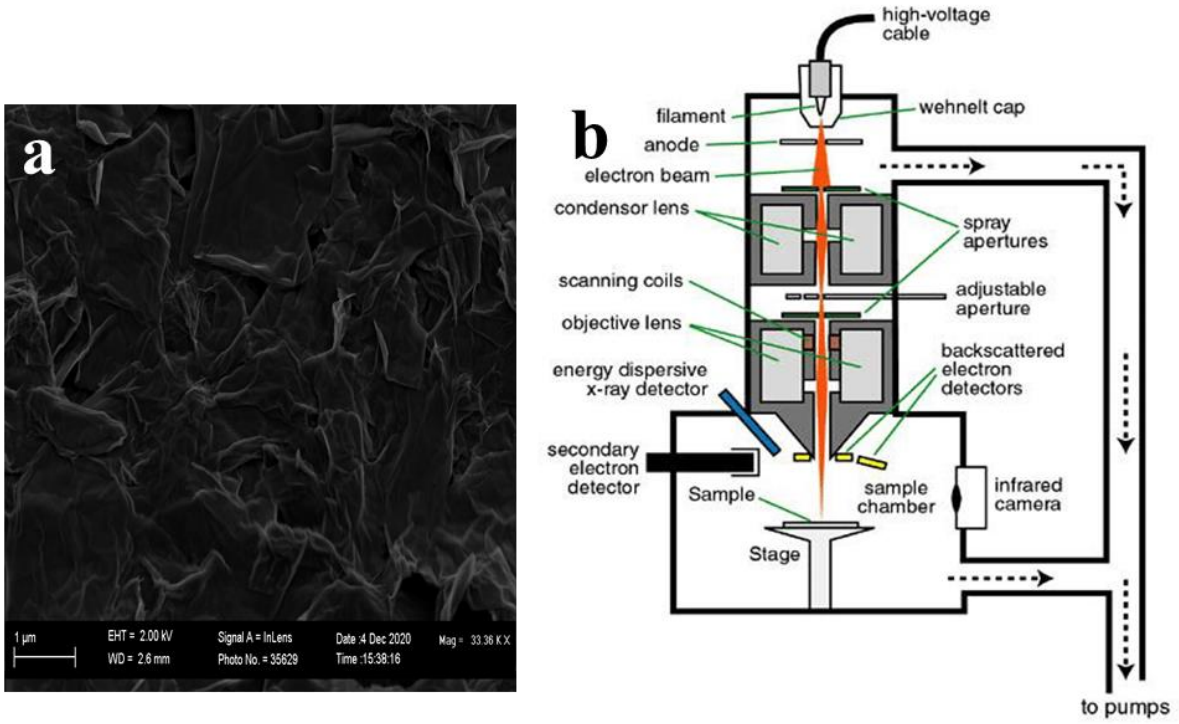

Figure 3.12. (a) Low magnification SEM image of GO (adopted from this study) and (b) schematic diagram of basic SEM components (Adopted from Ref [23]).

In addition, the X-rays that are emitted together with the low energy secondary electrons when the primary scanning electrons beam strikes the sample can be characterized by an

energy dispersive X-ray spectroscopy (EDS). The EDS detector (in Figure 3.12 (b)) is an add-on to the SEM equipment. Every element has a unique energy difference between the inner and outer electron shells, thus the X-ray emitted from the material yields elemental identification which gives the EDS the ability to provide elemental composition of the sample.

3.3.6. Ultraviolet–visible spectroscopy

Ultraviolet-visible spectroscopy (UV-Vis), like Raman and FTIR, is a technique which is useful for compound identification; this is mainly because most compounds contain chromophores. Chromophores are parts of the molecule where the absorption proceeds such as carbonyl (O = C<) chromophores within GO structures. The chromophore absorb specific wavelength from the ultra-violet or visible light [24,25]. Basic schematic of UV-Vis instrument is illustrated in Figure 3.12. There are two basic UV-Vis configurations namely single beam and double beam instrument. In general, the beam is generated at the source that enters the entrance slit onto the dispersion device with either a prism or monochromatic diffraction grating, it then enters an exit slit to the sample and finally, to the detector [24–27].

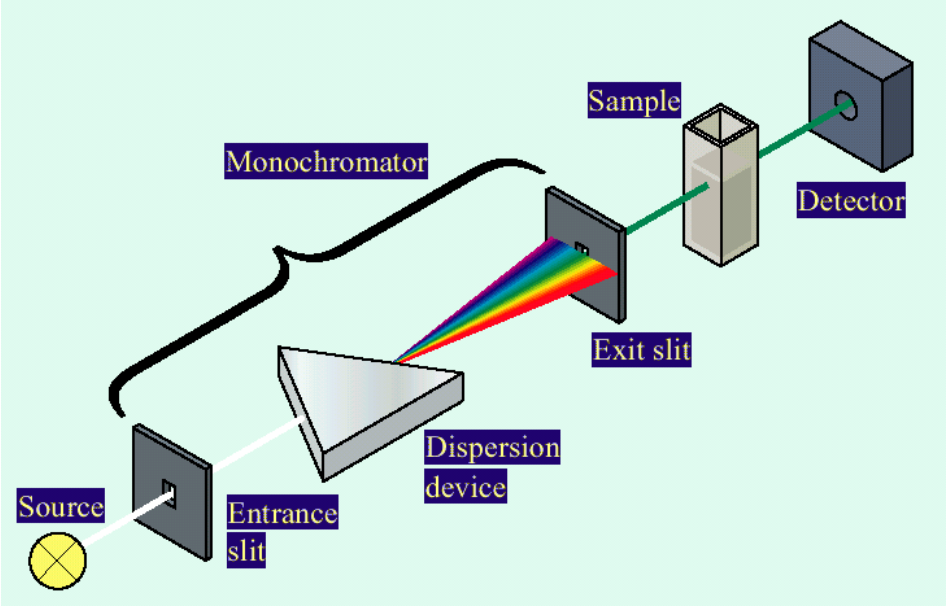

Figure 3.13. Schematic diagram of a single beam UV-Vis spectrometer. Adopted from Ref [26]

3.3.7. Four point probe

The four point probe (4PP) uses four sharp probes arranged in a linear array. 4PP is used in the determination of the bulk resistivity of materials especially semiconductors. The resistivity of material is very important since it is also related to the conductivity of the material, which plays a significant role in determining the flow of electrons. The sheet resistance of the thin film can be determined by dividing bulk resistivity with the known thickness of the bulk material. The schematic of the 4PP is illustrated in Figure 3.14, with the two outer probes sourcing the direct current (I) and the inner probes measuring the voltage

drop (V). From this voltage the sheet resistance (R_{sheet}) can be calculated using the following approach (3.4) which relies on the geometric factor (k) [19,28–30]:

$$\boldsymbol{R_{sheet} = k\,\frac{V}{I}} \qquad \ldots 3.4$$

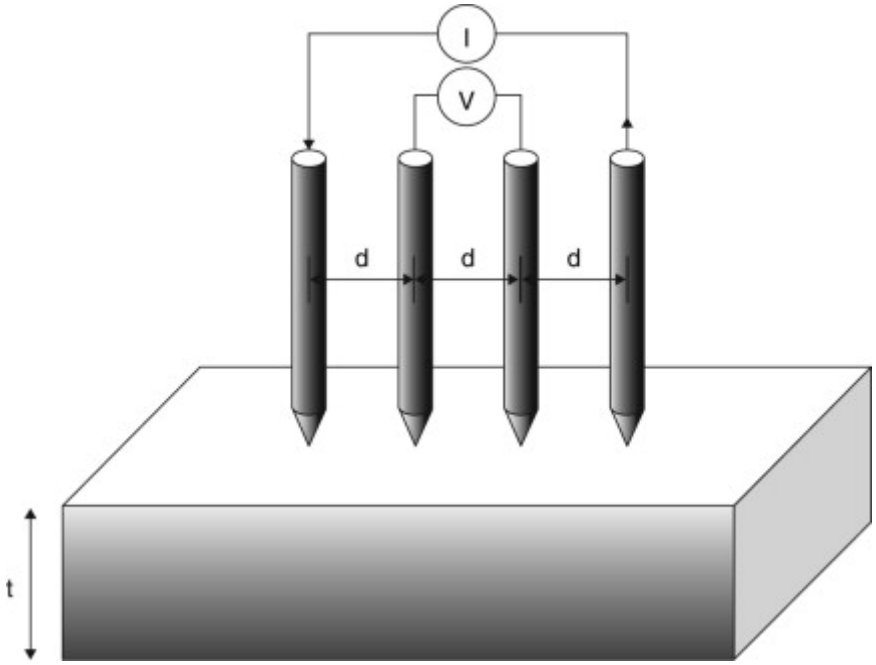

Figure 3.14. A typical schematic of a four-point probe/sheet resistance measuring system, with the two outer probes sourcing a direct current while the inner two probes are measuring the corresponding voltage drop. Adopted form Ref [28]

3.3.8. Electrochemical characterization

In this work, the electrochemical measurements of the electrode of the SC and μ-SC were performed within the standard laboratory conditions using Biologic VMP-300 16 channel potentiostat controlled by the EC-Lab V11.33 software as shown in Figure 3.15. A potentiostat is basically an analytical instrument used to control and also monitor the working electrode's potential in a multiple electrode electrochemical system. Briefly, with reference to three electrode configurations, external wires from the potentiostat connect to the working (WE), counter (CE) and reference (RE) electrodes. The potentiostat controls the applied signal on the WE with respect to the RE, simultaneously, the current flows between the WE and CE, with negligible current flow between the WE and RE [31,32]. The EC-Lab version VMP 11.33 software, allows it the potentiostat to monitor the electrochemical cell in different modes such as cyclic voltammetry (CV), galvanostatic charge-dischage (GCD), and electrochemical impedance spectroscopy (EIS) in either three- (half-cell) and two- (device or full-cell) electrode configuration.

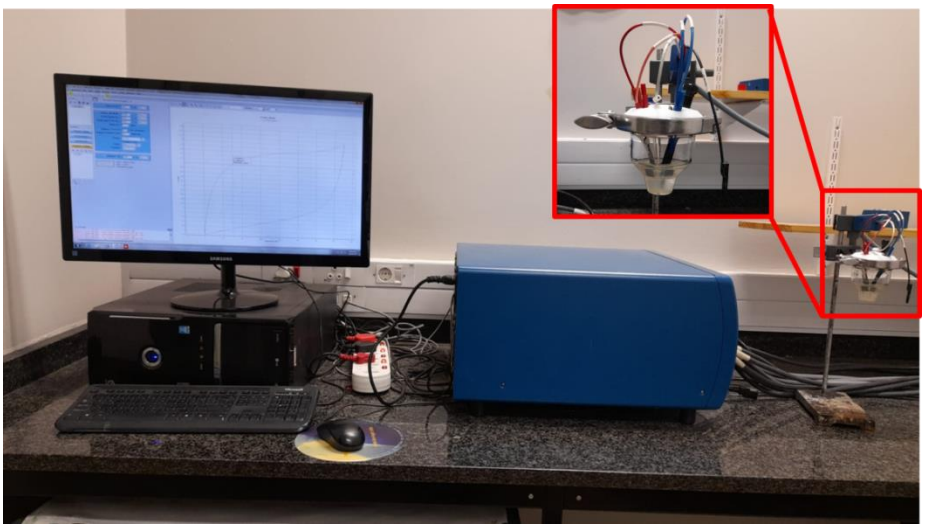

Figure 3.15. Biologic VMP-300 potentiostat equipped with 16 channels controlled with the EC-Lab software, inset illustrate three electrode configurations.

Figure 3.16 display the SC device in the coin cell design and interdigitated µ-SC design fabricated in this work. The entire SC electrodes within the coin cell device were fabricated by homogenously dissolving GO into ethanol, pasting the GO slurry solution onto the NF current collector, drying the GO/NF electrode, then finally thermally reducing using an AP-CVD at various temperatures. The obtained TRGO/NF electrodes were placed within the coin cell cases and other components such as separator, aqueous electrolyte and spring. The same electrode preparation methods for SC were followed on the µ-SC fabrication: GO solutions were sprayed on the microscopic glass (MSG), dried, thermally reduced and the obtained TRGO thin film on MSG were taken to an AxiDraw to pattern the µ-SC electrodes. Thin sheets of copper foils were connected onto the patterned µ-SC and secured in place with Kapton (also known as Polyimide) tape. PVA-H_3PO_4 gel electrolyte was drop casted onto the

interdigitate patterned electrodes, and then the fabricated SC and µ-SC devices were connected on the potentiostat to evaluate the electrochemical performance.

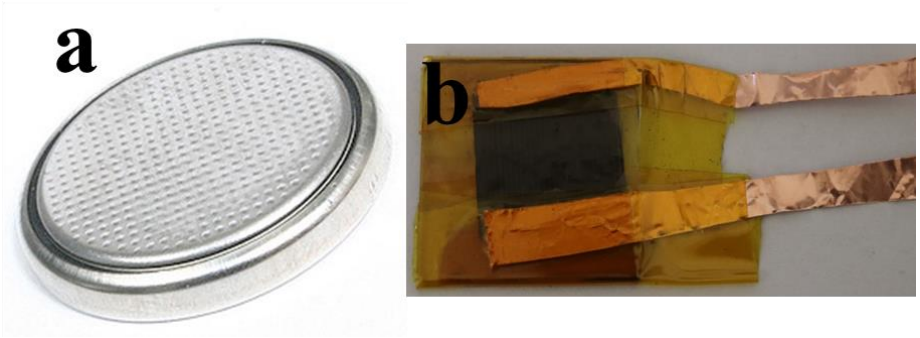

Figure 3.16. Electrochemical devices (a) SC coin cell design and (b) interdigitated µ-SC design.

Reference

[1] Q. Li, A.D. Smith, A. Vyas, F. Cornaglia, A. Anderson, M. Haque, P. Lundgren, P. Enoksson, Finger Number and Device Performance: A Case Study of Reduced Graphene Oxide Microsupercapacitors, Phys. Status Solidi Basic Res. 258 (2021) 1–7. https://doi.org/10.1002/pssb.202000354.

[2] N.F. Sylla, Activated carbon from peanut shell and its molybdenum based nanocomposites for supercapacitor applications, University of Pretoria, PhD Thesis (2020).

[3] M.N. Rantho, Synthesis and characterization of vanadium disulfide nanosheets and carbonized iron cations adsorbed onto polyaniline for high-perfomance supercapacitor applications, University of Pretoria, PhD Thesis (2019).

[4] V.M. Maphiri, G. Rutavi, N.F. Sylla, S.A. Adewinbi, O. Fasakin, N. Man-, Novel Thermally Reduced Graphene Oxide Microsupercapacitor Fabricated via Mask — Free AxiDraw Direct Writing, Nano material (2021) 1–15.

[5] P. Feicht, R. Siegel, H. Thurn, J.W. Neubauer, M. Seuss, T. Szabó, A. V. Talyzin, C.E. Halbig, S. Eigler, D.A. Kunz, A. Fery, G. Papastavrou, J. Senker, J. Breu, Systematic evaluation of different types of graphene oxide in respect to variations in their in-plane modulus, Carbon N. Y. 114 (2017) 700–705. https://doi.org/10.1016/j.carbon.2016.12.065.

[6] D.J. Tarimo, K.O. Oyedotun, A.A. Mirghni, N. Manyala, Sulphur-reduced graphene oxide composite with improved electrochemical performance for supercapacitor applications, Int. J. Hydrogen Energy. 45 (2020) 13189–13201. https://doi.org/10.1016/j.ijhydene.2020.03.059.

[7] E. Quain, T.S. Mathis, N. Kurra, K. Maleski, K.L. Van Aken, M. Alhabeb, H.N. Alshareef, Y. Gogotsi, Direct Writing of Additive-Free MXene-in-Water Ink for Electronics and Energy Storage, Adv. Mater. Technol. 4 (2019) 1800256. https://doi.org/10.1002/admt.201800256.

[8] M. Brycht, A. Leniart, J. Zavašnik, A. Nosal-Wiercińska, K. Wasiński, P. Półrolniczak, S. Skrzypek, K. Kalcher, Synthesis and characterization of the thermally reduced graphene oxide in argon atmosphere, and its application to construct graphene paste electrode as a naptalam electrochemical sensor, Anal. Chim. Acta. 1035 (2018) 22–31. https://doi.org/10.1016/j.aca.2018.06.057.

[9] B. Zhao, P. Liu, Y. Jiang, D. Pan, H. Tao, J. Song, T. Fang, W. Xu, Supercapacitor performances of thermally reduced graphene oxide, J. Power Sources. 198 (2012) 423–427. https://doi.org/10.1016/j.jpowsour.2011.09.074.

[10] P. Vázquez-Sánchez, M.A. Rodríguez-Escudero, F.J. Burgos, I. Llorente, O. Caballero-Calero, M.M. González, R. Fernández, M.C. García-Alonso, Synthesis of Cu/rGO composites by chemical and thermal reduction of graphene oxide, J. Alloys Compd. 800 (2019) 379–391. https://doi.org/10.1016/j.jallcom.2019.06.008.

[11] V.M. Maphiri, J. Wesley-Smith, S. V. Motloung, Phase transition and optical properties of Ba1-xZnxAl2O4:0.1% Eu3+ prepared via citrate sol-gel method, J. Lumin. 215 (2019) 116710. https://doi.org/10.1016/j.jlumin.2019.116710.

[12] V.M. Maphiri, F.B. Dejene, S. V. Motloung, Effects of Mg2+ concentration on the structure and optical properties of MgxAl2O3+x:0.88% Cd2+ ($0.25 \leq x \leq 4.5$) nano-powders synthesized via citrate sol-gel, Results Phys. 7 (2017) 3510–3521. https://doi.org/10.1016/j.rinp.2017.09.019.

[13] J.J.A. Lozeman, P. Führer, W. Olthuis, M. Odijk, Spectroelectrochemistry, the future of visualizing electrode processes by hyphenating electrochemistry with spectroscopic techniques, Analyst. 145 (2020) 2482–2509. https://doi.org/10.1039/C9AN02105A.

[14] M. Ciszewski, A. Mianowski, G. Nawrat, P. Szatkowski, Reduced Graphene Oxide Supported Antimony Species for High-Performance Supercapacitor Electrodes, ISRN Electrochem. 2014 (2014) 1–7. https://doi.org/10.1155/2014/826832.

[15] M.J. Madito, M.Y.A. Ismail, T.T. Hlatshwayo, C.B. Mtshali, The nature of surface defects in Xe ion-implanted glassy carbon annealed at high temperatures: Raman spectroscopy analysis, Appl. Surf. Sci. 506 (2020) 145001. https://doi.org/10.1016/j.apsusc.2019.145001.

[16] M.J. Madito, K.S. Matshoba, F.U. Ochai-Ejeh, N. Mongwaketsi, C.B. Mtshali, M. Fabiane, N. Manyala, Nickel-copper graphene foam prepared by atmospheric pressure chemical vapour deposition for supercapacitor applications, Surf. Coatings Technol.

383 (2020) 125230. https://doi.org/10.1016/j.surfcoat.2019.125230.

[17] Z. Çiplak, N. Yildiz, A. Cąlimli, Investigation of graphene/Ag nanocomposites synthesis parameters for two different synthesis methods, Fullerenes Nanotub. Carbon Nanostructures. 23 (2015) 361–370. https://doi.org/10.1080/1536383X.2014.894025.

[18] A. Downes, A. Elfick, Raman Spectroscopy and Related Techniques in Biomedicine, Sensors 2010, Vol. 10, Pages 1871-1889. 10 (2010) 1871–1889. https://doi.org/10.3390/S100301871.

[19] M.J. Madito , AB-stacked bilayer graphene films obtained on dilute Cu(Ni) foils using atmospheric pressure chemical vapour deposition University of Pretoria, PhD Thesis (2016).

[20] A. Eckmann, A. Felten, A. Mishchenko, L. Britnell, R. Krupke, K.S. Novoselov, C. Casiraghi, Probing the Nature of Defects in Graphene by Raman Spectroscopy, Nano Lett. 12 (2012) 3925. https://doi.org/10.1021/nl300901a.

[21] I.B. Olenych, O.I. Aksimentyeva, L.S. Monastyrskii, Y.Y. Horbenko, M. V. Partyka, Electrical and Photoelectrical Properties of Reduced Graphene Oxide—Porous Silicon Nanostructures, Nanoscale Res. Lett. 12 (2017). https://doi.org/10.1186/s11671-017-2043-7.

[22] N. Ishida, V.S.J. Craig, Direct Measurement of Interaction Forces between Surfaces in Liquids Using Atomic Force Microscopy, (2019).

https://doi.org/10.14356/kona.2019013.

[23] S. Kundu, Synthesis and characterizations of some nanocrystalline metal oxide semiconductors and composites with different morphologies, (2018).

[24] H.G. Kuball, T. Höfer, S. Kiesewalter, Chiroptical Spectroscopy, General Theory, Encycl. Spectrosc. Spectrom. (2017) 217–231. https://doi.org/10.1016/B978-0-12-409547-2.04980-5.

[25] N. NicDaéid, Forensic Sciences | Systematic Drug Identification, Encycl. Anal. Sci. (2019) 75–80. https://doi.org/10.1016/B978-0-12-409547-2.14457-9.

[26] N. Gohain, Studies on the structure and function of phenazine modifying enzymes PhzM and PhzS involved in the biosynthesis of pyocyanin, Phd Thesis. (2008). https://doi.org/10.17877/DE290R-8364.

[27] S. Pentassuglia, V. Agostino, T. Tommasi, EAB—Electroactive Biofilm: A Biotechnological Resource, Encycl. Interfacial Chem. Surf. Sci. Electrochem. (2018) 110–123. https://doi.org/10.1016/B978-0-12-409547-2.13461-4.

[28] T.G. Santos, Characterization of FSP by electrical conductivity, Surf. Modif. by Solid State Process. (2014) 153–176. https://doi.org/10.1533/9780857094698.153.

[29] V.M. Airaksinen, Silicon Wafer and Thin Film Measurements, Handb. Silicon Based MEMS Mater. Technol. Second Ed. (2015) 381–390. https://doi.org/10.1016/B978-0-323-29965-7.00015-4.

[30] F. Gaspari, 2.4 Thin Films, Compr. Energy Syst. 2–5 (2018) 88–116. https://doi.org/10.1016/B978-0-12-809597-3.00214-5.

[31] L. Yang, Galvanic sensors and zero-voltage ammeter, Tech. Corros. Monit. (2021) 123–140. https://doi.org/10.1016/B978-0-08-103003-5.00006-0.

[32] D. Fitzpatrick, Glucose Biosensors, Implant. Electron. Med. Devices. (2015) 37–51. https://doi.org/10.1016/B978-0-12-416556-4.00004-8.

Chapter 4 Results, discussion and conclusion

This chapter presents all the experimental findings of the structure, morphology and electrical properties of the substrates i.e. nickel foam and microscopic glass, precursor graphite, intermediate graphene oxide and finally thermal reduced graphene oxide. The electrochemical performance of the fabricated SC electrodes and devices together with the fabricated µ-SC devices are also discussed.

4.1. Supercapacitor

Supercapacitors (SCs) also referred to as Ultracapacitors, are devices known for high specific power and long life span, compared to batteries known for their higher specific energy [1,2]. Carbon based materials (predominately SC materials) have been modified to enhance the specific energy of SC. This modification has been done using two routes: Development of composite materials [3–5] and heterogeneous doping [3–7]. In this study, the specific energy of the TRGO-SC was increased by the presence of OFG which increase the psuedocapacitance behaviour and also serve as an ion pathway into the internal bulk material. The TRGO was only reduced enough to revive the conductivity, Zhao *et al*. [8] showed that GO reduced at lower than 200 ℃ is not conductive, which decrease the capacitance. The

proposed electrode preparation technique does not require a conductive enhancement and a binder. This approach gives us the possibility of evaluating the material's electrochemical behaviour, since literature has shown that additives affect the overall performance [9–11]. Zhu *et al*. [9] reported the effects of binders; Nafion, Polytetrafluorethylene (PTFE) and PVDF while using carbon nanotube as a conductive agent. The PTFE sample had higher capacitance retention of 90.8% while PVDF and Naflon had 79.7 and 87%, respectively. However, Liu *et al*. [11] reported the enhancement of the electrochemical performance of NiCo-MOF nanosheets by the addition of carbon acetylene black (CAB). The sample containing CAB had an increased specific capacitance and a lower solution resistance as compared to the ones without CAB. Additive free electrodes have been mostly reported for free standing electrodes [12–14], but Moyseowicz *et al*. [15] reported a binder free poly(aniline-co-pyrrole)/thermally reduced graphene oxide (PAP/TRGO) composite.

In this work, we focus on low temperature, binder and conductive enhancement free TRGO/NF for SC application. The main aim of the study is to investigate the effects of thermally reducing temperature and monitoring the electrochemical performance of untainted reduced graphene oxide. Moreover, directly reduced GO on NF without the binder and conductive additives avoids inactive surfaces with conversational binder electrodes and allows for more efficient charge transport. This allows the proper measurement of the material without any influence from additives. A device was fabricated with TRGO/NF being a positive electrode while the negative electrode was prepared from peanut shell activated carbon (PAC) [1,16] i.e. TRGO/NF//PAC.

4.1.1. Results and discussions

The study of the prepared TRGO/NF is presented in this section. The results obtained from this study are described in the publication and supplementary information below:

Journal of Energy Storage 52 (2022) 104967

Contents lists available at ScienceDirect

Journal of Energy Storage

journal homepage: www.elsevier.com/locate/est

Research Papers

Low temperature thermally reduced graphene oxide directly on Ni-Foam using atmospheric pressure-chemical vapour deposition for high performance supercapacitor application

Vusani M. Maphiri, Daba T. Bakhoum, Samba Sarr, Ndeye F. Sylla, Gift Rutavi, Ncholu Manyala *

Department of Physics, Institute of Applied Materials, SARChI Chair in Carbon Technology and Materials, University of Pretoria, Pretoria 0028, South Africa

ARTICLE INFO

Keywords:
Thermally reduced
Energy storage
Chemical vapour deposition
Graphene oxide
Ni-Foam
Binder-free supercapacitor

ABSTRACT

A binder free approach was use to prepare thermally reduced graphene oxide (TRGO) at 200 °C directly on Ni-Foam (NF) (current collector) via atmospheric pressure-chemical vapour deposition (AP-CVD) and used as a positive electrode for supercapacitor application. The TRGO/NF electrode preparation method is simpler, quicker, cheaper and more effective compared to other method. The half-cell electrochemical performances in 6 M KOH showed a maximum specific capacity of 52.64 mA h g^{-1} at 0.5 A g^{-1}. The device: TRGO/NF//PAC showed a specific energy and power of 18.72 Wh kg^{-1} and 547.52 W kg^{-1} respectively at 1 A g^{-1}; and 14.10 Wh kg^{-1} and 2.5 kW kg^{-1} respectively at 5 A g^{-1}. The high coulombic efficiency (99.9%) and capacitance retention (70%) indicate outstanding stability. These results represent a significant progress in the fabrication of binder and conductive enhancement free positive electrode for electrochemical energy storage devices.

1. Introduction

Recently researchers are paying a great attention in the development of alternative energy storage and conversion devices such as supercapacitors (SCs) and batteries, to help in combating energy related problems of environmental pollution, depletion of fossil fuels, efficient mobile (potable) energy source and many more [1–12]. SCs devices are unique and attractive due to their high power density, wide range of operation temperature, fast charge and discharge rates and long cycle life [13–16]. These devices bridge the gap between high power and low energy convention capacitors and low power and high energy batteries. SCs can be classified according to the energy storage mechanism which either involves electric double layer capacitors (EDLCs) or pseudocapacitors. EDLCs store their energy through surface charge adsorption related to the electrical double layer formation. Thus, the electrode materials are mainly characterized by large specific surface areas, being mostly carbon materials such as activated carbon, carbon onions and reduced graphene oxide. Meanwhile, pseudocapacitors store energy based on Faradaic processes which depends on the operational voltage. Most pseudocapacitors material are from the transition metal compounds like oxides, hydroxides or sulphides, and conductive polymers, such as polyaniline, polypyrrol, and poly (3,4-ethylenedioxythiophene). Carbon materials such as graphene suffer from poor electrochemical performance due to the undesirable ion diffusion inside its internal surface and only electrical layer absorption mechanism occurs [17,18].

Recently, efforts have been devoted in developing thermally reduced graphene oxide (TRGO) materials suitable for high-performance supercapacitor application. TRGO has been prepared via a combinations of chemical oxidization of carbon material like graphite using Hummer's method and the thermal reduction process which is simple, quick, cheap, effective, safe and easily scalable than other reduction methods such as bio reduction [19], chemical [20,21], photoreduction [22,23] and mechanochemical [24,16,25,26]. Zhao et al. [16] reported the increased performance of graphene oxide thermally reduced at low temperature using a horizontal tube furnace under nitrogen. The sample reduced at 200 °C had the highest capacitance of 260.5 Fg^{-1} due to the presence of functional groups on the external surface serving as a passage for ions to the internal surface. These functional groups were also reported to facilitate fast redox processes leading to pseudocapacitance behaviour and also enhancing the charge storage capabilities [17,27–29]. Graphene has been coated on different substrates via various methods such as chemical vapour deposition, slurry paste, spin coating, spray coating,

* Corresponding author.
E-mail address: ncholu.manyala@up.ac.za (N. Manyala).

https://doi.org/10.1016/j.est.2022.104967
Received 22 February 2022; Received in revised form 5 May 2022; Accepted 25 May 2022
Available online 31 May 2022

dip coating and electrophoretic deposition [28,30,31]. Among them, slurry paste is the simplest method to deposited GO nano sheets on Ni-Foam (NF). This method is well developed, quick, cheap, environmentally friendly as it does not require any sophisticated and expensive equipment. This method has been widely used to prepare activated carbon and metal compounds on NF [14,16,32–34]. Ramadoss et al. [28] reported TRGO coated fabric supercapacitor prepared via GO dip coating, followed by thermal treatment at 160 °C in Ar for 2 h. The fabricated symmetric supercapacitor yielded a specific energy and power of 5.8 Wh kg^{-1} and 27.7 kW kg^{-1} respectively, at a current density of 0.1 mA cm^{-2}. However, TRGO/NF as an electrode for supercapacitor applications prepared by slurry paste followed by thermal treatment has never been reported.

In this study, the GO was reduced directly on NF (current collector) at 200 °C eliminating the need for binders such as poly(vinylidenedifluoride) (PVDF) and conductive additives like carbon acetylene black (CAB) which tampers with the overall electrochemical performance of the material under study. This fabrication was only possible due to the restacking ability of reduced graphene oxide which occurs without the presence of binding agents, which formed a macroscopic assemble structure .i.e. graphene film around three dimensional (3D) NF structure [35,36]. This is not possible within other non-two dimensional carbon allotropes and carbon based nanocomposite material such as carbon nanotubes, activated carbon and iron carbide [37–42]. Inorganic active material such as Nickel subsulfide (Ni_3S_2) and Zinc sulphide have been successful deposited on NF without any additives [43,44]. Studies have been under taken to illustrate the effects of the binders [33,34] and conductive additives [45]. Zhu et al. [33] reported the effects of binders; Nafion, Polytetrafluorethylene (PTFE) and PVDF while using carbon nanotube as a conductive agent. The PTFE sample had higher capacitance retention of 90.8% while PVDF and Naflon had 79.7 and 87%, respectively. However, Liu et al. [45] reported the enhancement of the electrochemical performance of NiCo-MOF nanosheets by the addition of acetylene black. The sample containing CAB had an increased specific capacitance and a lower solution resistance as compared to the one without CAB. Additive free electrodes have been mostly reported for free standing electrodes [46–48], but Moyseowicz et al. [49] reported a binder free poly(aniline-*co*-pyrrole)/thermally reduced graphene oxide (PAP/TRGO) composite. The PAP/TRGO//PAP/TRGO device showed a high specific capacitance of 287 F g^{-1} and good rate capability of 205 F g^{-1} at 20 A g^{-1}. However, this material had a low specific energy of 6.3 Wh kg^{-1} and specific power of 100 W kg^{-1} at specific current of 0.2 A g^{-1}. Our prepared device TRGO/NF//PAC showed a better electrochemical performance with specific energy of 18.73 Wh kg^{-1} and specific power of 547.52 W kg^{-1} at specific current of 1 A g^{-1}, signifying the readiness of additive free electrode for supercapacitor application. Moreover directly reduced GO on NF without the binder and conductive additives avoids inactive surfaces with conversational binder electrodes and allows for more efficient charge transport. This allows the proper measurement of the material without any influence from additive.

2. Experimental

2.1. Materials

Reagents utilized in this work were analytical grade and used without any further purification. These include raw graphite, sulphuric acid [H_2SO_4 (98%)], potassium permanganate [$KMnO_4$], hydrogen peroxide [H_2O_2 (50%)], ethanol [C_2H_5OH], hydrogen [H_2], Argon [Ar] nickel foam [NF, thickness and areal density of 1.6 mm and 420 g m^{-2}], potassium hydroxide [KOH] pallets and distilled water (DW) at 18.2 MΩ.

2.2. Preparation of GO

The Hummer's method was used to prepare GO in the same manner as reported in our pervious study [30]. Briefly, 2 g of graphite powder was added into cooled 120 ml of H_2SO_4 and stirred using a magnetic stirrer until a homogenous black lump free solution is reached. 6 g of $KMnO_4$ was also added slowly into the cooled homogeneous solution of graphite and H_2SO_4. This mixture was stirred for 180min at a constant heating temperature of 50 °C. The brownish solution was allowed to cool to room temperature, and then further cooled in an ice bath for an hour. 100ml of H_2O and 20 ml of H_2O_2 were then added to stop the reaction. The mixture was stirred and left to settle. The suspended liquid was discarded; DW was added to the settled GO mixture and left to re-settle then followed by discarding the DW. This process was repeated several times to remove contaminants. The GO mixture was centrifuged at 5000 rpm for 5 min and dried in an oven at 60 °C overnight.

2.3. Preparation of TRGO/NF electrode

Dried GO was mixed with ethanol, then sonicated (approximately, 30 min) together with manual stirring until it reached a paste like. The GO paste was then pasted on NF and dried at room temperature. The dimensions of the pasted area on rectangular and circular NF are 1.0 × 1.0 cm^2 and thickness-diameter of 0.2–16 mm. The GO/NFs were placed in the atmospheric pressure-chemical vapour deposition (AP-CVD) for thermal reduction. The Ar was allowed to flow at 300standard cubic centimetres (sccm) throughout the entire reduction process, to avoid oxidation. The following heat settings were used: Heating rate was set to 10 °C/min until the desired temperature of 200 °C was reached; the AP-CVD was kept at that temperature for an hour. After an hour the CVD was moved away from the region with TRGO/NF to allow the electrode to cool down to room temperature. The TRGO/NF electrode preparation is displayed in Fig. 1.

2.4. Characterisation

The structural, morphology and compositional characterization were performed using the following: Bruker BV 2D PHASER Best Benchtop X-ray diffraction (XRD) with reflection geometry at 2θ values (15–90°) in a step size of 0.005° using Cu Kα radiation source (λ = 0.15406 nm) at 50 kV and 30 mA; Bruker Alpha platinum-ATR Fourier transform infrared spectroscopy (FTIR) at 32 scans in the range of 400–4000 cm^{-1}. WITec Raman 300RAS+ operated using Zeiss objective 10×, 20×, 50× and 100× at a laser of 532 nm and a power of <0.5 mW (to avoid further GO reduction due to sample heating or damage by the laser generated heat) at a grating of 600 g/mm BLZ = 500 nm. The Raman mapping was performed on a 25 × 25 μm^2 area and 300 by 300 lines per image and point per line at an integration time of 1 s. The optical image of the measured area is displayed on Fig. S1 in the supplementary information. The WITec Project five (Build 5.0.3043, plus version) software was used for data analysis and achieving the Raman mapping images. The morphology and elemental composition was obtained using Zeiss Ultra Plus 55 field emission scanning electron microscope (SEM) operated at 2.0 kV coupled with energy-dispersive X-ray spectroscopy (EDS) at 20 kV. The two and three electrode configurations measurements (cyclic voltammeter (CV), galvanostatic charge-discharge (GCD) and electrochemical impendence spectroscopy (EIS)) were performed using the Bio-Logic VMP-300 (Knoxville TN 37,930, USA) potentiostat monitored by the EC-Lab V11.33 software.

3. Results

3.1. Structural, morphological and compositional characterisation

The normalized XRD pattern of graphite, GO, NF and TRGO/NF were measured and displayed in Fig. 2(a). The obtained XRD pattern were indexed to the Joint Committee on Powder Diffraction Standards (JCPDS) 75 2078, JCPDS 41 1487 and JCPDS 04 0850 for graphite, GO and NF, respectively [50,51]. The precursor (graphite) showed a

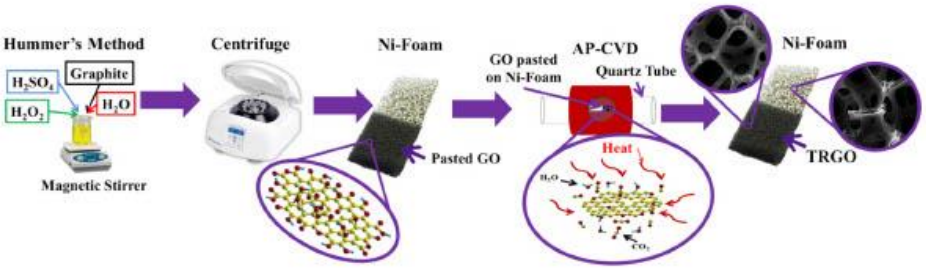

Fig. 1. Schematic of the synthesis route for TRGO/NF electrode.

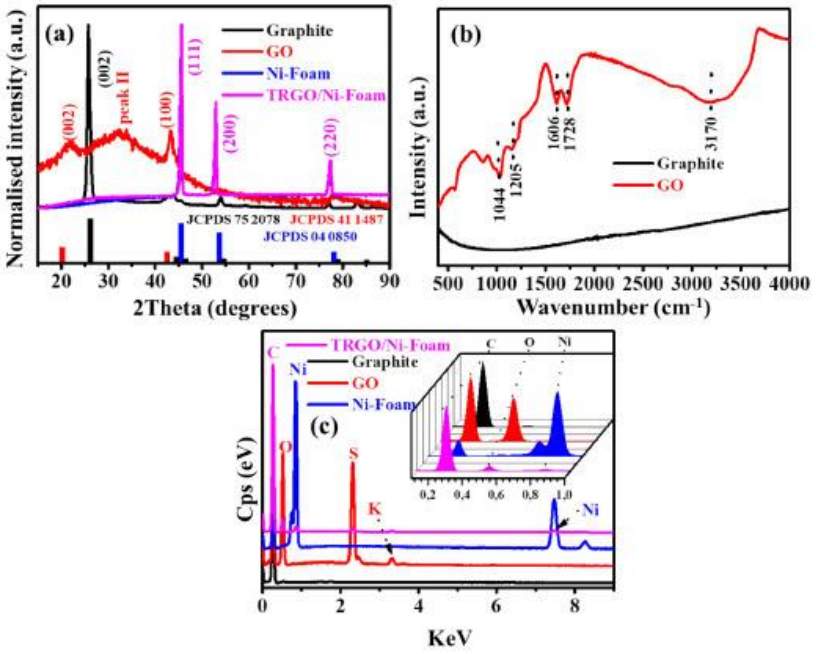

Fig. 2. (a) XRD pattern, (b) FTIR spectra and (c) EDS spectra of Graphite, GO, NF and TRGO/NF.

dominant peak around $2\theta = 25^{\circ}$ corresponding to the (002) plane due to the sp^2-bonded sheets. The GO show a reflection plane at $2\theta = 20^{\circ}$ corresponding to the (001) indices, a hump labelled peak II has been attributed to amorphous-like carbon comprising of impurities, defects or folding wrinkles [52] and the peak around $2\theta = 43^{\circ}$ is indexed to (100) plane [53]. The interplanar spacing calculated using the Bragg's equation showed 80% increase in the graphite sheet spacing. The interplanar spacing is small in comparison to those reported within Ref [16]. This is due to the 60 °C drying temperature which has mostly removed the intercalated H_2O, resulting in a reduction of the interplanar spacing. The pattern of NF showed the diffraction plane corresponding to the (111), (200) and (220). Similar diffraction peaks were reported on Refs [54–57]. The pattern from TRGO/NF only show peaks from pure NF because the TRGO reduced at 200 °C is not highly crystalline and it is of low amount with respect to NF. The FTIR spectra of graphite and GO are displayed in Fig. 2(b). Note that TRGO/NF sample was not measured due to its form. The graphite shows the absence of notches (i.e. showed a linear spectrum) due to the absence of surface functional groups on the graphene sheets, indicating chemical inertness of bulk graphite [58]. On the other hand GO showed the presence of many notches at various wavenumbers such as 3170, 1728, 1606, 1205, and 1044 cm^{-1}. The notch at around 3170 cm^{-1} is due to the stretching of hydroxyl (—OH) group. The dip at 1728 cm^{-1} is attributed to the stretching of carbonyl (—C═O) functional group and the 1606 cm^{-1} corresponds to the stretching vibrations of the un-oxidized graphitic domain, while the 1205 cm^{-1} is due to the epoxy (C—O) group. The alkoxy (C—O) group stretching vibration was attributed to the notch at 1044 cm^{-1}. These results are in line with those reported in literature [32,58,59] and also verify the increased interplanar distance seen on the XRD in Fig. 2(a) due to the functional groups on the surface of graphene sheets. The EDS spectra are displayed in Fig. 3(c) and the inset to the figure shows the zoomed (in the 0–1 keV region) spectra of graphite, GO, NF and TRGO/

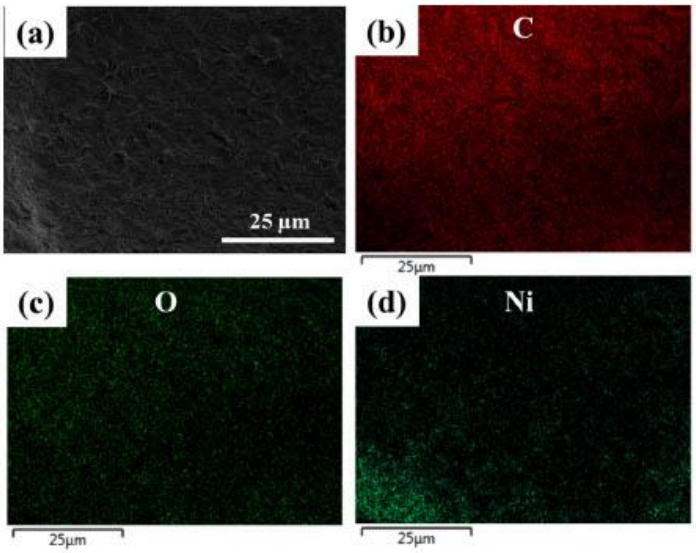

Fig. 3. (a) Scanning electron microscopy image and (b)–(d) the corresponding energy dispersive X-ray maps of C, O and Ni obtained from the TRGO sample.

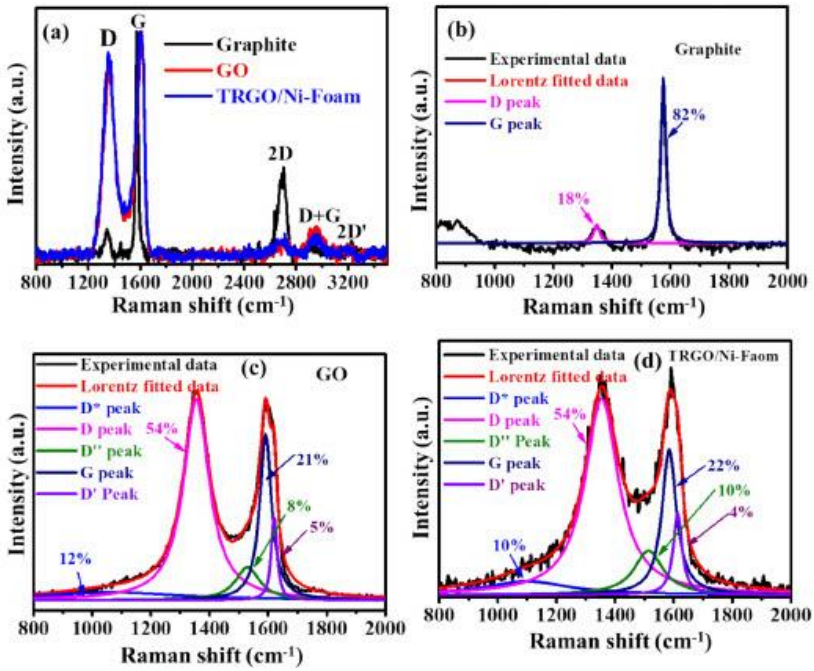

Fig. 4. (a) Raman spectra of graphite, GO and TRGO/NF and the deconvolution of (b) graphite, (c) GO and (d) TRGO/NF at the 800–2000 cm^{-1} region.

NF, respectively. The EDS spectra show the expected elements; carbon (C), oxygen (O), nickel (Ni) and traces of sulphur (S) and potassium (K) from the oxidation solution. Graphite is predominately a pure carbon material having a higher carbon content (calculated from peak intensity of carbon to oxygen) of 110. The GO powder has carbon from graphite and oxygen from the functional groups. The calculated carbon content of GO is 2. The TRGO/NF has Ni peaks in addition to those of GO. This is because GO was reduced on NF current collector and has a carbon content of 5. The carbon content increased because of removal of oxygen functional groups due to the thermal reduction. Similar, carbon content has been reported for low temperature TRGO [16,60]. The scanning electron microscopy image of the TRGO/NF is displayed in Fig. 3(a); while the corresponding EDS mapping are displayed in Fig. 3(b)–(d) which show a uniform distribution of elements.

Raman spectra of graphite, GO and TRGO/NF are displayed in Fig. 4 (a). The graphite sample only shows three peaks at ~1337, 1590 and 2694 cm^{-1} corresponding to the D, G and 2D peak, respectively, while the GO and TRGO/NF shows additional second order peaks at around 2964 and 3199 cm^{-1} corresponding to the D + G and 2D′ [52,61–63]. The D (defect-induced) peak is related to the A_{1g} breathing mode [64,65], while the G and 2D peaks are attributed to the first and second-order allowed Raman E_{2g} mode, respectively [63]. Furthermore, the D + G and 2D′ are attributed to the combination of the G and D modes characteristic for the disturbed graphitic structure and the overtone of the D′, respectively [31,52,62]. The de-convoluted one phonon region (800–2000 cm^{-1}) of graphite, GO and TRGO/NF are displaced in Fig. 4 (b), (c) and (d), respectively. Only two peaks (D and G) were observed for the graphite and five (D*, D, D″, G and D′) for the GO and TRGO/NF. The D* peak is due to the sp^2–sp^3 bonds at the edges of the network, while this peak has been also attributed to the ionic impurities [66,67]. The D″ peak has been attributed to the amorphous carbon [66] and D′ has been attributed to the disorder-induced phonon mode due to crystal defects i.e. the vacancy corresponding to pentagonal and octagonal rings [62,63,68,69]. The full width at half maximum (FWHM) of the D peak increased due to the high concentration of defects related to the oxidation and the alteration of the basal plane structure of graphene during the thermal reduction [52,62]. The integrated ratio of the D peak over the integrated ratio of the G peak (I_D/I_G) of graphite, GO and TRGO/NF were calculated to be 0.14, 2.63 and 3.09, respectively. Thus, graphite is highly ordered than GO and TRGO/NF due to the destruction of the sp^2 cluster during the oxidation process. Tuinstra–Koenig model [64,70] shows the relationship between I_D/I_G and the average crystallite size L_a (or the average sp^2 cluster) via the Knight equation (1) below [14,52,62,70]:

$$L_a = \frac{C(\lambda)}{I_D/I_G}\ [\text{nm}] \tag{1}$$

where $C(\lambda)$ is the wavelength-dependent pre-factor estimated using $C(\lambda) \approx C_0 + \lambda C_1$, for $400 < \lambda < 700$ nm and $C(\lambda) = 4.96$ nm for $\lambda = 532$ nm, where C_0 and C_1 were estimated to be −12.6 nm and 0.033, respectively [64]. The I_D/I_G is the ratio of the intergraded area of the D and G peak from the spectra in Fig. 4(b)–(d). The L_a for graphite, GO and TRGO/NF were calculated to be 35.43, 1.89 and 1.61 nm, respectively. More like I_D/I_G, the L_a decrease from graphite to GO due to the disruption of the sp^2 cluster during oxidation [62] and the thermal reduction. The degree of amorphous carbon was estimated by the intergraded area of D″ and G peaks ratio ($I_{D''}/I_G$). The $I_{D''}/I_G$ of GO is 0.40 and TRGO/NF is 0.82, and has increased due to the removal of the carbon atom together with the oxygen-functional groups upon reduction. Our previous results [14,71] showed the influence of the amorphous carbon on the electrochemical performance.

The images of the Raman mapping of integrated area (I_D/I_G) of the TRGO/NF is displayed in Fig. 5(a). The image (Fig. 5(a)) shows a minimum and maximum value of 2.47 and 3.20 (average I_D/I_G is 2.77) indicating that the prepared TRGO/NF is indeed highly defective. Unlike, the images of graphene/NF displayed on Ref [72] which show a subtle I_D/I_G within the range of 0.0–0.5. The corresponding crystallite size (L_a) image estimated from the knight formula (1) is displayed in Fig. 5(b). Emphasizing that indeed I_D/I_G is inversely proportional to the L_a as suggest by the Tuinstra–Koenig model [70]. The intensity ratio of

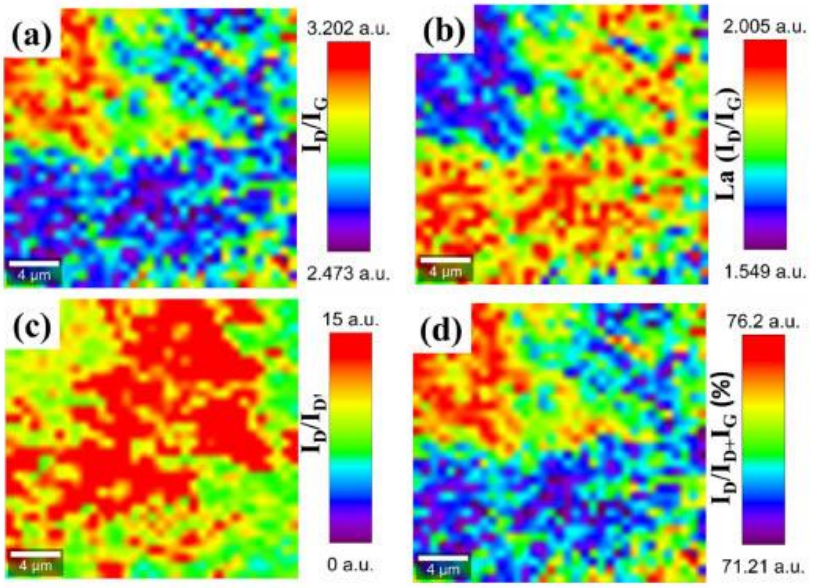

Fig. 5. Raman mapping of (a) I_D/I_G, crystallite size (L_a), (c) $I_D/I_{D'}$ and (d) $I_D/I_D + I_G$ together with their colour scale.

the defect-induced (I_D) peak relative to the defect-activated mode ($I_{D'}$) ($I_D/I_{D'}$) image is displayed in Fig. 5(c). The red area is due to the sp^3 defects while the green area is due to the hopping defect like vacancy defects [62,73,74]. The image of the $I_D/I_G + I_D$ (%) (Cuesta model [67]) in Fig. 5(d) shows that the TRGO/NF is composed of highly defected reduced GO with a minimum and maximum of 71.21 and 76.2 (%). The $I_D/I_G + I_D$ (%) and I_D/I_G in Fig. 5(a) show the same trend of defects.

The scanning electron microscopy image of graphite, GO, NF and TRGO/NF are displayed in Fig. 6. Graphite morphology in Fig. 6(a) shows micro-particles similar to that of a pine tree (*Pinus pinaster*) bark with various dimensions. The high magnification inset to Fig. 6(a) shows that the micro-particles are made of horizontally stacked planes. Fig. 6 (b) shows morphology of the dried GO showing the presence of randomly disordered stacked graphene sheets. The morphology of NF in Fig. 6(c) showed a smooth surface and complex interconnected Ni-fibers. Morphology of TRGO\NF is displayed in Fig. 6(d) which shows that the TRGO have adhered to the surface of NF. The TRGO is wrinkled as can be seen on Fig. 3(a), resulted in a higher surface area contributing in a higher electrochemical performance.

3.2. Electrochemistry characterisation

3.2.1. Three electrode conftguration

The electrochemical performance of the TRGO/NF was evaluated in the three-electrode configuration in the positive potential window using three different electrolytes at a scan rate of 20 mV s^{-1} as shown in Fig. S2 (a). The 6 M KOH electrolyte showed a better performance (higher current response) compared to 1 M Na_2SO_4 and 1 M NaOH electrolytes due to the higher concentration and ionic conductivity of OH^- anions within the 6 M KOH electrolyte [55,75]. The GCD curve in Fig. S2(b) also shows that the 6 M KOH shows the best electrochemical performance among other electrolytes. Fig. S2(c) compares the CV at 20 mV s^{-1} of TRGO/NF to that of pure NF, the TRGO/NF has a higher current response than pure NF due to the TRGO embedded on the NF. The 6 M KOH electrolyte was used for electrochemical evaluation throughout this study because it has shown much better electrochemical results as compared to other electrolytes for this electrode material. The electrochemical result that shows that the TRGO/NF reduced at 200 °C has a better performance than those reduced at higher temperature (400 and 800 °C) are displayed in Fig. S3. This is due to the presence of residual functional groups such as carbonyl and quinone which provide passage for ions into the internal surface, pseudocapacitive behaviour enhancing the charge storage capability [16,27–29] and high wettability between the electrolyte and active material yielding better electrochemical performance [14,76]. These results are in line with those reported by Zhao et al. [16] where the GO reduced at 200 °C has the highest specific capacitance of 260.5 F g^{-1} at a discharge specific current of 0.4 A g^{-1} and the lowest capacitance was attainted from GO reduced at the highest temperature of 900 °C. The capacitance of the TRGO micro-supercapacitor also decreased with increase in reducing temperature and the FTIR with that study indicated the removal of oxygen content [30]. The CV curves displayed in Fig. 7(a) are showing some Faradic behaviour due to the interaction between the high concentration 6 M KOH electrolyte and the functional groups on the TRGO/NF [16,27]. This Faradic behaviour can also be seen on the GCD curve displayed in Fig. 7(b). The specific capacity (Q_s) of the TRGO/NF was calculated from the GCD curve in Fig. 7(b) using Eq. (2) below [32,72].

$$Q_s = \left(\frac{I}{m}\right)\frac{t}{3.6}\ [\text{mA h g} - 1] \tag{2}$$

where I, m and t are current (mA), mass (mg) and discharge time (s), respectively. The specific capacity as a function of specific current is displayed in Fig. 7(c) showing a specific capacity of 52.64 mA h g^{-1} at 0.5 A g^{-1} and a small reduction at 5 A g^{-1} which can be allotted to the limited time that ions have to access the surface of the electrode [16,72]. Ramadoss et al. [28] attributed the decrease of the capacitance as a function of specific current of the TRGO-coated fabric to the interruption of the charge diffusions of graphene for the time constraint for fast charge/discharge. This led to the activation of the outer surface resulting in decreased capacitance at high scan rate.

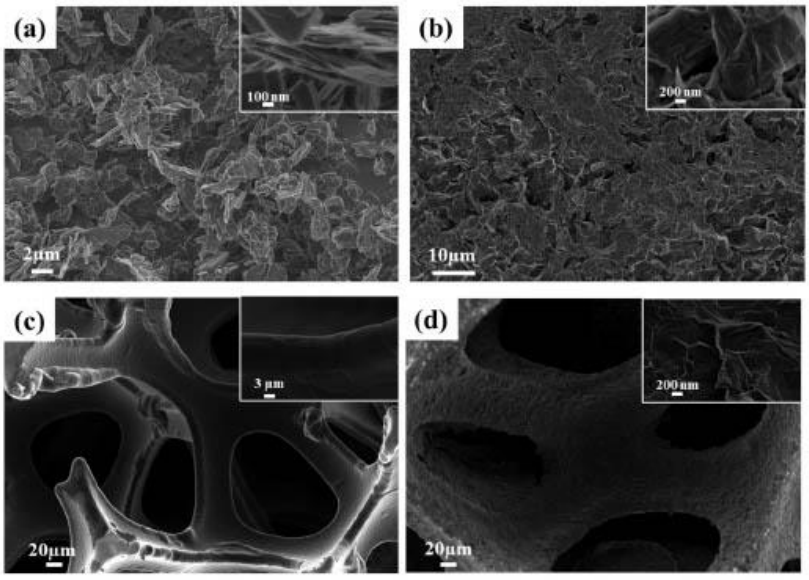

Fig. 6. SEM micrographs of (a) graphite, (b) GO, (c) NF and (d) TRGO/NF.

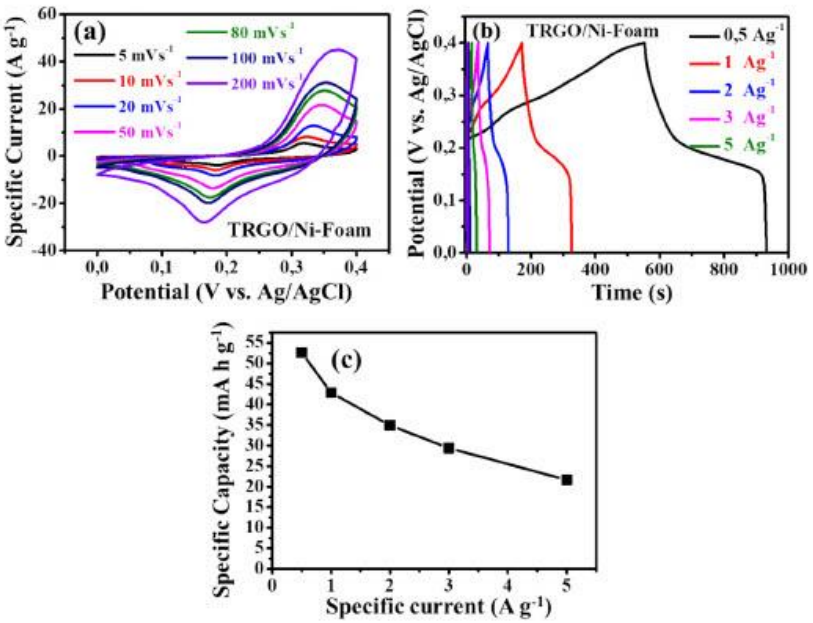

Fig. 7. (a) CV curves at various scan rates; (b) GCD curves at different specific currents and (c) specific capacity as a function of specific current for TRGO/NF sample.

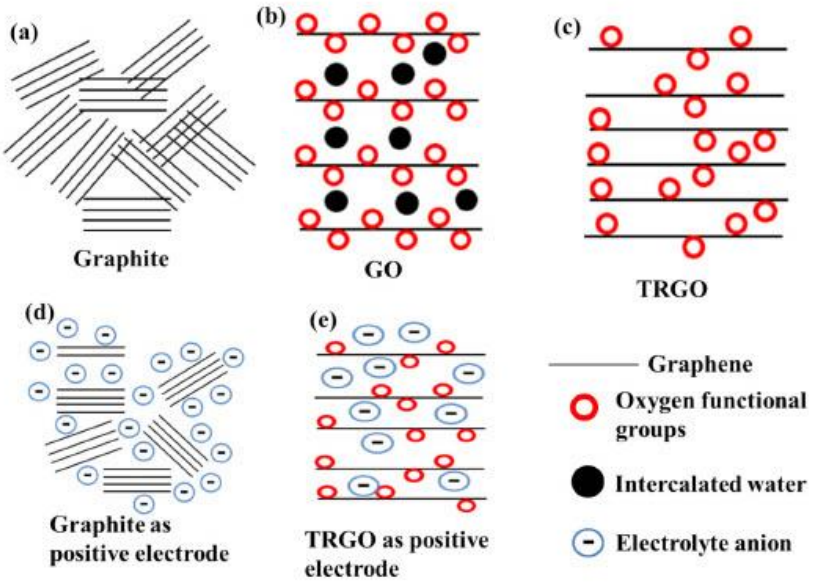

Fig. 8. Schematic illustrating the (a)–(b) transformation from graphite to TRGO and interaction of electrolyte with (d) graphite and (e) TRGO as positive electrodes.

Based on the above discussed results, we have illustrated the preparation and advantage of the TRGO as a positive electrode in Fig. 8. Fig. 8(a)–(c) shows the schematic of the transformation from graphite to TRGO. The schematic in Fig. 8(a) shows of particles of graphite composed of sheets of graphene (see Fig. 6(a) and its inset) and the small interspace distance determined from XRD on Fig. 2(a), while the

low power because of low electrical conductivity caused by high oxygen. GO reduced at above 200 °C, have increasing high power (depending on the reducing temperature) and low energy due to dominance of EDLC behaviour. Thus, Low temperature TRGO has a better electrochemical due to the adequate residual oxygen functional groups.

3.2.2. Two electrode configuration

Fig. 9(a) shows an asymmetric supercapacitor device in a form of a coin cell with the TRGO/NF as a positive electrode and peanut shell activated carbon (PAC) as a negative material. The PAC electrode material was effectively analysed and reported by Sylla et al. [14]. The three electrode CV curve measurement of TRGO/NF and PAC in 6 M KOH electrolyte at 20 mV s^{-1} is displayed in Fig. 9(b). TRGO/NF and PAC have positive and negative potential windows of 0 to 0.4 V and 0 to −0.9 V vs. Ag/AgCl, respectively. The charge balance was done using Eqs. (S1)–(S3). The CV curves of the asymmetric device in Fig. 9(c) were able to reach a maximum potential of 1.4 V which is greater than the combined potential windows of TRGO/NF and PAC in three electrode configurations. The CV curves of the device are asymmetric in shape, slightly distorted rectangular-like shape indicating electric double layer capacitor (EDLC) behaviour which is constant throughout the various scan rates, suggesting a good charge propagation and fast ionic transport [49]. The GCD curve obtained at various specific current displayed in Fig. 9(d) also shows an EDLC behaviour throughout the different specific currents agreeing with the CV curves in Fig. 9(c) confirming the good capacitive behaviour of the device. The absences of ohmic drops on the GCD curves indicate a low internal resistance [35,77]. The specific capacitance (C_s) was calculated using Eq. (3) below [14] due to its EDLC behaviour.

$$C_s = \frac{I_s \Delta t}{\Delta V} \left[\mathrm{F\ g-1}\right] \tag{3}$$

where I_s, Δt and ΔV are the specific current (A g^{-1}), discharge time (s) and cell potential (V), respectively. The device specific capacitance was calculated to be 78.78 F g^{-1} at 1 A g^{-1} and displayed in Fig. 9(e) showing rate capability of 80% at 5 A g^{-1}. The specific capacitance drop at higher specific current is attributed to the limited time that ions have to access the surface of the electrode at a higher specific current [28,72]. The Ragone plot showing specific energy (E_s) as a function of specific power (P_s) is displayed in Fig. 9(f) calculated from the GCD curve displayed in Fig. 9(d) using Eqs. (4) and (5), respectively.

$$E_s = \frac{I_s}{3.6} \int_{V_i}^{V_f} V\, dt \left[\mathrm{Wh\ kg^{-1}}\right] \tag{4}$$

$$P_s = \frac{E_s}{\Delta t} \times 3600 \left[\mathrm{Wh\ kg^{-1}}\right] \tag{5}$$

where I_s, $\int_{V_i}^{V_f} V\, dt$ and Δt are the specific current (A g^{-1}), integral under the area of the discharge time (V s) and discharge time (s), respectively. The device has a specific energy of 18.73 Wh kg^{-1} at corresponding specific power of 547.52 W kg^{-1} at 1 A g^{-1} and a higher specific power of 2.5 kW kg^{-1} at a corresponding specific energy of 14.10 Wh kg^{-1} at 5 A g^{-1}. These indicate stable device producing higher energy at a wide specific current. The obtained specific energy and power are higher and comparable to those previously reported TRGO and TRGO composites on conductive fabric and other metallic current collectors [28,29,35,49,77] (see Fig. 9(f)). The previously reported studies displayed on the Ragone plot are also displayed in Table 1. The table compares the steps, sample preparation, cell potential (Cp), capacitance retention (CR), electrolyte, specific energy (E_s) and specific power (E_s). The preparation of TRGO/NF requires one step from GO to electrochemical measureable electrode, whiles other requires 2 or more steps. This emphasis the simplicity of the preparation method, which is very safe since it does not requires any health threatening chemical such as hydrazine ($NH_2NH_2{\bullet}H_2O$). The table further shows that this method is not only simple but also produced a high performance supercapacitor device. The device showed a columbic efficiency (C_E) determined from Eq. (S4) (Fig. 9(g)) of 99.9% indicating good reversibility and a capacitance retention (Fig. 9(h)) of 70% after 16,000 cycles.

The electrical properties of the TRGO/NF//PAC device was analysed using EIS, as shown by Nyquist plot displayed in Fig. 10(a). The EIS also determines the nature of the active material on the electrode/electrolyte interface. This Nyquist plot lacks a higher region frequency semi-circle suggesting a low electrode/electrolyte interface charge transfer resistance suggesting a better capacitive behaviour [15]. The reported Nyquist is similar to the ideal supercapacitive behaviour, with a short 45° line starting from the equivalent series resistance (ESR) transitioning into the fast increase close to being parallel to the imaginary impedance

Table 1
Supercapacitor preparation conditions and electrochemical performance comparison between various thermally reduced GO materials reported in the literature and TRGO/NF in this work.

Device configuration	Steps	Preparation conditions	Cp (V)	Electrolyte	CR @ C_s@ Cn (% @ A g^{-1} @ cycles)	E_s @ P_s @ C_d (Wh kg^{-1} @ W kg^{-1} @ A g^{-1})	Ref.
TRGO/Ni-Foam//PAC	1	GO was slurry pasted on Ni-Foam then thermally reduced at 200 °C for an hour at heating rate of 10 °C min^{-1} under Ar	1.4	6 M KOH	70 @ 5@ 16,000	18.73 @ 547.52 @ 1 Ag^{-1}	This work
PAP/TRGO20†	3	Graphite oxide was thermal treated at 700 °C under N_2 flow at heating rate of 5 °C min^{-1}. Then used with pyrrole and aniline to create PAP/TRGO	1.0	1 M H_2SO_4	103 @ 1 @ 10,000	6.3 @ 100 @ 0.2	[49]
TRGO-coated FSSS†	1	GO was repeated dip-coated onto a conductive fabric and dried at 60 °C for 30 min. Then thermal treated at 160 °C in Ar for 2 h	1.0	PVA/ H_3PO_4	93 @ 2.5 mA cm^{-2} @1000 s	5.8 @ 27.7 k @ 0.1 mA cm^{-2}	[28]
N-HRGO/1.5/300†	3	HGO was chemical etched from GO using H_2O_2 and heating at 100 °C for 1.5 h, then centrifuge and washed. HGO was mixed with PPD and stirred for 2 h, and then vacuum filtrated. Membrane was freeze-dried for 12 h and lastly annealed at 300 °C at 5 °C min-1 under Ar.	1.0	6 M KOH	89.3 @ 2 @ 5000	14.0 @ 500 @ 0.5	[35]
rGO//rGO_An	2	rGO was obtained from mixing aqueous GO with NH_3 and $NH_2NH_2{\bullet}H_2O$, the heat at 95 °C under string for 45 min. Then thermal annealed at 280 °C under Ar atmosphere for 1 h	1.0	PVA – 2 M KOH	91.1 @ 2 @ 1000	9.26 @ 8.8 k @0.5	[77]
prGO†	3	ZnO powder was dispersed into GO aqueous solution, stirred overnight and sonicated for 1 h in ice bath. Then filtered and dried at 40 °C. The obtained GO/ZnO powders were dispersed in EG and HCl and microwave irradiated for 6 min at 180 °C then filtered and washed to obtain prGO.	1.0	1 M H_2SO_4	–	15.0 @ 250 @ 1	[29]

Abbreviations: Cp – cell potential, C_s – specific current, Cn – cycle number, CR – capacitance retention, PAC – peanut shell activated carbon, PAP – poly(aniline-co-pyrrole, FSSS – fabric solid state supercapacitor, N-HRGO/1.5/300 – N-rich holey reduced graphene oxide, prGO – porous reduced graphene oxide, † – symmetric device, s – single electrode and k – kilo.

schematic of GO is presented on Fig. 8(b). It is apparent that the spacing from the sheets has increased due to the attachment of the oxygen functional and intercalation of water (see Fig. 2). The XRD showed the increase of the interspace distance while the FTIR show the presence of oxygen functional groups, confirmed by the EDS showing the type of element constituting of those oxygen functional groups. Fig. 8(c) shows the schematic of TRGO elucidating the decrease of oxygen functional groups together with the extermination of intercalated water and a slight decrease of the interplanar spacing. Fig. 8(d) shows the schematic of graphite as a positive electrode and it is clear that the anion adhered on the surface of the graphite sheet. This behaviour is responsible for the decrease of the electrochemical at high reducing temperature, since the oxygen content has been exterminated [16,30]. While on TRGO (Fig. 8 (e)) electrolyte anions have travelled into the bulk surface with the aid of the graphene oxygen surface functionality increasing the capacitance due to pseudocapacitive activity. Thus, the oxygen functional groups increase the wettability and also prevent the π–π interaction from restacking of graphene sheets. Our previous work [30] and that of Zhao et al. [16] also indicate the importance of the oxygen functional groups. Thus, oxygen content associated with reducing temperature of 200 °C leads to high energy and slightly low power. Moreover, unreduced GO and reduced GO with temperature below 200 °C leads to low energy and

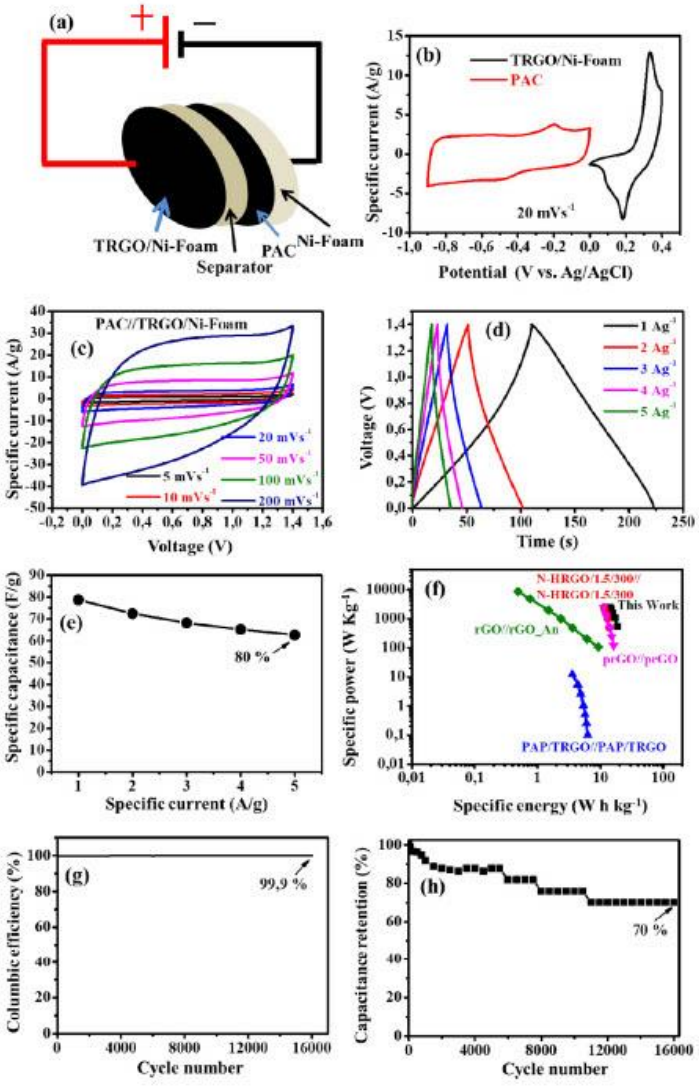

Fig. 9. TRGO/NF//PAC asymmetric (a) device schematic, (b) CV of positive and negative electrodes, (c) CV curves at different scan rates, (d) GCD curves at different specific currents, (e) specific capacitance versus specific current, (f) Ragone plot, (g) columbic efficiency and (h) capacitance retention.

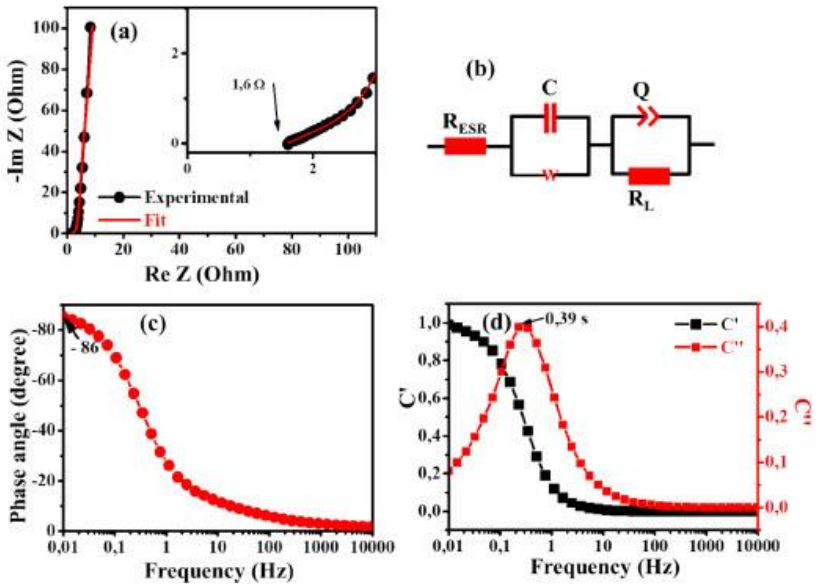

Fig. 10. (a) Nyquist plot of the device (the inset shows the enlarged high-frequency region of the plot), (b) equivalent circuit diagram used to fit the Nyquist plot in (c) (i.e. a red solid-line), (c) phase angle versus frequency and (d) real and imaginary plot of capacitance as a function of frequency. (For interpretation of the references to colour in this figure legend, the reader is referred to the web version of this article.)

(-Im Z) axis [15,78]. The Nyquist plot line being near parallel to the imaginary impedance (-Im Z) axis, is indication of the device being highly capacitive. The real impedance (Re Z) axis intercept in the high frequency region indicates the ESR of 1.6 Ω describing the interfacial contact resistance between the active materials and NF current collector, electrode/electrolyte interface and the internal resistance of the active material [14,15]. The low ESR agrees with the absence of ohmic drop in Fig. 9(d). Thus, The EIS confirms the device CV and GCD. The maximum power, P_{max} of the device was estimated from Eq. (6) below to be 306.25 kW kg^{-1}

$$P_{max} = \frac{\Delta V^2}{4m(ESR)} \ [\mathrm{W\ kg^{-1}}] \tag{6}$$

where ΔV, m and ESR are the cell potential (V), mass (of 4×10^{-6} kg) and ESR of 1.6 Ω determined from the Nyquist plot in Fig. 10(a), respectively. The Nyquist plot was fitted using the equivalent circuit diagram shown in Fig. 10(b) and the chi-square (χ^2) was 2.404 indicating a very good fitness. The equivalent circuit diagram shows the presence of the ESR connected in series to capacitor (C) and Warburg impedance (W). A deviation of the Nyquist plot from the imaginary axis is attributed to the leakage resistance R_L which is quite minimum in this case because the deviation from y-axis is not that much. The good capacitive behaviour seen on the CV (Fig. 9(c)), GCD (Fig. 9(d)) curves and Nyquist plot (Fig. 10(a)) is confirmed by the phase angle of -86° displayed in Fig. 10(c) of which is very close to the ideal phase angel of -90° [79]. The frequency dependent real ($C'(\omega)$) and imaginary ($C''(\omega)$) capacitances are displayed in Fig. 10(d) calculated from Eqs. (7)–(10) where the impedance $Z(\omega)$ with $\omega = 2\pi f$ is expressed as

$$Z(\omega) = \frac{1}{j\omega \times C(\omega)} \tag{7}$$

$$C'(\omega) = \frac{Z''(\omega)}{\omega |Z(\omega)|^2} \tag{8}$$

$$C''(\omega) = \frac{Z'(\omega)}{\omega |Z(\omega)|^2} \tag{9}$$

$$|Z(\omega)|^2 = Z'(\omega)^2 + Z''(\omega)^2 \tag{10}$$

Fig. 10(d) also shows that the real ($C'(\omega)$) accessible capacitance of 1.0 F and the imaginary $C''(\omega)$ gives a relaxation time ($\tau = 1/2\pi f$, where f is the peak of the frequency) of 0.39 s suggesting that the prepared device can be quickly charged. All of the aforementioned results confirm the outstanding electrochemical performance of TRGO/Ni-Foam as a suitable positive electrode for SC due to the following factors: (1) nanographene sheets are directly deposited on Ni Foam forming an integrated binder-free electrode improving the electrical conductivity between TRGO active material and Ni-Foam current collector, reducing resistance and facilitating a fast electrochemical reaction rate; (2) TRGO loosely stacked provides a large accessible surface area and allows access of ions during adsorption/desorption leading to more efficient transport; (3) surface oxygen functional groups serve as a passage to the bulker material and provide some pseudocapacitance and increase the charge caring capabilities and (4) the high conducting TRGO provided an effective pathway for charge transport. These suggest that TRGO/Ni-Foam hold great promise for supercapacitor devices.

4. Conclusion

In summary, additive (binder and conducive enhances) free TRGO/NF electrode was successfully prepared using a low temperature one step AP-CVD at 200 °C for an hour. The SEM showed the adhesion of graphene sheets on the surface of NF. Raman images show the dispersion of graphitization, also emphasized that Tuinsta–Koenig and Cuesta models

show a similar defect distribution. Absence of conductive enhance and binder allowed the determination of the real electrochemical performance. The presence of oxygen content significantly increased electrochemical performance of the positive TRGO electrode. The two electrodes (device) showed a high specific capacitance of 78.78 F g^{-1} at 1 A g^{-1} with the corresponding specific energy and power of 18.73 Wh kg^{-1} and 547.52 W kg^{-1}, respectively. The specific energy and power at 5 A g^{-1} was estimated to be 14.10 Wh kg^{-1} and 2.5 kW kg^{-1}, respectively. The maximum power from the device was estimated to be 306.25 kW kg^{-1}. The EIS showed that the device is highly capacitive due to lack of a semi-circle and high phase angle of −86°.

CRediT authorship contribution statement

V.M. Maphiri: Conceptualization, methodology, software, formal analysis, investigation, visualization, writing - original daft, writing-review and editing. **D.T. Bakhoum:** writing - review and editing. **S. Sarr:** writing - review and editing. **N.F. Sylla:** visualization, writing-review and editing. **G. Rutavi:** formal analysis, visualization, writing - review and editing. **N. Manyala:** resources, supervision, formal analysis, funding acquisition, writing - review and editing.

Declaration of competing interest

The authors declare that they have no known competing financial interests or personal relationships that could have appeared to influence the work reported in this paper.

Acknowledgements

This work was supported by the National Research Foundation (NRF) of South Africa through the South African Research Chairs Initiative (SARChI) (Grant Number 61056). Any idea, finding, conclusion or recommendation expressed in this publication is that of the author(s). The NRF does not accept any liability in this regard. V.M. Maphiri acknowledges NRF bursary through SARChI in Carbon Technology and Materials and University of Pretoria for his studies.

Appendix A. Supplementary data

Supplementary data to this article can be found online at https://doi.org/10.1016/j.est.2022.104967.

References

[1] Z. Peng, Q. Jiang, P. Peng, F. Li, Nh3-activated fullerene derivative hierarchical microstructures to porous fe3o4/n-c for oxygen reduction reaction and zn-air battery, Eng. Sci. 14 (2021) 27–38, https://doi.org/10.30919/ESSD1311.
[2] Z. Mohamed, G. Zhang, B. He, Y. Fan, Heterostructure necklace-like NiO-NiCo2O4 hybrid with superior catalytic capability as electrocatalyst for li-oxygen batteries, Eng. Sci. 17 (2022) 231–241, https://doi.org/10.30919/ESSD595.
[3] C. Lai Y. Wang L. Fu H. Song B. Liu D. Pan Z. Guo I. Seok K. Li H. Zhang M. Dong , Aqueous Flexible All-solid-state NiCo-Zn Batteries With High Capacity based on Advanced Ion-buffering Reservoirs of NiCo 2 O 4, (n.d.). doi:10.1007/s42114-021-00375-1.
[4] Y. Zhang, Y. An, L. Wu, H. Chen, Z. Li, H. Dou, V. Murugadoss, J. Fan, X. Zhang, X. Mai, Z. Guo, Metal-free energy storage systems: combining batteries with capacitors based on a methylene blue functionalized graphene cathode, J. Mater. Chem. A 7 (2019) 19668–19675, https://doi.org/10.1039/C9TA06734E.
[5] J. Zhao, D. Wei, C. Zhang, Q. Shao, V. Murugadoss, Z. Guo, Q. Jiang, X. Yang, An overview of oxygen reduction electrocatalysts for rechargeable zinc-air batteries enabled by carbon and carbon composites, Eng. Sci. 15 (2021) 1–19, https://doi.org/10.30919/ESSD420.
[6] M.T. Dizaji, W. Li, Higher voltage redox flow batteries with hybrid acid and base electrolytes, Eng. Sci. 11 (2020) 54–65, https://doi.org/10.30919/ESSD1118.
[7] C. Hou, B. Wang, V. Murugadoss, S. Vupputuri, Y. Chao, Z. Guo, C. Wang, W. Du, Recent advances in Co3O4as anode materials for high-performance lithium-ion batteries, Eng. Sci. 11 (2020) 19–30, https://doi.org/10.30919/ESSD1128.
[8] L. Liu, C. Wang, Z. He, R. Das, B. Dong, X. Xie, Z. Guo, An overview of amphoteric ion exchange membranes for vanadium redox flow batteries, J. Mater. Sci. Technol. 69 (2021) 212–227, https://doi.org/10.1016/J.JMST.2020.08.032.
[9] X. Jiang, Y. Chen, X. Meng, W. Cao, C. Liu, Q. Huang, N. Naik, V. Murugadoss, M. Huang, Z. Guo, The impact of electrode with carbon materials on safety performance of lithium-ion batteries: a review, Carbon N. Y. 191 (2022) 448–470, https://doi.org/10.1016/J.CARBON.2022.02.011.
[10] Z. Liu, G. Li, Q. Qin, L. Mi, G. Li, G. Zheng, C. Liu, Q. Li, X. Liu, Electrospun PVDF/PAN membrane for pressure sensor and sodium-ion battery separator, Adv. Compos. Hybrid Mater. 4 (2021) 1215–1225, https://doi.org/10.1007/S42114-021-00364-4/FIGURES/6.
[11] X. Dong, X. Zhao, Y. Chen, C. Wang, Investigations about the influence of different carbon matrixes on the electrochemical performance of Na3V2(PO4)3 cathode material for sodium ion batteries, Adv. Compos. Hybrid Mater. 4 (2021) 1070–1081, https://doi.org/10.1007/S42114-021-00319-9/FIGURES/10.
[12] G. Li, C. Dang, Y. Hou, F. Dang, Y. Fan, Z. Guo, Experimental and theoretical characteristic of single atom co-N-C catalyst for li-O2 batteries, Eng. Sci. 10 (2020) 85–94, https://doi.org/10.30919/ESSD1005.
[13] D.J. Tarimo, K.O. Oyedotun, A.A. Mirghni, N.F. Sylla, N. Manyala, High energy and excellent stability asymmetric supercapacitor derived from Sulphur-reduced graphene oxide/manganese dioxide composite and activated carbon from peanut shell, Electrochim. Acta 353 (2020), 136498, https://doi.org/10.1016/j.electacta.2020.136498.
[14] N.F. Sylla, N.M. Ndiaye, B.D. Ngom, D. Momodu, M.J. Madito, B.K. Mutuma, N. Manyala, Effect of porosity enhancing agents on the electrochemical performance of high-energy ultracapacitor electrodes derived from peanut shell waste, Sci. Rep. 9 (2019) 1–15, https://doi.org/10.1038/s41598-019-50189-x.
[15] T.S. Mathis, N. Kurra, X. Wang, D. Pinto, P. Simon, Y. Gogotsi, Energy storage data reporting in perspective—guidelines for interpreting the performance of electrochemical energy storage systems, Adv. Energy Mater. 9 (2019) 1–13, https://doi.org/10.1002/aenm.201902007.
[16] B. Zhao, P. Liu, Y. Jiang, D. Pan, H. Tao, J. Song, T. Fang, W. Xu, Supercapacitor performances of thermally reduced graphene oxide, J. Power Sources 198 (2012) 423–427, https://doi.org/10.1016/j.jpowsour.2011.09.074.
[17] S.S. Patil, T.S. Bhat, A.M. Teli, S.A. Beknalkar, S.B. Dhavale, M.M. Faras, M. M. Karanjkar, P.S. Patil, Hybrid solid state supercapacitors (HSSC's) for high energy & power density: an overview, Eng. Sci. 12 (2020) 38–51, https://doi.org/10.30919/ESSD1140.
[18] S. ur Rehman, R. Ahmed, K. Ma, S. Xu, T. Tao, M.A. Aalam, M. Amir, J. Wang, Composite of strip-shaped ZIF-67 with polypyrrole: a conductive polymer-MOF electrode system for stable and high specific capacitance, Eng. Sci. 13 (2021) 71–78, https://doi.org/10.30919/ESSD1263.
[19] X. Jiang, Z. Li, J. Yao, Z. Shao, X. Chen, One-step synthesis of soy protein/graphene nanocomposites and their application in photothermal therapy, Mater. Sci. Eng. C. 68 (2016) 798–804, https://doi.org/10.1016/j.msec.2016.07.034.
[20] L. Qiu, H. Zhang, W. Wang, Y. Chen, R. Wang, Effects of hydrazine hydrate treatment on the performance of reducedgraphene oxide film as counter electrode in dye-sensitized solar cells, Appl. Surf. Sci. 319 (2014) 339–343, https://doi.org/10.1016/j.apsusc.2014.07.133.
[21] P. Zhu, M. Shen, S. Xiao, D. Zhang, Experimental study on the reducibility of graphene oxide by hydrazine hydrate, Phys. B Condens. Matter 406 (2011) 498–502, https://doi.org/10.1016/j.physb.2010.11.022.
[22] S. Park, H. Lee, Y.-J. Kim, P.S. Lee, Fully laser-patterned stretchable microsupercapacitors integrated with soft electronic circuit components, NPG Asia Mater. 10 (2018) 959–969, https://doi.org/10.1038/s41427-018-0080-z.
[23] M. Gao, X. Dong, K. Wang, W. Duan, X. Sun, C. Zhu, W. Wang, Laser direct preparation and processing of graphene/MnO nanocomposite electrodes for microsupercapacitors, J. Energy Storage 33 (2021), 102162, https://doi.org/10.1016/j.est.2020.102162.
[24] O. Mondal, S. Mitra, M. Pal, A. Datta, S. Dhara, D. Chakravorty, Reduced graphene oxide synthesis by high energy ball milling, Mater. Chem. Phys. 161 (2015) 123–129, https://doi.org/10.1016/j.matchemphys.2015.05.023.
[25] P. Vázquez-Sánchez, M.A. Rodríguez-Escudero, P.J. Burgos, I. Llorente, O. Caballero-Calero, M.M. González, R. Fernández, M.C. García-Alonso, Synthesis of Cu/rGO composites by chemical and thermal reduction of graphene oxide, J. Alloys Compd. 800 (2019) 379–391, https://doi.org/10.1016/j.jallcom.2019.06.008.
[26] K.K.H. De Silva, H.H. Huang, R. Joshi, M. Yoshimura, Restoration of the graphitic structure by defect repair during the thermal reduction of graphene oxide, Carbon N. Y. 166 (2020) 74–90, https://doi.org/10.1016/j.carbon.2020.05.015.
[27] Q. Du, M. Zheng, L. Zhang, Y. Wang, J. Chen, L. Xue, W. Dai, G. Ji, J. Cao, Preparation of functionalized graphene sheets by a low-temperature thermal exfoliation approach and their electrochemical supercapacitive behaviors, Electrochim. Acta 55 (2010) 3897–3903, https://doi.org/10.1016/j.electacta.2010.01.089.
[28] A. Ramadoss, B. Saravanakumar, S.J. Kim, Thermally reduced graphene oxide-coated fabrics for flexible supercapacitors and self-powered systems, Nano Energy 15 (2015) 587–597, https://doi.org/10.1016/J.NANOEN.2015.05.009.
[29] J. Ma, Y. Yamamoto, C. Su, S. Badhulika, C. Fukuhara, C.Y. Kong, One-pot microwave-assisted synthesis of porous reduced graphene oxide as an electrode material for high capacitance supercapacitor, Electrochim. Acta 386 (2021), 138439, https://doi.org/10.1016/J.ELECTACTA.2021.138439.
[30] V.M. Maphiri, G. Rutavi, N.F. Sylla, S.A. Adewinbi, O. Fasakin, N. Man, in: Novel Thermally Reduced Graphene Oxide Microsupercapacitor Fabricated via Mask — Free AxiDraw Direct Writing, 2021, pp. 1–15.
[31] M.J. Madito, K.S. Matshoba, F.U. Ochai-Ejeh, N. Mongwaketsi, C.B. Mtshali, M. Fabiane, N. Manyala, Nickel-copper graphene foam prepared by atmospheric pressure chemical vapour deposition for supercapacitor applications, Surf. Coat. Technol. 383 (2020), 125230, https://doi.org/10.1016/j.surfcoat.2019.125230.

[32] D.J. Tarimo, K.O. Oyedotun, A.A. Mirghni, N. Manyala, Sulphur-reduced graphene oxide composite with improved electrochemical performance for supercapacitor applications, Int. J. Hydrog. Energy 45 (2020) 13189–13201, https://doi.org/10.1016/j.ijhydene.2020.03.059.
[33] Z. Zhu, S. Tang, J. Yuan, X. Qin, Y. Deng, R. Qu, G.M. Haarberg, Effects of various binders on supercapacitor performances, Int. J. Electrochem. Sci. 11 (2016) 8270–8279, https://doi.org/10.20964/2016.10.04.
[34] B. Xu, H. Wang, Q. Zhu, N. Sun, B. Anasori, L. Hu, F. Wang, Y. Guan, Y. Gogotsi, Reduced graphene oxide as a multi-functional conductive binder for supercapacitor electrodes, Energy Storage Mater. 12 (2018) 128–136, https://doi.org/10.1016/j.ensm.2017.12.006.
[35] Y. Xu, C. Huang, A. Hu, Z. Pan, C. Chen, Y. Yang, Q. Tang, C. Jiang, X. Chen, N-rich reduced graphene oxide film with cross-coupled porous networks as free-standing electrode for high performance supercapacitors, Appl. Surf. Sci. 563 (2021), 150303, https://doi.org/10.1016/J.APSUSC.2021.150303.
[36] T. Giannakopoulou, N. Todorova, A. Erotokritaki, N. Plakantonaki, A. Tsetsekou, C. Trapalis, Electrochemically deposited graphene oxide thin film supercapacitors: comparing liquid and solid electrolytes, Appl. Surf. Sci. 528 (2020), 146801, https://doi.org/10.1016/j.apsusc.2020.146801.
[37] P. Xie, Y. Liu, M. Peng, M. Niu, C. Liu, N. Wu, K. Sui, R.R. Patil, D. Pan, Z. Guo, R. Fan, Hierarchically porous Co/C nanocomposites for ultralight high-performance microwave absorption, Adv. Compos. Hybrid Mater. 4 (2021) 173–185, https://doi.org/10.1007/S42114-020-00202-Z/FIGURES/9.
[38] H. Wu, H. Sun, F. Han, P. Xie, Y. Zhong, B. Quan, Y. Zhao, C. Liu, R. Fan, Z. Guo, Negative permittivity behavior in flexible carbon nanofibers-polydimethylsiloxane films, Eng. Sci. 17 (2022) 113–120, https://doi.org/10.30919/ES8D576.
[39] H. Wu, Y. Zhong, Y. Tang, Y. Huang, G. Liu, W. Sun, P. Xie, D. Pan, C. Liu, Z. Guo, Precise regulation of weakly negative permittivity in CaCu3Ti4O12 metacomposites by synergistic effects of carbon nanotubes and grapheme, Adv. Compos. Hybrid Mater. 5 (2022) 419–430, https://doi.org/10.1007/S42114-021-00378-Y/FIGURES/5.
[40] G. Qi, Y. Liu, L. Chen, P. Xie, D. Pan, Z. Shi, B. Quan, Y. Zhong, C. Liu, R. Fan, Z. Guo, Lightweight Fe3C@Fe/C nanocomposites derived from wasted cornstalks with high-efficiency microwave absorption and ultrathin thickness, Adv. Compos. Hybrid Mater. 4 (2021) 1226–1238, https://doi.org/10.1007/S42114-021-00368-0/FIGURES/8.
[41] Y. Wang, Y. Liu, C. Wang, H. Liu, J. Zhang, J. Lin, J. Fan, T. Ding, J.E. Ryu, Z. Guo, Significantly enhanced ultrathin NiCo-based MOF nanosheet electrodes hybridied with Ti3C2Tx MXene for high performance asymmetric supercapacitors, Eng. Sci. 9 (2020) 50–59, https://doi.org/10.30919/ES8D903.
[42] Z. Sun, H. Qi, M. Chen, S. Guo, Z. Huang, S. Maganti, V. Murugadoss, M. Huang, Z. Guo, Progress in cellulose/carbon nanotube composite flexible electrodes for supercapacitors, Eng. Sci. (2021), https://doi.org/10.30919/ES8D588.
[43] S. Li, J. Pan, S. Li, H. Jin, W. Luo, Y. Ma, J. Wu, Z. Chao, N. Naik, D. Pan, Z. Guo, Synthesis of three dimensional Mo-doped nickel sulfide mesoporous nanostructures/ni foam composite for supercapacitor and overall water splitting, ES Energy Environ. (2022), https://doi.org/10.30919/ESEE8C646.
[44] P.M. Mana, P.K. Bhujbal, H.M. Pathan, Fabrication and characterization of ZnS based photoelectrochemical solar cell, ES Energy Environ. (2020), https://doi.org/10.30919/ESEE8C1021.
[45] Y. Liu, Y. Wang, H. Wang, P. Zhao, H. Hou, L. Guo, Acetylene black enhancing the electrochemical performance of NiCo-MOF nanosheets for supercapacitor electrodes, Appl. Surf. Sci. 492 (2019) 455–463, https://doi.org/10.1016/j.apsusc.2019.06.238.
[46] J. Sun, Y. Zhang, Y. Liu, H. Jiang, X. Dong, T. Hu, C. Meng, Hydrated vanadium pentoxide/reduced graphene oxide-polyvinyl alcohol (V2O5·nH2O/rGO-PVA) film as a binder-free electrode for solid-state Zn-ion batteries, J. Colloid Interface Sci. 587 (2021) 845–854, https://doi.org/10.1016/j.jcis.2020.10.148.
[47] N. Sun, Y. Guan, Y.T. Liu, Q. Zhu, J. Shen, H. Liu, S. Zhou, B. Xu, Facile synthesis of free-standing, flexible hard carbon anode for high-performance sodium ion batteries using graphene as a multi-functional binder, Carbon N. Y. 137 (2018) 475–483, https://doi.org/10.1016/j.carbon.2018.05.056.
[48] N. Radha, A. Kanakaraj, H.M. Manohar, M.R. Nidhi, D. Mondal, S.K. Nataraj, D. Ghosh, Binder free self-standing high performance supercapacitive electrode based on graphene/titanium carbide composite aerogel, Appl. Surf. Sci. 481 (2019) 892–899, https://doi.org/10.1016/j.apsusc.2019.03.086.
[49] A. Moyseowicz, Z. González, R. Menéndez, G. Gryglewicz, Three-dimensional poly (aniline-co-pyrrole)/thermally reduced graphene oxide composite as a binder-free electrode for high-performance supercapacitors, Compos. Part B Eng. 145 (2018) 232–239, https://doi.org/10.1016/j.compositesb.2018.03.018.
[50] D.Dsilva Winfred Rufuss, S. Iniyan, L. Suganthi, P.A. Davies, Low mass fraction impregnation with graphene oxide (GO) enhances thermo-physical properties of paraffin for heat storage applications, Thermochim. Acta 655 (2017) 226–233, https://doi.org/10.1016/J.TCA.2017.07.005.
[51] H. Yin, D. Wang, H. Zhu, W. Xiao, F. Gan, Growing highly capacitive nano-Ni(OH)2 on freshly cut graphite electrode by electrochemically enhanced self-assembly, Electrochim. Acta 99 (2013) 198–203, https://doi.org/10.1016/J.ELECTACTA.2013.03.137.
[52] S. Claramunt, A. Varea, D. López-López-Díaz, M.Mercedes Velázquez-velázquez, A. Cornet, A. Cirera, The importance of interbands on the interpretation of the Raman spectrum of graphene oxide, J. Phys. Chem. C 119 (2015) 10123–10129, https://doi.org/10.1021/acs.jpcc.5b01590.
[53] R. Siburian, H. Sihotang, S. Lumban Raja, M. Supeno, C. Simanjuntak, New route to synthesize of graphene nano sheets, Orient. J. Chem. 34 (2018) 182–187, https://doi.org/10.13005/ojc/340120.
[54] Y. Wei, Y. Wang, L. Wei, X. Zhao, X. Zhou, H. Liu, Highly efficient and reactivated electrocatalyst of ruthenium electrodeposited on nickel foam for hydrogen evolution from NaBH4 alkaline solution, Int. J. Hydrog. Energy 43 (2018) 592–600, https://doi.org/10.1016/j.ijhydene.2017.11.010.
[55] M.N. Rantho, M.J. Madito, N. Manyala, Symmetric supercapacitor with supercapattery behavior based on carbonized iron cations adsorbed onto polyaniline, Electrochim. Acta 262 (2018) 82–96, https://doi.org/10.1016/j.electacta.2018.01.001.
[56] G.K. Veerasubramani, K. Krishnamoorthy, S.J. Kim, Improved electrochemical performances of binder-free CoMoO4 nanoplate arrays@Ni foam electrode using redox additive electrolyte, J. Power Sources 306 (2016) 378–386, https://doi.org/10.1016/j.jpowsour.2015.12.034.
[57] Y. Li, Z. Hai, X. Hou, H. Xu, Z. Zhang, D. Cui, C. Xue, B. Zhang, Self-assembly of 3D fennel-like Co3O4 with thirty-six surfaces for high performance supercapacitor, J. Nanomater. 2017 (2017), https://doi.org/10.1155/2017/1404328.
[58] M. Bera, Chandravati, P. Gupta, P.K. Maji, Facile one-pot synthesis of graphene oxide by sonication assisted mechanochemical approach and its surface chemistry, J. Nanosci. Nanotechnol. 18 (2017) 902–912, https://doi.org/10.1166/jnn.2018.14306.
[59] M. Muniyalakshmi, K. Sethuraman, D. Silambarasan, Synthesis and characterization of graphene oxide nanosheets, Mater. Today Proc. 21 (2020) 408–410, https://doi.org/10.1016/j.matpr.2019.06.375.
[60] Z. Liu, Z. Diao, Y. Yuan, H. Jia, L. Wang, W. Fei, A two-step thermal treatment method to produce reduced graphene oxide with selectively increasing electrochemically active carbonyl group content for high-performance supercapacitor electrode, Colloids Surf. A Physicochem. Eng. Asp. 620 (2021), 126573, https://doi.org/10.1016/j.colsurfa.2021.126573.
[61] S.N. Alam, N. Sharma, L. Kumar, Synthesis of graphene oxide (GO) by modified hummers method and its thermal reduction to obtain reduced graphene oxide (rGO)*, Graphene. 06 (2017) 1–18, https://doi.org/10.4236/graphene.2017.61001.
[62] M.J. Madito, M.Y.A. Ismail, T.T. Hlatshwayo, C.B. Mtshali, The nature of surface defects in Xe ion-implanted glassy carbon annealed at high temperatures: Raman spectroscopy analysis, Appl. Surf. Sci. 506 (2020), 145001, https://doi.org/10.1016/j.apsusc.2019.145001.
[63] S. Vollebregt, R. Ishihara, P.D. Tichelaar, Y. Hou, C.I.M. Beenakker, Influence of the growth temperature on the first and second-order Raman band ratios and widths of carbon nanotubes and fibers, Carbon N. Y. 50 (2012) 3542–3554, https://doi.org/10.1016/j.carbon.2012.03.026.
[64] M.J. Matthews, M.A. Pimenta, G. Dresselhaus, M.S. Dresselhaus, M. Endo, Origin of dispersive effects of the Raman D band in carbon materials, Phys. Rev. B: Condens. Matter Mater. Phys. 59 (1999), https://doi.org/10.1103/physrevb.59.r6585.
[65] I. Pócsik, M. Hundhausen, M. Koós, L. Ley, Origin of the D peak in the Raman spectrum of microcrystalline graphite, J. Non-Cryst. Solids 227–230 (1998) 1083–1086, https://doi.org/10.1016/S0022-3093(98)00349-4.
[66] A. Sadezky, H. Muckenhuber, H. Grothe, R. Niessner, U. Pöschl, Raman microspectroscopy of soot and related carbonaceous materials: spectral analysis and structural information, Carbon N. Y. 43 (2005) 1731–1742, https://doi.org/10.1016/j.carbon.2005.02.018.
[67] A. Cuesta, P. Dhamelincourt, J. Laureyns, A. Martínez-Alonso, J.M.D. Tascón, Raman microprobe studies on carbon materials, Carbon N. Y. 32 (1994) 1523–1532, https://doi.org/10.1016/0008-6223(94)90148-1.
[68] B. Martín-García, M.M. Velázquez, F. Rossella, V. Bellani, E. Diez, J.L. García Fierro, J.A. Pérez-Hernández, J. Hernández-Toro, S. Claramunt, A. Cirera, Functionalization of reduced graphite oxide sheets with a zwitterionic surfactant, ChemPhysChem 13 (2012) 3682–3690, https://doi.org/10.1002/cphc.201200501.
[69] A. Alkhouzaam, H. Qiblawey, M. Khraisheh, M. Atieh, M. Al-Ghouti, Synthesis of graphene oxides particle of high oxidation degree using a modified Hummers method, Ceram. Int. 46 (2020) 23997–24007, https://doi.org/10.1016/j.ceramint.2020.06.177.
[70] F. Tuinstra, KOENIG JL, Raman spectrum of graphite, J. Chem. Phys. 53 (1970) 1126–1130, https://doi.org/10.1063/1.1674108.
[71] O. Pasakin, J.K. Dangbegnon, D.Y. Momodu, M.J. Madito, K.O. Oyedotun, M. A. Eleruja, N. Manyala, Synthesis and characterization of porous carbon derived from activated banana peels with hierarchical porosity for improved electrochemical performance, Electrochim. Acta 262 (2018) 187–196, https://doi.org/10.1016/j.electacta.2018.01.028.
[72] M.N. Rantho, M.J. Madito, N. Manyala, High-performance symmetric supercapacitor device based on carbonized iron-polyaniline/nickel graphene foam, J. Alloys Compd. 819 (2020), 152993, https://doi.org/10.1016/j.jallcom.2019.152993.
[73] R. Kumar, S.K. Dhawan, H.K. Singh, A. Kaur, Charge transport mechanism of thermally reduced graphene oxide and their fabrication for high performance shield against electromagnetic pollution, Mater. Chem. Phys. 180 (2016) 413–421, https://doi.org/10.1016/j.matchemphys.2016.06.025.
[74] A. Eckmann, A. Felten, A. Mishchenko, L. Britnell, R. Krupke, K.S. Novoselov, C. Casiraghi, Probing the nature of defects in graphene by Raman spectroscopy, Nano Lett. 12 (2012) 3925, https://doi.org/10.1021/nl300901a.
[75] Y. He, J. Pan, L. Wu, Y. Zhu, X. Ge, J. Ran, Z.J. Yang, T. Xu, A novel methodology to synthesize highly conductive anion exchange membranes, Sci. Rep. 5 (2015), https://doi.org/10.1038/srep13417.
[76] P. Murovhi, D.J. Tarimo, K.O. Oyedotun, N. Manyala, High specific energy asymmetric supercapacitor based on alpha-manganese dioxide/activated expanded graphite composite and activated carbon-polyvinyl alcohol, J. Energy Storage 32 (2020), 101797, https://doi.org/10.1016/j.est.2020.101797.

[77] A. Karaphun, C. Phrompet, W. Tuichai, N. Chanlek, C. Sriwong, C. Ruttanapun, The influence of annealing on a large specific surface area and enhancing electrochemical properties of reduced graphene oxide to improve the performance of the active electrode of supercapacitor devices, Mater. Sci. Eng. B 264 (2021), 114941, https://doi.org/10.1016/J.MSEB.2020.114941.

[78] J.P. Diard, B. Le Gorrec, C. Montella, Linear diffusion impedance. General expression and applications, J. Electroanal. Chem. 471 (1999) 126–131, https://doi.org/10.1016/S0022-0728(99)00262-4.

[79] M. Mahdavian, M.M. Attar, Another approach in analysis of paint coatings with EIS measurement: phase angle at high frequencies, Corros. Sci. 48 (2006) 4152–4157, https://doi.org/10.1016/j.corsci.2006.03.012.

Supplementary information

Low temperature thermally reduced graphene oxide directly on Ni – Foam using atmospheric pressure - chemical vapour deposition for high performance supercapacitor application

Vusani M. Maphiri, Daba T. Bakhoum, Samba Sarr, Ndeye F. Sylla, Gift Rutavi, Ncholu Manyala*

Department of Physics, Institute of Applied Materials, SARChI Chair in Carbon Technology and Materials, University of Pretoria, Pretoria 0028, SouthAfrica

*Corresponding author email: ncholu.manyala@up.ac.za, Tel.: + (27)12 420 3549 Fax: + (27)12 420 2516

The digital image displayed on Fig. S1 was taken using a Witec Raman confocal equipped with the Zeiss EC Epiplan 50× / 0.75 objective with a camera exposure of 1/25.

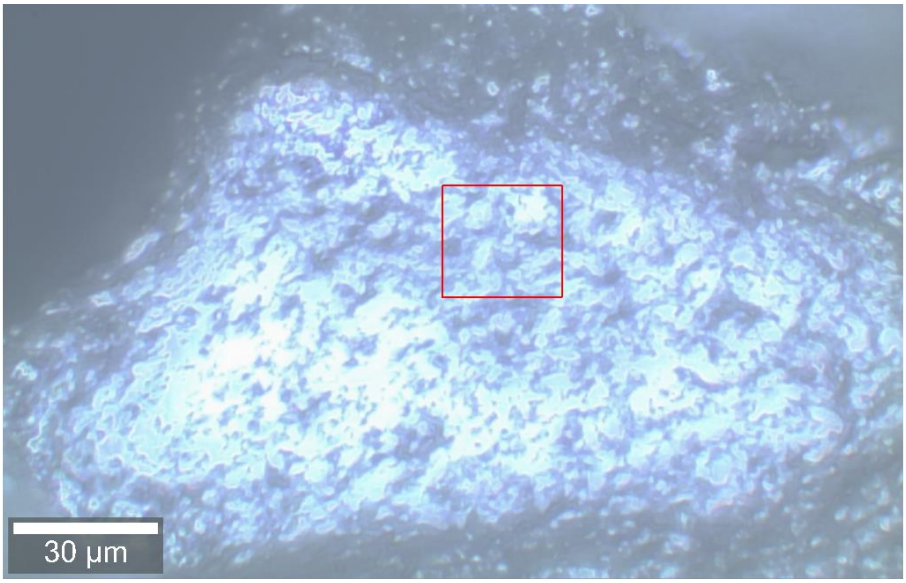

Fig. S1. Digital image of TRGO/Ni-Foam

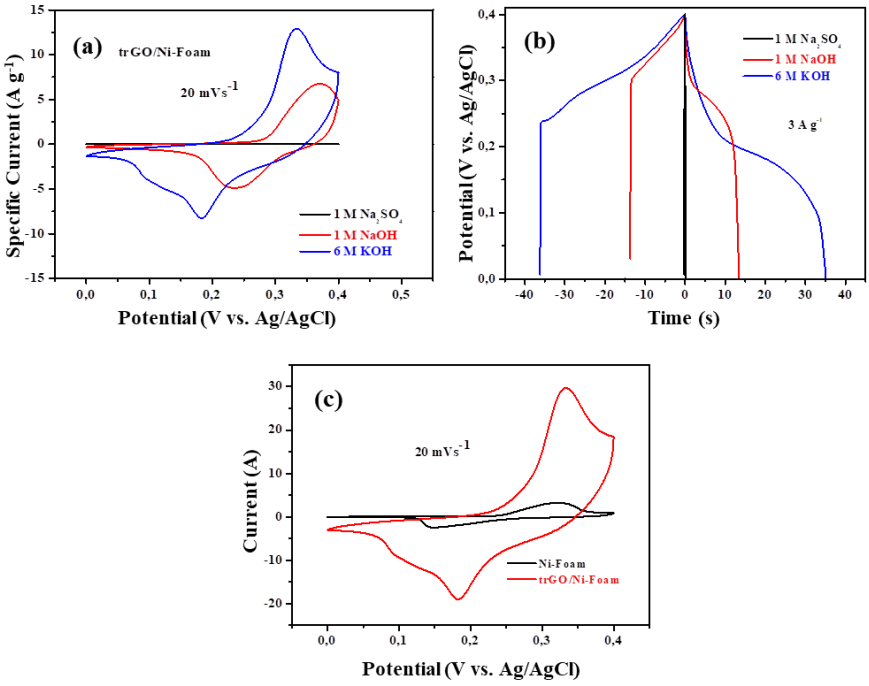

Fig. S2. (a) CV curve at 20 mVs^{-1} and (b) GCD curve at 5 A g^{-1} for 1 M Na_2SO_4, 1 M NaOH and 6M KOH, (c) is the CV curve at 20 mVs^{-1} for Ni-Foam and TRGO/Ni-Foam

The 400 and 800 ℃ samples were prepared the same way as the TRGO/Ni-Foam at 200 ℃. The only difference is the desired temperatures of 400 and 800 ℃ were used. The heating rate was also set to 10 ℃/min and the material was also reduced for an hour at the respective desired temperature. After an hour the AP-CVD was moved away from quartz region with TRGO/Ni-Foam to allow it to cool down to room temperature.

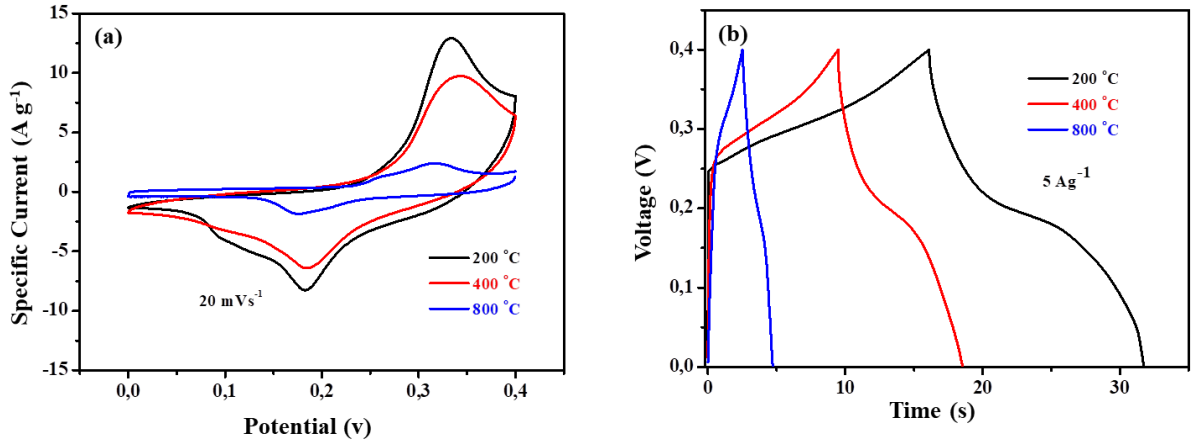

Fig. S3. (a) CV curve at 20 mVs^{-1} and (b) GCD curve at 5 A g^{-1} for TRGO/Ni-Foam reduced at 200, 400 and 800 ℃

Charge balance, for the two-electrode evaluation where TRGO/Ni-Foam was used as a positive electrode and peanut shell activated carbon (PAC) with an EDLC behaviour in the negative. The masses of the electrodes were determined based on the charge balancing equation below:

$$Q_+ = Q_- \quad \ldots (S1)$$

$$3.6m_+ \times Q_{s+} = m_- \times \Delta V_- \times C_{s-} \quad \ldots (S2)$$

$$\frac{m_+}{m_-} = \frac{C_{s-} \times \Delta V_-}{3.6 \times Q_{s+}} \quad \ldots (S3)$$

where Q_+, Q_-, Q_{s+}, C_{s-}, m_+, m_- and ΔV are the charge for positive, charge for negative, specific capacity for the positive electrode (mAh g^{-1}), specific capacitance (F g^{-1}) for the negative electrode, masses (mg) of the positive and negative electrodes and ΔV is the potential window (V), respectively.

The columbic efficiency was calculated using equation (S4)

$$C_E = \frac{t_D}{t_C} \times 100\ [\%] \qquad \ldots (S4)$$

where t_D and t_C are the discharge and charge time (s), respectively.

4.1.2. Concluding remarks

In summary, additives (binder and condutive enhancement) free TRGO/NF electrode was successfully prepared using a low temperature one step AP-CVD at 200 ℃ for an hour. The SEM showed the adhesion of graphene sheets on the surface of NF. Absence of conductive enhancement and binder allowed the determination of the real electrochemical performance. The presence of oxygen content significantly increased electrochemical performance of the positive TRGO electrode. This is because the CV and GCD of the TRGO electrode prepared at higher reducing temperature had a small capacitance and specific energy in comparison to that prepared at 200℃, also illustrated by Zhoa *et al*. [8]. The two electrodes (device) showed a high specific capacitance of 78.78 F g^{-1} at 1 A g^{-1} with the corresponding specific energy and power of 18.73 W h kg^{-1} and 547.52 W kg^{-1}, respectively. The specific energy and power at 5 A g^{-1} was estimated to be 14.10 W h kg^{-1} and 2.5 kW kg^{-1}, respectively. The maximum power from the device was estimated to be 306.25 kW kg^{-1}. The EIS showed that the device is highly capacitive due to lack of a semi-circle and high impendence phase angle of – 86 °

4.2. Microsupercapacitor

The preparation and fabrication method of conventional SCs are not compatible with the fabrication requirement of µ-SC devices. As discussed in Chapter 2, the µ-SCs require new fabrication techniques which can be classified as masked and mask-free techniques. Some masked techniques such as photolithography use a photoresist material that is very expensive and has a tendency of contaminating the patterned material upon removal [2,17–19]. However, the mask-free techniques are better, since they do not require any photoresist and also do not require large amounts of precursor material just to pattern a few µ-SC devices like electrodeposition and electrochemical polymerization methods [20–22]. Here are the examples of mask-free techniques: Inkjet printing, extrusion printing and stage driven patterning techniques such as micro-plasma-jet, AxiDraw and laser reducing [2,23–26]. All these printing and patterning techniques are computer controlled. In general, the stage driven techniques are relatively quick and cost effective. Liu *et al*. [2] used ambient micro-plasma-jet etching to pattern µ-SC on multi-walled carbon nanotubes (MWNTs) on a Polyethylene terephthalate (PET) substrate. A solid-state polyvinyl alcohol-H_3PO_4 gel electrolyte was used and a stack capacitance of 2.02 F cm^{-3} was obtained at a scan rate of 10 mV s^{-1}. In this part of the study, AxiDraw was used similar to Ref [23,24] that reported patterning of MXene-based material for µ-SC application. Among the stage driven patterning techniques, AxiDraw coupled with a sharp pen blade is the most cost effective patterning approach when comparing to the accessories required for laser and plasma jet equipment.

A deep electrochemical analysis was done using several approaches such as power law and Trasatti's analysis which estimated the contribution of the diffusion and surface controlled behaviour. These were attributed to the impact of oxygen content present within the TRGO µ-SC electrodes. Note that the ion diffusion coefficients of the TRGO µ-SCs estimated and attributed to the amount of OFGs (from FTIR) and large interplanar distance (from XRD) allowing passage of ions into the inner bulk material. Thus, higher specific power was achieved.

4.2.1. Results and discussions

4.2.1.1. Part I

The results obtained from the study of thermally reduced graphene oxide microsupercapacitor fabricated via Mask-free AxiDraw Direct Writing are described in the publication and supplementary information below:

nanomaterials

MDPI

Article

Novel Thermally Reduced Graphene Oxide Microsupercapacitor Fabricated via Mask—Free AxiDraw Direct Writing

Vusani M. Maphiri [1], Gift Rutavi [1], Ndeye F. Sylla [1], Saheed A. Adewinbi [2], Oladepo Fasakin [1] and Ncholu Manyala [1,*]

[1] Department of Physics, Institute of Applied Materials, SARChI Chair in Carbon Technology and Materials, University of Pretoria, Pretoria 0028, South Africa; vusanimuswamaphiri@gmail.com (V.M.M.); rutavi-gift@yahoo.com (G.R.); ntoufasylla@gmail.com (N.F.S.); fasakinoladepo@gmail.com (O.F.)

[2] Department of Physics, Osun State University, Osogbo, Osun State 210001, Nigeria; adeksa-heed007@gmail.com

* Correspondence: ncholu.manyala@up.ac.za; Tel.: +27-12-420-3549; Fax: +27-12-420-2516

Abstract: We demonstrate a simple method to fabricate all solid state, thermally reduced Graphene Oxide (TRGO) microsupercapacitors (μ-SCs) prepared using the atmospheric pressure chemical vapor deposition (APCVD) and a mask-free axiDraw sketching apparatus. The Fourier transform infrared spectroscopy (FTIR) shows the extermination of oxygen functional groups as the reducing temperature (RT) increases, while the Raman shows the presence of the defect and graphitic peaks. The electrochemical performance of the μ-SCs showed cyclic voltammetry (CV) potential window of 0–0.8 V at various scan rates of 5–1000 mVs^{-1} with a rectangular shape, depicting characteristics of electric double layer capacitor (EDLC) behavior. The μ-SC with 14 cm^{-2} (number of digits per unit area) showed a 46% increment in capacitance from that of 6 cm^{-2}, which is also higher than the μ-SCs with 22 and 26 cm^{-2}. The TRGO-500 exhibits volumetric energy and power density of 14.61 mW h cm^{-3} and 142.67 mW cm^{-3}, respectively. The electrochemical impedance spectroscopy (EIS) showed the decrease in the equivalent series resistance (ESR) as a function of RT due to reduction of the resistive functional groups present in the sample. Bode plot showed a phase angel of –85° for the TRGO-500 μ-SC device. The electrochemical performance of the μ-SC devices can be tuned by varying the RT, number of digits per unity area, and connection configuration (parallel or series).

Keywords: microsupercapacitor; direct writing; energy storage; Graphene oxide; thermally reduced

Citation: Maphiri, V.M.; Rutavi, G.; Sylla, N.F.; Adewinbi, S.A.; Fasakin, O.; Manyala, N. Novel Thermally Reduced Graphene Oxide Microsupercapacitor Fabricated via Mask—Free AxiDraw Direct Writing. *Nanomaterials* **2021**, *11*, 1909. https://doi.org/10.3390/nano11081909

Academic Editor: Fabrizio Pirri

Received: 7 July 2021
Accepted: 21 July 2021
Published: 25 July 2021

1. Introduction

Carbon is a naturally abundant element, which is also very interesting due to its ability to self-bind in different ways giving rise to various carbon structural allotropes such as graphene, carbon nanotubes, diamond, and fullerenes [1–4]. Some of the allotropes have attracted great attention due to their nanoscale, surface area, shape, and peculiar dimensions. Graphene is a two-dimensional single layer of carbon atoms with astonishing electrical, thermal, and mechanical properties. This is because atoms are bonded through sp^2 hybridization, giving rise to the three in-plane σ bonds reposible for flexibility and strength. The weak, out-of-plane π bond is responsible for electrical and thermal properties [5,6]. The presence of these bondings makes graphene one of the best materials suitable for microsupercapacitor (μ-SC) application [6,7]. However, the abovementioned properties are only observed in defect-free graphene, which is difficult and expensive to mass produce. Alternatively, there are cheaper and more simple ways to mass produce a slightly defective graphene, such as atmospheric pressure chemical vapor deposition (APCVD) [8,9]. The chemical phase exfoliation via the Hummer's method of graphite oxide

has been widely used, but this method produces a highly oxidized version of graphene [5,10–18].

Several techniques have been used to reduce oxygen on GO, such as the use of chemicals, UV radiation, and electrochemical and thermal methods [6,11,18,19]. Thermal reduction of graphene oxide is a quick, cheap, safe, and relatively easy method and has never been reported on the fabrication of μ-SC in this manner. On the contrary, thermal reduction has been reported for supercapacitor application by Zhao et al. [13] where the reducing temperature (RT) was varied from 200 to 900 °C in a nitrogen environment for two hours. The Fourier transform infrared spectroscopy (FTIR) showed the decrease in notches attributed to the various oxygen related vibrations as a function of the RT. This behavior was attributed to the removal of oxygen functional groups and the intercalated H_2O. The highest capacitance of 260.5 F g^{-1} at 0.4 A g^{-1} was obtained at the RT of 200 °C, and 11.7% (30.6 Fg^{-1} at 0.4 Ag^{-1}) of the initial capacitance was retained at a RT of 900 °C. This decrease was also attributed to the removal of the oxygen functional groups which served as an ion passage to the internal surface. Like supercapacitors, μ-SC are new μ-energy-storage units with similar energy storage mechanisms but are smaller in size. This expands the already huge potential applications of supercapacitors into the realm of small and high power density devices, with practical applications in medical implants, wearable technology, and many more [20–22]. These devices outperform other μ-energy-storage devices like micro-batteries because of ultra-fast charge and discharge rates, long cycling lifetime, cost efficiency, and operational safety and efficiency [2].

μ-SCs have been fabricated and patterned via several techniques classified as masked and mask-free techniques. The masked techniques use a photoresist such as Poly (methyl methacrylate) (PMMA) which can be removed by acetone, but these possess a problem of photoresistant impurities on the active material. However, mask-free is a better alternative since it does not require any photoresist. There are several mask-free techniques such as micro-plasma-jet, axiDraw, and laser reducing [2,23–26]. These methods are integrated into a computer driven stage control which is very different to the masked technique. Liu et al. [2] used mask-free ambient micro-plasma-jet etching to pattern μ-SC on a multi-walled carbon nanotube (MWNT) on a Polyethylene terephthalate (PET) substrate. A solid-state polyvinyl alcohol-H_3PO_4 gel electrolyte was used and a stack capacitance of 2.02 F cm^{-3} was obtained at a scan rate of 10 mV s^{-1}. Park et al. [26] reported a laser-patterned stretchable μ-SC for soft electronic circuit components using Polydimethysiloxane as a substrate. The reduced graphene oxide/gold composite active material showed a higher volumetric energy density of 290 μWh cm^{-3}. In this study, we used the axiDraw, similar to Ref [23,24] who reported the pattern MXene-based material for μ-SC application. This is because axiDraw does not involve expensive patterning accessories such as laser and plasma jet equipment. The axiDraw was equipped with an inexpensive sharp blade pen that requires sharpening and can have a long lifespan compared to the laser and helium and oxygen cylinder for the plasma jet.

This work demonstrates a novel μ-SC fabricating method, where GO films are thermally reduced directly on the microscopic glass (MSG) substrate followed by a patterning via a mask-free axiDraw apparatus. In comparison with other μ-SC preparation techniques [24,25], thermal reduction combined with axiDraw direct writing is a relatively quick, easily scalable, and safe method for production of μ-SCs. Mao et al. [25] reported an all-solid-state flexible microsupercapacitors (μ-SCs) based on reduced graphene oxide/multi-walled carbon nanotube (MWCNT) composite; the GO/MWCNT was sprayed on PET and dried for 24 h and followed by the laser reduction process for 30 min. The μ-SC showed a volumetric energy density of 6.47 mW h cm^{-3} and a cycling stability retention of 88.6% after 10,000 cycles. Li et al. [24] reported a MXene-conducting polymer electrochromic microsupercapacitor prepared by electrochemical deposition of poly(3,4-ethylenedioxthiophene) on $Ti_3C_2T_x$ MXene. The as prepared PEDOT/ $Ti_3C_2T_x$ was washed and dried for 6 h and showed an areal capacitance of 2.4 mF cm^{-2} at 100 nm thickness. These methods, reported in references [24,25], took more time as compared to the proposed

method which yielded a volumetric energy density of 14.61 mW cm^{-3} and volumetric power density of 142.67 mW h cm^{-3} for TRGO-500. This high RT yielded μ-SCs with rectangular cyclic voltammetry (CV) curves with high scan rate, isosceles triangle galvanostatic charge-discharge (GCD) curves, higher capacitance retention, low equivalent series resistance (ESR), high phase angle and diffusion length closer to the imaginary impendence axes.

1. Experimental

1.1. Materials

Chemicals used in this article were analytical grade and were used without any further purification. The used material and chemicals are as follows: Natural graphite, sulphuric acid (H_2SO_4 (98%)) (associated chemical enterprises, Johannesburg, GP, South Africa), ortho-phosphoric acid (H_3PO_4) (MERCK, Darmstadt, HE, Germany), microscopic glass (MSG) (B&C Glass Ltd, Haverhill, CB9, United Kingdom), potassium permanganate ($KMnO_4$) (associated chemical enterprises, Johannesburg, GP, South Africa), hydrogen peroxide (H_2O_2 (50%)) (associated chemical enterprises, Johannesburg, GP, South Africa), poly (Vinyl Alcohol) (PVA, Mw 89,000–98,000) (sigma-aldrich, Steinheim, NW, Germany), ethanol (C_2H_5OH) (associated chemical enterprises, Johannesburg, GP, South Africa)and deionized water (H_2O) (DW) (prepared using DRAWELL, laboratory water purification system) at 18.2 MΩ.

1.2. Preparation of GO

GO was prepared using the modified Hummer's method [10]. Graphite powder was slowly added into a cooled H_2SO_4 and stirred until it reached homogeneity. $KMnO_4$ was then added into the cooled homogeneous solution. The solution was stirred for 180 min at a constant temperature of 50 °C and then left to cool to room temperature. Then 100 mL of H_2O was added followed by 20 mL of H_2O_2 to stop the reaction by reducing the remaining $KMnO_4$ into a water-soluble Manganese sulphate ($MnSO_4$), as described by Equation (1) below:

$$2KMnO_4 + 3H_2SO_4 + 5H_2O_2 = 2MnSO_4 + K_2SO_4 + 8H_2O + 5O_2 \quad (1)$$

The GO was cleaned by adding DW into the GO solution and letting it settle, then decanting the DW. This process was repeated several times to ensure that GO was free of impurities. The GO mixture was then centrifuged at 5000 rpm for 5 min. Obtained GO subsequently dried in an oven at 60 °C and was stored for μ-SC fabrication and characterization.

1.3. Preparation of Microscopic Glass (MSG)

The MSG was cleaned with acetonitrile soap to remove any greasy substances, then rinsed with DW. The MSG was then ultrasonicated for 30 min in a piranha solution with a ratio of 1:4 of H_2SO_4 to H_2O_2. The MSG was then rinsed with DW and blown dry using N_2 gas.

1.4. Preparation of TRGO Film and μ-SC Assembly

In total, 5 mg of dried GO was added into 1 mL of ethanol and the mixture was sonicated for 30 min. The GO/ethanol solution was loaded into the spay gun (MASTER AIRBRUSH, Model G233, San Diego, CA, USA) and spray coated onto MSG. The GO film on the microscopic glass was thermally reduced using atmospheric pressure chemical vapour deposition (APCVD) at various temperatures from 100–500 °C for 10 min at a heating rate of 10 °C min^{-1} in the presence of argon (Ar = 200 sccm) and hydrogen (H_2 = 20 sccm). The samples were labelled as TRGO-100, TRGO-200, TRGO-300 TRGO-400, and TRGO-500; and the numerical value at the end of "TRGO-" signifies the RT. At temperatures higher than 500 °C the MSG melted/deformed, and the material also peeled off the surface of the MSG. axiDraw (Model V3, Evil Mad Science LLC, Sunnyvale, CA, USA) controlled via

Inkscape (0.92.4, Boston, Massachusetts, USA) using the extension axiDraw Control version 2.5.3 was used as an X-Y stage controller for the μ-SC pattern. A sharp blade pen attached to the axiDraw was used to write μ-SC patterns on the thermally reduced graphene oxide (TRGO) film. This process is schematically depicted in Figure 1. The unwanted TRGO was scraped off the MSG. Copper strips were placed on to the edges of the μ-SC and adhered using a kapton tape. The digital images of the spray gun, GO thin film on microscopic glass, axiDraw, sharp blade pen, and TRGO film patterned μ-SC with 6, 14, 22, and 26 digits on microscopic glass are displayed in the Supplementary Information (Figure S1).

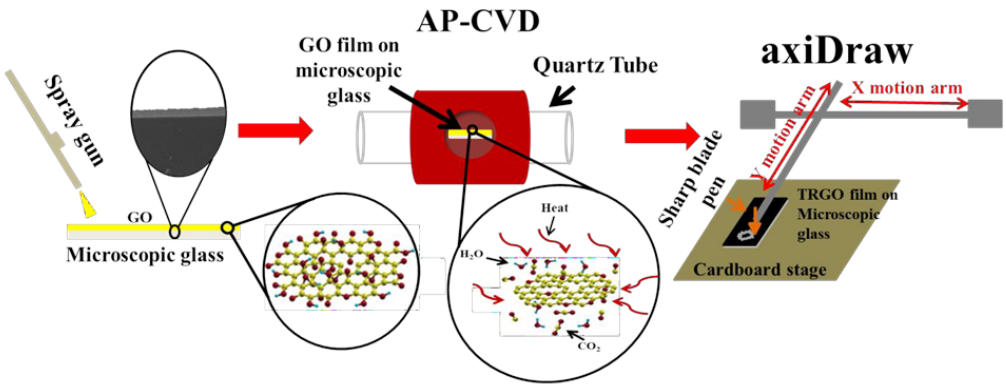

Figure 1. Schematic showing the TRGO μ-SC fabrication process. Spray coating prepared GO film on the MSG, thermally reducing GO film into TRGO film. Direct writing interdigitated patterns on TRGO film was completed using axiDraw for μ-SC electrodes.

1.1. Preparation of PVA-H_3PO_4 Gel Electrolyte

Proton conducting polymeric electrolyte (PVA-H_3PO_4) was prepared by adding 1 g PVA powder into 10 mL DW. This mixture was heated at 90 °C under constant stirring until the solution turned from milky white into a clear viscous solution. The prepared PVA was placed in an oven at 60 °C to remove excess water; 30% (in volume) of H_3PO_4 was then added into the PVA gel and stirred for 30 min. The gel electrolyte was then drop-casted onto the μ-SC digits.

1.2. Compositional, Morphological, and Structural Characterization

The TRGO samples, together with precursor graphite, intermitted with GO and MSG substrate were analyzed using the following techniques: Fourier transformation infrared (FT-IR) spectroscopy was performed using the Bruker Alpha platinum-ATR (Billerica, MA, USA) (attenuated total reflection) in the range of 4000 to 400 cm^{-1} to effectively study the functional groups. Confocal WITec alpha (Ulm, BW, Germany) 300RAS+ Raman microscopy was used to investigate the graphitic structure with 532 nm excitation laser at room temperature. The laser power was set to lesser than 2 mW to avoid heating the sample. The surface morphology of graphite and the GO and TRGO films were analyzed using a Zeiss Ultra-plus 55 field emission scanning electron microscopy (FE-SEM) (Akishima-shi, ABA, Japan) at 2 kV for high resolution.

1.3. Electrochemical Characterization

The electrochemical analysis (cyclic voltammetry (CV), galvanostatic charge-discharge (GCD), and stability) and electrochemical impendence spectroscopy (EIS) were measured at room temperature using the Bio-Logic VMP-300 potentiostat (Knoxville, TN,

USA), controlled using the EC-Lab software (V10.37, Edmonton, AB, Canada). The measurements were performed in a two-electrode configuration (or device).

1. Results and Discussion

1.1. Vibrational Spectroscopy

The ATR-FTIR was deployed to analyze the functional groups of the prepared sample, and the obtained spectra are displayed in Figure 2a. The spectrum of graphite show the absence of any absorption bands indicating chemical inertness [12]. Upon the oxidation of graphite, the spectrum of the sprayed GO on MSG showed several absorption bands attributed to various O-functional groups. The broad band at 3314 cm^{-1} was ascribed to the stretching vibration of O-H, indicating the presence of hydroxyl (-OH) and/or carboxylic (-COOH) functional groups within the GO structure. Less intense stretching vibration of the carbonyl (C=O) and unoxidized graphitic corresponding to the (C=C) were attributed to the 1734 and 1633 cm^{-1} notches, respectively. The oxygen singly bonded to the stretching vibration of O-H deformation; C-O of the epoxy group and C-O of the alkoxy group were attributed to the 1407, 1220, and 1047 cm^{-1}, respectively. Similar, FTIR spectra of GO was reported in Refs. [12–14]. As the GO thin film was subjected to a thermally RT of 100 °C, some O-containing groups were removed as part of the H_2O and CO_2 gases. This can be seen by the peak intensity decrease of the 3341, 1734, and 1407 cm^{-1} attributed to either O-H or C=O stretching vibration. The peak at 878 cm^{-1} can be attributed to the Si-O from the MSG substrate [27,28]. Above the thermal RT of 100 °C, the spectra are slightly like that of graphite, showing a low degree of oxygen function groups. Similar results were reported by Zhao et al. [13] when varying the thermal RT of powder GO: the FTIR showed the removal of O-containing functional groups as temperature increased.

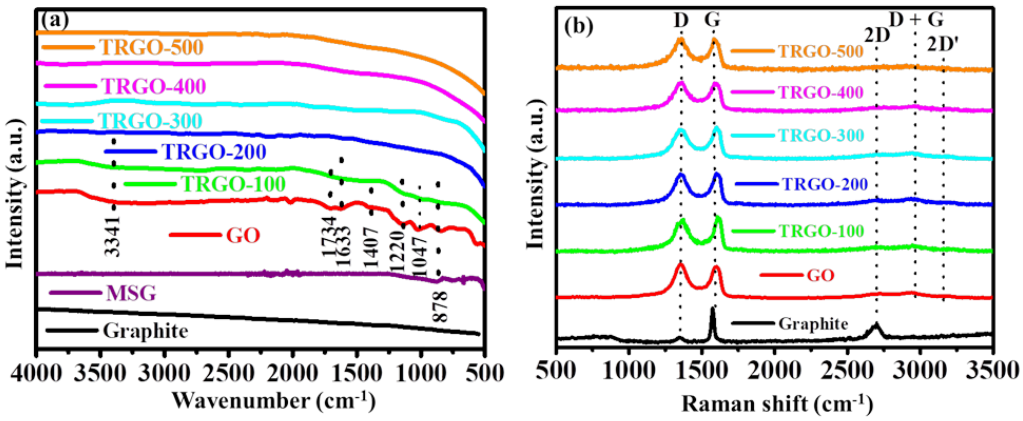

Figure 2. (**a**) ATR-FTIR and (**b**) Raman spectra for graphite, MSG, GO, and TRGO-100 to TRGO-500.

Raman spectra of the prepared sample are displayed in Figure 2b. In general, the obtained spectra showed the presences of D, G, 2D, D + G, and 2D' occurring at around 1363, 1604, 2714, 2936, and 3197 cm^{-1}, respectively. The graphite only exhibited the D, G, and 2D peaks. The D peak is due to breathing mode of k-point phonons of A_{1g} symmetry (associated with the local defects and disorder of the edges of graphene and graphite materials). The G peak is due to the first-order scattering of E_{2g} phonon of sp^2 C atoms (associated with the high-order hexagonal structure within graphite). The 2D is an overtone of the D peaks which is a fingerprint of the graphene sheet formation and number of layers [12–14,17,29]. Upon oxidation of the graphite, the Raman spectra of GO showed significant differences which include the broadening of phonon range peaks and the emergence of two overtone peaks (D + G and 2D′). The broadening of the D peak from the full width

at half maximum (FWHM) of 34.9 to 117.1 cm^{-1} is due to the attachment of the O-containing functional groups on the graphitic sheets in the oxidation reaction process [30]. The FWHM of the G peak increasing from 20.1 to 66.9 cm^{-1} is also due to the bond angle disorder caused by the attachment of the O-containing functional groups. This causes the average ideal graphite-like hexagonal 120° bond angle to change. The FWHM of the D and G peak seems not to decrease regardless of the increase in temperature. This was also observed by Claramunt et al. [31] when thermally reducing GO in the range of 100 to 900 °C. The only noticeable difference is the fading of the overtone peaks which suggests that the layers are increasing (or restacking), since they only dominate in graphitic materials containing few layers of graphene sheets. Thus, the stacking increases as temperature increases, leading to low 2D intensity. This is also confirmed by the FTIR spectra showing the decrease of oxygen functional groups present on the graphene sheets causing them to restack into graphite-like material.

1.1. Scanning Electron Microscopy

The SEM micrographs of the graphite, GO, TRGO, and µ-SC (interspace distance and digit width) are displayed in Figure 3. The micrograph in Figure 3a shows particles of graphite with random particles sizes which are flat or disc in nature and are highly stacked together. This morphology has been previously reported by Dai et al. [32] and Montagna et. al. [33]. The morphology in Figure 3b–d depicts a flat sheet stacked together [18]. In Figure 3b, the GO sheets are lousily stacked compared to TRGO-100 (Figure 3c) and TRGO-500 (Figure 3d). The insets on Figure 3b–d show that the GO and TRGO sheets are wrinkled. The SEM micrographs of µ-SC interspace *i* and digit width *W* are displayed in Figure 3e,f, respectively. The interspace of all the prepared µ-SC is ~38µm, which is due to the dimension of the pattering apparatus (sharp blade pen) which has a sharp tip (see Figure S1d). The 1.6 mm digit width corresponds to the digit width of the µ-SC (6). The µ-SC dimensions of all fabricated µ-SC are given in Table S1.

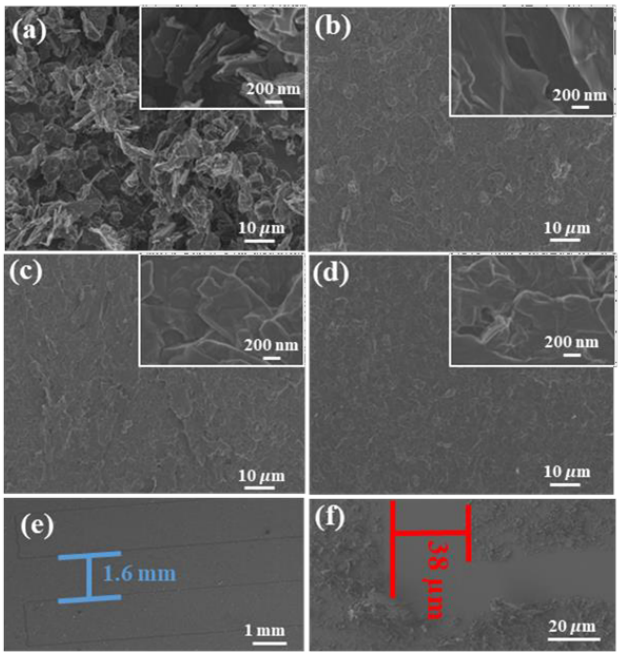

Figure 3. SEM micrograph of (**a**) graphite, (**b**) GO, (**c**) TRGO-100, and (**d**) TRGO-500 with high magnification micrograph displayed as insets to the figures, including the (**e**) digit width and (**f**) interspace distance of μ-SC (6).

1.1. Electrochemical Results

The digital photography image of the fabricated μ-SC is displayed in Figure 4. The μ-SC is composed of only five components (also mentioned in Section 2.4, the preparation of TRGO films and μ-SC assembly): MSG as a substrate, TRGO as an active material and a current collector because of its conductivity; copper foils as positive and negative terminals; and kapton tape which adheres the copper foil onto the current collector (edge (E) of the μ-SC). The inkscape schematics of the μ-SCs are displayed in Figure S2, showing various numbers of digits per unit area (n) of 6, 14, 22, and 26; and other parameter such as breadth (B), length (L) and width (W) of the μ-SC, respectively. The digital photograph of those μ-SC patterns on TRGO are displayed in Figure 5a. To determine the number of digits per unit area giving the best electrochemical performance, electrochemical studies were performed on the TRGO-300. The CV and GCD curves of the TRGO-300 μ-SC are displayed in Figure 5b,c, respectively. Note that the number within the parenthesis at the end of "μ-SC" denotes the number of digits per unit area (cm^{-2}). The CV curves depict a rectangular shape indicating the electric double-layer capacitor behavior, while the GCD curves show a triangular shape further confirming the EDLC nature of the material. The CV and GCD curves suggest that the μ-SC (14) has the better charge carrying ability because it shows higher current response and longer discharge time than others. The areal capacitance (C_{Areal}) displayed in Figure 5d of the TRGO-300 μ-SC was estimated from the CV curves using Equation (2) below [2,24]:

$$C_{Areal} = \frac{\int_{V_i}^{V_f} i dV}{2S(V_f - V_i)A} \quad (2)$$

where V_i and V_f are the initial and final values of the working potential, respectively. i, S, and A are the current, scan rate (20 mVs^{-1}), and total surface area of the μ-SC, which is including the inter-digit space between the adjacent digits. The surface area of all the μ-SC is 1 cm^2 (see Table S1, Figure S2). The areal capacitance versus the number of digits per unit area is illustrated in Figure 5d which shows that the best areal capacitance occurred at 14 cm^{-2}. The increase of the areal capacitance up to 14 cm^{-2} can be attributed to the reduction of the average ionic diffusion pathway between adjacent digits [2,34]. This was shown by Liu et al. [2] where the μ-SC with 12 digits had more capacitance than those with four and eight digits. This increase can be also explained by the distributed capacitance effect in Ref. [20] which suggests that higher digits lead to higher electrochemical performance. From previous studies, it seems that more digits per unit area results in a better electrochemical performance, which includes more power and energy. This seems to be true for a certain range of digits per unit area due to external factors such as the removal of active electrode mass which increases as the number of digits increase [35] (see Table S1,Figure S2) and the electric field strength which increases as the number of digits increases due to the edging effect [21]. The areal capacitance of the TRGO-300 determined from the total surface area (area of the entire μ-SC including the interspace) and effective area (excluding the interspace) is displayed in Figure S3. The effective area and total interspace area were calculated using the derived Equations (S1) and (S2), respectively. It is clear that the removed material while pattering accounts only for a small fraction of the loss of capacitance [20,21]. Thus, the increase and decrease of capacitance can be attributed to the increase of the electric field strength around the edges of the interdigitated electrode. It is well known that the electric field line strength increases for edge intensive electrodes rather than a continuous or round shape electrode [36]. This was illustrated by Hota et al. [21] in a simulation comparing the electric field generated between the interdigitated and fractal electrode. The Moore fractal electrode design showed a 32% increase in energy density over the conversational interdigitated electrode. This is because the Moore fractal

is more edge intensive than the interdigitated electrode design. This behavior suggests that increasing the number of digits per unit area subsequently increases the number of edges leading to a high electric field distributed along the edges within the μ-SC. In this work, the areal capacitance of the 14 cm^{-2} increased by 46% over the capacitance of 6 cm^{-2}. Moreover, a very strong electric field concentrated within the same region (between the end and edge of the μ-SC, Figure S2) separated by a narrow interspace (38 μm, Figure 3f) leading to charge flow leakage (short circuit) between electrolyte and electrode led to a decrease in capacitance [21,37]. Thus, 14 cm^{-2} is the optimum electrode design due to an adequate ratio of interdigitated electrodes per unit area and electrode width interspace ratio [37–39] that maximizes the electric field strength while avoiding electric charge leakage and manages to reduce the ionic diffusion pathway.

Figure 4. Digital photograph of TRGO μ-SC device.

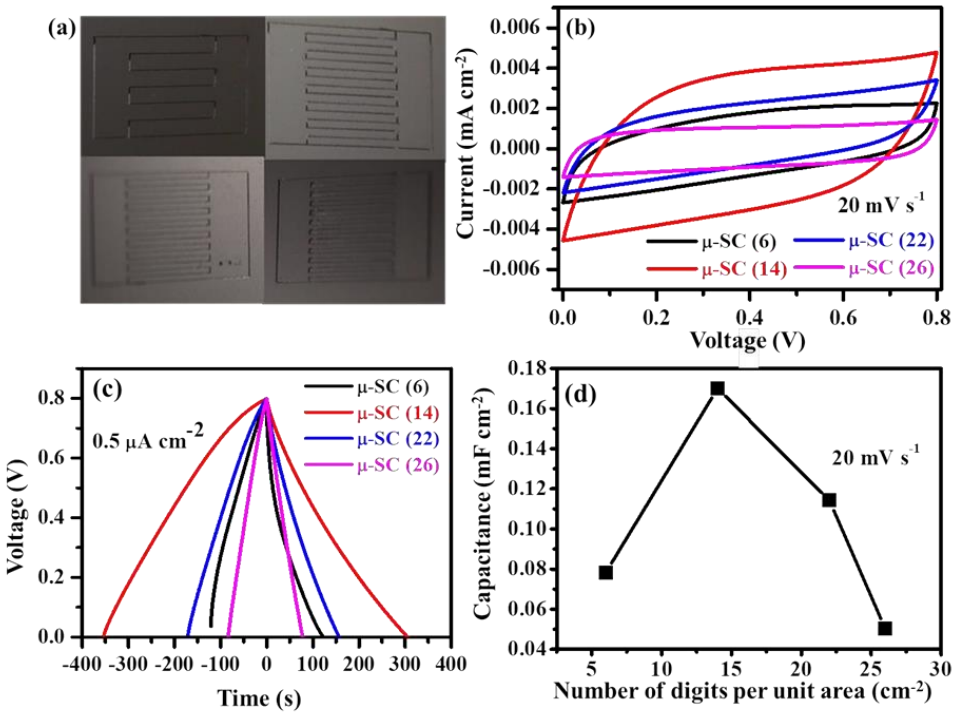

Figure 5. (**a**) Digital photographs; (**b**) CV curve at 20 mVs^{-1}; (**c**) GCD curve at 0.5 μA cm^{-2} of TRGO μ-SC patterns with 6, 14, 22, and 26 cm^{-2}; and (**d**) areal capacitances versus number of digits per unit area of the TRGO-300.

Since 14 cm^{-2} μ-SC configurations gave the best electrochemical results as compared to the other digit configurations, it was used throughout the entire study to analyze the effect of thermal reduction on the μ-SC electrochemical performance. The CV curve measurements at 20 mV s^{-1} of the μ-SCs at different RTs are displayed in Figure 6a. Note that the CV of TRGO-100 was not measured due to its high oxygen functional groups (see the FTIR in Figure 2a) present within the sample. All the CV curves at various RTs were measured in the voltage window ranging from 0 to 0.8 V. Figure 6a shows that the response in current density (mA cm^{-2}) decreases as the RT increases due to the decrease of the oxygen functional groups on the surface of the graphene sheet. This is because these functional groups play a very important role as they serve as a passage for the ions into the internal surface [13] and also provide wettability between the electrolyte and active material [40]. Figure 6b shows the areal capacitance (displayed in Table S2) at various scan rates at different temperatures. The TRGO-200 μ-SC has a higher areal capacitance of 0.5421 mF cm^{-2} at 10 mV s^{-1} and retains 27% (0.1498 mF cm^{-2}) at a scan rate of 80 mV s^{-1}. TRGO-300 μ-SC has an initial areal capacitance of 0.1227 mF cm^{-2} at 10 mVs^{-1} while retaining 41% (0.0506 mF cm^{-2}) at 200 mV s^{-1}, and TRGO-400 and TRGO-500 have areal capacitances of 0.0382 and 0.0298 mF cm^{-2} at 10 mV s^{-1} while retaining 36% (0.0140 mF cm^{-2}) and 53% (0.0159 mF cm^{-2}) at 1 V s^{-1}, respectively. Despite the low areal capacitance, TRGO-500 has a better retention and shape.

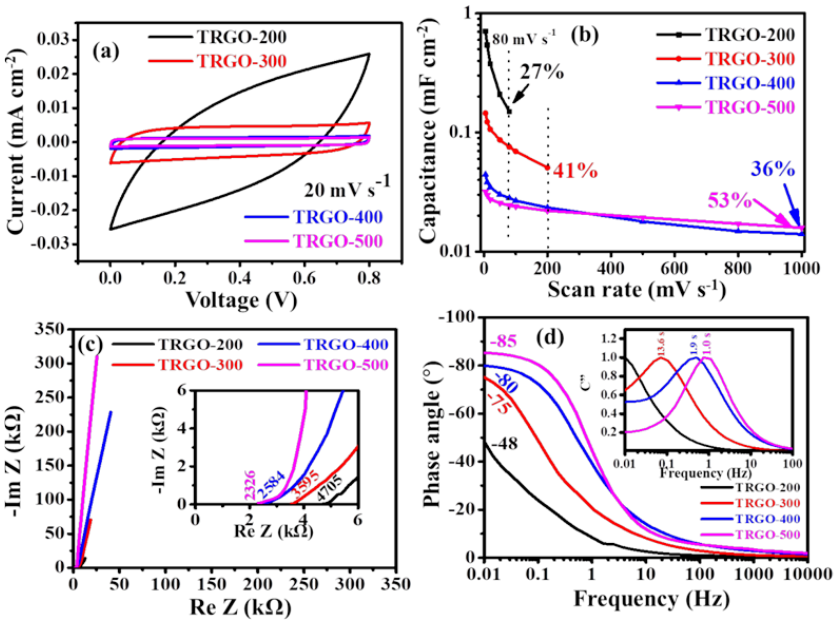

Figure 6. (**a**) CV curves at a scan rate of 20 mVs^{-1}, (**b**) areal capacitance at various scan rates, (**c**) nyquist plot with the inset showing a magnified view of the high-frequency region and (**d**) phase angle as a function of frequency (inset: normalized imaginary capacitance (C″) as a function of frequency calculated from the EIS) for μ-SC (14) at different RT.

The Nyquist plots, showing imaginary (ImZ) and real (ReZ) impedances at various frequencies of different RTs, are displayed in Figure 6c, with an inset showing a zoomed view of the high-frequency region. This behavior of the EIS (Nyquist plot) was suggestedby Mathis et al. [41] as an ideal SC behavior [42], when a 45° line starting from the equiv- alent series resistance (ESR) quickly transcends into a vertical line that is parallel or closeto parallel to the ImZ axis at the low-frequency region. This also means that the reactive

sites leading to a capacitor-like behavior are fully accessible in a short time. The absence of a semi-circle at the high-frequency region shows the absence of the charge transfer. The μ-SCs have equivalent series (or solution) resistances (ESR) of 4705, 3595, 2584, and 2326 Ω for TRGO-200, TRGO-300, TRGO-400, and TRGO-500, respectively. The ESR as a function of RT is displayed in Figure S3b, and it can be seen that the ESR reduces as RT increases, suggesting that oxygen has a great influence on the ESR. The TRGO-500 shows a vertical line in the low-frequency region which is more closer to the Im Z (Y-axis) axis indicating a better capacitive behavior evident that all the reactive sites are fully accessible in a short time [41,43] due to the increase of higher carbon content (see Figure 2a). This is verified by the phase angle (as a function of frequency) shown in the bode plot in Figure 6d. The phase angle in the low-frequency region shows an increase from −48 to −85° as the RT increases from 200 to 500 °C. At 500 °C, the obtained phase angle is very close to the ideal value of −90 which suggests an ideal capacitive behavior [41,42]. This was also seen on the normalized CV curves displayed in Figure 6b where the TRGO-500 μ-SC has the better rectangular shape than those at low RTs. The normalized capacitance C″ versus frequency is illustrated in the insert. The relaxation time (τ_0) which is the transition point of the electrochemical capacitor from capacitive to resistive behavior—which also corresponds to the point of maximum energy dissipation—shows a decrease as the RT increases. The estimated relaxation time constant τ_0 (reciprocal of the frequency f_0) for TRGO-300, TRGO-400, and TRGO-500 was approximately 13.6, 1.9, and 1.0 s, respectively. The TRGO-500 has a smallest relaxation time, confirming that indeed all the reactive sites are fully accessible within a short period of time.

The CV curve of the TRGO-500 at various scan rates is displayed in Figure 7a, while those of low temperature are displayed in Figure S4. The TRGO-500 μ-SC has a high sweeping scan rate tolerance over those μ-SC prepared at low temperatures. The rectangular shape is still maintained at a higher scan rate of 1 Vs^{-1} showing a better capacitive device. The GCD curves of TRGO-500 at different areal current are displayed in Figure 7b and those of low temperature are displayed in Figure S5. All the GCD curves show a triangular shape, signifying the EDLC behavior of the μ-SC devices. The areal capacitances from the GCD curve were estimated using Equation (S3) and are given in Table S3. The decrease of the capacitance can still be attributed to the removal of the oxygen functional groups. Figures 7b,S5 also show that high reduced temperature μ-SC (300 to 500 °C) has a wide current density range and can be charged and discharged by small current density and still manage to maintain a triangular shape, similar to the CV curves in Figures 7a,S4. The areal and volumetric capacitances calculated from Equation (S3) are displayed in Figure 7c,d, respectively. Maximum areal and volumetric capacitances of 0.0387 mF cm^{-2} and 14.8981 mF cm^{-3} were observed for the TRGO-500 μ-SC and the thickness was calculated from the SEM image displayed in Figure S6a. Both areal and volumetric capacitance decreased with increasing current density, having a rate capability of 87.2% at 1.66 μA cm^{-2}.

The areal/volumetric energy ($E_{density}$) and power ($P_{density}$) densities calculated from the Equations (3) and (4) below:

$$E_{density} = \frac{1}{3600\Gamma}\int iVdt \quad (3)$$

$$P_{density} = 3600 \times \frac{E_{density}}{\Delta t} \quad (4)$$

where Γ, $\int iVdt$, and Δt are the area or volume of the μ-SC, the integral of the discharge curve, and discharge time, respectively. The TRGO-500 μ-SC produced a volumetric energy density of 14.61 mW cm^{-3} and volumetric power density of 140.89 mW h cm^{-2} at 0.0083 μA cm^{-2} while producing volumetric energy density of 0.6449 mW cm^{-2} and volumetric power density of 142.67 mW h cm^{-2} at 1.66 μA cm^{-2}. The Ragone plot of the TRGO-500 is displayed in Figure 8a compared to similar devices in the literature. The TRGO-500 μ-SC has volumetric energy and power densities similar to those reported in Refs. [24,26,44], including lithium film batteries. This simple method produces a μ-SC device

with similar energy and power to those devices prepared via a complex and sophisticated method. Note that the Ragone comparing different RTs is displayed in Figure S6b. The TRGO-500 μ-SC displayed in Figure 8b shows a capacitance retention and columbic efficiency of 95% and 100%, respectively, at a current density of 0.83 μA cm^{-2} for 4000 cycles. The adaptability of the TRGO-500 μ-SC was demonstrated by fabricating two μ-SC devices together in parallel and in series. The digital photographs together with the inkscape schematic diagram of the two μ-SCs in parallel and series are displayed in Figure S7. The CV curves at 20 mV s^{-1} and GCD curves at 0.16 μA cm^{-2} are presented in Figure 8c,d, respectively. The voltage window for the single and parallel devices ranges from 0 to 0.8 V and that in series ranges from 0 to 1.6 V. The CV curves still show the rectangular shapes which imply fast ion diffusion. The GCD curve of the μ-SC in series has a 1.6 V charge/discharge at a similar time range as the single μ-SC, signifying good capacitive behavior at minimal internal resistance. In contrast, parallel μ-SC discharge time increased twice at the same current density as the single μ-SC. The areal energy density of the μ-SC connected in series is 0.0392 mW h cm^{-2} and parallel is 0.0402 mW h cm^{-2}, which is approximately twice that of a single (0.0191 mW h cm^{-2}) device. The areal power density of the μ-SC in series is 0.7650 mW cm^{-2}, which is approximately twice that of single (0.3762 mW cm^{-2}) and parallel connected devices (0.3825 mW cm^{-2}).

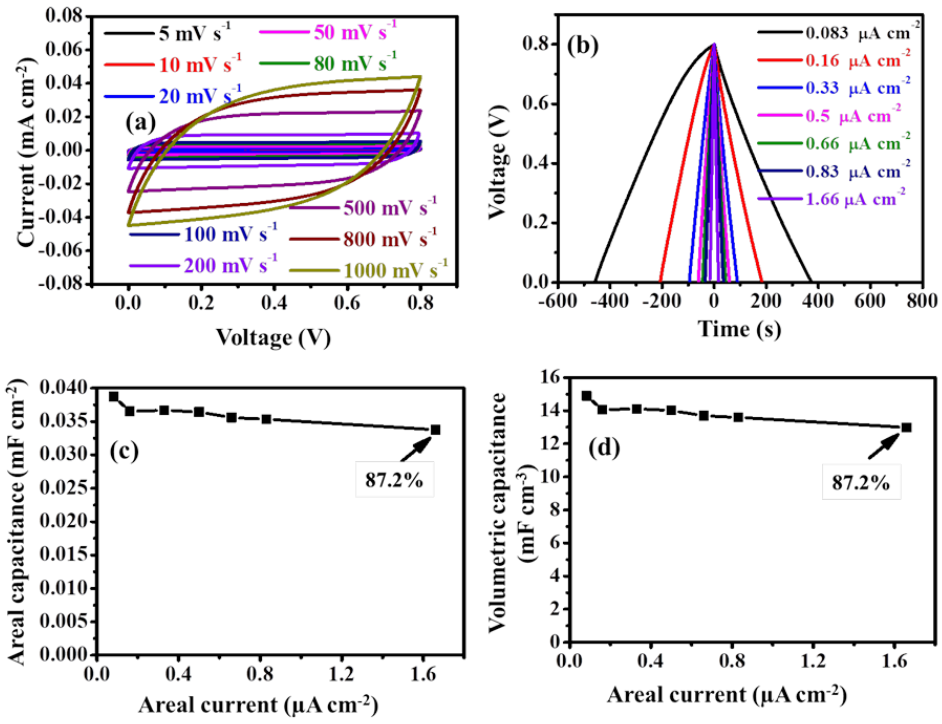

Figure 7. (**a**) CV curves at various scan rates, (**b**) GCD curves at various current density, (**c**) areal capacitance, and (**d**) volumetric capacitance as a function of current density for the TRGO-500 μ-SC (14).

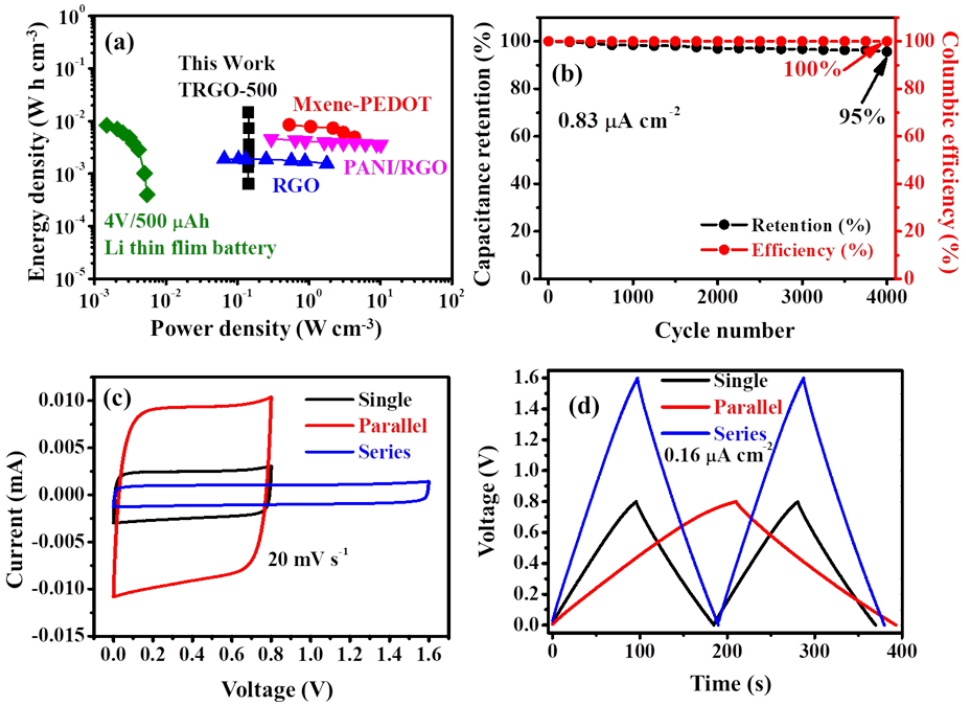

Figure 8. (**a**) Ragone plot of the TRGO-500 μ-SC compared to other similar devices and (**b**) capacitance retention and columbic efficiency of TRGO-500 versus cycling number at current density of 0.83 μA cm^{-2}. The TRGO-500 (**c**) CV and (**d**) GCD curves of a single μ-SC, two μ-SC connected in series and parallel at a scan rate of 20 mV s^{-1}, and a current density of 0.16 μA cm^{-2}, respectively.

4. Conclusions

In summary, we successfully demonstrated the possibility of fabricating thermally reduced μ-SC via the novel GO film reduction to TRGO film via AP-CVD combined witha musk-free direct writing via axiDraw. The FTIR showed a decrease in functional oxygen as the RT increased. Raman spectrum shows the fading of the overtone peaks due to re- stacking. The 14-digit cm^{-2} was found to show better electrochemical properties than those μ-SCs with 4-, 22-, and 26-digits cm^{-2}; this behavior is attributed to the increase of electricfield leading to an increase and decrease of capacitance. The TRGO-500 μ-SC showed to be the better performing device amongst μ-SCs reduced at low temperature, regardless of the small capacitance due to lack of oxygen functional groups that serve as pathways into the bulk material/wettability. The increase of thermally reducing temperature with μ-SC yielded a better EDLC behavior and rate capability due to the presence of low oxygen. The TRGO-500 μ-SC had the smallest relaxation time constant τ_0 of 1s, higher phase an- gle of −85°, diffusion length close to the imaginary impendence, higher CV scan rate and GCD current density range, and a CV rate capability of 56% at 1 V s^{-1}, indicating excep- tional capacitive properties. The ability to vary RT, the number of digits per unit area, and the integration of μ-SC in a series or parallel configuration gives the possibility of control- ling energy and power performance to meet different requirements of the miniaturized devices.

Supplementary Materials: The following are available online at www.mdpi.com/article/10.3390/nano11081909/s1, Figure S1: Optical image of (a) Spray gun, (b) GO thin film on microscopic glass (MSG), (c) axiDraw, (d) sharp blade pen and (e) TRGO patterned with μ-SC of various digits per unit area on microscopic glass, Figure S2: Inkscape blueprint schematic for the *n* (a) 6, (b) 14, (c) 22 and (d) 26 digits μ-SC, Table S1: Dimensions and parameters of μ – SC (6), (14), (22) and (26), Figure S3: (a) Areal capacitance of the total surface area versus effective area at 6, 14, 22 and 26 digits per unit area (cm^{-2}) and (b) ESR and phase angle as a function of reducing temperature, Figure S4: The CV curves at (a) TRGO-200, (b) TRGO-300, (c) TRGO-400 and (d) TRGO-500 at various scan rates, Table S2: The areal capacitance determined from the CV curve, Figure S5: The GCD curves of μ-SC at different current densities for (a) TRGO-200, (b) TRGO-300, (c) TRGO-300 and (d) TRGO-500, Table S3: The areal capacitance determined from the GCD curve, Figure S6: (a) SEM cross-sectional image of the TRGO-500 μ-SC and (b) Ragone plot of the TRGO-200, TRGO-300, TRGO-400 and TRGO-500 and Figure S7: Digital photography of μ-SC in (a) parallel and (c) series. Inkscape blueprint of μ-SC in (b) parallel and (d) series.

Author Contributions: V.M.M.: Conceptualization, methodology, software, formal analysis, investigation, visualization, writing – original daft, writing- review and editing. N.F.S.: methodology, visualization. G.R.: methodology, formal analysis, writing- review and editing. S.A.A.: visualization. O.F.: writing- review and editing. N.M.: resources, supervision, funding acquisition, writing-review and editing.

Funding: This study was supported by the National Research Foundation (NRF) of South Africa (Grant Number 61056) together with the South African Research Chairs Initiative (SARChI) of the Department of Science and Technology

Institutional Review Board Statement: Not applicable

Informed Consent Statement: Not applicable

Data Availability Statement: Data is contained within the article or supplementary material

Acknowledgments: V.M. Maphiri acknowledges NRF bursary through SARChI in Carbon Technology and Materials and University of Pretoria for financial support.

Conflicts of Interest: The authors declare no conflict of interest. The funders had no role in the design of the study; in the collection, analyses, or interpretation of data; in the writing of the manuscript, or in the decision to publish the results.

Reference

1. Chen, X.; Tian, F.; Persson, C.; Duan, W.; Chen, N.-X. Interlayer interactions in graphites. *Sci. Rep.* **2013**, doi:10.1038/srep03046.
2. Liu, L.; Ye, D.; Yu, Y.; Liu, L.; Wu, Y. Carbon-based flexible micro-supercapacitor fabrication via mask-free ambient micro-plasma-jet etching. *Carbon* **2017**, *111*, 121–127, doi:10.1016/j.carbon.2016.09.037.
3. Malard, L.M.; Pimenta, M.A.; Dresselhaus, G.; Dresselhaus, M.S. Raman spectroscopy in graphene. *Phys. Rep.* **2009**, *473*, 51–87, doi:10.1016/j.physrep.2009.02.003.
4. Ferrari, A.C. Raman spectroscopy of graphene and graphite: Disorder, electron-phonon coupling, doping and nonadiabatic effects. *Solid State Commun.* **2007**, *143*, 47–57, doi:10.1016/j.ssc.2007.03.052.
5. Jimenez-Cervantes, E.; López-Barroso, J.; Martínez-Hernández, A.L.; Velasco-Santos, C. Graphene-Based Materials Functionalization with Natural Polymeric Biomolecules. In *Recent Advances in Graphene Research*; InTech,London, UK, 2016.
6. De Lima, B.S.; Bernardi, M.I.B.; Mastelaro, V.R. Wavelength effect of ns-pulsed radiation on the reduction of graphene oxide. *Appl. Surf. Sci.* **2020**, *506*, doi:10.1016/j.apsusc.2019.144808.
7. Peng, X.; Peng, L.; Wu, C.; Xie, Y. Two dimensional nanomaterials for flexible supercapacitors. *Chem. Soc. Rev.* **2014**, *43*, 3303–3323, doi:10.1039/c3cs60407a.
8. Madito, M.J.; Matshoba, K.S.; Ochai-Ejeh, F.U.; Mongwaketsi, N.; Mtshali, C.B.; Fabiane, M.; Manyala, N. Nickel-copper graphene foam prepared by atmospheric pressure chemical vapour deposition for supercapacitor applications. *Surf. Coat. Technol.* **2020**, *383*, doi:10.1016/j.surfcoat.2019.125230.
9. Madito, M.J. AB-Stacked Bilayer Graphene Films Obtained on Dilute Cu (Ni) Foils using Atmospheric Pressure Chemical Vapour Deposition. by Philosophiæ Doctor (PhD). Ph.D. Thesis, University of Pretoria, Pretoria, South Africa, 2016.
10. Tarimo, D.J.; Oyedotun, K.O.; Mirghni, A.A.; Manyala, N. Sulphur-reduced graphene oxide composite with improved electrochemical performance for supercapacitor applications. *Int. J. Hydrog. Energy* **2020**, *45*, 13189–13201, doi:10.1016/j.ijhydene.2020.03.059.
11. Guo, J.; Mao, B.; Li, J.; Wang, X.; Yang, X. Rethinking the Reaction Pathways of Chemical Reduction of Graphene Oxide. *Carbon* **2021**, *171*, 963–967, doi:10.1016/j.carbon.2020.09.049.

12. Bera, M.; Chandravati; Gupta, P.; Maji, P.K. Facile One-Pot Synthesis of Graphene Oxide by Sonication Assisted Mechanochemical Approach and Its Surface Chemistry. *J. Nanosci. Nanotechnol.* **2017**, *18*, 902–912, doi:10.1166/jnn.2018.14306.
13. Zhao, B.; Liu, P.; Jiang, Y.; Pan, D.; Tao, H.; Song, J.; Fang, T.; Xu, W. Supercapacitor performances of thermally reducedgraphene oxide. *J. Power Sources* **2012**, *198*, 423–427, doi:10.1016/j.jpowsour.2011.09.074.
14. Muniyalakshmi, M.; Sethuraman, K.; Silambarasan, D. Synthesis and characterization of graphene oxide nanosheets. *Mater.Today Proc.* **2020**, *21*, 408–410, doi:10.1016/j.matpr.2019.06.375.
15. Ibrahim, A.F.M.; Lin, Y.S. Synthesis of graphene oxide membranes on polyester substrate by spray coating for gas separation. *Chem. Eng. Sci.* **2018**, *190*, 312–319, doi:10.1016/j.ces.2018.06.031.
16. Vivekanandan, A.K.; Subash, V.; Chen, S. ming; Chen, S.H. Sonochemical synthesis of nickel-manganous oxide nanocrumbs decorated partially reduced graphene oxide for efficient electrochemical reduction of metronidazole. *Ultrason. Sonochem.* **2020**,*68*, doi:10.1016/j.ultsonch.2020.105176.
17. Akhavan, O. The effect of heat treatment on formation of graphene thin films from graphene oxide nanosheets. *Carbon* **2010**, *48*,509–519, doi:10.1016/j.carbon.2009.09.069.
18. Brycht, M.; Leniart, A.; Zavašnik, J.; Nosal-Wiercińska, A.; Wasiński, K.; Półrolniczak, P.; Skrzypek, S.; Kalcher, K. Synthesis and characterization of the thermally reduced graphene oxide in argon atmosphere, and its application to construct graphene paste electrode as a naptalam electrochemical sensor. *Anal. Chim. Acta* **2018**, *1035*, 22–31, doi:10.1016/j.aca.2018.06.057.
19. Marrani, A.G.; Motta, A.; Schrebler, R.; Zanoni, R.; Dalchiele, E.A. Insights from experiment and theory into the electrochemical reduction mechanism of graphene oxide. *Electrochim. Acta* **2019**, *304*, 231–238, doi:10.1016/j.electacta.2019.02.108.
20. Tiliakos, A.; Trefilov, A.M.I.I.; Tanasă, E.; Balan, A.; Stamatin, I. Space-Filling Supercapacitor Carpets: Highly scalable fractal architecture for energy storage. *J. Power Sources* **2018**, *384*, 145–155, doi:10.1016/j.jpowsour.2018.02.061.
21. Hota, M.K.; Jiang, Q.; Mashraei, Y.; Salama, K.N.; Alshareef, H.N. Fractal Electrochemical Microsupercapacitors. *Adv. Electron.Mater.* **2017**, *3*, 1–9, doi:10.1002/aelm.201700185.
22. Cai, X.; Peng, M.; Yu, X.; Fu, Y.; Zou, D. Flexible planar/fiber-architectured supercapacitors for wearable energy storage. *J. Mater.Chem. C* **2014**, *2*, 1184–1200, doi:10.1039/c3tc31706d.
23. Quain, E.; Mathis, T.S.; Kurra, N.; Maleski, K.; Van Aken, K.L.; Alhabeb, M.; Alshareef, H.N.; Gogotsi, Y. Direct Writing of Additive- Free MXene-in-Water Ink for Electronics and Energy Storage. *Adv. Mater. Technol.* **2019**, *4*, doi:10.1002/admt.201800256.
24. Li, J.; Levitt, A.; Kurra, N.; Juan, K.; Noriega, N.; Xiao, X.; Wang, X.; Wang, H.; Alshareef, H.N.; Gogotsi, Y. MXene-conducting polymer electrochromic microsupercapacitors. *Energy Storage Mater.* **2019**, *20*, 455–461, doi:10.1016/j.ensm.2019.04.028.
25. Mao, X.; Xu, J.; He, X.; Yang, W.; Yang, Y.; Xu, L.; Zhao, Y.; Zhou, Y. All-solid-state flexible microsupercapacitors based on reduced graphene oxide/multi-walled carbon nanotube composite electrodes. *Appl. Surf. Sci.* **2018**, *435*, 1228–1236, doi:10.1016/j.apsusc.2017.11.248.
26. Park, S.; Lee, H.; Kim, Y.-J.; Lee, P.S. Fully laser-patterned stretchable microsupercapacitors integrated with soft electronic circuit components. *NPG Asia Mater.* **2018**, *10*, 959–969, doi:10.1038/s41427-018-0080-z.
27. Jiang, L.; Park-Lee, K.J.; Clinton, R.M.; Tang, Z.; Breedveld, V.; Hess, D.W. Mechanical durability of liquid repellent coatings. *Surf. Coat. Technol.* **2017**, *328*, 182–191, doi:10.1016/j.surfcoat.2017.08.007.
28. Jutarosaga, T.; Jeoung, J.S.; Seraphin, S. Infrared spectroscopy of Si-O bonding in low-dose low-energy separation by implantedoxygen materials. *Thin Solid Films* **2005**, *476*, 303–311, doi:10.1016/j.tsf.2004.10.006.
29. Pawlyta, M.; Rouzaud, J.N.; Duber, S. Raman microspectroscopy characterization of carbon blacks: Spectral analysis and structural information. *Carbon* **2015**, *84*, 479–490, doi:10.1016/j.carbon.2014.12.030.
30. Madito, M.J.; Ismail, M.Y.A.; Hlatshwayo, T.T.; Mtshali, C.B. The nature of surface defects in Xe ion-implanted glassy carbon annealed at high temperatures: Raman spectroscopy analysis. *Appl. Surf. Sci.* **2020**, *506*, doi:10.1016/j.apsusc.2019.145001.
31. Claramunt, S.; Varea, A.; López-López -Díaz, D.; Mercedes Velázquez-Velázquez, M.; Cornet, A.; Cirera, A. The Importance of Interbands on the Interpretation of the Raman Spectrum of Graphene Oxide. *J. Phys. Chem. C* **2015**, *119*, 10123–10129,doi:10.1021/acs.jpcc.5b01590.
32. Dai, C.; Gu, C.; Liu, B.; Lyu, Y.; Yao, X.; He, H.; Fang, J.; Zhao, G. Preparation of low-temperature expandable graphite as a novel steam plugging agent in heavy oil reservoirs. *J. Mol. Liq.* **2019**, *293*, doi:10.1016/j.molliq.2019.111535.
33. Montagna, L.S.; Fim, F.D.C.; Galland, G.B.; Basso, N.R.D.S. Synthesis of poly(propylene)/graphite nanocomposites by in situ polymerization. In *Proceedings of the Macromolecular Symposia*; 2011; Volume 299–300, pp. 48–56.
34. Chen, C.M.; Huang, J.Q.; Zhang, Q.; Gong, W.Z.; Yang, Q.H.; Wang, M.Z.; Yang, Y.G. Annealing a graphene oxide film to produce a free standing high conductive graphene film. *Carbon* **2012**, *50*, 659–667, doi:10.1016/j.carbon.2011.09.022.
35. Li, Q.; Smith, A.D.; Vyas, A.; Cornaglia, F.; Anderson, A.; Haque, M.; Lundgren, P.; Enoksson, P. Finger Number and Device Performance: A Case Study of Reduced Graphene Oxide Microsupercapacitors. *Phys. Status Solidi Basic Res.* **2021**, *258*, 1–7, doi:10.1002/pssb.202000354.
36. Tsang, T. *Classical Electrodynamics*; World Scientific, Singapore, 1998.
37. Liu, N.; Gao, Y. Recent Progress in Micro-Supercapacitors with In-Plane Interdigital Electrode Architecture. *Small* **2017**, *13*,doi:10.1002/smll.201701989.
38. Shen, C.; Wang, X.; Zhang, W.; Kang, F. A high-performance three-dimensional micro supercapacitor based on self-supporting composite materials. *J. Power Sources* **2011**, *196*, 10465–10471, doi:10.1016/j.jpowsour.2011.08.007.
39. Xiong, G.; Meng, C.; Reifenberger, R.G.; Irazoqui, P.P.; Fisher, T.S. A review of graphene-based

40. Sylla, N.F.; Ndiaye, N.M.; Ngom, B.D.; Momodu, D.; Madito, M.J.; Mutuma, B.K.; Manyala, N. Effect of porosity enhancing agents on the electrochemical performance of high-energy ultracapacitor electrodes derived from peanut shell waste. *Sci. Rep.* **2019**, *9*, 13673, doi:10.1038/s41598-019-50189-x.
41. Mathis, T.S.; Kurra, N.; Wang, X.; Pinto, D.; Simon, P.; Gogotsi, Y. Energy Storage Data Reporting in Perspective—Guidelines for Interpreting the Performance of Electrochemical Energy Storage Systems. *Adv. Energy Mater.* **2019**, *9*, 1902007, doi:10.1002/aenm.201902007.
42. Rantho, M.N.; Madito, M.J.; Manyala, N. Symmetric supercapacitor with supercapattery behavior based on carbonized iron cations adsorbed onto polyaniline. *Electrochim. Acta* **2018**, *262*, 82–96, doi:10.1016/j.electacta.2018.01.001.
43. Diard, J.P.; Le Gorrec, B.; Montella, C. Linear diffusion impedance. General expression and applications. *J. Electroanal. Chem.* **1999**, *471*, 126–131, doi:10.1016/S0022-0728(99)00262-4.
44. Gao, M.; Dong, X.; Wang, K.; Duan, W.; Sun, X.; Zhu, C.; Wang, W. Laser direct preparation and processing of graphene/MnOnanocomposite electrodes for microsupercapacitors. *J. Energy Storage* **2021**, *33*, doi:10.1016/j.est.2020.102162.

Supplementary information

Novel thermally reduce graphene oxide microsupercapacitor fabricated via mask – free axiDraw direct writing

V.M. Maphiri[1], G. Rutavi[1], N.F. Sylla[1], S.A. Adewinbi[2], O. Fasakin[1], N. Manyala[1]*

[1]Department of Physics, Institute of Applied Materials, SARChI Chair in Carbon Technology and Materials, University of Pretoria, Pretoria 0028, South Africa

[2]Department of physics, Osun State University, Osogbo, Osun State 210001, Nigeria

*Corresponding author email: ncholu.manyala@up.ac.za, Tel.: + (27)12 420 3549 Fax: + (27)12 420 2516

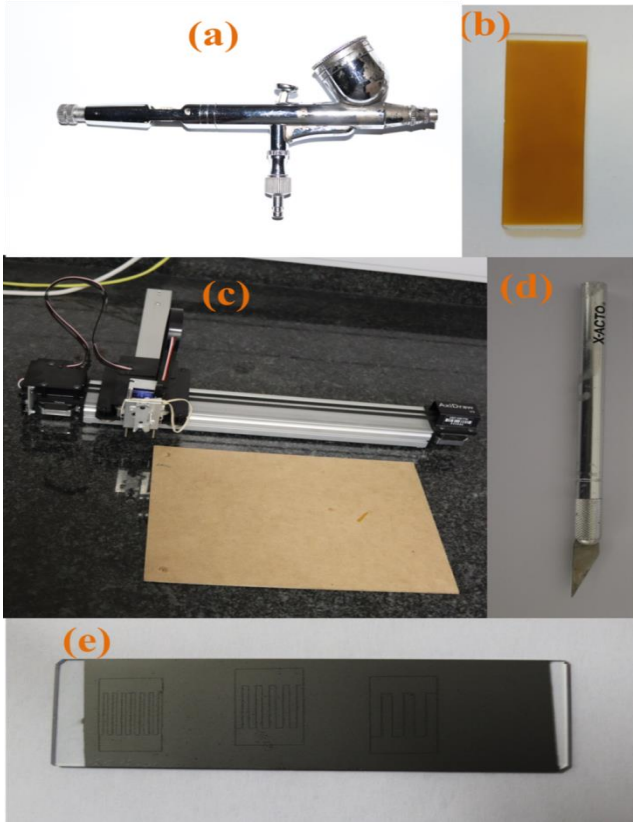

Fig. S1 Optical image of (a) Spray gun, (b) GO thin film on microscopic glass (MSG), (c) axiDraw, (d) sharp blade pen and (e) TRGO patterned with μ-SC of various digits per unit area on microscopic glass

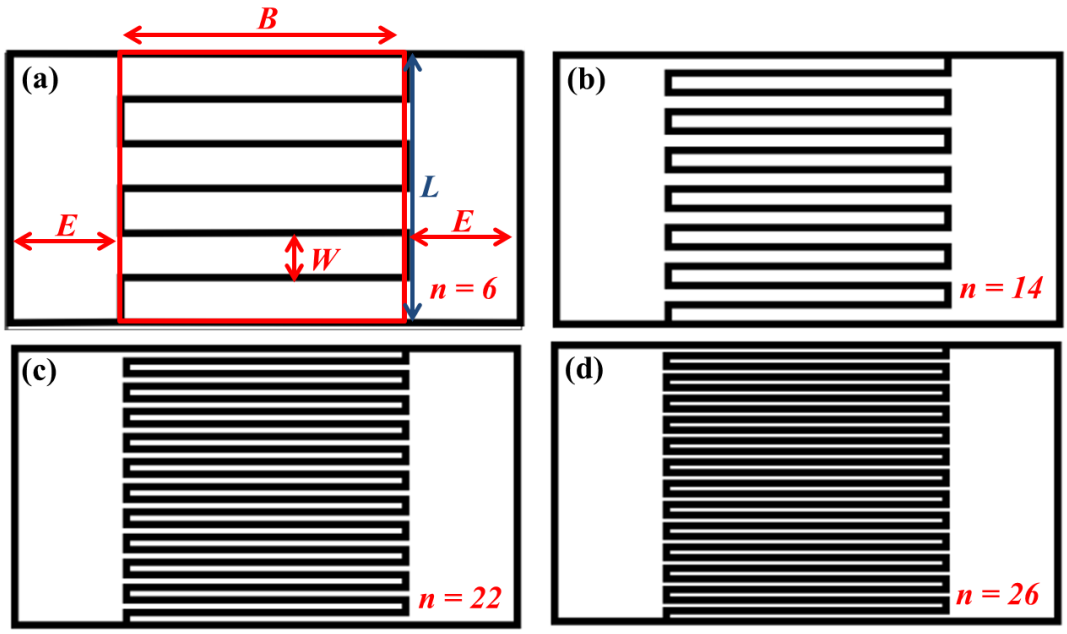

Fig. S2 Inkscape blueprint schematic for the *n* (a) 6, (b) 14, (c) 22 and (d) 26 digits µ-SC

The effective area was calculated using the formula (equation S1) derived below. The interspace area was subtracted from the total surface area. The interspace area has two components which is the horizontal (along the breadth) and vertical (along the length) component.

Effective area = Total surface area – Total interspace area

= Total surface area – (Horizontal interspace area + Vertical interspace area)

$$= \mathrm{L} \times \mathrm{B} - ((n \times \mathrm{W} \times i) + \mathrm{B} \times (n - 1) \times i)$$

$$= L \times B - (i \times ((n \times W) + B \times (n - 1)))$$

$$= L \times B - (i \times (L + B \times (n - 1))) \quad \ldots (S1)$$

Thus, Total interspace area is given by (equation S2)

$$i \times (L + B \times (n - 1)) \quad \ldots (S2)$$

Table S1. Dimensions and parameters of μ – SC (6), (14), (22) and (26)

Parameters	μ-SC (6)	μ-SC (14)	μ-SC (22)	μ-SC (26)
Number of digits per unit area, n (cm^{-2})	6	14	22	26
Width, W (mm)	1.66	0.71	0.45	0.38
Length, L and Breadth, B (mm)	10	10	10	10
Interspace, i(μm)	38	38	38	38

Edge, E (mm)	4	4	4	4
Total surface area (mm^2)*	100	100	100	100
Total interspace area(mm^2)	2.28	5.32	8.36	9.88
Effective area (mm^2)	97.72	94.68	91.64	90.12

*Total surface area and effective area doesn't include μ-SC edge area (see Fig. S7)

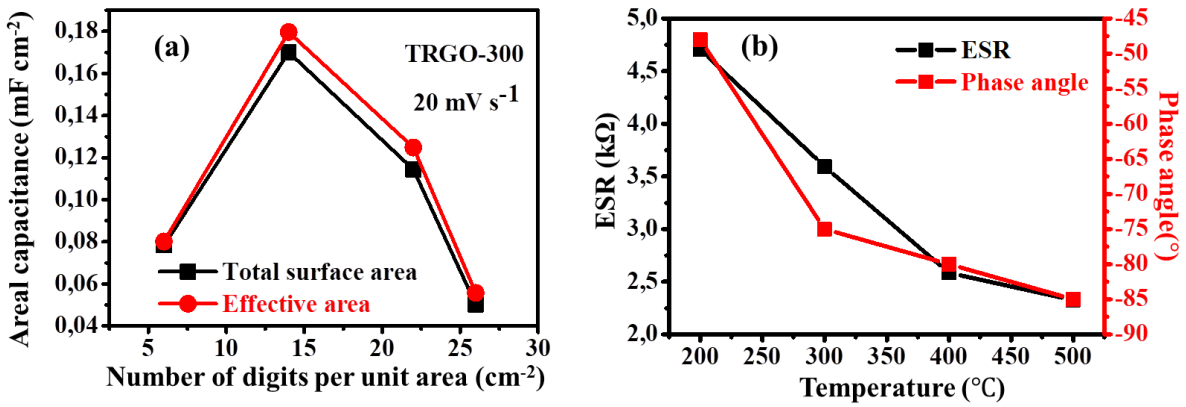

Fig. S3 (a) Areal capacitance of the total surface area versus effective area at 6, 14, 22 and 26 digits per unit area (cm^{-2}) and (b) ESR and phase angle as a function of reducing temperature

The CV curves of the µ-SC are displayed in Figs. S11 and S12 where (a) – (d) corresponds to the TRGO 200 to TRGO-500, respectively, measured at the potential window of 0 – 0.8V. The scan rate of these µ-SCs increased from 50 to 1000 mVs^{-1} as the reducing temperature increased from 200 to 500℃. Thus, the scan rate is directly proportional to the reducing temperature.

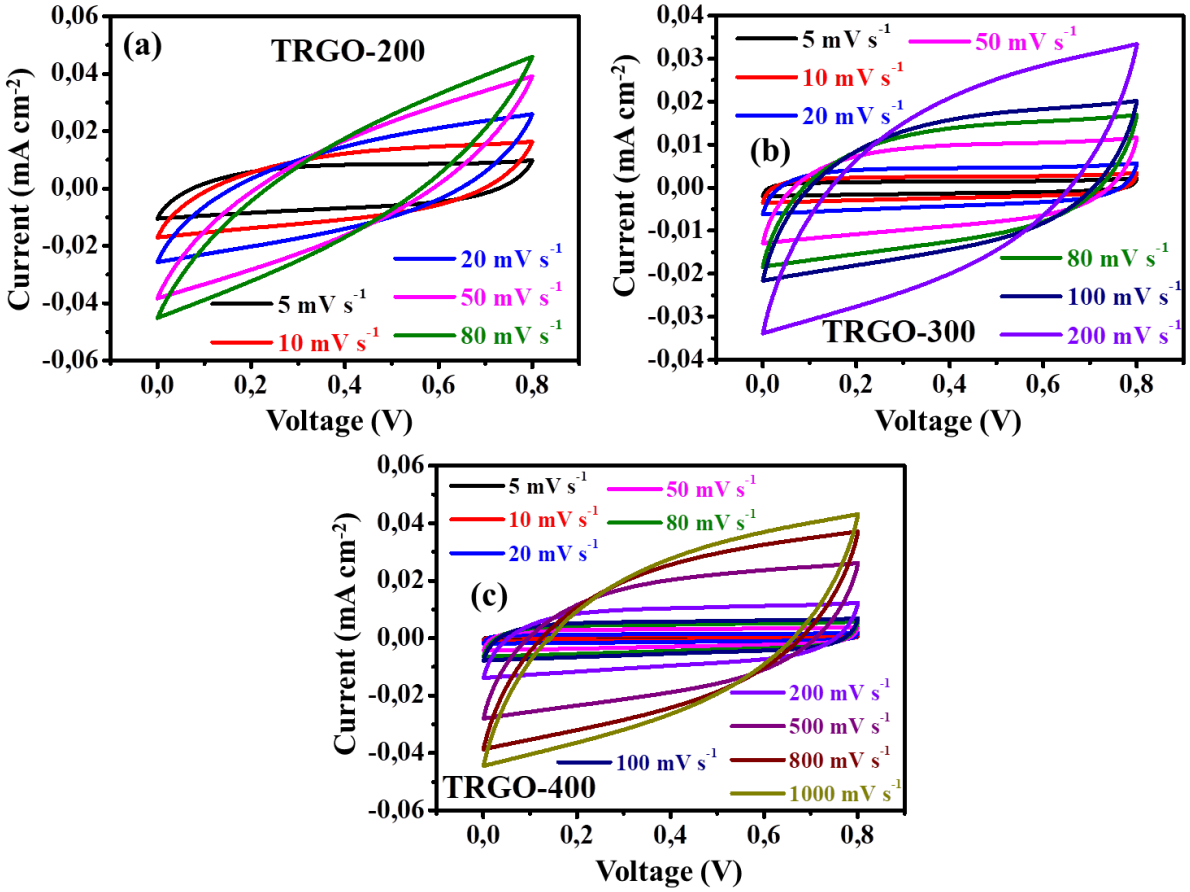

Fig. S4 The CV curves at (a) TRGO-200, (b) TRGO-300 and (c) TRGO-400 at various scan rates

Table S2. The areal capacitance determined from the CV curve

Scan rate mV s^{-1}	Areal capacitance (mF cm^{-2})			
	TRGO-200	TRGO-300	TRGO-400	TRGO-500
5	0.7074	0.1451	0.0444	0.0319
10	0.5421	0.1227	0.0382	0.0298
20	0.3773	0.1061	0.0348	0.0274
50	0.2085	0.0865	0.0301	0.0256
80	0.1498	0.0756	0.0282	0.0244
100	-	0.0695	0.0267	0.0239
200	-	0.0506	0.0234	0.0220
500	-	-	0.0179	0.0194
800	-	-	0.0148	0.0172
1000	-	-	0.0140	0.0159

The area capacitance (C) was evaluated from the GCD curve by applying equation (S3) as shown below

$$C = \frac{I \times \Delta t}{\Gamma \times \Delta V} \quad \ldots(S3)$$

where, I is the discharge current, Δt is the discharge time, Γ is the area and ΔV is the voltage.

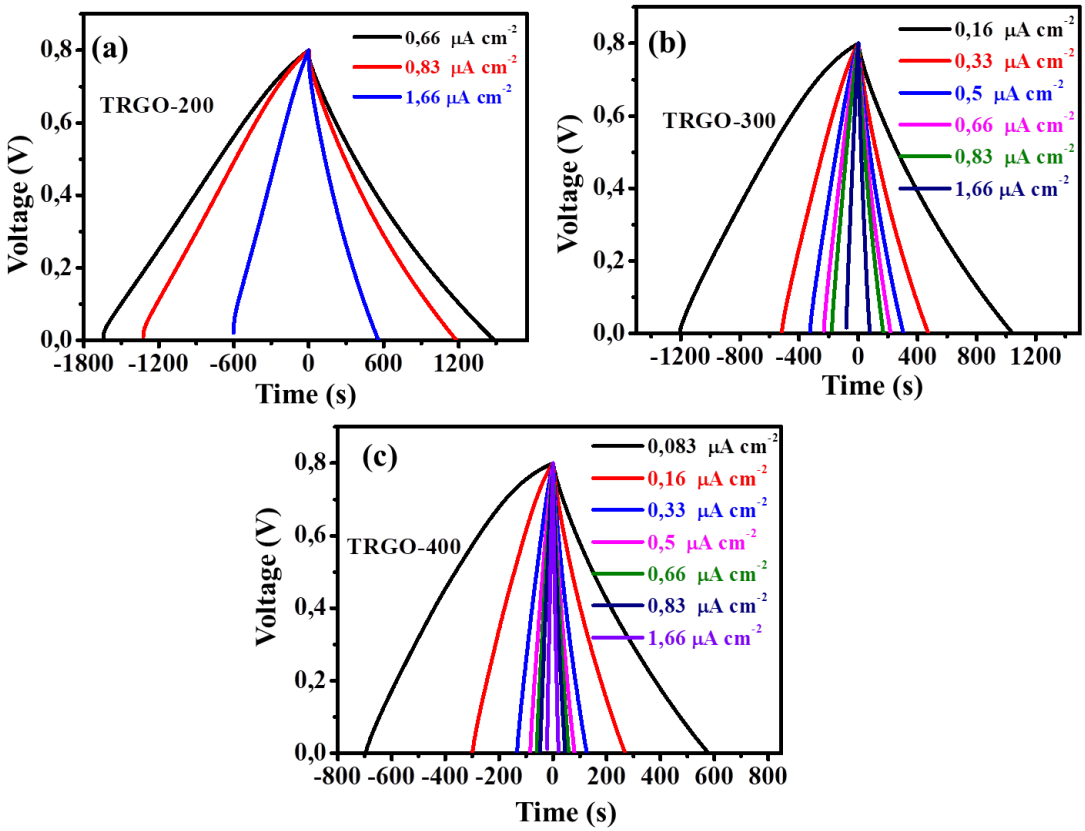

Fig. S5 The GCD curves of μ-SC at different current densities for (a) TRGO-200, (b) TRGO-300 and (c) TRGO-300

Table S3. The areal capacitance determined from the GCD curve

Current density ($\mu A\ cm^{-2}$)	Areal capacitance ($mF\ cm^{-2}$)			
	TRGO-200	TRGO-300	TRGO-400	TRGO-500
0.083	-	-	0.0600	0.0387
0.16	-	0.2143	0.0536	0.0366

0.33	-	0.1952	0.0517	0.0367
0.5	-	0.1904	0.0501	0.0364
0.66	1.2255	0.1809	0.0481	0.0356
0.83	1.2262	0.1754	0.0472	0.0354
1.66	1.1569	0.1506	0.0434	0.0338

The µ-SCs of TRGO-200 to TRGO-500 delivered an areal power density ranging from 0.3316 to 0.3709 mW cm^{-2} corresponding to the areal energy density in the range of 0.1368 – 0.0017 mW h cm^{-2}. It is very clear that the delivered energy decreased as the reducing temperature increased while the power is increasing.

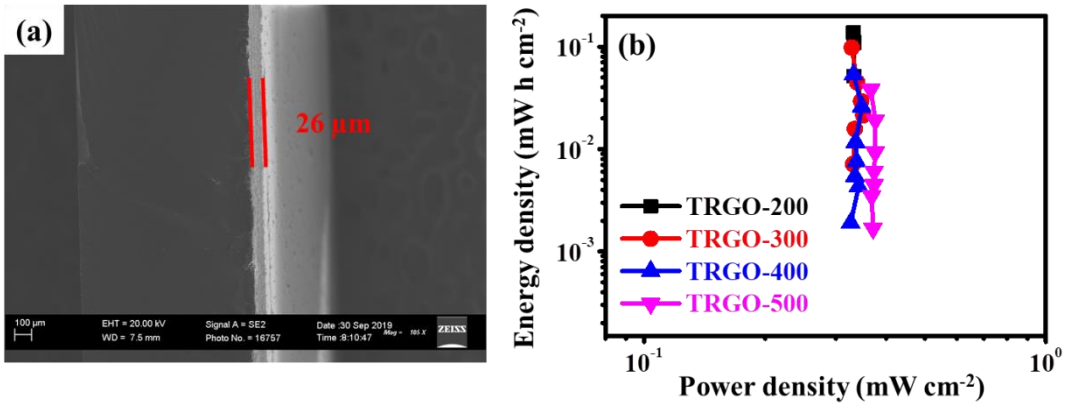

Fig. S6. (a) SEM cross-sectional image of the TRGO-500 µ-SC and (b) Ragone plot of the TRGO-200, TRGO-300, TRGO-400 and TRGO-500

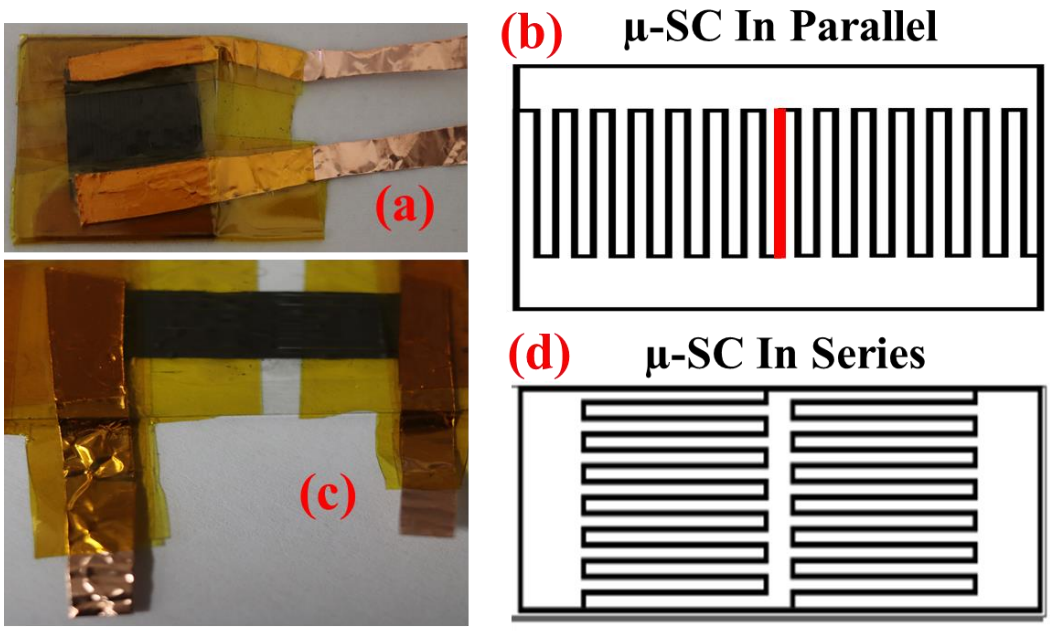

Fig. S7 Digital photography of μ-SC in (a) parallel and (c) series. Inkscape blueprint of μ-SC in (b) parallel and (d) series

4.2.1.1. Part II

The results obtained from the study of thermally reduced graphene oxide microsupercapacitor fabricated via Mask-free AxiDraw Direct Writing were further analysed and are described in the publication and supplementary information below:

nanomaterials

MDPI

Article

Impact of Thermally Reducing Temperature on Graphene Oxide Thin Films and Microsupercapacitor Performance

Vusani M. Maphiri, Daba T. Bakhoum, Samba Sarr, Ndeye F. Sylla, Gift Rutavi and Ncholu Manyala *

Department of Physics, Institute of Applied Materials, SARChI Chair in Carbon Technology and Materials, University of Pretoria, Pretoria 0028, South Africa; vusanimuswamaphiri@gmail.com (V.M.M.); thiogna@yahoo.fr (D.T.B.); ssarr3112@gmail.com (S.S.); ntoufasylla@gmail.com (N.F.S.); rutavigift@yahoo.com (G.R.)

* Correspondence: ncholu.manyala@up.ac.za; Tel.: +27-12-420-3549; Fax: +27-12-420-3546

Abstract: In this work, a thermally reduced graphene oxide (TRGO) thin film on microscopic glass was prepared using spray coating and atmospheric pressure chemical vapour deposition. The structure of TRGO was analysed using X-ray diffraction (XRD) spectroscopy, scanning electron microscope (SEM), energy-dispersive X-ray spectroscopy (EDS), Fourier transform infrared (FTIR) spectroscopy, and ultraviolet–visible spectroscopy (UV-Vis) suggesting a decrease in oxygen functional groups (OFGs), leading to the restacking, change in colour, and transparency of the graphene sheets. Raman spectrum deconvolution detailed the film's parameters, such as the crystallite size, degree of defect, degree of amorphousness, and type of defect. The electrochemical performance of the microsupercapacitor (μ-SC) showed a rectangular cyclic voltammetry shape, which was maintained at a high scan rate, revealing phenomenal electric double-layer capacitor (EDLC) behaviour. The power law and Trasatti's analysis indicated that low-temperature TRGO μ-SC is dominated by diffusion-controlled behaviour, while higher temperature TRGO μ-SC is dominated by surface-controlled behaviour.

Keywords: graphene oxide; thermally reduced; Raman spectroscopy; sheet resistance; energy storage

Citation: Maphiri, V.M.; Bakhoum, D.T.; Sarr, S.; Sylla, N.F.; Rutavi, G.; Manyala, N. Impact of Thermally Reducing Temperature on Graphene Oxide Thin Films and Microsupercapacitor Performance. *Nanomaterials* 2022, *12*, 2211. https://doi.org/10.3390/nano12132211

Academic Editor: Jung Woo Lee

Received: 31 May 2022
Accepted: 24 June 2022
Published: 28 June 2022

1. Introduction

Graphene has been widely studied and used in advanced technological applications due to its excellent properties, which make it a possible candidate for the fabrication of gas sensors [1], energy [2], and hydrogen storage devices [3], and transparent conducting electrodes for photovoltaic application [4]. Moreover, each application requires a different set of graphene properties. Thus, different graphene preparation methods are suitable for certain applications. For instance, while high-quality graphene (synthesised by chemical vapour deposition (CVD), bottom-up approach, low yield) is more suitable for electronic applications, it is not compatible with the production of conductive inks due to the lack of functional groups [5]. In addition, functionalised graphene prepared via the chemical exfoliation method (e.g., hummer's method, top-down approach, high yield) of graphite is more suitable for energy-storage applications and other applications, such as gas sensors and polymer composites, because the oxygen functional groups (OFGs) on the graphitic surface act as polymers [6] or nanoparticle anchors [7], as well as increasing pseudocapacitive behaviour [2].

Graphene oxide (GO) was first reported by Brodie and later modified by Staudenmaier and Hummers [5]. These authors proposed that the chemical structure of GO consists of two main regions comprising hydrophobic conjugates C-sp^2 and C-sp^3 domains. Thus, GO contains alcohol and epoxy groups located at the basal plane, while carboxylic acids attaches at the surface edges [5]. The advantage of preparing graphene from the thermal reduction of GO is that physical, mechanical, electronic, and electrochemical properties can be easily modified by controlling the OFGs attached to the graphene sheets. Moreover, while thermal reduction does not leave residual compounds, the chemical reduction method using

hydrazine hydrate has been reported to have residual molecules of N_2H_4 and incorporate NH_3 within reduced GO sheets [8,9]. Chen et al. [10] and Zhao et al. [11] reported thermal reduction with GO and X-ray diffraction (XRD) spectroscopy, Fourier transform infrared (FTIR) spectroscopy, scanning electron microscopes (SEM), and energy-dispersive X-ray dispersion spectroscopy (EDS), which were used to analyse the structure and surface morphology. It was concluded that the XRD showed a decrease in the interplanar distance, while the FTIR and EDS showed a decrease in the oxygen functional groups. The SEM showed the presence of a sheet-like material, which was similar for pre- and post-reduction. The electrochemical performance showed an increase in the power density and a decrease in the energy density as a function of RT [11]. This behaviour was allotted to the removal of resistive OFGs, i.e., the carboxylic acids attached to the surface edges resisting the flow of electrons [5] (confirmed by the increase in electrical conductivity as the reducing temperature increased). These OFGs also served as a passage for the ions to the bulk internal surface, as well as facilitating the fast redox processes occurring at or near the electrode surface, which can provide pseudocapacitance, as shown by our previously reported results [2,12]. Our electrochemical impedance spectroscopy (EIS) results showed a decrease in the solution resistance, further confirming the removal of the surface-edges functional group.

The shape of the electrochemical cyclic voltammetry (CV) has been used to distinguish between different electrochemical systems, i.e., capacitive and faradic behaviour. Further electrochemical analysis, such as Trasatti's [13,14] and Dunn's [14] analysis, can be used to understand the electrode material storage mechanism. Trasatti's analysis relies on the assumption that diffusion and surface-controlled contributions are controlled by different kinetics, which respond differently as the scan rate increases. Xu et al. [14] used this analysis on the prepared nitrogen-rich holey graphene oxide film reduced at 200–400 °C under an Ar environment. The Trasatti analysis showed that for an optimum sample reduced at 300 °C, the capacitance contribution from the inner surface (pseudocapacitance) is almost 64.1% of the total capacitance. Huang et al. [13] used Trasatti's method to understand the different CV curve calculated capacitance levels generated from the three prepared electrodes, i.e., c-TiO_2 + MWNT, p-TiO_2 + MWNT, and p-TiO_2 + c-TiO_2 + MWNT. The results showed that the presence of c-TiO_2 resulted in a decrease in the total capacitance due to pore blockage (c-TiO_2 = 20 nm).

This study is a continuation of our previously published work on TRGO thin film on microscopic glass (MSG) for microsupercapacitor applications [12]. Here, we focus mainly on the structural, electrical, optical characterisation, and electrochemical analyses, such as the electrolyte-ion diffusion of the TRGO μ-SC. In addition, this study presents the fundamental understanding of the influence of oxygen on the surface of graphene sheets and its impact on the electrochemical performance. Similar studies have been reported on powder GO [10], in which the GO exfoliated at around 200 °C, while the GO within this study changed colour from yellowish to dark black at 200 °C and then turned to shiny black as the temperature increased. This work offers a pioneering characterisation of TRGO thin films prepared in this fashion, i.e., an inexpressive, simple, and quick way to fabricate TRGO thin films that does not contain chemical residue from chemical reduction. These thin films can be used in various applications, such as energy storage [12], counter electrodes for dye-sensitised solar cells [15], and temperature sensors [16].

2. Experimental Methods

2.1. Materials

Chemicals used in this article were of analytical grade and were used without any further purification. The materials and chemicals used were as follows: natural graphite, sulphuric acid (H_2SO_4 (98%)) (Associated Chemical Enterprises, Johannesburg, South Africa), microscopic glass (MSG) (B&C Glass Ltd, Haverhill, UK), potassium permanganate ($KMnO_4$) %)) (Associated Chemical Enterprises, Johannesburg, South Africa), ethanol (C_2H_5OH (98%)) %)) (Associated Chemical Enterprises, Johannesburg, South Africa), hy-

drogen peroxide (H_2O_2 (50%)) %)) (Associated Chemical Enterprises, Johannesburg, South Africa), Argon gas (Ar (99%)) (AFROX, Johannesburg, South Africa) and deionised water (H_2O) (DW) (prepared using DRAWELL, laboratory water purification system, available at the Physics Department, University of Pretoria, Pretoria, South Africa) at 18.2 MΩ.

2.2. Preparation of TRGO Thin Film

TRGO thin films were prepared using a series of methods that were modified Hummer's method, cleaning MSG using piranha solution, spray-coating GO on the cleaned MSG, and then thermally reducing GO using atmospheric pressure chemical vapour deposition (AP-CVD) as per our previously published results [12]. In summary, graphite powder was added into an agitating cooled H_2SO_4, followed by $KMnO_4$. The agitation continued for 180 min at a constant heating temperature of 50 °C. The solution was left to cool to room temperature, then DW and H_2O_2 were added into the solution. GO was cleaned via decantation, then centrifuged at 5000 rpm for 5 min, and dried at 60 °C for 3 h. Dried GO was mixed with ethanol, then sonicated to obtain a GO-ethanol which was sprayed onto a clean MSG. The GO/MSG thin film was subsequently reduced at a temperature ranging from 100 to 500 °C. Note that the samples were denoted as TRGO-100, TRGO-200, TRGO-300, TRGO-400, and TRGO-500, depending on the reducing temperature used. These preparation methods and appearance of the prepared thin film are schematically illustrated in Figure 1. The digital images of the prepared thin film are also displayed in Figure S1 (supplementary information).

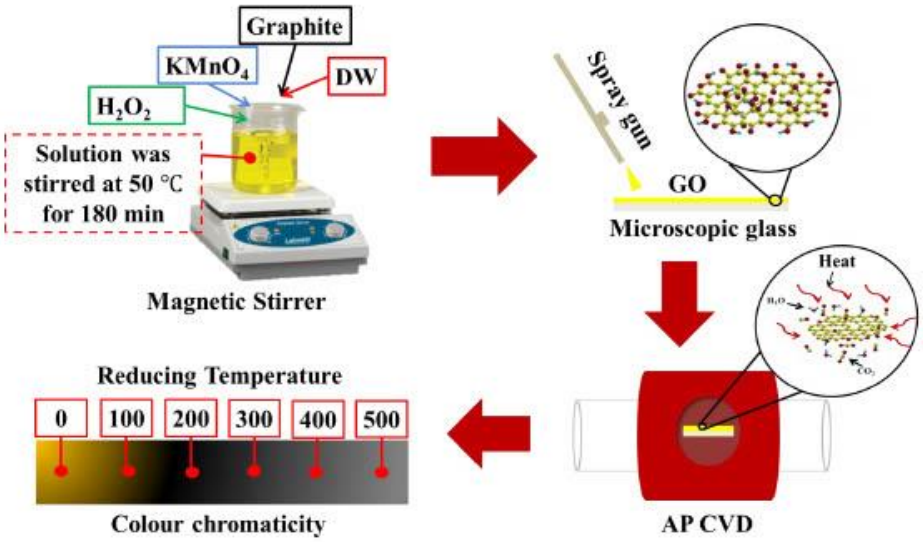

Figure 1. Schematic detailing TRGO thin-film preparation and the colour chromaticity showing the appearance of the prepared thin film.

2.3. Structural, Morphological, and Electrochemical Characterisation

The prepared TRGO thin-film samples, together with precursor graphite and intermitted GO and MSG substrates were analysed using various techniques: Bruker BV 2D phaser benchtop X-ray diffraction (XRD) (PANalytical BV, Amsterdam, The Netherland) using CuKα radiation source was used to investigate the crystal structure. Zeiss Ultra-plus 55 field emission scanning electron microscope (FE–SEM) (Akishima-shi, Japan) operated at voltage of 2.0 kV was used to capture the surface morphology (SEM micrograph) and Oxford energy-dispersive X-ray spectroscopy (EDS) operated at 20.0 kV and controlled

using Aztec 3.0 SP1 software was to obtained elemental information. Confocal WITec alpha 300RAS+ (Ulm, Germany) Raman microscopy was used to obtain the Raman spectra and the atomic force microscope (AFM) images. The Raman spectra were collected using a 532-nanometer excitation laser (the laser power was set to less than 2 mW to avoid heating the sample) at a single accumulation for 60 s at room temperature. The AFM images were collected using the tapping mode configuration and a silicon tip on a 30 × 30 μm^2 area to examine surface topography of the GO and TRGO at different reducing temperatures. The three-dimensional AFM images and height profile were prepared using the WITec project five (build 5.1.18.79). Fourier transform infrared (FT-IR) spectroscopy was performed using the Bruker Alpha platinum-ATR (attenuated total reflection) (Billerica, MA, USA) in the range of 4000 to 400 cm^{-1}. The light transparency and absorption effect of the prepared samples were examined by the transmittance and absorption spectra in wavelength range of 200–1000 nm using the Agilent cary 60 UV-Vis spectrophotometer (Santa Clara, CA, USA). The transmittance and absorbance of the substrate glass was taken first after the completion of the baseline correction with air background. The sheet resistance of the TRGO films was measured using the Ossila (Sheffield, UK) four-point probe (4PP) set-up, with a collinear and equidistant geometrical configuration. The two-electrode configuration measurements of the μ-SC device were measured using cyclic voltammeter (CV), galvanostatic charge–discharge (GCD), and electrochemical impendence spectroscopy (EIS) at 10 mV in a frequency range of 0.1 to 100 kHz using the Bio–Logic VMP-300 potentiostat (Knoxville, TN, USA) monitored by EC-Lab V11.33 software (Edmonton, AB, Canada).

3. Results and Discussion

3.1. X-ray Diffraction Spectroscopy

The XRD was deployed to investigate the structural properties of the thermally reduced samples, together with the precursor graphite powder, intermediate GO thin film, and MSG substrate. The obtained XRD patterns are displayed in Figure 2 and Figure S2. The pattern were indexed to the XRD patterns of GO (JCPDS 41 1487) and graphite (JCPDS 75 2078). The XRD diffraction peak of the graphite at $2\theta \approx 25^{\circ}$ resulted from the (002) reflection plane, which completely disappeared upon oxidation and evolved into a new peak at a diffraction angle of $2\theta \approx 15^{\circ}$, which was indexed to the (001) reflection of the GO [17,18]. This indicated the successful oxidation of graphite, which was in line with the results reported in several other studies [11,19]. The absence of additional peaks on the GO, except the peak indicated with a Daggar (†), suggests an impurity-free GO. The diffraction peak assigned to † was the diffraction from the microscope glass substrate (MGS; see Figure S2a, comparing the diffraction patterns of the GO and the MGS). When the TR temperature increased, the XRD pattern peaks changed back from the (001) to (002) reflection planes. The (002) peak shifted from around $2\theta = 15$ (TRGO-100) to 25° (TRGO-500), which suggests that the GO restacked (decreasing the interplanar distance) into a disordered graphite-like material due to the removal of the OFG, increasing the van der Waals attraction force [11,18]. This behaviour can be seen on the SEM and AFM images displayed in Figures S4 and S5 and the roughness information is displayed in Table S2. In addition, similar results were reported by Zhao et al. [11], in whose study the diffraction peak also shifted as a function of the RT. The diffraction peaks assigned to the asterisk (*) were due to the diffraction peaks of both the substrate and the GO/graphite-like material. These diffraction patterns are clearly shown in Figure S2b–d, where the diffraction pattern of the TRGO on the MGS were compared to the annealed MGS. We suggest that the diffraction peak denoted with a bullet (•) represents the highly reduced GO at the MSG interface caused by the prolonged heating exposure from the hot-glass substrate during cooling. This peak cannot be attributed to the MGS-related diffraction peak because the diffraction pattern of the MSG depicted in Figure S2c–e does not resemble such a peak. On the TRGO-500 (see also Figure S2f), the • denoted peak is not visible due to the homogenous reduction caused by the high

reduction temperature. The interplanar distances of the (001) and (002) diffraction peaks were estimated using the Bragg's Equation (1) and depicted in Table S1 and Figure S3a.

$$n\lambda = 2d \sin\theta \quad (1)$$

where n, λ, d, and θ are the integers, the wavelength of the Cuk$_\alpha$, the interplanar distance at (001) and (002) miller indices, and the diffraction angle in rad, respectively. The above-mentioned dramatic shift to a lower diffraction angle can also be explained in terms of the interplanar distance caused by the insertion of H_2O molecules within the layers and the attachment of O-containing functional groups, such as hydroxyl (-OH), carbonyl (-CO-), carboxylic (-COOH), and epoxy (-O-) on the graphene layers within the graphite [11,20]. Similar results were obtained in the study by Bao et al. [21], where GO was also synthesised by the improved Hummer's method and the obtained GO had an interspacing distance of around 0.803 nm. As a result of the RT ranging from 100–500 °C, the diffraction angle shift to a higher diffraction angle corresponded to the contraction of the interplanar distance allotted to the thermal removal of the H_2O and O-containing functional groups. These results are confirmed by the FTIR displayed in Figure S6, showing the presence of H_2O- and oxygen-related functional groups on the GO. The FTIR spectrum notches related to the H_2O and OFGs fade as the temperature increases, which further confirms the XRD behaviour.

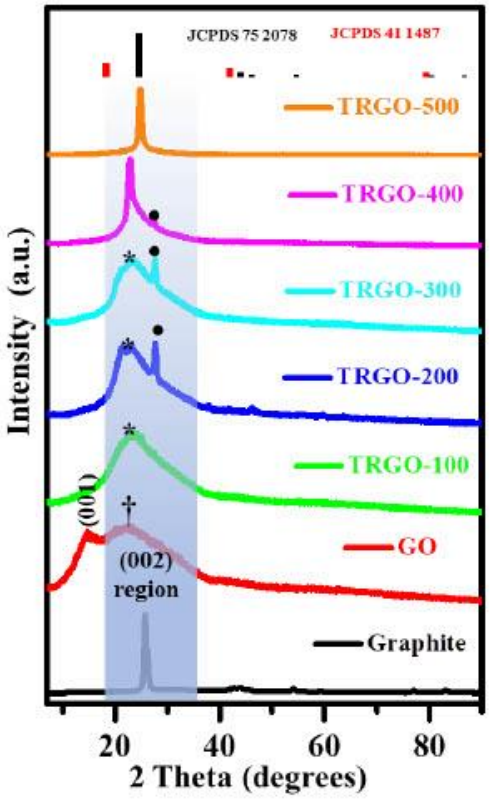

Figure 2. The XRD spectra for graphite, GO, and TRGO-100 to TRGO-500.

3.2. Energy Dispersive X-ray Spectroscopy

The elemental composition of the graphite, GO and TRGO-100 to TRGO-500 was obtained via the EDS. The obtained EDS spectra of these samples are presented in Figure 3. The spectra show the presence of multiple peaks attributed to various elements and/or the same element with different characteristic X-rays [22]. The graphite sample is indicated by the dominant peak at 0.277 KeV, which is due to carbon. This is because graphite is predominantly a carbon-based material. In order to determine the origin of the unexpected peaks within the spectra of the GO and TRGO samples, the EDS of the MSG were also measured, and they are displayed in Figure 3. Most of the peaks seen in the GO and TRGO spectra represent the MSG. The peaks at 0.525, 1.041, 1.254, 1.487, 1.740, and 3.692 KeV are due to the k_α characterisation peaks of oxygen (O), sodium (Na), magnesium (Mg), aluminium (Al), silicon (Si), and calcium (Ca), respectively. The EDS spectra of the GO and TRGO possess two peaks in addition to those of the MSG due to carbon (C) and sulphur (S) occurring at 2.308 KeV. Even though EDS is not a quantification technique, it is interesting to see that as the RT increases, the carbon and oxygen peaks increase and decrease, respectively, further confirming the XRD and FTIR results. Figure S3b and Table S1 indicate the carbon content measured by the increase in the intensity of the carbon over that of the oxygen as a result of the extermination of the OFGs.

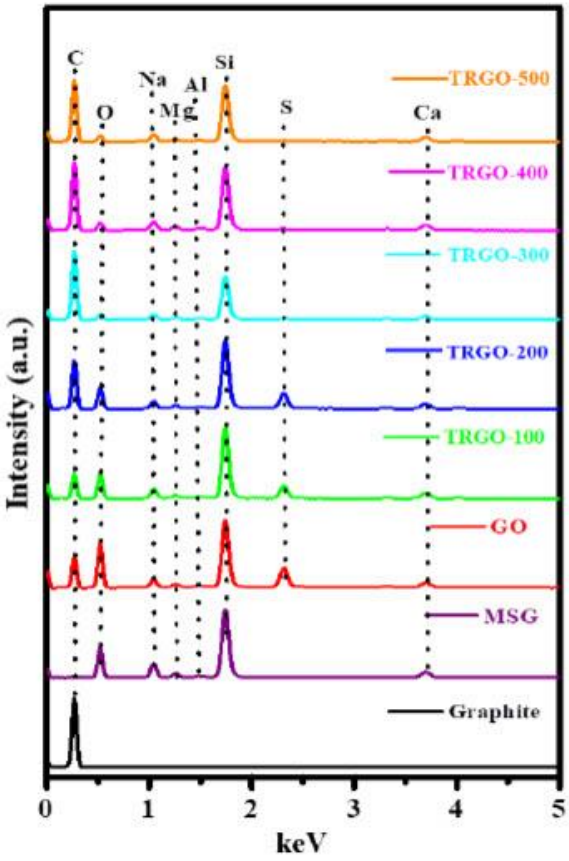

Figure 3. EDS spectrum of graphite, MSG, GO, and TRGO samples.

3.3. Optical Studies

The optical studies were measured with the aid of the UV-Vis. The absorbance and transmittance of the MSG are displayed in Figure S7. It can be seen that the MSG is highly transmissive in the visible and infrared (IR) region and only absorbs in the ultraviolet (UV) region [23]. The absorbance and transmittance of the GO and TRGO samples in Figure 4 are presented from the visible to the IR region. The GO and TRGO-100 absorbs (Figure 4a) highly in the visible range, which is confirmed by the zero transmittance within the same region. The hump around 300 nm can be attributed to the $n \rightarrow \pi^*$ transitions of the carbonyl (C=O) groups on the GO and TRGO-100 [24–26]. The lack of a hump at 300 nm after the 200 °C RT shows a successful oxygen reduction. Thus, the TRGO samples were reduced at 200 °C. Unlike the reduced GO oxide dispersed in water, which shows a similar absorption curve to that of the GO, albeit at a slightly increased absorption intensity (see absorption UV-Vis in [24,25]). The TRGO with RT $\geq$ 200 °C has a linear absorption curve similar to that of graphite [26]. Figure 4b shows that the GO and TRGO-100 have transmittance in the infrared region, unlike the other TRGO samples. These results confirm the appearance of the prepared thin films displayed in Figure S1, where the GO thin film is transparent and yellow-brownish, while the TRGO-100 is also semi-transparent and brown-blackish [12,19]. The other TRGO samples prepared at above 200 °C are opaque and dull black turning to shiny graphite grey. This further confirms that the reduction process occurred at 200 °C.

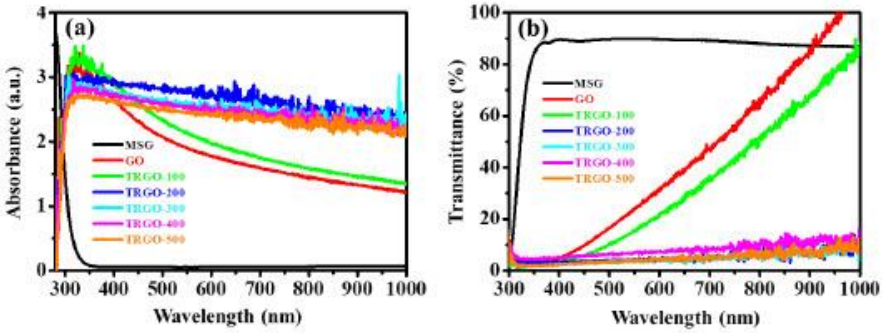

Figure 4. UV-Vis. (a) Absorbance and (b) transmittance of the GO, MSC, and TRGO-100 to TRGO–500.

3.4. Raman Spectroscopy

Raman spectroscopy was used to analyse the structural changes that occurred during the oxidation from graphite to GO and the reduction from GO to TRGO. The spectra of the natural graphite powder and GO/TRGO were measured at an excitation wavelength of 532 nm at room temperature and are displayed fully in Figure S8, while the one-phonon peaks are displayed in Figure 5a. In general, the obtained spectra exhibited peaks occurring in both one- and two-phonon Raman regions, D, G, 2D, D+G, and 2D′, occurring at around 1363, 1604, 2714, 2936, and 3197 cm^{-1}, respectively. The D peak is associated with the local defects and disorder of the edges of the graphene and graphite materials, while the G peak is due to the highly ordered hexagonal structure within the graphite [17,19]. The 2D is an overtone of the D peaks, which is a fingerprint of the graphene-sheet formation and number of layers. The D+G and 2D′ are the overtone peaks of the combination of the D, G, and D′ peaks [27]. Upon the oxidation of the graphite, the Raman spectra of the GO showed significant differences bordering the one-phonon-range peaks. The broadening of the D peak from the full width at half maximum (FWHM) of 34.9 to 117.1 cm^{-1} is due to the defects caused by the attachment of the O-containing functional groups on the graphitic sheets in the oxidation reaction process. The increase in the FWHM of the G peak from 20.1 to 66.9 cm^{-1} is also due to the bond-angle disorder caused by the attachment of the

O-containing functional groups. This caused the average ideal graphite-like hexagonal 120° bond angle to change [28] (see Figure 6a). As the temperature increases, there is no significant difference in the overall spectra, except the fading of the overtone peaks, which was probably due to restacking, as seen on the XRD, and the damage of the graphene sheets due to the defects. The FWHM of the D and G peaks seemed not to decrease, regardless of the removal of the OFGs. This was also observed by Claramunt et al. [29] when reducing the GO in the temperature range of 100 to 900 °C. The fading of the overtone peaks suggests that the layers increased (or restacked), since they only appear from graphitic crystallites containing few layers of graphene sheets. Thus, the stacking increased as temperature increased. As seen on the XRD, the interspace distance decreased, implying a high level of stacking, which will have led to low 2D intensity. Papani et al. [30] showed that the quality of graphene sheets is determined by the presence of 2D peaks; thus, the absence of a 2D peak suggests highly defective graphene sheets similar to the Raman spectra of activated carbon [31,32].

The Raman spectra in Figure 6a show that there is no D-peak shift, since it has been shown that Raman is insensitive to oxygen-related defects, such as -OH and -OOH [33]. The G band has a slightly red shift, which was attributed to the oxygen reduction, since this peak shifted to the oxygen-free graphite peak [29,34]. This was confirmed by the XRD and EDS, since they also showed the increasing removal of the OFGs as a function of the increasing RT. The Raman spectra of these samples were deconvoluted using the Lorentzian function in the D and G regions and are displayed in Figure 5b–h. The obtained additional peaks, labelled D*, D, and D′ were attributed to the lattice vibration of the sp^2-sp^3 bonds and phonon modes in the density of states of the graphitic crystallites, the amorphous carbon in the interstitial sites of the carbon lattice, and the carbon-lattice vibrations corresponding to that of the G band, respectively [28,35]. Note that the D*, D″, and D′ peaks were not observed in the graphite spectrum. The ratios (measured by the decrease in the X/G, where X = D, D*, D″, D′, and D/D′) of the area under the different deconvoluted peaks are displayed in Figure 6b–d. The D/G displayed in Figure 6b shows an increase from the graphite to the GO because of the defects during the reduction process. Upon the reduction at 100 °C, the graph increased because of the vacancy caused by the removal of the intercalated H_2O, the low thermal OFGs, and the crumpling of the graphene sheets. The remaining functional groups also contributed to the D band. Figure 6b shows the crystallite size (L_a) determined by the Knight formula using Equation (2) [28,31]

$$L_a = C(\lambda)/(D/G) \quad (2)$$

where $C(\lambda)$ is the wavelength-dependent pre-factor determined from the $C(\lambda) \approx C_0 + \lambda C_1$ for the wavelength in the visible range (400 nm< λ < 700 nm) $C(\lambda) = 4.96$ nm for $\lambda = 532$ nm, C_0 and C_1, which were estimated to be around −12.6 nm and 0.033, respectively [28,31]. The crystallite size decreased dramatically from 22 (graphite) to ~1.5 nm (GO/TRGO-100) due to the graphene-sheet breakdown during oxidation via Hummer's method. The crystallite size (sp^2 cluster) also increased as the RT increased, suggesting a slight structural recovery. The D″/G and D′/G are displayed in Figure 6c. The amorphous carbon (D″/G) increases from the GO to the TRGO-100 were due to the removal of OFGs, which resulted in damage to the graphene sheets. When the RT increased beyond 100 °C, the degree of amorphous carbon reduced, further confirming the structural recovery of the graphene. The ratio of the defect-activated mode (D′) relative to the graphitic carbon (G) (D′/G) shows an increase between the GO and the TRGO-100 (i.e., from 0.24 to 2.07) and a decrease to 0.36 in the TRGO-500, showing that the amount of defects reduced. Moreover, studies have shown that defect-activated modes (D/D′) (Figure 6d) are proportional to the defect concentration (n_d). The n_d can be estimated from the assumption that $I_D \sim A_d n_d$ and $I_{D'} \sim B_d n_d$, where A_d and B_d are constants, depending on the type of perturbation introduced by the defect in the crystal lattice (or the nature of the defects). Thus, $I_{D'}/I_D \sim A_d/B_d$, and the ratio can be used to acquire the information on the nature (or types) of defects. If $I_{D'}/I_D \cong 13$, the defects are associated with sp^3 hybridisation for vacancy-related defects

$I_{D'}/I_D \cong 7$ and $\cong 3.5$ for boundary defects [28,36]. Thus, the TRGO samples featured various defects.

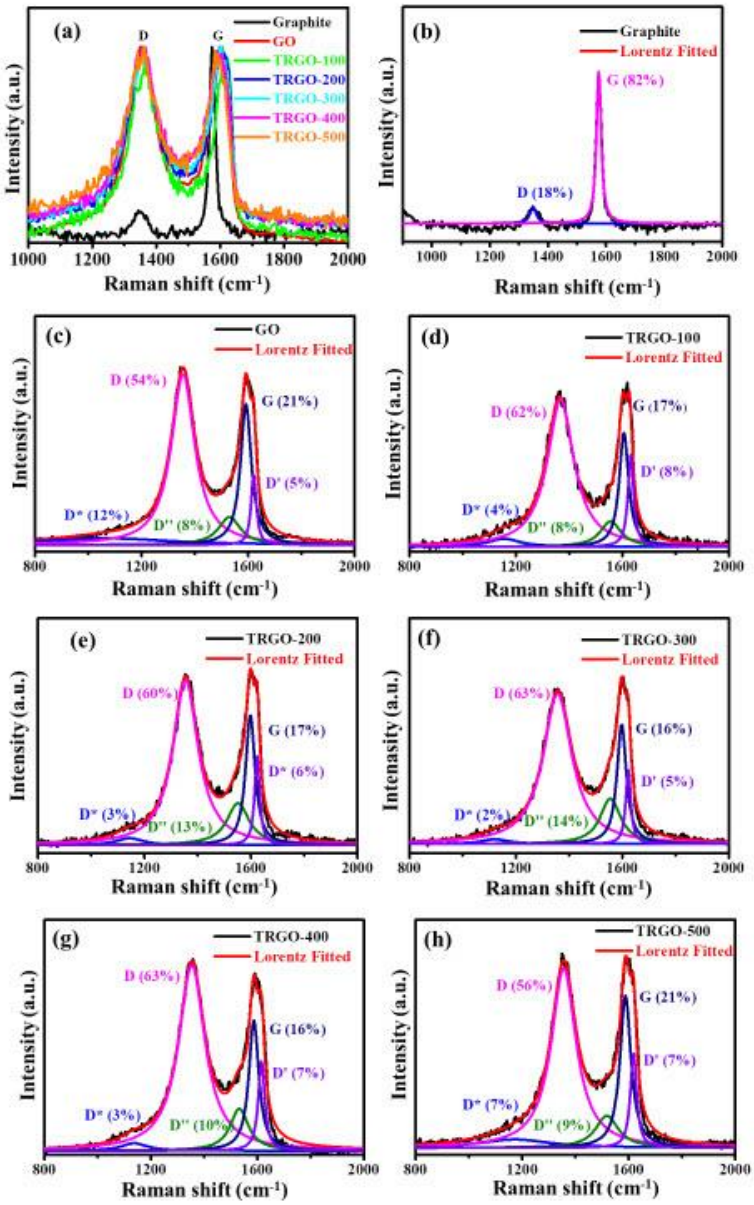

Figure 5. Raman spectra intensity of graphite, GO, and TRGO-100 to TRGO-500. One-phonon region of the Raman spectra of (**a**) graphite, (**b**) GO, and (**c**–**h**) TRGO-100–TRGO-500, plotted together with the best fit ($R^2 > 0.95$ and $\chi^2 < 100$) of the experiment to the sum of the five components (D*, D, D'', G, and D').

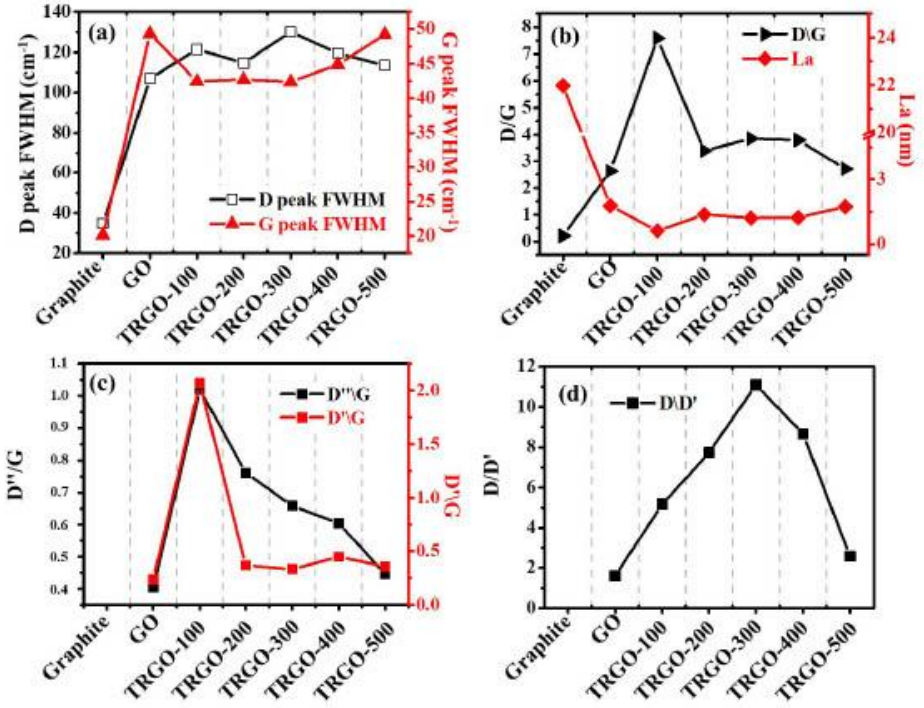

Figure 6. The (a) D- and G-peak FWHM, (b) D/G and La, (c) D″/G and (d) D/D′ as a function of graphite, GO, and TRGO-100 to TRGO-500.

3.5. Electric Studies

The electrical properties of the TRGO thin film at various temperatures were measured using the four-point-probe (4PP) method [37,38]. The sheet resistance (R_s) measurement was determined using Equation (3)

$$R_S = 4.53 \times \frac{V}{I} \ (\Omega/\text{sq.}) \quad (3)$$

where 4.53 is the thickness-correction constant, V is the voltage in volts, and I is the current in amperes between probes, respectively. The sheet resistance as a function of RT is displayed in Figure 7a. Note that the sheet resistance for GO and TRGO-100 could not be determined due to the high oxygen content and intercalated water. This is in line with the FTIR and EDS displayed in Figure S6 and Figure 3, which show that the GO and TRGO-100 had pronounced notch and oxygen peaks due to high concentration of OFGs compared to those reduced at 200 °C and above. These results are also confirmed by the UV-Vis in Figure 4, showing the presence of the carbonyl (C=O) groups on the GO and TRGO-100. The UV-Vis shows the correlation between the transparent thin films; the light green area is transparent and the dark green is opaque at 550 nm. It can be seen that the sheet resistance decreases with the increase in RT. This is due to the removal of the surface-attached OFGs, such as -OH. Thus, the TRGO-500 has the lowest oxygen content, which causes the least resistance. Figure 7b shows the possible relationship between the carbon content in the EDS and the amorphous (D″/G) of the TRGO-200 to TRGO-500 for the sheet resistance. It can be easily inferred that a higher degree of lower carbon content, i.e., higher oxygen content (C/O), increases the resistivity. Such results have been also observed in non-carbon-based

materials. Marciel et al. [39] showed that MoO_x thin film grown at a higher O_2/Ar flow rate is more resistive compared to that grown in the absence of O_2. It is clear that the carbon content is directly proportional to the sheet resistance and indirectly proportional to the degree of amorphousity. This behaviour can be also attributed to the slight structural recovery shown in Figure 6, according to which the sp^2 cluster (L_a), degree of defect (D/G), and amount of defects (D′/G) decreased to those of the graphite.

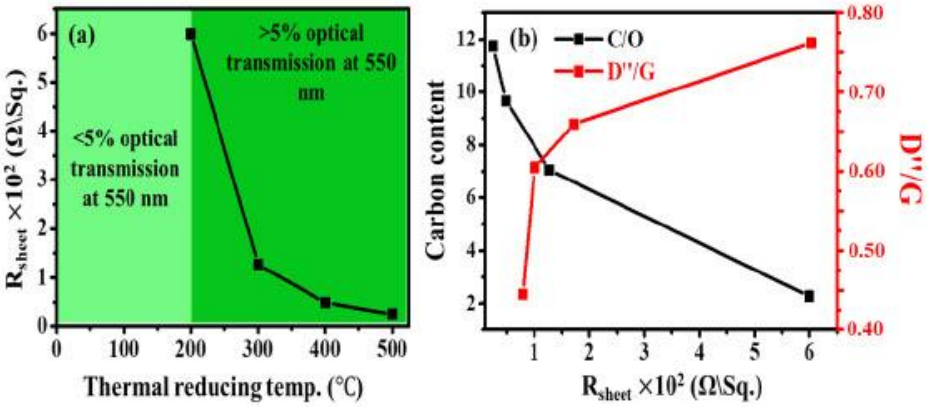

Figure 7. (**a**) Sheet resistance as a function of RT of the TRGO-200 to TRGO-500 and (**b**) carbon content and D″/G as function of sheet resistance.

3.6. Electrochemistry

The electrochemical performance of the prepared TRGO thin films was tested on a microsupercapacitor (μ-SC) configuration, displayed in Figure S9. The μ-SC schematic is displayed in Figure 8a. The detail of the schematic is presented in Table S3. Note that the detailed preparation and fabrication μ-SC is shown in our previous study [12], which also elucidated that the optimum capacitance was obtained at 14 digits per unit area due to the balance of the following factors: the average ionic diffusion pathway between adjacent digits [40,41]; the distributed capacitance effect, which suggests that higher digits lead to superior electrochemical performance [42]; the removal of the active electrode mass, which increases as the number of digits increase, resulting in reduced capacitance and an increase in the electric field strength around the edges of the interdigitated electrode. It is well known that the electric field line strength increases for edge-intensive electrodes rather than continuous or round-shaped electrodes [43,44]. The measured (CV) curves of the prepared μ-SC from the TRGO samples are displayed in Figure S10. The rectangular- shaped CV curves clearly indicate electrochemical double-layer capacitance (EDLC) characteristics within a working potential of 0.8 V. The CV curves show an increase in the scan rate relative to the RT (Figure 8b). This behaviour could be attributed to the increase in conductivity caused by the removal of the OFGs. Figure 8c illustrates the areal capacitance calculated from the CV curves in Figure S10 at various RT using Equation (S1), and the calculated value are also displayed in Table S4. It can be clearly seen that the areal capacitance decreased as the RT increased. This can also be attributed to the decrease in the oxygen content, which has been shown to enhance the pseudocapacitive behaviour of graphene oxide [45], provide high wettability [19], and serve as a passage for ions into the inner bulk material [11]. The high interplanar distance determined from the XRD also provides easy access for the ions within the μ-SC material. The areal capacitance also dramatically decreases for μ-SC with higher oxygen content compared to those with lower oxygen content due to a lack of interaction time. This suggests that high-oxygen-content μ-SC makes a higher contribution of diffusion-controlled behaviour. Thus, oxygen-deprived TRGO has a better rate capability.

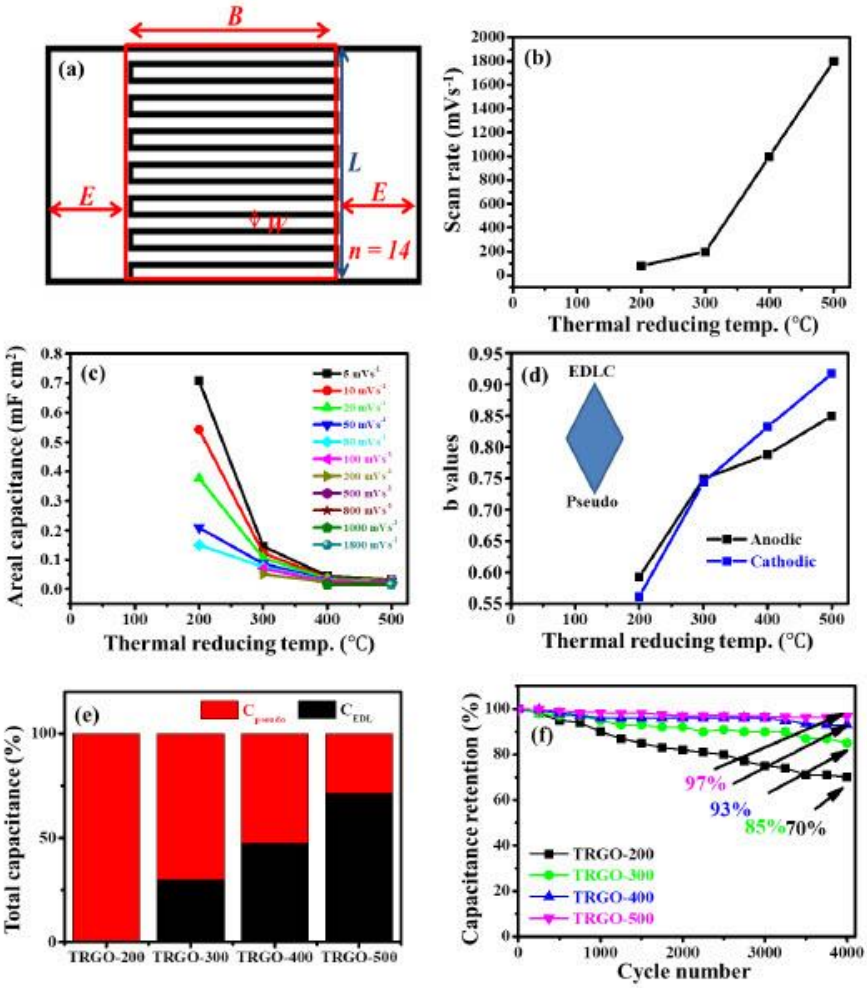

Figure 8. (a) μ-SC schematic, (b) scan rate, (c) areal capacitance, (d) b values versus RT, (e) Trasatti analysis capacitive contribution, and (f) capacitance retention as a function of cycle number of TRGO samples.

To extensively analyse the contributions of surface- and diffusion-controlled behaviours within the prepared TRGO μ-SC, the CV curves displayed in Figure S10 were utilised to obtain the values of the current (i) corresponding to the scan rate (v). According to the power law ($i = av^b$), a and b are adjustable values, whereas the b value of 0.5 indicates that the current is controlled by diffusion-controlled behaviour, and the b value of 1 indicates that the current is controlled by surface-controlled behaviour. The graph of the log scan rate versus the log current is displayed in Figure S11, while Figure 8d illustrates the b values versus RT. These figures signify an increase in the dominance of the capacitive-controlled process as the RT increases. This is due to the decrease in OFGs limiting the diffusion-controlled behaviour [46].

A Trasatti analysis (Figure S12) was performed to calculate the pseudocapacitance and EDL capacitance contributions. The maximum total capacitance (C_T) was obtained from the reciprocal of the extrapolated intercept of the $1/C_T$ versus $v^{0.5}$ and the maximum EDL capacitance (C_{EDL}) was estimated from the extrapolated intercept of C_{EDL} versus $v^{-0.5}$, while the maximum pseudocapacitance (C_p) was obtained from the difference between C_T and C_{EDL} (Equation (S2)). The obtained values are displayed in Table S5 and Figure 8e. It can also be seen that the capacitive mechanism dominated as the RT increased. The GCD curves are displayed in Figure S13; they show an isosceles-triangle-like curves, indicating EDLC behaviour. Thus, these results coincide with the CV curves and their analysis. The areal capacitances were also calculated from the GCD, and the obtained values are displayed in Table S6 and Figure S14a. Figure S14a shows similar behaviour to that of the areal capacitance from the CV curves versus the RT, displayed in Figure 8c. The areal capacitance also decreased, as mentioned above, and, interestingly, the high-temperature-reduced μ-SC can function at an extremely low current density compared to the low-temperature-reduced μ-SC, due to its low electrical resistance, as determined by the 4PP. The GCD stability of the four TRGO samples was analysed, and the results are displayed in Figure S14b–e. The capacitance columbic efficiency was 100% throughout the measurement, while the capacitance retention, also displayed in Figure 8f, showed an increase as the RT increased due to the removal of the oxygen during the electrochemical stability measurement [47]. These results are in agreement with the studies reported by Yang et al. [48,49], which showed the possibility of electrochemically reducing graphene oxide by repetitive cathodic cycling, which resulted in the elimination of electrochemically unstable functional groups. Thus, the high capacitance retention can be attributed to the maintenance of the structural integrity of the μ-SC active material after continuous GCD cycling. The areal energy (E_{areal}) and power (P_{areal}) densities were calculated using Equations (S3) and (S4), respectively. The TRGO-200-to-TRGO-500 μ-SCs delivered areal power ranging from 0.3316 to 0.3709 mW cm^{-2}, corresponding to areal energy in the range of 0.1368–0.0017 mW h cm^{-2} at various areal current densities. It is very clear that the delivered areal energy decreased as the reducing temperature increased, while the power increased due the removal of pseudocapacitive OFGs and increased conductivity. Note that the electrochemical performances of the prepared μ-SC are displayed on Table 1 and also compared with the performances of other μ-devices.

Furthermore, the TRGO μ-SCs were also analysed using the EIS. The obtained Nyquist plot is displayed in Figure 9a, while the high-frequency zoom of the Nyquist plot is displayed in Figure S14f. The Nyquist plot indicates that the TRGO-200 to TRGO-500 had a solution resistance (R_s) of 4705, 3595, 2584, and 2326 Ω, respectively. The R_s decreased as the RT increased due to the removal of the resistive OFGs on the edge of the GO sheets. The R_s was used to calculate the maximum specific power (P_{max}) using Equation (4). The maximum specific energy (E_{max}) was calculated using Equation (5).

$$P_{max} = \frac{V^2}{4 \times (ESR) \times A_{area}} \quad (4)$$

$$E_{max} = \frac{C_T V^2}{7.2 \times A_{area}} \quad (5)$$

where V, ESR, A_{area}, and C_T are the operating potential (v), equivalent series resistance (Ω), total active μ-SC area (cm^2), and total capacitance (F cm^{-2}) from the Trasatti analysis displayed in Figure S12. The obtained values for the maximum specific power and maximum specific energy are displayed in Table S7.

Table 1. Comparison of electrochemical performance of carbon-based micro-devices.

Device Configuration	GO Reduction Method	Electrolyte	*V* (v)	CR (%)	Capacitance	E_S @ P_S @ C_d	Ref.
TRGO-200 †	Thermally treated at 200 °C in Ar for 10 min	PVA/H_3PO_4	0.8	95	0.7074 mF cm^{-2} @ 5 mVs^{-1}	0.3329 mW h cm^{-2} @ 0.1093 mW cm^{-2} @ 8.3 mA cm^{-2}	This work
TRGO-500 †	Thermally treated at 500 °C in Ar for 10 min	PVA/H_3PO_4	0.8	70	0.0319 mF cm^{-2} @ 5 mVs^{-1}	0.0380 mW h cm^{-2} @ 0.3663 mW cm^{-2} @ 8.3 mA cm^{-2}	This work
rGO/MWCNT †	788-nanometer-infrared-laser-treated at a power output of 5 mW	PVA/H_3PO_4	1	85.5	46.6 F cm^{-3}	6.47 mW h cm^{-3} @ 10 mW cm^{-3} @ 20 mA cm^{-3}	[50]
TRGO-coated fabric †	Thermally treated at 160 °C in Ar for 2 h	PVA/H_3PO_4	1	93	70.4 F g^{-1} at 5 mV s^{-1}	5.8 W h kg^{-1} @ 27.7 k W kg^{-1} @ 0.1 mA cm^{-2}	[51]
pErGO@Cuf	Electrochemically reduced at an applied potential of −1.2 V for 20 CV cycles.	PVA/H_3PO_4	1	94.5	283.5 mF cm^{-2} at 0.5 Ag^{-1}	39.3 µW h cm^{-2} @17.6 mW cm^{-2}	[47]
Hydrothermally reduced GO	Hydrothermal method at 150 °C for 10 h in water	PVA/H_3PO_4-Na_2MoO_4	1	~100	38.2 mF cm^{-2}	5.3 µW h cm^{-2}	[52]
rGO/PEDOT	GO was laser-reduced and PEDOT was vapour-phase-polymerised onto rGO	PVA/H_3PO_4	0.8	90.2	35.12 Fcm^{-3} at 80 mAcm^{-3}	4.876 mW h cm^{-3} @ 40 mW cm^{-3}	[53]
LSG/MnO	Laser-educed at 532 nm	PVA/H_3PO_4	0.8	96	55 mF cm^{-2} @ 0.1 mA cm^{-2}	4.89 µW h cm^{-2} @ 0.72 mW cm^{-2} @ 0.1 mA cm^{-2}	[45]

†–symmetric device; *V*–voltage, CR–capacitor retention, rGO/MWCNT–reduced graphene oxide/multi-wall carbon nanotube; pErGO@Cuf–porous electrochemically reduced graphene oxide on cupper foam, PEDOT-poly(3,4-ethylenedioxythiophene), and LSG—laser-scan graphene.

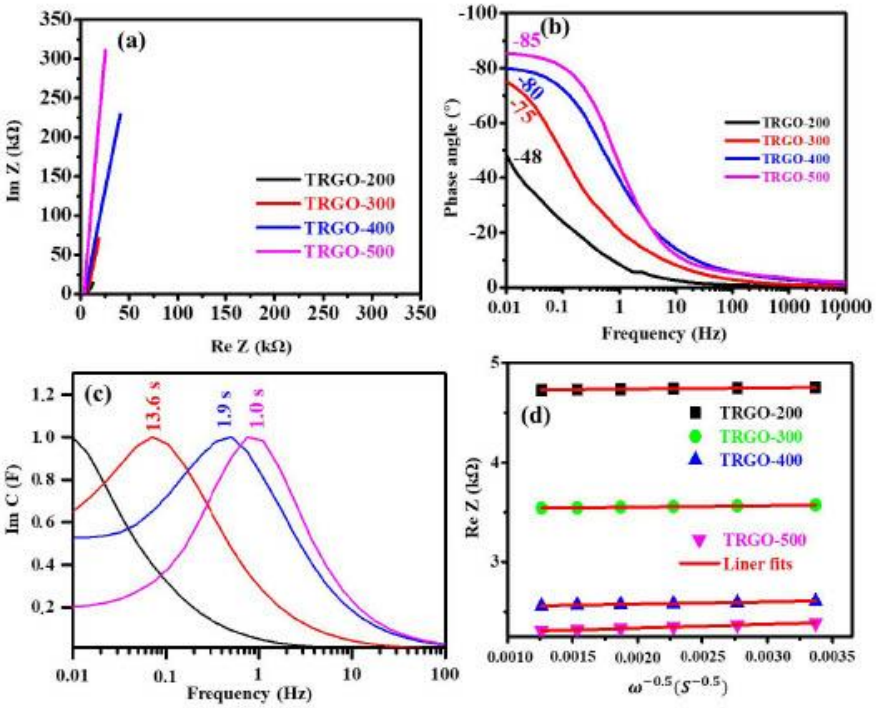

Figure 9. (a) EIS Nyquist plot, (b) phase angle versus frequency, (c) imaginary plot of capacitance as a function of frequency, and (d) real Z versus $\omega^{-0.5}$ at low frequencies for the TRGO samples, as labelled in the figures.

The Nyquist plot shows that the shape of the TRGO sample is similar to that of the porous carbon supercapacitors [54]. The plot does not show any semi-circular regions, indicating that the TRGO materials possessed very low charge-transfer resistance [54,55]. The plot also intersects with the real axis at 45°; this was attributed to Warburg impendence, in which electrolyte ions diffuse into porous electrodes, characterised by the linear part of the sloped line parallel to y-axis. A pure capacitor should exhibit a vertical line at low frequency, and the deviation from the vertical line is attributable to the diffusion resistance of the electrolyte ions [56]. The Bode plot displayed in Figure 9b shows the dependence of the impedance phase angle on the frequency of the TRGO samples. The phase angle increased as the temperature increased from −48 to −85°, which is close to the ideal value of the full capacitive behaviour of any supercapacitor [47,54]. The frequency dependence of the real and imaginary part of the capacitance (Re C and −Im Z) were evaluated using the complex capacitance model presented in Equations (S5)–(S9) [57,58] and displayed in Figure S15. The Re C signifies the real accessible capacitance of the μ-SC and Im C corresponds to the energy loss by the irreversible process. The Im C in Figure 9c shows the peak frequency (knee frequency), which corresponds to the relaxation time ($\tau_o = f_0^{-1}$), indicating the minimum time required to charge/discharge the μ-SC with an efficiency greater than 50% [47,58]. The TRGO-500 μ-SC showed the lowest relaxation time compared to the other TRGO μ-SC. In Figure 9a, the Nyquist plot shows a slightly inclined line, which is attributable to the diffusion of the electrolyte ions into the bulk of the active electrode

material, also referred to as Warburg diffusion. The Warburg coefficient σ_w was estimated using the Equation (6) [59]:

$$Re\,Z = R_e + R_{ct} + \sigma_w \omega^{-0.5} \quad (6)$$

where R_e, R_{ct}, $Re\,Z$, and $\omega^{-0.5}$ are the electrolyte resistance, charge-transfer resistance, real impendence corresponding to the angular frequency in the low-frequency region and the square root of the lower angular frequency. Note that the R_e and R_{ct} parameters are independent of the frequency. Thus, the slope obtained from the $Re\,Z$ dependence on the reciprocal square root of the lower angular frequencies ($\omega^{-0.5}$) correspond to the Warburg coefficient σ_w. The obtained values are displayed in Table S7 and Figure 9d, and replotted for clarity in Figure S16. It can be observed that the TRGO-200 had the lowest Warburg coefficient σ_w of 12.4831 Ω cm^2 s$^{-0.5}$, compared to the other µ-SCs. Thus, the TRGO-200 had the highest ion diffusion coefficient of 4.3075 $\times$ 10^{-13} cm^2 s^{-1}, since the Warburg coefficient is directly proportional to the ion diffusion coefficient (Equation (S10)). The TRGO-200 had a higher ion diffusion because many OFGs were present on the surface of the TRGO-200 graphene sheets, i.e., hydroxyl, carboxyl, and epoxy groups, which served as passages to the internal surface for the ions [11]. In addition, the XRD showed a large interplanar distance on the TRGO-200. This allowed the easy diffusion of ions into the internal surface.

4. Conclusions

A detailed investigation of the GO/TRGO thin film on MSG following different reduction temperatures was presented. This study follows from our previous work, which mainly focused on microsupercapacitor applications [12]. It was demonstrated that the XRD-calculated interspace distance decreased, while the EDS also showed an increase in carbon content as the RT increased. The amorphous carbon ($I_{D''}/I_G$) and degree of defect (I_D/I_G) decreased with increases in RT, suggesting structural recovery. The four-point probe (4PP) showed that the TRGO at higher temperatures had a lower sheet resistance, i.e., it was highly conductive. The electrochemical performance showed that the TRGO-200 µ-SC had higher areal energy and lower areal power because more ions diffused into the internal surface, as suggested by the power law and Trasatti's analysis. The TRGO-200 µ-SC had lower capacitance retention than the other µ-SCs due to the further reduction of the GO due to the repetitive GCD electrochemical measurements. The µ-SCs prepared at higher RT showed lower areal energy and higher areal power due to the narrow interplanar distance and a lack of OFGs preventing intercalation and promoting ion adsorption. Thus, lower and higher RT µ-SC are governed by diffusion- and surface-controlled behaviour, respectively.

Supplementary Materials: The following supporting information can be downloaded at: https://www.mdpi.com/article/10.3390/nano12132211/s1, Figure S1: The digital images showing the appearance (colour) of the prepared thin film on MSG, Figure S2: The XRD patterns of (a) GO and (b)–(f) TRGO-100 to TRGO-500, plotted together with the diffraction pattern of the microscopic glass under the same conditions, Table S1: Sample ID, interplanar distance and carbon content, Figure S3: (a) Interspace distance and (b) C/O ratio as a function for graphite, GO and TRGO-100, TRGO-200, TRGO-300, TRGO-400 and TRGO-500, Figure S4: SEM images of (a) graphite, (b) GO, (c) TRGO-300 and (d) TRGO-500, Figure S5: The AFM micrograph of (a) GO and (b)–(f) TRGO-100 to TRGO-500; and (g) corresponding height colour scale, Figure S6: The FTIR of graphite, MSG, GO and TRGO samples, Table S2: Roughness parameter of the prepared GO/TRGO thin film, Figure S7: (a) Absorbance and (b) transmittance of microscope glass, Figure S8: Raman spectra of graphite, GO and TRGO-100–TRGO-500, Figure S9: Digital image of µ-SC, Table S3: Dimensions and parameters of µ-SC, Figure S10: (a)–(d) CV curves of TRGO 200–TRGO 500, Table S4: The areal capacitance determined from the CV curve, Figure S11: log I versus log v curves for the anodic and cathodic currents at (a) TRGO-200, (b) TRGO-300, (c) TRGO-400 and (d) TRGO-500 reducing temperatures, respectively, Figure S12: Trasatti's method for the TRGO micro-supercapacitors: (a,c,e,g) inverse capacitance as a function of square root of scan rate and (b,d,f,h) capacitance as a function of inverse

square root of scan rate, Table S5: Sample ID, maximum total capacitance, maximum EDL capacitance and maximum pseudocapacitance, Figure S13: (a)–(d) GCD curves of TRGO 200–TRGO 500, Table S6: The areal capacitance determined from the GCD curve, Figure S14: (a) Area capacitance as a function of reducing temperature at various current densities, (b)–(e) the capacitance retention and capacitance columbic efficiency of the TRGO sample and (f) EIS Nyquist plot at high frequency region, Table S7: Sample ID, resistance electrolyte plus charge transfer resistance ($R_e + R_{ct}$), Warburg coefficient (σ_w) and ion diffusion coefficient (D), Figure S15: The frequency dependence of the Re C and Im C for (a)–(b) TRGO-200 to TRGO-500 and Figure S16: The relationship between Re Z and $\omega^{-0.5}$ at low frequencies for TRGO samples [60].

Author Contributions: V.M.M.: conceptualisation, methodology, software, formal analysis, investigation, visualisation, writing—original daft, and writing—review and editing. D.T.B.: visualisation and writing—review and editing. S.S.: visualisation and writing—review and editing. N.F.S.: methodology and visualisation. G.R.: methodology, visualisation, formal analysis, and writing—review and editing. N.M.: resources, supervision, funding acquisition, visualisation, formal analysis, and writing—review and editing. All authors have read and agreed to the published version of the manuscript.

Funding: This study was supported by the National Research Foundation (NRF) of South Africa (grant number 61056) together with the South African Research Chairs Initiative (SARChI) of the Department of Science and Technology.

Institutional Review Board Statement: Not applicable.

Informed Consent Statement: Not applicable.

Data Availability Statement: Data is contained within the article or supplementary material.

Acknowledgments: Vusani M. Maphiri acknowledges the NRF bursary through SARChI in Carbon Technology and Materials and the University of Pretoria for financial support.

Conflicts of Interest: The authors declare no conflict of interest.

References

1. Shin, D.H.; Choi, Y.S.; Park, S.Y.; Yeo, C.S.; Park, Y.Y.; Song, J.Y.; Lee, S.K.; Kim, T.W.; Bae, S.; Hong, B.H. Fast and complete recovery of TMDs-decorated rGO fiber gas sensors at room temperature. *Appl. Surf. Sci.* **2022**, *578*, 151832. [CrossRef]
2. Maphiri, V.M.; Bakhoum, D.T.; Sarr, S.; Sylla, N.F.; Rutavi, G.; Manyala, N. Low temperature thermally reduced graphene oxide directly on Ni-Foam using atmospheric pressure-chemical vapour deposition for high performance supercapacitor application. *J. Energy Storage* **2022**, *52*, 104967. [CrossRef]
3. Xu, T.; Chen, J.; Yuan, W.; Li, L.; Sun, Y.; Wu, H.; Yang, L. Investigating the hydrogen storage capacity of surfactant modified graphene. *Energy Procedia* **2019**, *158*, 2112–2117. [CrossRef]
4. Díez-Betriu, X.; Álvarez-García, S.; Botas, C.; Álvarez, P.; Sánchez-Marcos, J.; Prieto, C.; Menéndez, R.; de Andrés, A. Raman spectroscopy for the study of reduction mechanisms and optimization of conductivity in graphene oxide thin films. *J. Mater. Chem. C* **2013**, *1*, 6905–6912. [CrossRef]
5. Sengupta, I.; Chakraborty, S.; Talukdar, M.; Pal, S.K.; Chakraborty, S. Thermal reduction of graphene oxide: How temperature influences purity. *J. Mater. Res.* **2018**, *33*, 4113–4122. [CrossRef]
6. Moyseowicz, A.; González, Z.; Menéndez, R.; Gryglewicz, G. Three-dimensional poly(aniline-co-pyrrole)/thermally reduced graphene oxide composite as a binder-free electrode for high-performance supercapacitors. *Compos. Part B Eng.* **2018**, *145*, 232–239. [CrossRef]
7. Wang, W.; Guo, S.; Lee, I.; Ahmed, K.; Zhong, J.; Favors, Z.; Zaera, F.; Ozkan, M.; Ozkan, C.S. Hydrous Ruthenium Oxide Nanoparticles Anchored to Graphene and Carbon Nanotube Hybrid Foam for Supercapacitors. *Sci. Rep.* **2014**, *4*, 4452. [CrossRef]
8. Karaphun, A.; Phrompet, C.; Tuichai, W.; Chanlek, N.; Sriwong, C.; Ruttanapun, C. The influence of annealing on a large specific surface area and enhancing electrochemical properties of reduced graphene oxide to improve the performance of the active electrode of supercapacitor devices. *Mater. Sci. Eng. B* **2021**, *264*, 114941. [CrossRef]
9. Zhu, P.; Shen, M.; Xiao, S.; Zhang, D. Experimental study on the reducibility of graphene oxide by hydrazine hydrate. *Phys. B Condens. Matter.* **2011**, *406*, 498–502. [CrossRef]
10. Chen, C.M.; Zhang, Q.; Yang, M.G.; Huang, C.H.; Yang, Y.G.; Wang, M.Z. Structural evolution during annealing of thermally reduced graphene nanosheets for application in supercapacitors. *Carbon N. Y.* **2012**, *50*, 3572–3584. [CrossRef]
11. Zhao, B.; Liu, P.; Jiang, Y.; Pan, D.; Tao, H.; Song, J.; Fang, T.; Xu, W. Supercapacitor performances of thermally reduced graphene oxide. *J. Power Sources* **2012**, *198*, 423–427. [CrossRef]
12. Maphiri, V.M.; Rutavi, G.; Sylla, N.F.; Adewinbi, S.A.; Fasakin, O.; Man, N. Novel Thermally Reduced Graphene Oxide Microsupercapacitor Fabricated via Mask—Free AxiDraw Direct Writing. *Nanomaterials* **2021**, *11*, 1909. [CrossRef] [PubMed]

13. Huang, C.; Zhang, J.; Young, N.P.; Snaith, H.J.; Grant, P.S. Solid-state supercapacitors with rationally designed heterogeneous electrodes fabricated by large area spray processing for wearable energy storage applications. *Sci. Rep.* **2016**, *6*, 25684. [CrossRef] [PubMed]
14. Xu, Y.; Huang, C.; Hu, A.; Fan, Z.; Chen, C.; Yang, Y.; Tang, Q.; Jiang, C.; Chen, X. N-rich reduced graphene oxide film with cross-coupled porous networks as free-standing electrode for high performance supercapacitors. *Appl. Surf. Sci.* **2021**, *563*, 150303. [CrossRef]
15. Yuliasari, F.; Aprilia, A.; Syakir, N.; Safriani, L.; Saragi, T.; Risdiana; Hidayat, S.; Bahtiar, A.; Siregar, R.; Fitrilawati. Characteristics of Thermally Reduced Graphene Oxide Thin Film as DSSC Counter Electrode. *IOP Conf. Ser. Mater. Sci. Eng.* **2017**, *196*, 012049. [CrossRef]
16. Zeng, Y.; Li, T.; Yao, Y.; Li, T.; Hu, L.; Marconnet, A. Thermally Conductive Reduced Graphene Oxide Thin Films for Extreme Temperature Sensors. *Adv. Funct. Mater.* **2019**, *29*, 1901388. [CrossRef]
17. Muniyalakshmi, M.; Sethuraman, K.; Silambarasan, D. Synthesis and characterization of graphene oxide nanosheets. *Mater. Today Proc.* **2020**, *21*, 408–410. [CrossRef]
18. Siburian, R.; Sihotang, H.; Raja, S.L.; Supeno, M.; Simanjuntak, C. New route to synthesize of graphene nano sheets. *Orient. J. Chem.* **2018**, *34*, 182–187. [CrossRef]
19. Bera, M.; Chandravati; Gupta, P.; Maji, P.K. Facile One-Pot Synthesis of Graphene Oxide by Sonication Assisted Mechanochemical Approach and Its Surface Chemistry. *J. Nanosci. Nanotechnol.* **2017**, *18*, 902–912. [CrossRef]
20. Brycht, M.; Leniart, A.; Zavašnik, J.; Nosal-Wiercińska, A.; Wasiński, K.; Półrolniczak, P.; Skrzypek, S.; Kalcher, K. Synthesis and characterization of the thermally reduced graphene oxide in argon atmosphere, and its application to construct graphene paste electrode as a naptalam electrochemical sensor. *Anal. Chim. Acta* **2018**, *1035*, 22–31. [CrossRef]
21. Bao, C.; Song, L.; Xing, W.; Yuan, B.; Wilkie, C.A.; Huang, J.; Guo, Y.; Hu, Y. Preparation of graphene by pressurized oxidation and multiplex reduction and its polymer nanocomposites by masterbatch-based melt blending. *J. Mater. Chem.* **2012**, *22*, 6088–6096. [CrossRef]
22. Rossouw, C.J.; Forwood, C.T.; Gibson, M.A.; Miller, P.R. Generation and absorption of characteristic X-rays under dynamical electron diffraction conditions. *Micron* **1997**, *28*, 125–137. [CrossRef]
23. Olenych, I.B.; Aksimentyeva, O.I.; Monastyrskii, L.S.; Horbenko, Y.Y.; Partyka, M.V. Electrical and Photoelectrical Properties of Reduced Graphene Oxide—Porous Silicon Nanostructures. *Nanoscale Res. Lett.* **2017**, *12*, 272. [CrossRef] [PubMed]
24. Çiplak, Z.; Yildiz, N.; Çalimli, A. Investigation of graphene/Ag nanocomposites synthesis parameters for two different synthesis methods, Fullerenes Nanotub. *Carbon Nanostructures* **2015**, *23*, 361–370. [CrossRef]
25. Sunderrajan, S.; Miranda, L.R.; Pennathur, G. Improved stability and catalytic activity of graphene oxide/chitosan hybrid beads loaded with porcine liver esterase. *Prep. Biochem. Biotechnol.* **2018**, *48*, 343–351. [CrossRef]
26. Theerthagiri, J.; Sudha, R.; Premnath, K.; Arunachalam, P.; Madhavan, J.; Al-Mayouf, A.M. Growth of iron diselenide nanorods on graphene oxide nanosheets as advanced electrocatalyst for hydrogen evolution reaction. *Int. J. Hydrogen Energy* **2017**, *42*, 13020–13030. [CrossRef]
27. Pawlyta, M.; Rouzaud, J.N.; Duber, S. Raman microspectroscopy characterization of carbon blacks: Spectral analysis and structural information. *Carbon N. Y.* **2015**, *84*, 479–490. [CrossRef]
28. Madito, M.J.; Ismail, M.Y.A.; Hlatshwayo, T.T.; Mtshali, C.B. The nature of surface defects in Xe ion-implanted glassy carbon annealed at high temperatures: Raman spectroscopy analysis. *Appl. Surf. Sci.* **2020**, *506*, 145001. [CrossRef]
29. Claramunt, S.; Varea, A.; López-López-Díaz, D.; Velázquez-Velázquez, M.M.; Cornet, A.; Cirera, A. The Importance of Interbands on the Interpretation of the Raman Spectrum of Graphene Oxide. *J. Phys. Chem. C* **2015**, *119*, 10123–10129. [CrossRef]
30. Papanai, G.S.; Sharma, I.; Gupta, B.K. Probing number of layers and quality assessment of mechanically exfoliated graphene via Raman fingerprint. *Mater. Today Commun.* **2020**, *22*, 100795. [CrossRef]
31. Sylla, N.F.; Ndiaye, N.M.; Ngom, B.D.; Momodu, D.; Madito, M.J.; Mutuma, B.K.; Manyala, N. Effect of porosity enhancing agents on the electrochemical performance of high-energy ultracapacitor electrodes derived from peanut shell waste. *Sci. Rep.* **2019**, *9*, 13673. [CrossRef] [PubMed]
32. Cuesta, A.; Dhamelincourt, P.; Laureyns, J.; Martínez-Alonso, A.; Tascón, J.M.D. Raman microprobe studies on carbon materials. *Carbon N. Y.* **1994**, *32*, 1523–1532. [CrossRef]
33. Sahoo, M.; Antony, R.P.; Mathews, T.; Dash, S.; Tyagi, A.K. Raman studies of chemically and thermally reduced graphene oxide. *AIP Conf. Proc.* **2013**, *1512*, 1262–1263. [CrossRef]
34. Krishnamoorthy, K.; Veerapandian, M.; Mohan, R.; Kim, S.J. Investigation of Raman and photoluminescence studies of reduced graphene oxide sheets. *Appl. Phys. A Mater. Sci. Process* **2012**, *106*, 501–506. [CrossRef]
35. de Lima, B.S.; Bernardi, M.I.B.; Mastelaro, V.R. Wavelength effect of ns-pulsed radiation on the reduction of graphene oxide. *Appl. Surf. Sci.* **2020**, *506*, 144808. [CrossRef]
36. Eckmann, A.; Felten, A.; Mishchenko, A.; Britnell, L.; Krupke, R.; Novoselov, K.S.; Casiraghi, C. Probing the Nature of Defects in Graphene by Raman Spectroscopy. *Nano Lett.* **2012**, *12*, 3925. [CrossRef]
37. Ahmed, M.; Bakry, A.; Qasem, A.; Dalir, H. The main role of thermal annealing in controlling the structural and optical properties of ITO thin film layer. *Opt. Mater.* **2021**, *113*, 110866. [CrossRef]

38. Adewinbi, S.A.; Taleatu, B.A.; Busari, R.A.; Maphiri, V.M.; Oyedotun, K.O.; Manyala, N. Synthesis and electrochemical characterization of pseudocapacitive α-MoO3 thin film as transparent electrode material in optoelectronic and energy storage devices. *Mater. Chem. Phys.* **2021**, *264*, 124468. [CrossRef]
39. Marciel, A.; Graça, M.; Bastos, A.; Pereira, L.; Kumar, J.S.; Borges, J.; Vaz, F.; Peres, M.; Magalhães, S.; Lorenz, K.; et al. Molybdenum oxide thin films grown on flexible ito-coated pet substrates. *Materials* **2021**, *14*, 821. [CrossRef]
40. Liu, L.; Ye, D.; Yu, Y.; Liu, L.; Wu, Y. Carbon-based flexible micro-supercapacitor fabrication via mask-free ambient micro-plasma-jet etching. *Carbon N. Y.* **2017**, *111*, 121–127. [CrossRef]
41. Chen, C.M.; Huang, J.Q.; Zhang, Q.; Gong, W.Z.; Yang, Q.H.; Wang, M.Z.; Yang, Y.G. Annealing a graphene oxide film to produce a free standing high conductive graphene film. *Carbon N. Y.* **2012**, *50*, 659–667. [CrossRef]
42. Tiliakos, A.; Trefilov, A.M.I.I.; Tanasă, E.; Balan, A.; Stamatin, I. Space-Filling Supercapacitor Carpets: Highly scalable fractal architecture for energy storage. *J. Power Sources* **2018**, *384*, 145–155. [CrossRef]
43. Tsang, T. Classical Electrodynamics. In *Classical Electrodynamics*; World Scientific: Singapore, 1998; p. 102. [CrossRef]
44. Hota, M.K.; Jiang, Q.; Mashraei, Y.; Salama, K.N.; Alshareef, H.N. Fractal Electrochemical Microsupercapacitors. *Adv. Electron. Mater.* **2017**, *3*, 1700185. [CrossRef]
45. Gao, M.; Dong, X.; Wang, K.; Duan, W.; Sun, X.; Zhu, C.; Wang, W. Laser direct preparation and processing of graphene/MnO nanocomposite electrodes for microsupercapacitors. *J. Energy Storage* **2021**, *33*, 102162. [CrossRef]
46. Augustyn, V.; Come, J.; Lowe, M.A.; Kim, J.W.; Taberna, P.L.; Tolbert, S.H.; Abruña, H.D.; Simon, P.; Dunn, B. High-rate electrochemical energy storage through Li + intercalation pseudocapacitance. *Nat. Mater.* **2013**, *12*, 518–522. [CrossRef]
47. Purkait, T.; Singh, G.; Kumar, D.; Singh, M.; Dey, R.S. High-performance flexible supercapacitors based on electrochemically tailored three-dimensional reduced graphene oxide networks OPEN. *Sci. Rep.* **2018**, *8*, 640. [CrossRef]
48. Yang, J.; Gunasekaran, S. Electrochemically reduced graphene oxide sheets for use in high performance supercapacitors. *Carbon N. Y.* **2013**, *51*, 36–44. [CrossRef]
49. Yang, J.; Deng, S.; Lei, J.; Ju, H.; Gunasekaran, S. Electrochemical synthesis of reduced graphene sheet–AuPd alloy nanoparticle composites for enzymatic biosensing. *Biosens. Bioelectron.* **2011**, *29*, 159–166. [CrossRef]
50. Mao, X.; Xu, J.; He, X.; Yang, W.; Yang, Y.; Xu, L.; Zhao, Y.; Zhou, Y. All-solid-state flexible microsupercapacitors based on reduced graphene oxide/multi-walled carbon nanotube composite electrodes. *Appl. Surf. Sci.* **2018**, *435*, 1228–1236. [CrossRef]
51. Ramadoss, A.; Saravanakumar, B.; Kim, S.J. Thermally reduced graphene oxide-coated fabrics for flexible supercapacitors and self-powered systems. *Nano Energy* **2015**, *15*, 587–597. [CrossRef]
52. Veerasubramani, G.K.; Krishnamoorthy, K.; Pazhamalai, P.; Kim, S.J. Enhanced electrochemical performances of graphene based solid-state flexible cable type supercapacitor using redox mediated polymer gel electrolyte. *Carbon N. Y.* **2016**, *105*, 638–648. [CrossRef]
53. Mao, X.; He, X.; Xu, J.; Yang, W.; Liu, H.; Yang, Y.; Zhou, Y. Three-Dimensional Reduced Graphene Oxide/Poly(3,4-Ethylenedioxythiophene) Composite Open Network Architectures for Microsupercapacitors. *Nanoscale Res. Lett.* **2019**, *14*, 267. [CrossRef] [PubMed]
54. Mathis, T.S.; Kurra, N.; Wang, X.; Pinto, D.; Simon, P.; Gogotsi, Y. Energy Storage Data Reporting in Perspective—Guidelines for Interpreting the Performance of Electrochemical Energy Storage Systems. *Adv. Energy Mater.* **2019**, *9*, 1902007. [CrossRef]
55. Quain, E.; Mathis, T.S.; Kurra, N.; Maleski, K.; van Aken, K.L.; Alhabeb, M.; Alshareef, H.N.; Gogotsi, Y. Direct Writing of Additive-Free MXene-in-Water Ink for Electronics and Energy Storage. *Adv. Mater. Technol.* **2019**, *4*, 1800256. [CrossRef]
56. Yuan, D.; Chen, J.; Tan, S.; Xia, N.; Liu, Y. Worm-like mesoporous carbon synthesized from metal–organic coordination polymers for supercapacitors. *Electrochem. Commun.* **2009**, *11*, 1191–1194. [CrossRef]
57. Rantho, M.N.; Madito, M.J.; Manyala, N. Symmetric supercapacitor with supercapattery behavior based on carbonized iron cations adsorbed onto polyaniline. *Electrochim. Acta* **2018**, *262*, 82–96. [CrossRef]
58. Oz, A.; Hershkovitz, S.; Belman, N.; Tal-Gutelmacher, E.; Tsur, Y. Analysis of impedance spectroscopy of aqueous supercapacitors by evolutionary programming: Finding DFRT from complex capacitance. *Solid State Ionics* **2016**, *288*, 311–314. [CrossRef]
59. Cui, Y.; Zhao, X.; Guo, R. Improved electrochemical performance of La0.7Sr0.3MnO_3 and carbon co-coated LiFePO4 synthesized by freeze-drying process. *Electrochim. Acta* **2010**, *55*, 922–926. [CrossRef]
60. Li, J.; Levitt, A.; Kurra, N.; Juan, K.; Noriega, N.; Xiao, X.; Wang, X.; Wang, H.; Alshareef, H.N.; Gogotsi, Y. MXene-conducting polymer electrochromic microsupercapacitors. *Energy Storage Mater.* **2019**, *20*, 455–461. [CrossRef]

Supplementary information

nanomaterials

MDPI

Supplementary Materials

Impact of Thermally Reducing Temperature on Graphene Oxide Thin Films and Microsupercapacitor Performance

Vusani M. Maphiri, Daba T. Bakhoum, Samba Sarr, Ndeye F. Sylla, Gift Rutavi and Ncholu Manyala *

Department of Physics, Institute of Applied Materials, SARChI Chair in Carbon Technology and Materials, University of Pretoria, Pretoria 0028, South Africa; vusanimuswamaphiri@gmail.com (V.M.M.); thiogna@yahoo.fr (D.T.B.); ssarr3112@gmail.com (S.S.); ntoufasylla@gmail.com (N.F.S.); rutavigift@yahoo.com (G.R.)

* Correspondence: ncholu.manyala@up.ac.za; Tel.: +27-12-420-3549; Fax: +27-12-420-3546

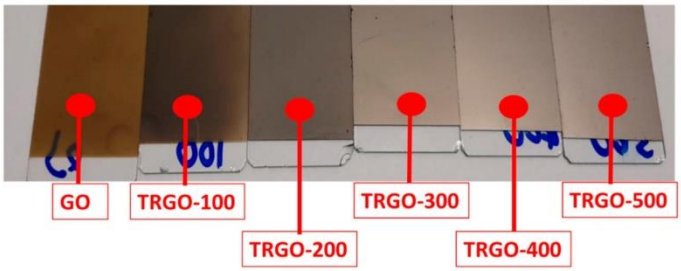

Figure S1. The digital images showing the appearance (colour) of the prepared thin film on MSG.

Figure S2a shows the interspacing distance of Graphite, GO and TRGO thin films. The interspacing distance of the TRGO-100 to TRGO-300 could not be calculated because of the diffraction peak of the MSG which has occurred at the same passion as the TRGO. This can be seen on Figure 2 and Figure S1b–d.

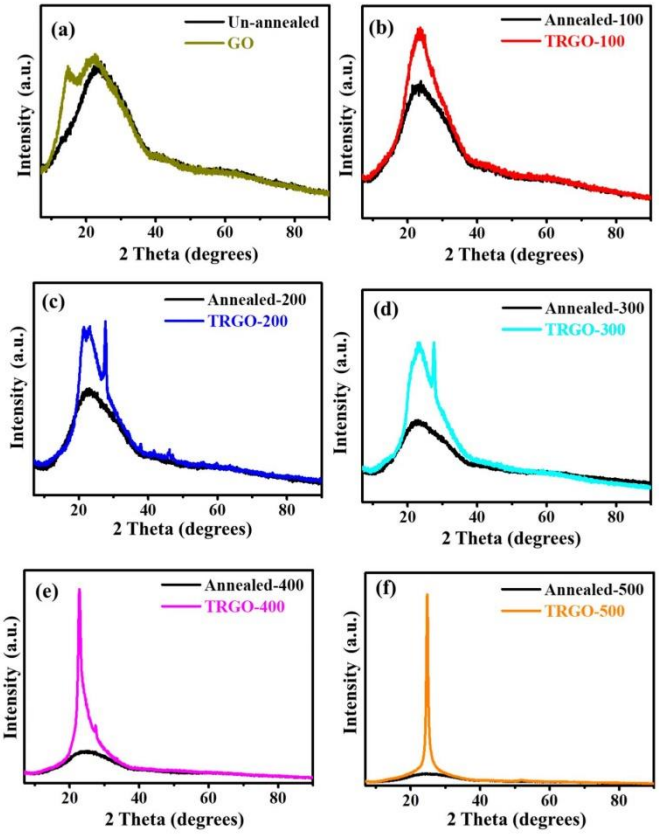

Figure S2. The XRD patterns of (a) GO and **(b)–(f)** TRGO-100 to TRGO-500, plotted together with the diffraction pattern of the microscopic glass under the same conditions.

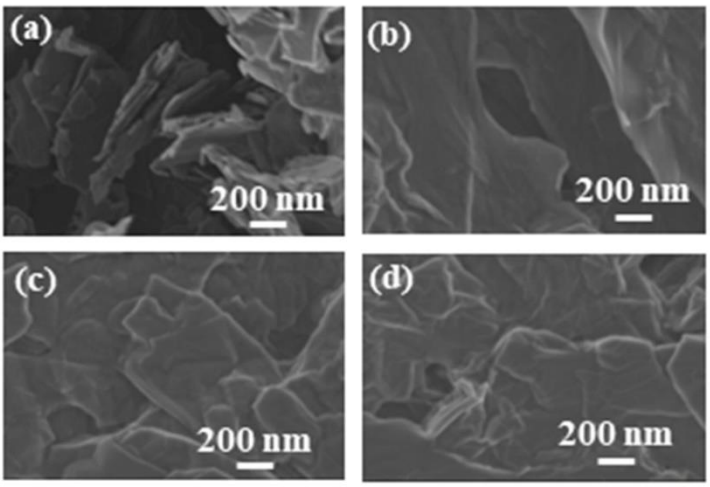

Figure S3. SEM images of (a) graphite, (b) GO, (c) TRGO-300 and (d) TRGO-500.

Surface Topography

The three-dimensional AFM images of the GO and TRGO samples are displayed in Figure S4 (a)–(f), while the corresponding colour scale is displayed in Fig.ureS4 (g) and the Roughness parameter are displayed on Table S1. The AFM of GO and TRGO-100 shows an average sheet height of approximately 1–1.5 μm due to the presence of the surface oxygen functional group. After the thermal reduction process, it can be easily elucidated that average sheet height has dramatically reduced due to the reduced oxygen content encouraging the van der Waals force through the π–π interaction of the adjacent sheet from restacking. The spike-like feathers at TRGO-200 to TRGO-500 are due to the wrinkle and crumbling of the GO sheets during the TR process.

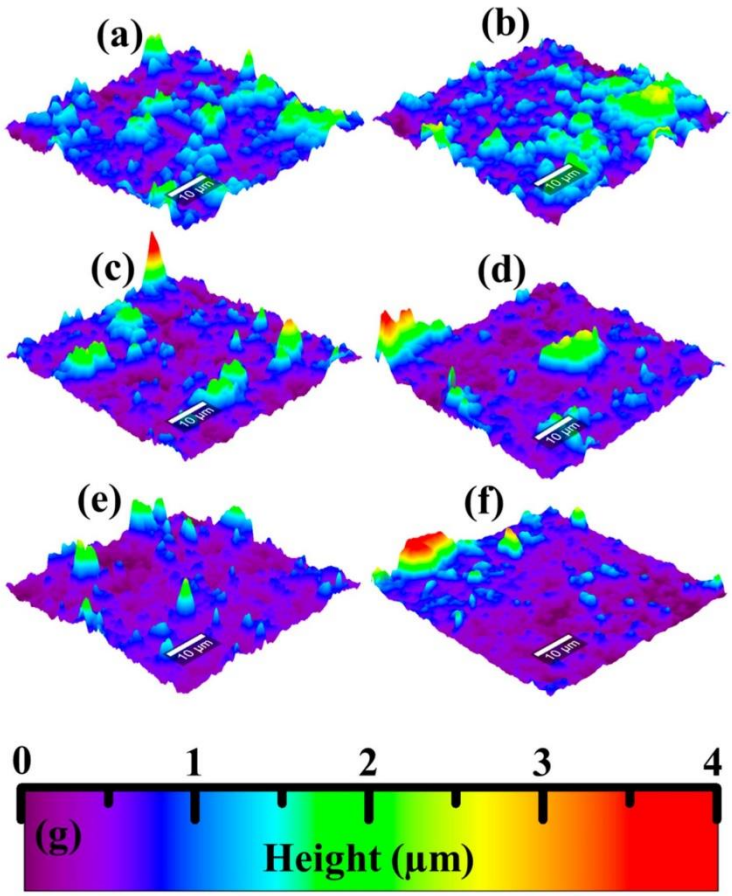

Figure S4. The AFM micrograph of **(a)** GO and **(b)**–**(f)** TRGO-100 to TRGO-500; and **(g)** corresponding height colour scale.

Table S1. Roughness parameter of the prepared GO/TRGO thin film.

Roughness Parameters	GO	TRGO-100	TRGO-200	TRGO-300	TRGO-400	TRGO-500
Number of Pixels	262144	262144	262144	262144	262144	262144
True Area [µm²]	3893.59	3939.16	3886.2	3827.2	3792.93	3803.26
Reference Area [µm²]	3585.95	3585.95	3585.95	3585.95	3585.95	3585.95
SDR [%]	9.11892	10.5894	9.02563	7.27021	6.28532	6.66457
SDQ [nm]	0.442367	0.47824	0.442939	0.408333	0.369572	0.39462
SSC [1/µm]	0.17374	0.191549	0.178306	0.164417	0.158343	0.141028

Table S2. Sample ID, interplanar distance and carbon content.

Sample ID	Interplanar distance (nm)	Carbon content
Graphite	0.3458	-
GO	0.6019	0.068
TRGO-100	-	0.97
TRGO-200	-	2.26
TRGO-300	-	7.05
TRGO-400	0.3864	9.657
TRGO-500	0.3566	11.74

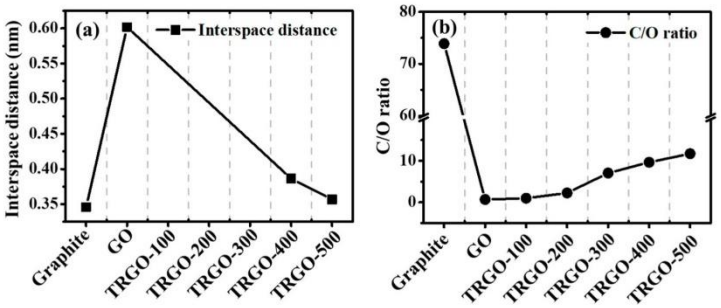

Figure S5. (a) Interspace distance and **(b)** C/O ratio as a function for graphite, GO and TRGO-100, TRGO-200, TRGO-300, TRGO-400 and TRGO-500.

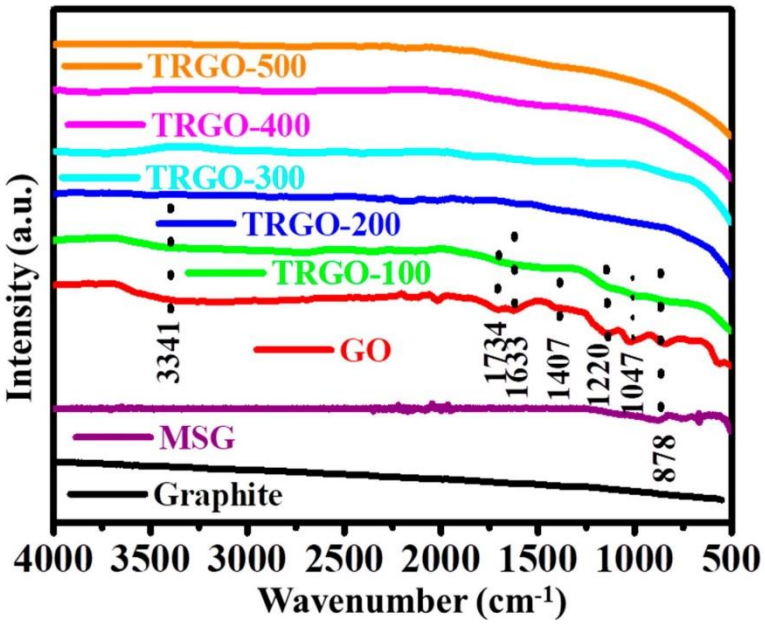

Figure S6. The FTIR of graphite, MSG, GO and TRGO samples.

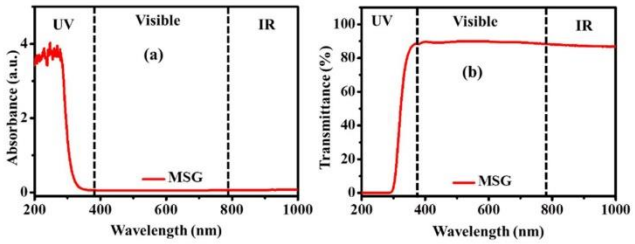

Figure S7. (a) Absorbance and **(b)** transmittance of microscope glass.

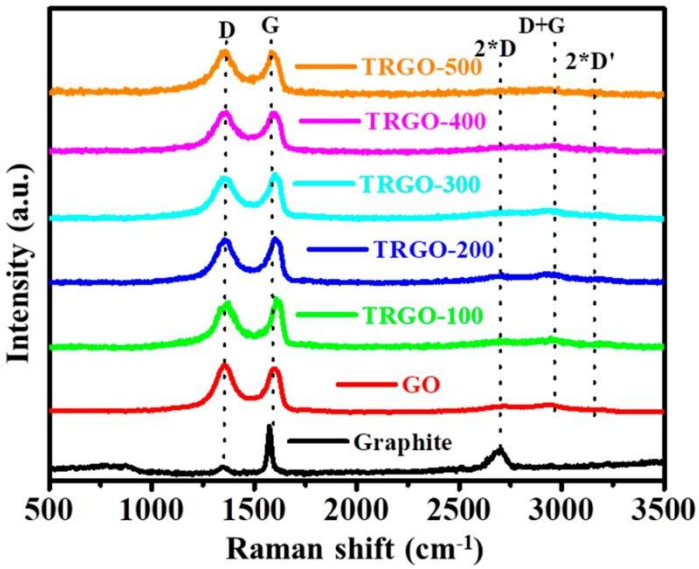

Figure S8. Raman spectra of graphite, GO and TRGO-100–TRGO-500.

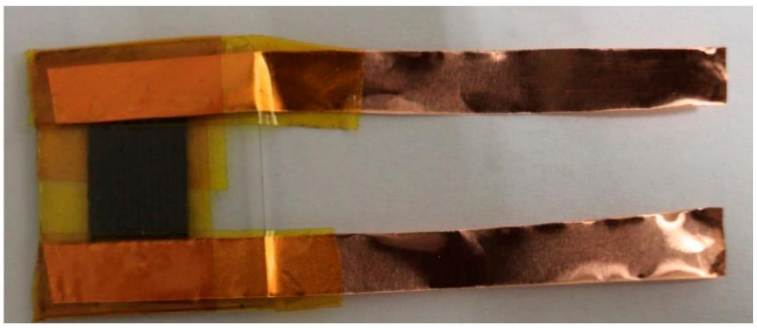

Figure S9. Digital image of μ-SC.

Table S3. Dimensions and parameters of μ-SC.

Parameters	μ-SC
Number of digits per unit area, n (cm^{-2})	14
Width, W (mm)	0.71
Length, L and Breadth, B (mm)	10
Interspace, i(μm)	38
Edge, E (mm)	4
Total surface area (mm^2)	100

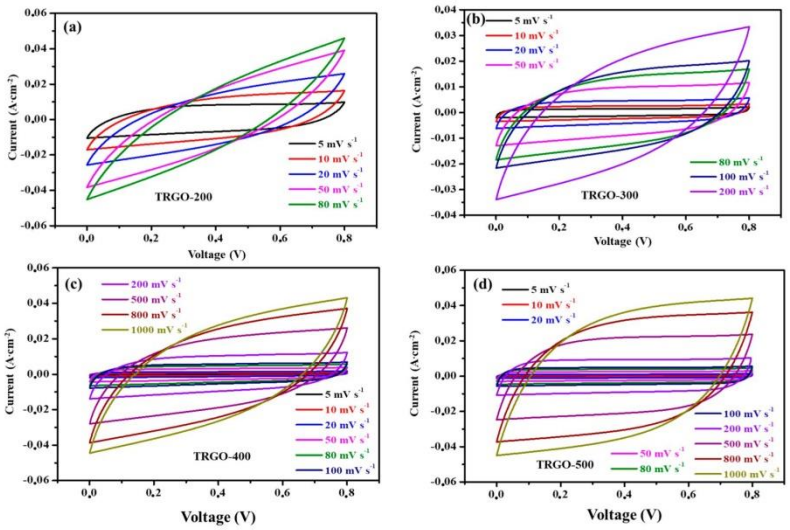

Figure S10 (a)–(d) CV curves of TRGO-200–TRGO-500.

The areal capacitance (C_{Areal}) displayed in Figure 8c and Table S4 of the TRGO samples was estimated from the CV curves using Equation (S1) [1–3]

$$C_{\mathrm{Areal}} = \frac{\int_{V_i}^{V_f} i\,dV}{2\upsilon(V_f - V_i)A} \quad \text{(S1)}$$

where V_f and V_i are the final and initial values of the working potential (v), respectively. i, υ, and A are the current (mA), various scan rate (mVs^{-1}), and total surface area (cm^2) of the μ-SC including the interdigit space.

Table S4. The areal capacitance determined from the CV curve.

Scan rate mV s^{-1}	Areal capacitance (mF cm^{-2})			
	TRGO-200	TRGO-300	TRGO-400	TRGO-500
5	0.7074	0.1451	0.0444	0.0319
10	0.5421	0.1227	0.0382	0.0298
20	0.3773	0.1061	0.0348	0.0274
50	0.2085	0.0865	0.0301	0.0256
80	0.1498	0.0756	0.0282	0.0244
100	-	0.0695	0.0267	0.0239
200	-	0.0506	0.0234	0.0220
500	-	-	0.0179	0.0194
800	-	-	0.0148	0.0172

1000	-	-	0.0140	0.0159
1800				0.0149

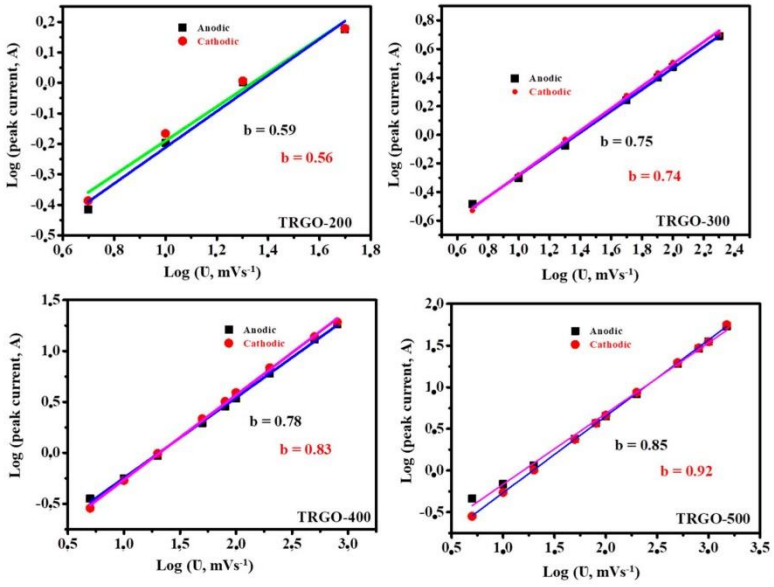

Figure S11. log I versus log υ curves for the anodic and cathodic currents at **(a)** TRGO-200, **(b)** TRGO-300, **(c)** TRGO-400 and **(d)** TRGO-500 reducing temperatures, respectively.

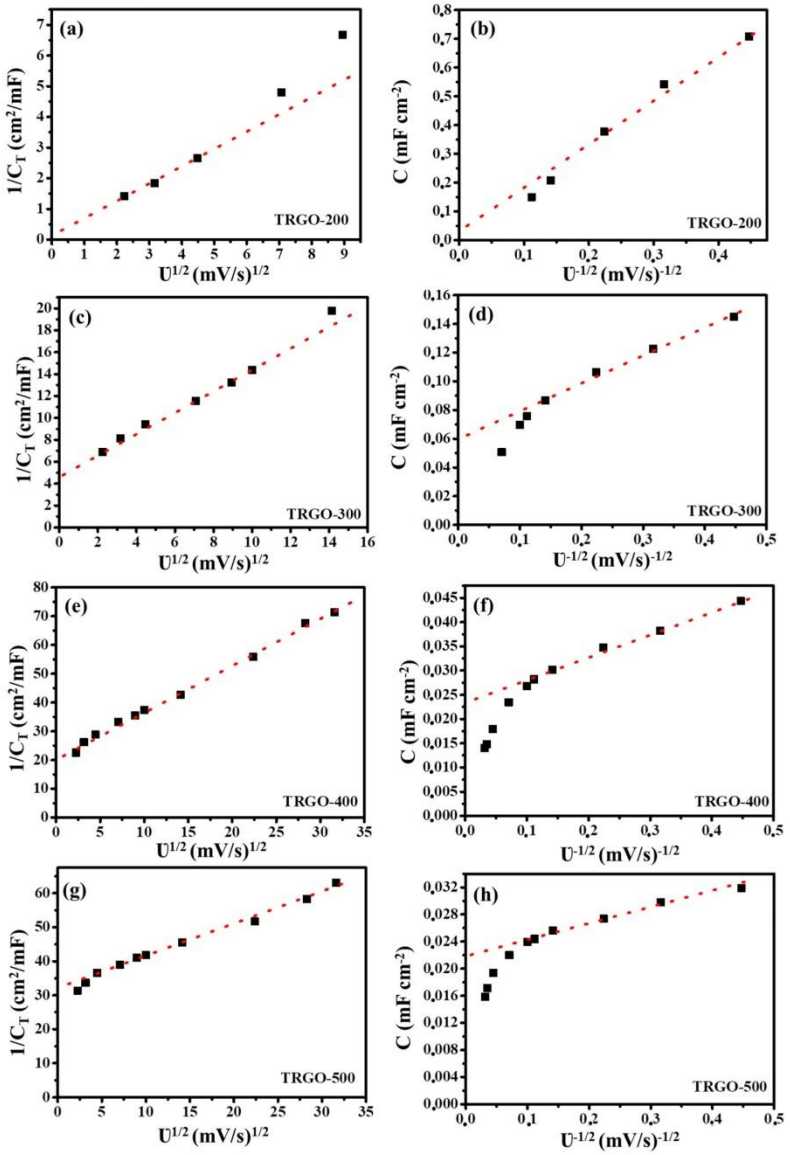

Figure S12 Trasatti's method for the TRGO micro-supercapacitors: **(a,c,e,g)** inverse capacitance as a function of square root of scan rate and **(b,d,f,h)** capacitance as a function of inverse square root of scan rate.

The Equation (S2) was used to calculate the diffusion (C_{pseudo}) contribution.

$$C_{\text{T}} = C_{\text{EDL}} + C_{\text{pseudo}} \quad \text{(S2)}$$

Table S5. Sample ID, maximum total capacitance, maximum EDL capacitance and maximum pseudocapacitance.

Sample ID	C_T (F g^{-1})	C_{EDL} (F g^{-1})	C_{pseudo} (F g^{-1})
TRGO-200	5.6524	0.0334	5.6190
TRGO-300	0.2058	0.0613	0.1445
TRGO-400	0.0497	0.0236	0.0261
TRGO-500	0.0311	0.0222	0.0089

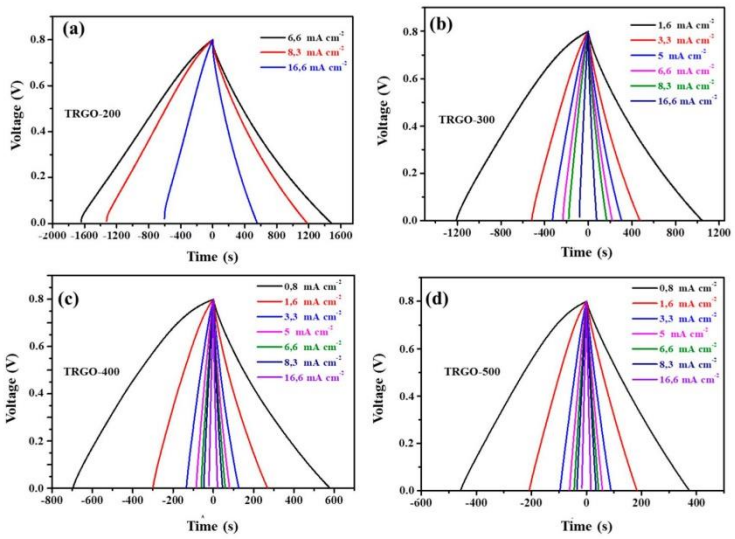

Figure S13. (a)–(d) GCD curves of TRGO-200–TRGO-500.

Table S6. The areal capacitance determined from the GCD curve.

Current density	Areal capacitance (mF cm^{-2})			
(μA cm^{-2})	TRGO-200	TRGO-300	TRGO-400	TRGO-500
0.083	-	-	0.0600	0.0387
0.16	-	0.2143	0.0536	0.0366
0.33	-	0.1952	0.0517	0.0367
0.5	-	0.1904	0.0501	0.0364
0.66	1.2255	0.1809	0.0481	0.0356
0.83	1.2262	0.1754	0.0472	0.0354
1.66	1.1569	0.1506	0.0434	0.0338

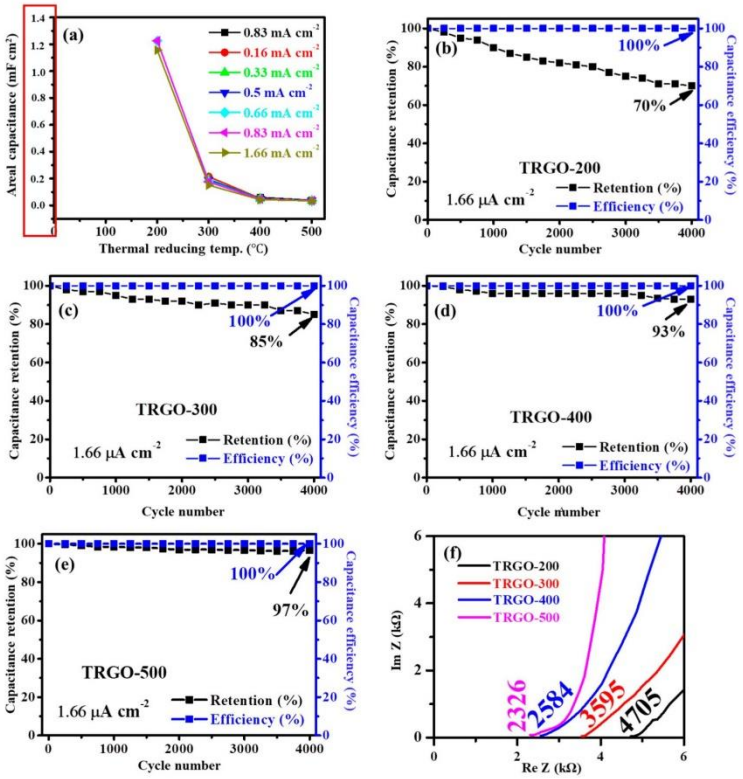

Figure S14. (a) Area capacitance as a function of reducing temperature at various current densities, **(b)–(e)** the capacitance retention and capacitance columbic efficiency of the TRGO sample and **(f)** EIS Nyquist plot at high frequency region.

The areal energy (E_{areal}) and power (P_{areal}) calculated from the below Equations (S3) and (S4)

$$E_{\text{areal}} = \frac{1}{3600\Gamma}\int iVdt \tag{S3}$$

$$P_{\text{areal}} = 3600 \times \frac{E_{areal}}{\Delta t} \tag{S4}$$

where Γ, $\int iVdt$ and Δt are the area or volume of the μ-SC, the integral of the discharge curve and discharge time, respectively.

Table S7. Sample ID, resistance electrolyte plus charge transfer resistance ($R_e + R_{ct}$), Warburg coefficient (σ_w) and ion diffusion coefficient (D).

Sample ID	Maximum specific power (W cm^{-2})	Maximum specific energy (W h cm^{-2})	$R_e + R_{ct}$ (Ω)	σ_w (Ω cm^2 s$^{-0.5}$)	D (cm^2 s^{-1})

TRGO-200	3.4006×10^{-5}	0.5024	4.71236	12.4831±0.002	4.3075×10^{-13}
TRGO-300	4.4506×10^{-5}	0.0183	3.52368	14.6329±0.001	3.1351×10^{-13}
TRGO-400	6.1950×10^{-5}	0.0044	2.53551	21.8812±0.001	1.4021×10^{-13}
TRGO-500	6.8788×10^{-5}	0.0028	2.26279	37.7070±0.002	4.7214×10^{-14}

The impedance ($Z(\omega)$) is expressed by Equation (S5)

$$Z(\omega) = \frac{1}{j\omega \times C(\omega)} \quad \text{(S5)}$$

Therefore,

$$Re\ C = \frac{Im\ Z(\omega)}{\omega|Z(\omega)|^2} \quad \text{(S6)}$$

$$Im\ C = \frac{Re\ Z(\omega)}{\omega|Z(\omega)|^2} \quad \text{(S7)}$$

where $Re\ Z(\omega)$ and $Im\ Z(\omega)$ are defined as

$$|Z(\omega)|^2 = Re\ Z(\omega)^2 + Im\ Z(\omega)^2 \quad \text{(S8)}$$

And

$$\omega = 2\pi f \quad \text{(S9)}$$

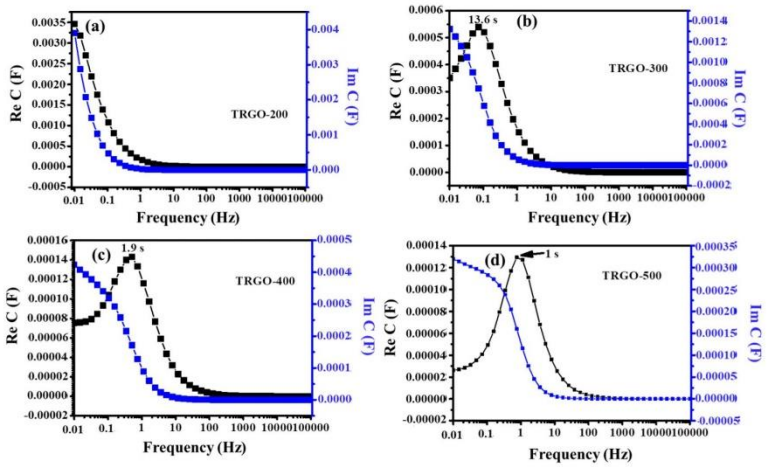

Figure S15. The frequency dependence of the Re C and Im C for **(a)–(b)** TRGO-200 to TRGO-500.

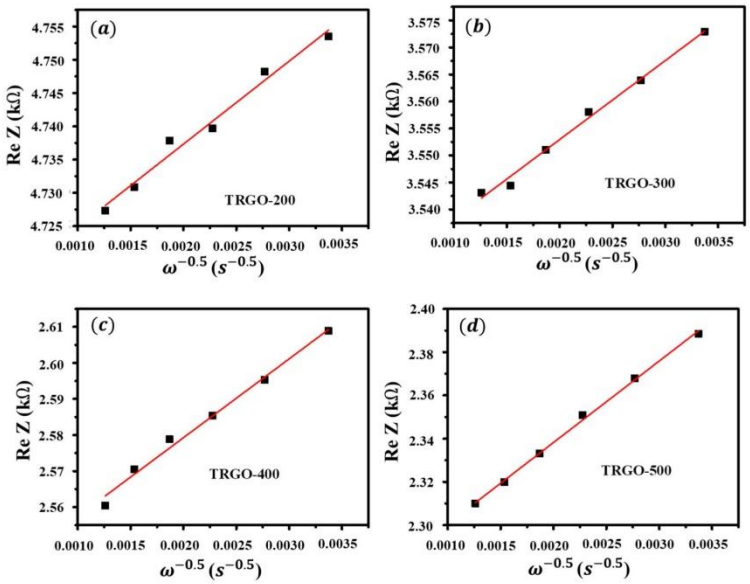

Figure S16. The relationship between Re Z and $\omega^{-0.5}$ at low frequencies for TRGO samples

Equation (S10) [4] was used to calculate ion diffusion coefficient (D)

$$D = 0.5\left(\frac{RT}{AF^2\sigma_w C}\right)^2 \quad \text{(S10)}$$

where R is the gas constant (8.314 J mol^{-1} K^{-1}), T is the temperature (298.5 K), A is the total area (cm^2) of the μ-SC fingers, F is the Faraday's constant (96,500C mol^{-1}) and C is the molar concentration of H^+ ions calculated using Equations (S11) and (S12).

The proton concentration $[H^+]$ of the used PVA/H_3PO_4 electrolyte was calculated using Equations (S11) and (S12).

$$Ph = -\log[H^+] \quad \text{(S11)}$$

$$[H^+] = 10^{-Ph} \quad \text{(S12)}$$

where, the Ph was measured to be 1.64 corresponding to $[H^+]$ of 0.023

Reference

1. Maphiri, V.M.; Rutavi, G.; Sylla, N.F.; Adewinbi, S.A.; Fasakin, O.; Man, N. Novel Thermally Reduced Graphene Oxide Microsupercapacitor Fabricated via Mask—Free AxiDraw Direct Writing. *Nanomaterials* **2021**, *11*, 1909.
2. Liu, L.; Ye, D.; Yu, Y.; Liu, L.; Wu, Y. Carbon-based flexible micro-supercapacitor fabrication via mask-free ambient micro-plasma-jet etching. *Carbon N. Y.* **2017**, *111*, 121–127. https://doi.org/10.1016/j.carbon.2016.09.037.
3. Li, J.; Levitt, A.; Kurra, N.; Juan, K.; Noriega, N.; Xiao, X.; Wang, X.; Wang, H.; Alshareef, H.N.; Gogotsi, Y. MXene-conducting polymer electrochromic microsupercapacitors. *Energy Storage Mater.* **2019**, *20*, 455–461. https://doi.org/10.1016/j.ensm.2019.04.028.
4. Cui, Y.; Zhao, X.; Guo, R. Improved electrochemical performance of La0.7Sr0.3MnO_3 and carbon co-coated LiFePO4 synthesized by freeze-drying process. *Electrochim. Acta* **2010**, *55*, 922–926. https://doi.org/10.1016/J.ELECTACTA.2009.08.020.

4.2.2. Concluding remarks

In brief, we have successful in fabricated TRGOs thin films on MSG via spray coating and AP-CVD annealing process. The XRD of the prepared TRGO thin films showed a decrease of the interspace distance, while the EDS and UV-Vis showed an increase of carbon content and decrease in transparency, respectively as the RT increases. The Raman spectra indicated the presence of D and G peaks commonly observed on carbon based materials such as soot and activated carbon. The 4PP showed an increase in TRGO thin film conductivity as a function of RT. The TRGO thin film was patterned using an AxiDraw sketching apparatus into TRGO µ-SC. The µ-SC with 14 numbers of digits per unit area (cm^{-2}) was found to show better electrochemical properties than those µ-SCs with 4, 22 and 26 digits cm^{-2} due to the increased electric field strength leading to an increase of capacitance. The TRGO-500 µ-SC proved to be a better performing device against µ-SCs reduced at lower temperatures, regardless of the small capacitance due to lack of OFGs that serves as pathways into the bulk material and increase wettability. The increase of temperature resulted in a µ-SC with a better EDLC behaviour and rate capability due to the presence of low resistive oxygen content. The TRGO-500 µ-SC has the smallest relaxation time (τ_O) of 1s, higher phase angle of -85°, diffusion length close to the imaginary impendence, higher CV scan rate and GCD current density range and a CV rate capability of 56% at 1 V s^{-1} indicating exceptional capacitive properties.

Furthermore, the electrochemical performance showed that the TRGO-200 µ-SC has higher areal energy due to more ion diffusion to the internal surface, this was confirmed by the

power law and Trasatti's analysis. While the μ-SCs prepared at higher RT show a lower areal energy, the XRD showed a narrow interplanar distance and lack of OFGs forbids intercalation, thus enhancing surface controlled behaviour leading to an increased areal power also confirmed by the power law and Trasatti's analysis. The ability to vary RT, number of digits per unit area and integrating μ-SC in a series or parallel configuration gives the possibility of controlling the energy and power performance to meet different requirements of the miniaturised devices.

Reference

[1] N.F. Sylla, Activated carbon from peanut shell and its molybdenum based nanocomposites for supercapacitor applications, University of Pretoria, PhD Thesis (2020).

[2] Q. Jiang, Y. Lei, H. Liang, K. Xi, C. Xia, H.N. Alshareef, Review of MXene electrochemical microsupercapacitors, Energy Storage Mater. 27 (2020) 78–95. https://doi.org/10.1016/J.ENSM.2020.01.018.

[3] X. Mao, X. He, J. Xu, W. Yang, H. Liu, Y. Yang, Y. Zhou, Three-Dimensional Reduced Graphene Oxide/Poly(3,4-Ethylenedioxythiophene) Composite Open Network Architectures for Microsupercapacitors, Nanoscale Res. Lett. 14 (2019). https://doi.org/10.1186/s11671-019-3098-4.

[4] M.J. Madito, AB-stacked bilayer graphene films obtained on dilute Cu(Ni) foils using atmospheric pressure chemical vapour deposition, University of Pretoria, PhD Thesis (2016).

[5] V.A. Samson, S.B. Bernadsha, R. Xavier, C.S.T. Rueshwin, S. Prathap, J. Madhavan, M.V.A. Raj, One pot hydrothermal synthesis and characterization of NiFe2O4 nanoparticles, Mater. Today Proc. (2020). https://doi.org/10.1016/j.matpr.2020.07.600.

[6] D.J. Tarimo, K.O. Oyedotun, A.A. Mirghni, N. Manyala, Sulphur-reduced graphene

oxide composite with improved electrochemical performance for supercapacitor applications, Int. J. Hydrogen Energy. 45 (2020) 13189–13201. https://doi.org/10.1016/j.ijhydene.2020.03.059.

[7] C. Karaman, E. Bayram, O. Karaman, Z. Aktaş, Preparation of high surface area nitrogen doped graphene for the assessment of morphologic properties and nitrogen content impacts on supercapacitors, J. Electroanal. Chem. 868 (2020) 114197. https://doi.org/10.1016/j.jelechem.2020.114197.

[8] B. Zhao, P. Liu, Y. Jiang, D. Pan, H. Tao, J. Song, T. Fang, W. Xu, Supercapacitor performances of thermally reduced graphene oxide, J. Power Sources. 198 (2012) 423–427. https://doi.org/10.1016/j.jpowsour.2011.09.074.

[9] Z. Zhu, S. Tang, J. Yuan, X. Qin, Y. Deng, R. Qu, G.M. Haarberg, Effects of Various Binders on Supercapacitor Performances, Int. J. Electrochem. Sci. 11 (2016) 8270–8279. https://doi.org/10.20964/2016.10.04.

[10] B. Xu, H. Wang, Q. Zhu, N. Sun, B. Anasori, L. Hu, F. Wang, Y. Guan, Y. Gogotsi, Reduced graphene oxide as a multi-functional conductive binder for supercapacitor electrodes, Energy Storage Mater. 12 (2018) 128–136. https://doi.org/10.1016/j.ensm.2017.12.006.

[11] Y. Liu, Y. Wang, H. Wang, P. Zhao, H. Hou, L. Guo, Acetylene black enhancing the electrochemical performance of NiCo-MOF nanosheets for supercapacitor electrodes, Appl. Surf. Sci. 492 (2019) 455–463. https://doi.org/10.1016/j.apsusc.2019.06.238.

[12] J. Sun, Y. Zhang, Y. Liu, H. Jiang, X. Dong, T. Hu, C. Meng, Hydrated vanadium pentoxide/reduced graphene oxide-polyvinyl alcohol (V2O5·nH2O/rGO-PVA) film as a binder-free electrode for solid-state Zn-ion batteries, J. Colloid Interface Sci. 587 (2021) 845–854. https://doi.org/10.1016/j.jcis.2020.10.148.

[13] N. Sun, Y. Guan, Y.T. Liu, Q. Zhu, J. Shen, H. Liu, S. Zhou, B. Xu, Facile synthesis of free-standing, flexible hard carbon anode for high-performance sodium ion batteries using graphene as a multi-functional binder, Carbon N. Y. 137 (2018) 475–483. https://doi.org/10.1016/j.carbon.2018.05.056.

[14] N. Radha, A. Kanakaraj, H.M. Manohar, M.R. Nidhi, D. Mondal, S.K. Nataraj, D. Ghosh, Binder free self-standing high performance supercapacitive electrode based on graphene/titanium carbide composite aerogel, Appl. Surf. Sci. 481 (2019) 892–899. https://doi.org/10.1016/j.apsusc.2019.03.086.

[15] A. Moyseowicz, Z. González, R. Menéndez, G. Gryglewicz, Three-dimensional poly(aniline-co-pyrrole)/thermally reduced graphene oxide composite as a binder-free electrode for high-performance supercapacitors, Compos. Part B Eng. 145 (2018) 232–239. https://doi.org/10.1016/j.compositesb.2018.03.018.

[16] N.F. Sylla, N.M. Ndiaye, B.D. Ngom, D. Momodu, M.J. Madito, B.K. Mutuma, N. Manyala, Effect of porosity enhancing agents on the electrochemical performance of high-energy ultracapacitor electrodes derived from peanut shell waste, Sci. Rep. 9 (2019) 1–15. https://doi.org/10.1038/s41598-019-50189-x.

[17] R. Jia, G. Shen, F. Qu, D. Chen, Flexible on-chip micro-supercapacitors: Efficient power units for wearable electronics, Energy Storage Mater. 27 (2020) 169–186. https://doi.org/10.1016/J.ENSM.2020.01.030.

[18] L. Liu, D. Ye, Y. Yu, L. Liu, Y. Wu, Carbon-based flexible micro-supercapacitor fabrication via mask-free ambient micro-plasma-jet etching, Carbon N. Y. 111 (2017) 121–127. https://doi.org/10.1016/j.carbon.2016.09.037.

[19] Y. Wu, Q. Ou, Y. Yin, Y. Li, W. Ma, W. Yu, G. Liu, X. Cui, X. Bao, J. Duan, G. Álvarez-Pérez, Z. Dai, B. Shabbir, N. Medhekar, X. Li, C.M. Li, P. Alonso-González, Q. Bao, Chemical switching of low-loss phonon polaritons in α-MoO3 by hydrogen intercalation, Nat. Commun. 11 (2020). https://doi.org/10.1038/s41467-020-16459-3.

[20] M. Wang, Y. Ma, J. Ye, Controllable layer-by-layer assembly of metal-organic frameworks/polyaniline membranes for flexible solid-state microsupercapacitors, J. Power Sources. 474 (2020) 228681. https://doi.org/10.1016/J.JPOWSOUR.2020.228681.

[21] L.B. Karroubi, S.G. Patnaik, B.D. Assresahegn, B. Bounor, C.C.H. Tran, S.H. Choudhury, D. Bourrier, D. Guay, D. Pech, Highly porous scaffolds for Ru-based microsupercapacitor electrodes using hydrogen bubble templated electrodeposition, Energy Storage Mater. 47 (2022) 134–140. https://doi.org/10.1016/J.ENSM.2022.02.009.

[22] J.O. Omale, R. Rupp, P. Van Velthem, V. Van Kerckhoven, V.A. Antohe, A. Vlad, L.

Piraux, Three-dimensional microsupercapacitors based on interdigitated patterns of interconnected nanowire networks, Energy Storage Mater. 21 (2019) 77–84. https://doi.org/10.1016/J.ENSM.2019.05.025.

Chapter 5 General conclusions and future work

5.1. General conclusion

In this work, the electrochemical performances of TRGO in SC and μ-SC devices were investigated. The TRGO on different substrates i.e. NF and MSG were successfully synthesized using a series of techniques: Oxidation of graphite using Hummers' methods, spraying of GO on MSG or slurry pasting GO on NF, thermally reducing GO on their respective substrate. TRGO on NF was electrochemically tested, while TRGO on MSG was patterned into TRGO μ-SCs then electrochemical tested.

The structural, morphological and electrical properties of the substrates, precursor graphite, intermediate GO, and final material TRGO were characterised using: X-ray diffraction (XRD), Raman spectroscopy, Fourier transform infrared (FTIR) spectroscopy, scanning electron microscopy (SEM), energy-dispersive X-ray spectrometer (EDS), atomic force microscopy (AFM), ultraviolet–visible spectroscopy (UV-Vis), and four point probe (4PP). The XRD analysis of GO showed a successful oxidation of graphite, and that of TRGO on NF and MSG also showed a successful reduction of GO. This was evidenced by the change of peak and also to the peak shift as the reducing temperature increased. Just like in the XRD, the Raman, FTIR, EDS and UV-Vis spectra of GO and TRGO revealed several features such as graphitized carbon material and reduction of OFGs. In addition, EDS analysis of the prepared sample confirmed that carbon and oxygen are the main elements. The SEM images

of the TRGO on NF/MSG showed sheet like material, while the 4PP showed increasing conductivity as the reducing temperature increased.

The electrochemical behaviour of the TRGO/NF was first analysed in a three-electrochemical configuration using different electrolytes (1 M Na_2SO_4, 1 M NaOH and 6 M KOH). The 6 M KOH electrolyte showed the best performance (higher current response) compared to other electrolytes due to the high concentration of OH^- anions and ionic conductivity [1,2]. An asymmetric device was fabricated using TRGO/NF as a positive and PAC as negative electrode i.e. TRGO/NF//PAC device. A detail report of the structural, morphological and electrochemical performance of PAC can be obtained from Ref [3,4]. The prepared asymmetric electrochemical device showed a higher specific energy and power comparable to other similar devices. The fabrication method used in this work gave a symmetric μ-SC and the obtained electrochemical performances are comparable with those in the published reports as shown in Figure 5.1. The TRGO-500 μ-SC has volumetric energy and power densities similar to those reported in Refs. [5–7] including lithium film batteries. This simple method produces μ-SC device with similar energy and power to those device's prepared via a complex and sophisticated method.

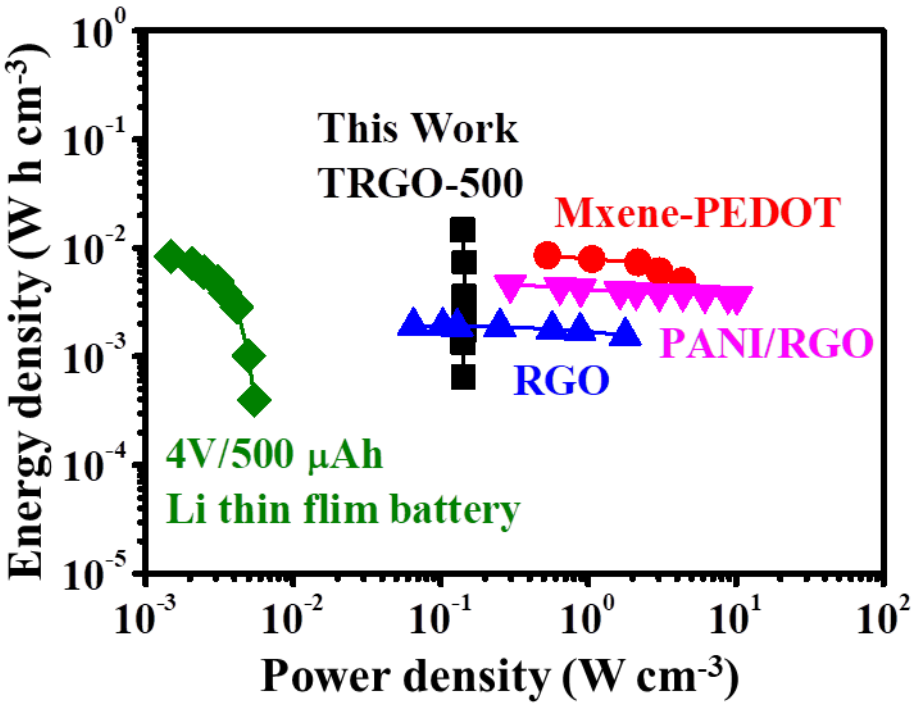

Figure 5.1. Ragone plot of the TRGO-500 µ-SC compared to other similar devices

5.2. Future work

In future work, a negative carbon based electrode fabricated using binder and conductive enhancer-free route will be developed and electrochemically investigated for supercapacitor application. These will lead to the proper electrochemical investigation of additive free SC devices. Different electrolytes will be investigated with an aim of trying to extend the operating potential window, subsequently leading to an increased capacitance leading to

higher specific energy. In addition, heteroatom doping with elements such as nitrogen and sulphur will be investigated.

Furthermore, heteroatom doping and composite material of TRGO will be used to prepare mask free doped TRGO µ-SCs. The heteroatom or metal oxide/polymer will increase the specific energy. The Axidraw will be used to pattern TRGO µ-SCs array, this will give the TRGO µ-SCs an increased potential window and specific energy, since in arrays, devices can be connected in parallel and series configurations.

References

[1] M.N. Rantho, M.J. Madito, N. Manyala, Symmetric supercapacitor with supercapattery behavior based on carbonized iron cations adsorbed onto polyaniline, Electrochim. Acta. 262 (2018) 82–96. https://doi.org/10.1016/j.electacta.2018.01.001.

[2] Y. He, J. Pan, L. Wu, Y. Zhu, X. Ge, J. Ran, Z.J. Yang, T. Xu, A novel methodology to synthesize highly conductive anion exchange membranes, Sci. Rep. 5 (2015). https://doi.org/10.1038/srep13417.

[3] N.F. Sylla, Activated carbon from peanut shell and its molybdenum based nanocomposites for supercapacitor applications, University of Pretoria, PhD Thesis (2020).

[4] N.F. Sylla, N.M. Ndiaye, B.D. Ngom, D. Momodu, M.J. Madito, B.K. Mutuma, N. Manyala, Effect of porosity enhancing agents on the electrochemical performance of high-energy ultracapacitor electrodes derived from peanut shell waste, Sci. Rep. 9 (2019) 1–15. https://doi.org/10.1038/s41598-019-50189-x.

[5] J. Li, A. Levitt, N. Kurra, K. Juan, N. Noriega, X. Xiao, X. Wang, H. Wang, H.N. Alshareef, Y. Gogotsi, MXene-conducting polymer electrochromic microsupercapacitors, Energy Storage Mater. 20 (2019) 455–461. https://doi.org/10.1016/j.ensm.2019.04.028.

[6] S. Park, H. Lee, Y.-J. Kim, P.S. Lee, Fully laser-patterned stretchable microsupercapacitors integrated with soft electronic circuit components, NPG Asia Mater. 10 (2018) 959–969. https://doi.org/10.1038/s41427-018-0080-z.

[7] M. Gao, X. Dong, K. Wang, W. Duan, X. Sun, C. Zhu, W. Wang, Laser direct preparation and processing of graphene/MnO nanocomposite electrodes for

microsupercapacitors, J. Energy Storage. 33 (2021) 102162. https://doi.org/10.1016/j.est.2020.102162.